PATTERNED HUMAN PRIMITIVE HEART ORGANOIDS GENERATED BY PLURIPOTENT STEM CELL SELF-ORGANIZATION TO STUDY HUMAN HEART DEVELOPMENT AND DISEASE

By

Brett Douglas Volmert

A DISSERTATION

Submitted to
Michigan State University
in partial fulfillment of the requirements
for the degree of

Biomedical Engineering – Doctor of Philosophy

2024

ABSTRACT

Pluripotent stem cell-derived organoids can recapitulate significant features of organ development *in vitro*. We hypothesized that organoids thus created can be made substantially more relevant by mimicking aspects of *in utero* gestation, leading to higher physiological and anatomical resemblance to their *in vivo* counterparts. This dissertation introduces developmentally inspired methodologies to differentiate early human heart organoids into patterned heart tube organoids in a reproducible and high-throughput fashion by self-organization. Our strategy is based on controlled and stepwise exposure to crucial metabolic and hormonal factors eliciting important molecular, cellular, morphological, and functional changes in heart organoids over a 10-day period consistent with human cardiac development. Single-cell transcriptomics revealed the emergence of all cell types present in the developing heart tube, and past this stage. Structurally, heart organoids developed distinct atrial and ventricular chambers, a polarized proepicardial organ and anterior-posterior patterning due to endogenous retinoic acid signaling, mimicking the developmental processes found in the primitive heart post heart tube formation. Moreover, we showed the importance of our system for disease modeling by exploring the effects of ondansetron, a drug administered to pregnant women and associated with congenital heart defects, on embryonic heart development. Taken together, our results constitute a significant technical advance in human synthetic development and provide a powerful tool for cardiac disease modeling and pharmacological studies.

This dissertation is dedicated to my grandparents, my parents, my brothers, and my fiancée for being the foundation of my life, for providing essential support and guidance, for being lifelong friends, and for teaching me what it means to live.

ACKNOWLEDGEMENTS

I would like to thank Dr. Aitor Aguirre for his guidance and mentorship throughout my time at MSU, members of my committee: Dr. Christina Chan, Dr. Adam Lauver, and Dr. Wen Li, and all members of the Aguirre lab both past and present.

Special thanks to Yoni Lewis Israeli, who was a tremendous help in teaching me the basics of cell culture, organoid biology, and lab techniques upon my entry into the lab; Aaron Wasserman, who was a great scientific mentor; Kristen Ball, Amanda Huang, and Lauren Squire who were all incredible lab managers and helped the lab in myriad fashions including cell culture, lentiviral work and qPCR; Erin Bosman and Ashlin Riggs, who aided my projects in countless ways including protocol troubleshooting, data analysis, cell culture, and scRNA-seq analysis; and Colin O'Hern, Aleksandra Kostina, Priyadarshni Muniyandi, Freyda Mannering, and Shakhlo Aminova who all boosted lab morale, were always there for weekday and weekend help, and were great friends.

This work would not have been possible without our myriad collaborators, including: Dr. Chao Zhao's lab at Washington University in St. Louis with Fei Wang and Yixuan Ming who performed OCT imaging and analysis; Dr. Zhen Qiu's lab at Michigan State University with Aniwat Juhong and Yifan Li who performed microelectronics recordings, including OCT, Raman, and lightsheet imaging; Dr. Wen Li's lab at Michigan State University with Weiyang Yang and Xiang Liu who performed microelectrode array recordings; Dr. Sangbum Park, Dr. Artem Kiselev, Dr. Sudin Bhattacharya, and Vishal Panda for their assistance with scRNA-seq analyses.

I’d also like to thank the Genomics Core for their sequencing services and the Center for Advanced Microscopy, including Dr. Melinda Frame for her reliability and kindness surrounding the use of the confocal microscope lab and imaging techniques.

Work in Dr. Aguirre’s laboratory was supported by startup funds from MSU, the NIH under award numbers K01HL135464, R01HL151505, by the American Heart Association under award number 19IPLOI34660342 and by the Spectrum-MSU Foundation. Work in Dr. Zhou’s laboratory was supported by a startup funds from Washington University in St. Louis and NIH grants R01EB025209, R01HL156265 and R21EB03268401A1. Work in Dr. Qiu’s laboratory was supported by startup funds from MSU and the U.S. National Science Foundation (1808436, 1918074). Work in Dr. Park’s lab was supported by startup funds from MSU and by MSU’s Discretionary Funding Initiative.

TABLE OF CONTENTS

LIST OF ABBREVIATIONS

ACM	Atrial Cardiomyocytes
ANOVA	Analysis of Variance
APD30	Action Potential Duration 30
APD90	Action Potential Duration 90
BMP4	Bone Morphogenetic Protein 4
BSA	Bovine Serum Albumin
CC	Conductance Cells
cDNA	Complementary Deoxyribonucleic Acid
CHD	Congenital Heart Defect
CPC	Cardiac Progenitor Cells
CT	Computed Tomography
CVD	Cardiovascular Disease
DEAB	4-diethylaminobenzaldehyde
DMSO	Dimethyl Sulfoxide
DNA	Deoxyribonucleic Acid
EC	Endothelial Cells
ECM	Extracellular Matrix
EMM1	Enhanced Maturation Medium 1
EMM2	Enhanced Maturation Medium 2
EMM2/1	Enhanced Maturation Medium 2/1
EPC	Epicardial Cells
ESC	Embryonic Stem Cell
FCCP	Trifluoromethoxy Carbonylcyanide Phenylhydrazone
FDA	Federal Drug Administration
FHF	First Heart Field
FITC	Fluorescein Isothiocyanate
GD45	Gestational Day 45
GFP	Green Fluorescent Protein

GO	Gene Ontology
hERG	Human Ether-a-go-go Related Gene
hESC	Human Embryonic Stem Cell
hiPSC	Human Induced Pluripotent Stem Cell
hPSC	Human Pluripotent Stem Cell
Hz	Hertz
IGF1	Insulin-like Growth Hormone 1
iPSC	Induced Pluripotent Stem Cell
MM	Maturation Medium
MRI	Magnetic Resonance Imaging
mRNA	Messenger Ribonucleic Acid
ms	Millisecond
NIH	National Institutes of Health
OCT	Optical Coherence Tomography
PBS	Phosphate Buffered Saline
PCA	Principal Component Analysis
PCR	Polymerase Chain Reaction
PEDC	Proepicardial-derived Cells
PSC	Pluripotent Stem Cell
PVDF	Polyvinylidene Difluoride
QC	Quality Control
qPCR	Quantitative Polymerase Chain Reaction
RA	Retinoic Acid
RNA	Ribonucleic Acid
Rot/AA	Rotenone/Antimycin A
RT-qPCR	Real Time Quantitative Polymerase Chain Reaction
SC	Stromal Cells
scRNA-seq	Single Cell RNA Sequencing
SHF	Second Heart Field
T3	Triiodothyronine

UMAP	Uniform Manifold Approximation and Projection
UMI	Unique Molecular Identifier
VC	Valve Cells
VCM	Ventricular Cardiomyocytes
WGA	Wheat Germ Agglutinin
3D	Three Dimensional

CHAPTER 1: INTRODUCTION

1.1. CARDIOVASCULAR DISEASE AND CONGENITAL HEART DISEASE

Cardiovascular diseases (CVDs), including disorders of the heart and blood vessels, are the leading causes of death globally, contributing to over 18 million deaths annually[1–3] (**Figure 1**).

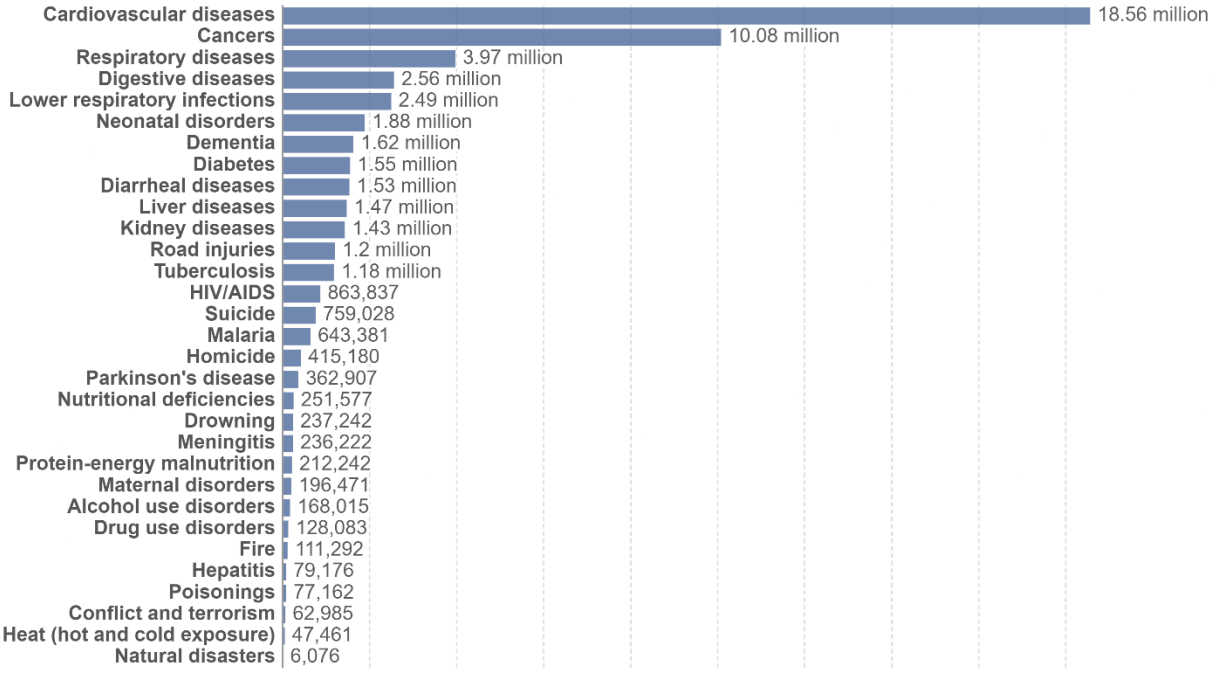

Figure 1. Global causes of death in 2019. Data and figure obtained from ourworldindata.org.[2]

In 2011, the American Heart Association predicted that by 2030, more than 40% of Americans would suffer from some form of CVD. In fact, this burden was reached only four years later in 2015. By the year 2035, it is estimated that nearly 50% of Americans will have CVD, and that CVDs will contribute to over 1 trillion US dollars in total costs, an incredible financial burden to economic systems.[4] Additionally, congenital heart defects (CHDs) are the most common type of birth defect in the United States, with over 40,000

newborns being born with a heart defect each year. In fact, CHDs are the leading cause of death in the first year of infant life.[5] A major hurdle towards human-relevant study of CVDs and CHDs lies in the ethical hurdles that surround the acquisition of both adult and fetal heart tissue.[6] Heart disease can be multifaceted in origin, with both genetic and epigenetic contributions playing major and incompletely understood roles.[7] Taken together, CVDs and CHDs remain major detriments to human health and require novel solutions to address this current heart health crisis.

1.2. MODELING THE HEART IN VITRO AND IN VIVO

Cardiovascular research can be broadly categorized into two main facets: *in vitro* (cellular) models and *in vivo* (animal) models. The utility of *in vitro* cardiovascular models itself is multifaceted. Both human and animal-derived cells are used, cells can be of cardiac or extracardiac origin, and the models themselves can be either two dimensional (2D) or three dimensional (3D). Human cells used for cardiovascular research typically consist of primary cardiomyocyte culture or hPSC-derived cardiomyocytes (**Figure 2**).

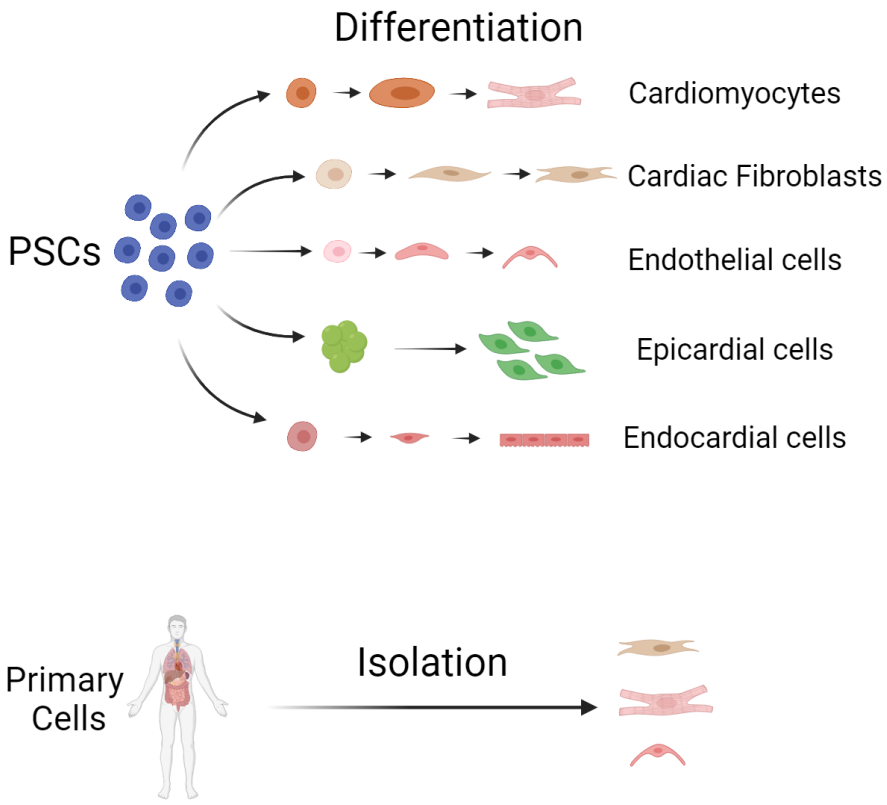

Figure 2. Pluripotent stem cell-derived cardiac cells and primary cardiac cells. Created with BioRender.com.

Primary cardiomyocytes are derived from human donor hearts and are cultured for a limited time *in vitro*. hPSC-derived cardiomyocytes can either be derived from hESCs or hiPSCs and represent the origin of a nearly unlimited source of cardiac cells. PSCs are cells that have the potential to differentiate into a wide range of cell types from all three germ layers, the mesoderm, endoderm, and ectoderm. PSCs have an indefinite capacity for self-renewal, opening the door to a wide range of biotechnological advancements in regenerative medicine, disease modeling, and therapeutic applications. ESCs are derived from the inner cell mass of the blastocyst, an early stage of embryonic development. As such, ESCs have implicit ethical considerations. However, the field of PSCs was transformed in 2008 when Shinya Yamanaka and Kazutoshi Takahashi published their

work on PSC reprogramming.[8] Here, they described a method for the encoding and expression of four transcription factors, Klf4, Oct4, Sox2, and c-MYC that control and override a cell's somatic identity and create a pluripotent-like cell – birthing the term "induced pluripotent stem cells" **(Figure 3**). These iPSCs demonstrated the capacity to differentiate into cell derivatives from all three germ layers, including cardiac tissue. Patient-specific iPSCs can be created from any person, causing an explosion in *in vitro* precision medicine and disease modeling research.

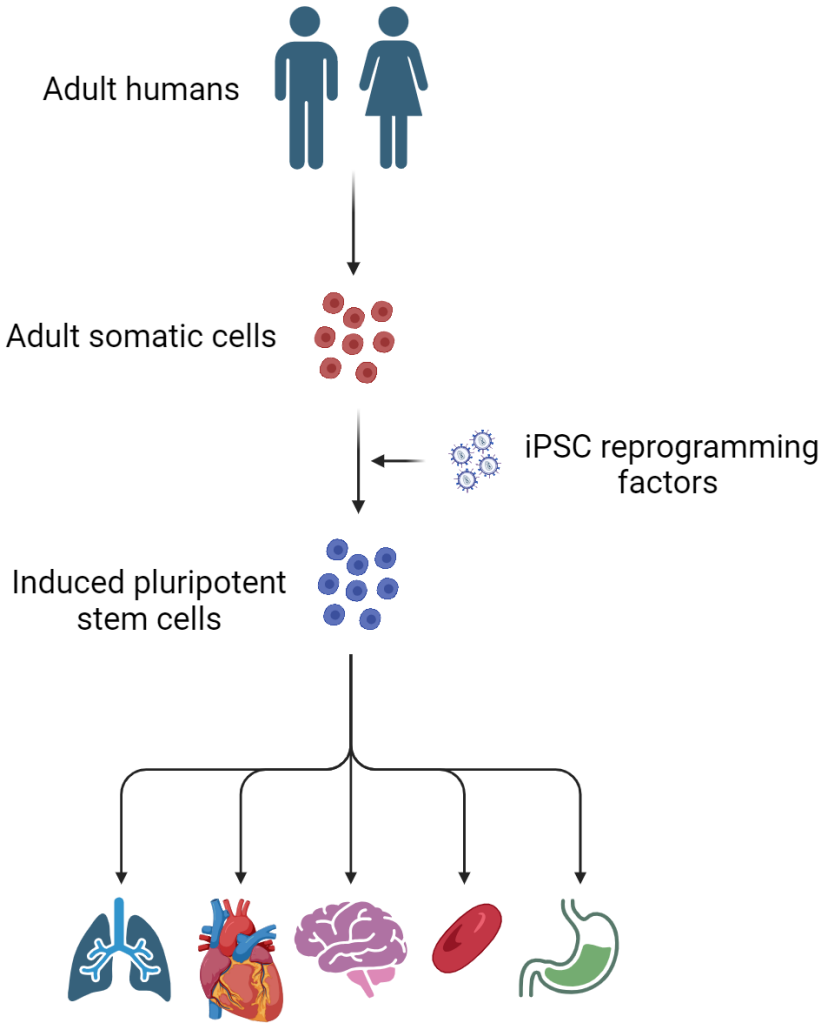

Figure 3. iPSC reprogramming for multi-lineage differentiation. Created with BioRender.com.

In vitro hESC and hiPSC cardiomyocyte derivation protocols typically consist of a temporal modulation of the Wnt or GSK3 pathways[9] - a transcriptional regulation cascade that orchestrates cardiac development *in utero* - or by manipulating proteins in the transforming growth factor beta superfamily.[10] Taking this one step further, PSC-derived cardiomyocyte protocols now exist for the generation of atrial[11], ventricular[12,13], nodal[14], and even compacted cardiomyocytes[15]. Even further, derivation methods for epicardial cells[16,17], cardiac fibroblasts[18], cardiac stromal cells[19], and endothelial cells[20] are routinely used (**Figure 2**). Creating a vast repository and platform for specific cardiac cell type investigation *in vitro* has never been more accessible. These platforms have been used to investigate cardiovascular diseases like long QT syndrome[21], arrhythmogenic right ventricular cardiomyopathy[22], dilated or hypertrophic cardiomyopathy[23–25], left ventricular non-compaction cardiomyopathy[26], hypoplastic left heart syndrome[27], Duchenne muscular dystrophy[28], and many more with increasing precision.

Cardiovascular phenotypes are not always studied with cardiac cells *in vitro*. For pharmaceutical studies, human embryonic kidney cells are used for their longevity, robustness, and ease of use. These cells are engineered to express cardiac ion channels on their membranes, such as the hERG channel, to study the potential off-target electrical effects of drugs.

The approaches to *in vitro* cardiovascular research described above are all routinely performed in a 2D manner. However, in recent years, 3D *in vitro* cardiovascular research has reached new heights thanks to advances in tissue engineering, 3D printing, and microfabrication. A variety of approaches to 3D culture are taken, with the most popular being cardiac spheroids and scaffold-based engineered heart tissue (EHT) (**Figure 4**).

Cardiac spheroids are commonly employed as spherical aggregates of cells that are free-floating in solution, with either only cardiomyocytes as the cell population[29], or a multi-cellular population consisting of cardiomyocytes, fibroblasts, or other cardiac cell types[30,31]. In a recent study, Richards et al. used human cardiac spheroids to model the effects of myocardial infarction *in vitro* by combining iPSC-derived cardiomyocytes with human primary ventricular fibroblasts, human umbilical vein endothelial cells, and human adipose-derived stem cells to form spherical aggregates and found that these structures could model cardiac infarcts by quantifying hypoxia response through confocal microscopy, RNA sequencing, metabolic assays, ECM protein distribution, tensile strength, and calcium handling. On the other hand, EHTs utilize scaffolds of biomaterials or other ECM proteins for cell attachment. Successful EHT systems include Heart-Dyno[32], Biowire[33], anisotropic nanofibrous ventricular constructs[34], and other hydrogel-based platforms[35]. These systems employ sophisticated engineering approaches for their generation, culture, or measurement, such as elastomeric posts for mechanical force generation and measurement (Heart-Dyno), polydimethylsiloxane (PDMS) and type 1 collagen channels with electrical stimulation (Biowire), and electrospinning (anisotropic nanofibrous ventricular constructs). Another 3D culture field of rising popularity is the field of organoids, in which ESCs are differentiated to mimic embryonic development. This field will be discussed in a subsequent section.

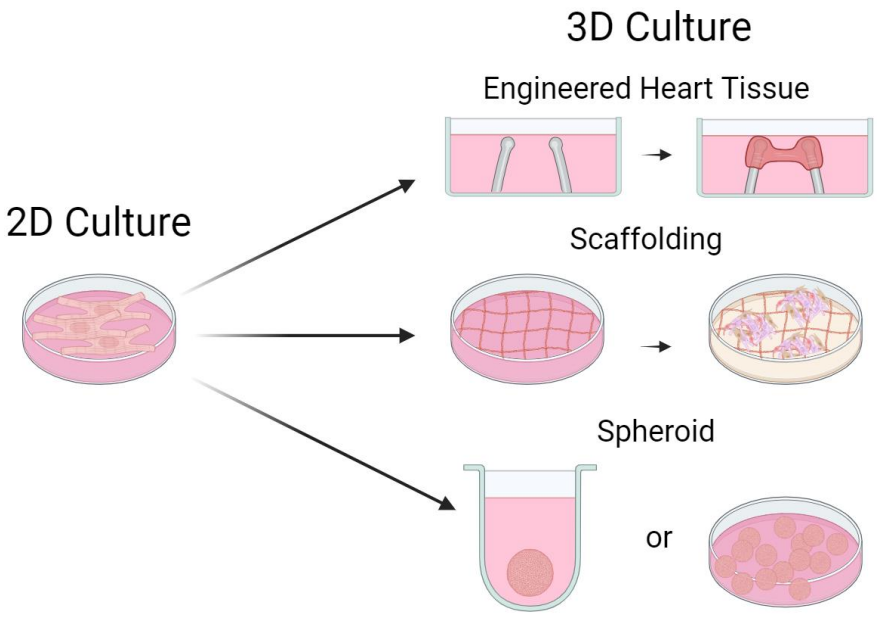

Figure 4. 2D cell culture compared to 3D cell culture approaches. Created with BioRender.com.

In addition to human cells, animal-derived cardiomyocytes and ESCs are used for *in vitro* cardiovascular research. In recent studies, mouse ESCs were utilized to study mouse heart development *in vitro*, where the authors showed atrioventricular chamber specification[36], and cardiac crescent formation[37].

Aside from studies performed *in vitro*, *in vivo* animal models are perhaps one of the most traditional methods for cardiovascular research, as they stand as pillars for systems biology and toxicology studies. Commonly, mice, rats, sheep, pigs, and zebrafish are used to study heart development and disease due to their developmental similarity to human hearts. For example, mice models have been used to model coronary artery disease[38], myocardial infarction[39], dilated cardiomyopathy[40], and lipidemia[41]. Meanwhile, sheep studies have shown the sexual dimorphisms of heart development and disease[42], and zebrafish experiments have shown the regenerative capacity of zebrafish hearts

following myocardial infarction and potential compounds or molecules to activate this regenerative capacity in humans[43]. For decades, proving the safety and efficacy of pharmaceuticals was a requirement by the FDA for clinical trials. However, this is no longer true due to the amendment of the FDA Modernization Act 2.0 which allows for greater utility of *in vitro* systems to be used for this process.

Of note, an additional, emerging category of cardiovascular research is computational cardiology or *in silico* cardiology. Here, computational models simulate heart development and disease, predict the efficacy or toxicity of a potential drug candidate, and are routinely used in the clinic for MRI, CT and echocardiograms.

1.3. ADVANTAGES AND LIMITATIONS OF CURRENT HEART MODELS

CVD research has grown exponentially over recent years thanks to the advancement of myriad model systems and methods. For decades, *in vitro* research has been performed in 2D formats due to its ease of culture and maintenance, rapid and high-throughput analytical methods, and cost-effective materials used. These monolayer culture approaches have yielded significant findings and model systems for the identification of novel cardiac therapeutics and even drivers of cardiovascular disease. Nonetheless, these approaches are limited by their ability to fully reflect and model the total complexity of the human heart, including a lack of physiological morphology, simplistic or irrelevant ECM, lack of multiple relevant cardiac cell types, and the absence of cell-cell signaling – all of which contribute immensely to proper *in vivo* cardiac development and physiology, and are large contributors or indicators of CVDs. Primary cardiomyocytes can offer mature and authentic insights to adult physiology with established protocols for their isolation, but suffer from limited culture times, difficulty acquiring samples, and variability

between donors. On the other hand, PSC-derived cardiomyocytes and PSC-derived cardiac cells offer a near-unlimited sources of cells, but suffer from immature structural, metabolic, or functional phenotypes, and differentiation protocols remain in their infancy. The *in vivo* heart possesses much more complexity than monolayer systems can provide.

Along the same lines, human embryonic kidney cells and other genetically engineered non-cardiac cells are extremely limited in their physiological relevance and are strictly used to screen the potential cardiotoxicity of early drug candidates due to their robustness and simplicity of culture and maintenance requirements.

Attempts to answer this lack of complexity have arisen in spheroid and EHT technologies. Here, typically, multiple cardiac cell types are cultured together as a “coculture” system, which increases the physiological relevance of the tissue (**Figure 5**). Additionally, often, a relevant cardiac ECM protein, such as fibronectin or collagen IV, is used as a scaffold for cell attachment or molding. Further, EHTs can introduce alignment of cardiomyocytes to encourage proper, physiological anisotropic fiber formation and conduction velocity. While these steps certainly represent a step forward for proper cardiovascular modeling, they fall short in their lack of completely recapitulating the cellular make-up of the human heart, which consists of over 11 unique, major populations of cells, including atrial, nodal, and ventricular cardiomyocytes, epicardial and proepicardial-derived cells, cardiac fibroblasts, neuronal and conductance cells, endocardial cells, endothelial cells, immune cells and more. Multicellular spheroids and EHTs can certainly aid in studying the specific interactions and effects between two or three unique cell types, but ultimately lacks too many cell types, spatial organization, and anatomical features to accurately model the full picture of heart development or disease. Moreover, while the utility of cardiac-relevant

ECM proteins can increase the physiological relevance and behavior of EHTs, there are many cardiac ECM proteins that play unique functions in cardiac disease and development, such as fibronectin, collagen I, III, and IV, elastin, laminin and even other nonstructural ECM proteins like periostin and perlecan. In fact, a large part of the cardiac ECM is secreted by cardiac fibroblasts and other mesenchymal cells endogenously – a facet of human physiology that is often ignored in *in vitro* cardiac tissue engineering designs.

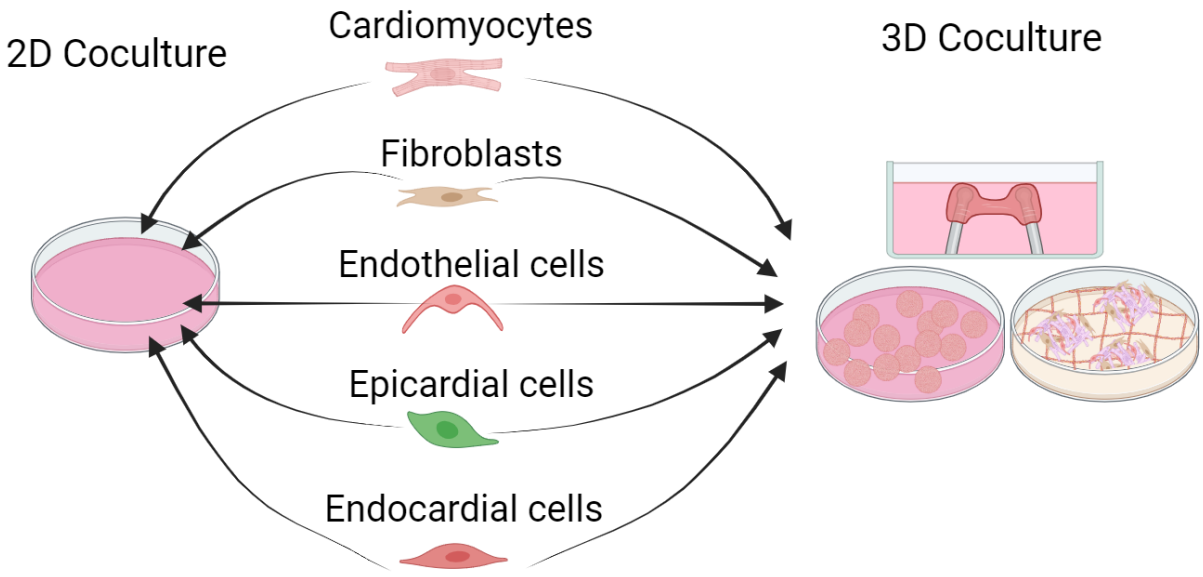

Figure 5. 2D and 3D coculture of cardiac cells in vitro. Created with BioRender.com.

Animal derived cells offer the advantages of mitigating ethical concerns related to the acquisition of hESCs and their ability to be compared with *in vivo* animal-based studies. Nonetheless, alternative *in vitro* approaches such as hiPSCs avoid the ethical dilemma surrounding hESCs while also providing human-relevant material.

While human-relevant *in vitro* research has expanded in novelty and physiological relevance, a large drawback to consider is the isolated and static nature of *in vitro* models compared to *in vivo* physiology encompassing the circulatory system, endocrine signaling, organ-organ crosstalk, drug metabolism, and responses to external stimuli. In these fashions, *in vivo* research can be thought superior to *in vitro* research. However, the subjects of *in vivo* research are animals, not humans. While animals do offer the aforementioned advantages over *in vitro* methods, it is important to consider the inherent and distinct differences of animal physiology to human physiology. For example, a mouse's heart has a resting heart rate that is 10-fold higher than a human's, and the mouse QT interval is only 13% that of the average human (~45 ms vs. 350-450 ms).[44,45] Further, while zebrafish offer invaluable insights towards cardiac regeneration, zebrafish only have a single atria and ventricle – a vastly different architecture compared to human physiology.

Computational cardiology allows for a personalized approach to medicine and offers precise insights into cardiac physiology. Additionally, it offers the ability to test scenarios that may be difficult or unethical to study *in vivo* and facilitate screening of a nearly unlimited amount of drug candidates. However, the data available to create accurate models, paired with the mechanistic and physiological complexity of the human heart offer distinct challenges.

1.4. MATURATION OF IN VITRO CARDIAC SYSTEMS

Increasing physiological complexity and mimicry has been at the forefront of cardiac medicine for decades. Unfortunately, a major bottleneck to *in vitro* cardiac research is the immaturity of PSC-derived cells compared to their *in vivo* counterparts. Cardiomyocytes

in vivo possess distinct structure, metabolism, and functionality that orchestrate their physiological behavior (**Figure 6**). Structural features of mature cardiomyocytes include anisotropic, aligned fiber morphology, rod-shaped cell structures, aligned, long sarcomeres (~2.2 um between z-disks), and large mitochondria near or interspersed within sarcomeres. Metabolic features of *in vivo* cardiomyocytes include increases in *PPARGC1A* (master regulator of mitochondrial biogenesis) and *CPT1B* (gene encoding the principal transporter of fatty acids into mitochondria) expression and a distinct utilization of fatty acid oxidation for energy generation instead of glycolysis. Functional characteristics of mature cardiomyocytes include increases in contractile force, robust presence of t-tubules, and increased action potential duration and upstroke velocities. Cardiac *in vitro* systems commonly lack these features, hampering their utility for proper disease modeling, drug discovery, and translational relevance. These distinctions, including additional hallmarks of cardiomyocyte maturation, are described in **Table 1**.

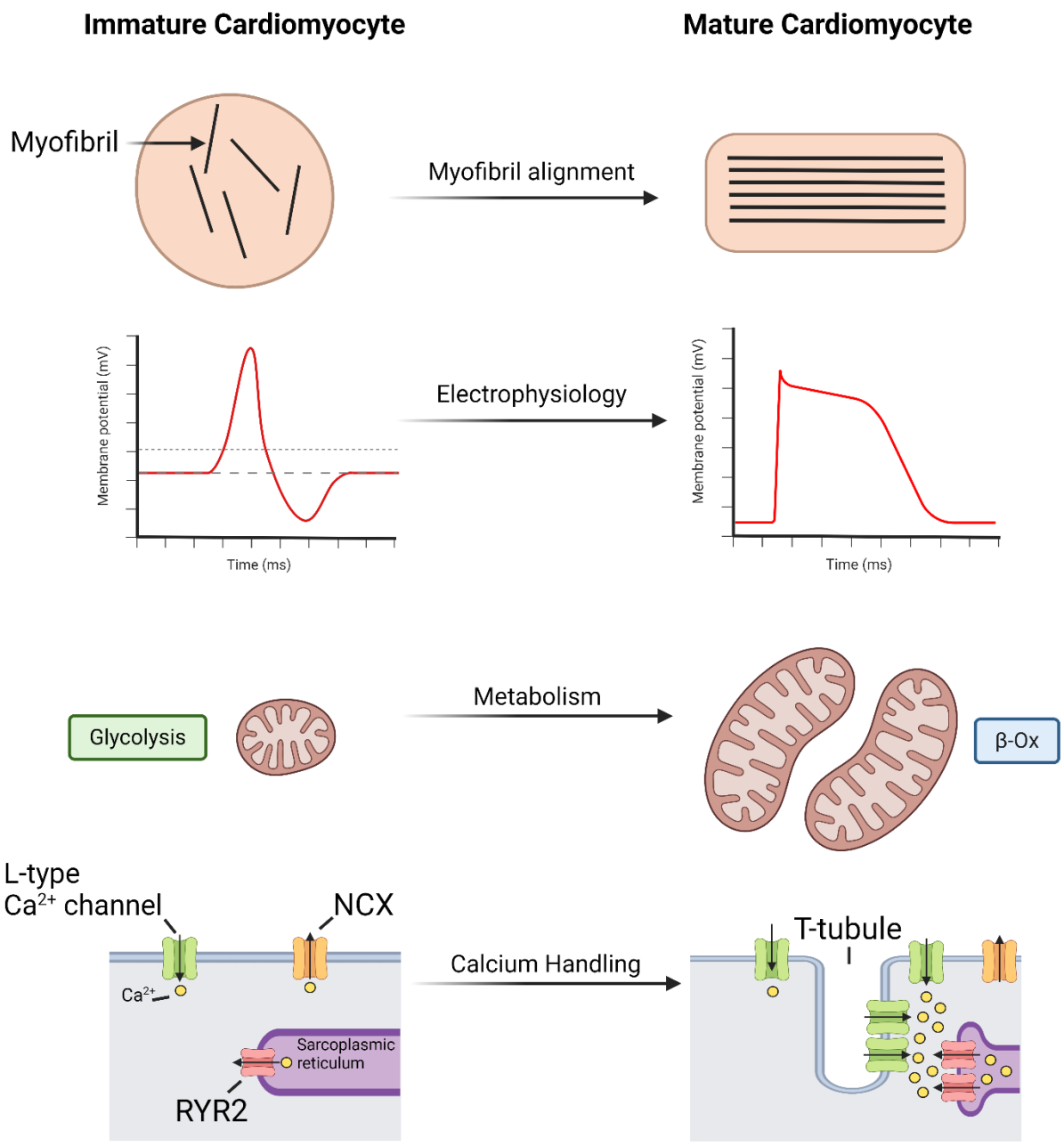

Figure 6. Cardiomyocyte maturation for enhanced in vitro biological modeling. Created with BioRender.com.

The encouragement of mature phenotypes in *in vitro* cardiac systems has been a rising field of ongoing research. A variety of approaches have been taken to simulate and stimulate cardiac maturation, with an emphasis on cardiomyocytes. Common approaches include providing metabolic and hormonal cues, such as modulating fatty acid content

(oleic acid, linoleic acid, palmitic acid) and glucose levels, introducing tension or force to cells or tissue, electrical stimulation, modification of membrane stiffness, and confining the geometry of growth.

Metabolic and hormonal modulation for *in vitro* cardiomyocyte maturation attempts to recreate or encourage the shift that occurs from fatty acid oxidation to glycolysis during heart development and growth. Standard cell culture media contains significantly higher levels of glucose than that observed in the heart *in vivo*, and most cell culture mediums do not contain relevant levels of fatty acids. Lowering glucose levels to physiological concentrations and introducing relevant levels of fatty acids appears to trigger metabolic maturation *in vitro*. Feyen et al.[46] show how the combination of physiological glucose levels (less than half the concentration of standard cell culture medium) and fatty acids (oleic acid, linoleic acid, and palmitic acid) influence an increase in sarcomere organization, force production, calcium handling, and aerobic respiration in iPSC-derived cardiomyocytes. Additionally, in two independent studies, Yang et al.[47,48] showed that T3 hormone and prenatal concentrations of fatty acids stimulate an increase in CM size, anisotropy, sarcomere length, contractile force, calcium kinetics, and mitochondrial respiratory capacity in iPSC-derived cardiomyocytes.

More direct methods, such as the introduction of tension[49], electrical stimulation[50], membrane stiffness modification[51], and geometric confinement[52] also appear to orchestrate cardiac growth and maturity. Mihic et al.[49] investigated the effects of cyclical and mechanical stretching on hESC-derived CMs and showed increases in CM elongation, sarcomere, ion channel, and gap junction gene expression, and enhanced calcium transient profiles. Chan et al.[50] studied whether electrical stimulation of

cardiomyocytes would influence their therapeutic potential by enhancing differentiation and maturation of hESC-derived CMs. They stimulated CMs with an electric field potential at 6.6 V/cm and 1 Hz with 2ms pulses and found an increase in cardiac gene expression including *HCN1*, *MYL2*, *SCN5A*, and *GATA4*. Additionally, they found an increase in ventricular-like action potentials with a lengthening of action potential duration. Lastly, Ronaldson-Bouchard et al.[52] investigated the role of geometric confinement with electrical stimulation on iPSC-derived CMs and found maturational benefits including increases in conduction and structural gene expression (*KCNJ2*, *KCNH2*, *TNNT2*, *MYH7*, and *GJA5*), oxidative phosphorylation and mitochondrial organization, and calcium handling. Methods for inducing cardiomyocyte maturation *in vitro* are described and summarized in **Table 2**.

Table 1. Characteristics and features of mature cardiomyocytes *in vivo*.

Characteristic	**Features**	**Genes**
Morphology	Rod-shaped	*TNNT2, TNNI3*
	Increased cell size	
	Aligned Sarcomeres	
Electrophysiology	Increased upstroke velocity	*SCN5A*
	Decreased resting membrane potential	*KCNJ2*
	Gap Junctions	*GJA1, GJA5*
	Increased action potential duration	*CACNA1C*
	Robust t-tubule network	*BIN1*
Contractility	Increased contractile force	*MYL2*
	Increased sarcomere length	*TNNI3*
	Increased MYH6 to MYH7 ratio	*MYH6, MYH7*
Metabolism	Increased utility of fatty acids	*CPT1B*
	Increased mitochondrial presence	*PPARGC1A, TFAM*
Cell cycle	Decreased proliferation & increased ploidy	

Table 2. Methods for inducing cardiomyocyte maturation *in vitro.*

Reference	Method	Result
Feyen et al. 2020	Metabolic factors; High fatty acids, low glucose	Increased sarcomere organization, force production, calcium handling, and aerobic respiration
Yang et al. 2019	Postnatal concentrations of fatty acids	CM growth, increases in force production, calcium transient kinetics, and mitochondrial function
Yang et al. 2014	T3 hormone	Increased CM size, anisotropy, sarcomere length, contractile force, calcium kinetics, and mitochondrial respiratory capacity
Mihic et al. 2014	Mechanical stretch	Cyclic mechanical stretch promotes hESC-derived CM maturation
Young and Engler 2011	Hydrogel stiffness	Transcriptional mimicry to adult CMs and improved contractile properties
Chan et al. 2013	Electrical stimulation	Improved sarcomere gene expression and CM elongation in hESC-derived CMs
Ronaldson-Bouchard et al. 2018	Confined geometry microtissues with electrical stimulation	Improved calcium handling, gene expression, and mitochondrial density in iPSC-derived CMs

1.5. RECAPITULATION OF HEART DEVELOPMENT IN A DISH

Human development and embryogenesis are perhaps one of life's greatest beauties. A living, sentient being is created, molded, and established from the elusive mechanisms of stem cell biology – all beginning from a single cell. Proper formation of the human body, including the heart, depends on sequential, stepwise events that orchestrate the differentiation, specification, and even migration of cells. Unraveling and understanding human embryonic development represents a playground of building blocks just waiting to be assembled.

Elucidating physiologically-relevant cardiac platforms *in vitro* has always depended loosely upon the recapitulation of developmental paradigms, such as manipulating the

Wnt pathway to guide and direct cardiomyocyte differentiation through the use of small molecule inhibitors and activators.[9,15,53] However, many protocols focus only on the isolation of cardiomyocytes, ignore contributions of non-myocyte cells, utilize synthetic ECM, and perform studies in 2D environments, all which hamper and limit the developmental and physiological relevance of the platforms to fully model *in vivo* cardiac phenotypes. A holistic approach to capture human heart development in a dish will consider, initiate, and embrace all stages of cardiac development.

The heart develops from mesodermal cells that migrate from the primitive streak to a location under the headfold. Here, they form a structure known as the cardiac crescent, an epithelial structure that fuses at the midline to create the linear primitive heart tube.[54] A key feature of the primitive heart tube is its patterning along the anterior-posterior axis. This patterning creates distinct and localized poles that contain unique pools of progenitor cells, known as first heart field (FHF) and second heart field (SHF) progenitor cells[54,55], along with endocardial and epicardial progenitor cells.[56,57] FHF and SHF progenitor cells have distinct gene expression profiles and proliferate and contribute to distinct structures of the heart. FHF progenitors are *ISL1*$^{-}$/*NKX2-5*$^{+}$/*TBX5*$^{+}$ while SHF progenitors are *ISL1*$^{+}$/*NKX2-5*$^{+}$.[56] Progenitor cells at the anterior pole of the primitive heart tube differentiate prior to those found at the posterior pole and give rise to the ventricles. Posterior progenitor cells later differentiate to form the atria and sinus venosus. The development and formation of the ventricular and atrial chambers is a tightly regulated process, with genes such as *Irx5*, *Irx4*, *Myl2*, and ANF being shown to have specific roles and localizations in mouse and rat heart development, pioneered by Christoffels et al.[54]. In subsequent studies, atrial chambers have been shown to be identifiable by expression

of *NR2F2*, *TBX5*, *NPPA*, and *NR2F1*[58–65], while ventricular chamber myocardium can be identified by markers such as *MYL3*, *HEY2*, *IRX4*, and *HAND1*[66–71].

Moreover, the epicardium is an essential structure involved in cardiac development, contributing to coronary vasculature and connective tissue while supplying the myocardium with growth factors and morphogens that induce and support the growth and maturation of the heart. The epicardium arises from a structure known as the proepicardium which is located on the outside of the developing heart tube near the septum transversum. These proepicardial cells migrate and spread across the surface of the heart tube, covering first the left ventricle and atrioventricular canal, then covering the atrium, right ventricle, and the outflow tract.[72–74] Li et al.[75] demonstrated the importance of epicardial-secreted IGF in activating the ERK proliferation pathway in the developing heart. Disruption of the *Igf2* gene resulted in significant decreases in ventricular wall proliferation and in the growth of the ventricles. Gise et al.[76] investigated the role of the epicardium and the transcription factor WT1 in endothelial to mesenchymal transition through the Wnt and retinoic acid signaling pathways. Further, Stuckmann et al.[77] investigated signals from the epicardium, erythropoietin and retinoic acid, that played essential roles in the proliferation of cardiomyocytes.

While Israeli et al.[78], Hofbauer et al.[79], Drakhlis et al.[80], and Andersen et al.[81] have created complex *in vitro* heart models that seek to better understand human heart development (covered in the next section), they lack critical structures, maturation states, cellular organization, and endogenous morphogen gradients that play key roles in disease progression and cardiogenesis. In addition, there are many other contributions to heart development that do not arise from cardiac mesoderm. For example, neural crest cells

migrate to the heart to contribute to cardiac innervation and the development of the outflow tract[82] and macrophages infiltrate the heart to become cardiac-resident macrophages which contribute to proper formation of cardiac lymphatic vessels[83]. Altogether, the proper formation of the human heart relies upon an intricate balance of communication, signaling, and maturation to yield diverse cell types and functional, physiological structures – a balance that remains incompletely explored *in vitro*.

1.6. HEART ORGANOIDS FOR CARDIOVASCULAR RESEARCH

While methods for *in vitro* cardiovascular maturation have proven fruitful in their recapitulation of myriad mature cardiomyocyte properties observed *in vivo*, *in vitro* models of the human heart remain unable to fully capture the mechanisms of human heart development and disease, such as the intricate cell-cell crosstalk between multiple cardiomyocyte subtypes (atrial, ventricular, and nodal cardiomyocytes), epicardial cells, cardiac fibroblasts, endothelial cells, and more. Other physiological elements that remain elusive in *in vitro* cardiac systems include the presence of specified heart chambers and other structures paramount to cardiac functionality like the outflow tract and valves, and perfusable vasculature.

Remarkably, stepping stones towards this end have been laid in recent years, representing the field of organoids. Organoids are 3D constructs of differentiated PSCs that recapitulate the structure, organization, and function of their *in vivo* organ counterparts to a significant degree. In recent years, organoids have been derived for the brain[84], lung[85], kidney[86], and gastrointestinal tract[87] and have been used to study human-relevant mechanisms and perturbations involved in neurodevelopmental disorders[88–90], chronic kidney disease[91], and even COVID-19[92].

Nonetheless, the generation of cardiac organoids has remained elusive, likely due to the difficulty to properly differentiate cardiac cells *in vitro*, the sophistication of structures and function relating to the heart, or the mechanical forces both necessary for proper cardiac function and destructive for immature ECM scaffolding present *in vitro*. However, in recent years, four novel protocols for the generation of human heart organoids by self-assembly have been unveiled by Andersen et al.[81], Israeli et al.[78], Hofbauer et al.[79], and Drakhlis et al.[80] These methods utilize similar but varying means to derive 3D heart organoids resembling early embryonic hearts form hPSCs, containing multiple cardiac cell types and showcasing the ability to recapitulate significant features of human cardiac development.

Andersen et al. report a method to generate precardiac organoids from both mESCs and hiPSCs to model the formation of the FHF and SHF. They differentiated mESCs using Activin A (ActA) and BMP4, and differentiated hiPSCs using BMP4 and CHIR99021 to activate the Wnt pathway. While the mESC-derived organoids contained cells from both the FHF and SHF, the precardiac organoids had vastly different gene expression profiles compared to their counterparts *in vivo*. Nonetheless, these organoids possessed cardiomyocytes, endothelial cells, smooth muscle cells, and fibroblasts, confirmed by immunofluorescence imaging for cTnT, Pecam-1, α-SMA, and Thy1, respectively. Further, this platform was able to identify the distinct roles of the FHF progenitors to differentiate preferentially into cardiomyocytes while SHF progenitors differentiated to non-myocyte lineages such as cardiac fibroblasts and endothelial cells. Moreover, they used both their mouse and human PSC-derived organoids to show that CXCR4 is a marker for SHF progenitors and can be used to identify cardiomyocyte and non-myocyte lineages in their *in vitro* systems. This study showcased the power of in vitro systems to investigate the

fates of cardiac progenitors involved in human and mouse heart development yet suffers in its relevance due to the lack of cardiac-relevant cell populations it is able to elicit.

Israeli et al. show the generation of a unified cardiac organoid model for human heart development, capturing critical steps of heart development while elucidating multiple cardiac-specific cell types with structural complexity and organization through hPSC self-assembly. In this study, the authors use hiPSCs and hESCs to show the reproducibility of their three-step Wnt modulation strategy with BMP4 and ActA to create heart-like structures with sophisticated internal chambers possessing well-organized FHF and SHF cardiomyocytes, cardiac fibroblasts, epicardial cells, endocardial cells, and a robust vascular network throughout the entire organoid. Moreover, these heart organoids demonstrate robust functional and electrical activity, as quantified through both multielectrode array (MEA) and calcium dye studies. The heart organoids were comparable to age-matched human fetal cardiac tissues and demonstrated enhanced features over traditional monolayer cardiac differentiation strategies at the cellular, transcriptomic, and structural levels. Remarkably, this model was used to investigate the role of pregestational diabetes in human cardiac development at the morphological, functional, metabolic, ultrastructural, sarcomeric, and organizational levels. This study also employed an innovative and novel approach to image the entirety of organoids longitudinally using optical coherence tomography (OCT) and showed dynamic internal chambers within the organoids. Altogether, this study set the stage for advanced studies involving human heart development, representing an essential model system as an alternative to conventional animal and monolayer-based studies.

Near the same time, Drakhlis et al. and Hofbauer et al. reported protocols for the derivation of human heart organoids generated from hESCs (Drakhlis et al. and Hofbauer et al.) and hiPSCs (Hofbauer et al.). Drakhlis et al. utilized a two-step Wnt modulation strategy with hESCs embedded in Matrigel to generate layered organoids containing both cardiac and non-cardiac cells. The organoid interior contained endodermal cells and was surrounded by endocardial cells, endothelial cells, and cardiomyocytes. Meanwhile, the surface of the organoid had liver cells with the marker HNF4α. By using NKX2.5 knockout hESCs, they show how NKX2.5 yields less structured and compacted heart organoids with disorganized sarcomeres and increased sizes of cardiomyocytes. NKX2.5 is a critical transcription factor involved in cardiac development *in vivo*, with perturbations resulting in embryonic lethality.[93] While this protocol generated structures that were not exclusively cardiac, thus limiting their relevance to cardiac development and disease modeling, the organoid model was able to demonstrate its utility to capture basic phenotypes associated with cardiac developmental abnormalities. Hofbauer et al. describe a heart organoid protocol that elucidates complex morphological features such as chamber formation and vascularization via a two-step Wnt modulation strategy. In addition, the protocol features an intricate and complicated co-culture with separately differentiated epicardial aggregates to mimic the formation of the proepicardial organ *in vivo*. Heart organoid generated via this strategy yield larger chambers than that described by Israeli et al., and contain endothelial cells, fibroblasts, and endocardial cells. They further show the relevance and utility of this model by demonstrating the role of HAND1 in the self-organization of their organoids and by investigating the roles of cardiac fibroblasts and apoptosis following myocardial injury.

The characteristics of self-assembling human heart organoid protocols are summarized and expanded upon in **Table 3**.

Table 3. Characteristics of self-assembling human heart organoid platforms.

Reference	Cell Source	Cell Types	Developmental Stage	Translational Relevance
Andersen et al., 2018	mESCs, hiPSCs	Cardiac progenitor cells, FHF and SHF cells, CMs, endothelial and smooth muscle cells and fibroblasts	Precardiac heart field specification	CXCR4 is SHF marker in human heart organoids
Israeli et al., 2021	hiPSCs, hESCs	FHF and SHF cells, CMs, endothelial, endocardial, epicardial cells and cardiac fibroblasts	Early embryonic heart	Human heart organoids serve as a model for pregestational diabetes.
Drakhlis et al., 2021	hESCs	Cardiac progenitor cells, CMs, mesenchymal, endothelial, endocardial cells and liver anlagen	Cardiac mesoderm and foregut endoderm specification	NKX2.5 knockout captures features of congenital heart defects
Hofbauer et al., 2021	hiPSCs, hESCs	Cardiac progenitor cells, FHF cells, atrial and ventricular CMs, endothelial, epicardial, endocardial cells, and fibroblasts	FHF specification and chamber formation	Cardiac injury model

However, many organoid systems, including all cardiac organoid systems to date, suffer from immature and early embryological physiological states which limit their ability to model the full spectrum of human heart development or disease states. A unified model that incorporates human heart development with cardiac maturation, eliciting more complex physiological features and relevant, spatially organized cell types has yet to be created.

1.7. HEART ORGANOIDS FOR DEVELOPMENTAL TOXICITY STUDIES

Organoids possess the unique capacity to better model and investigate human development, organogenesis, and disease modeling at an unprecedented scale and with greater precision compared to existing platforms. However, in the contexts of organogenesis and disease modeling, until now, human heart organoids have only been used to model developmental perturbations in diabetes-induced cardiomyopathy during pregnancy[78], gene knockout studies[80], developmental cryoinjuries[79], and hypertrophic and fibrotic remodeling[94]. Therefore, while heart organoids show promise towards unraveling unanswered questions surrounding cardiogenesis and pathology, critical areas such as investigating developmental drug toxicity and broader morphological perturbations in cardiac pathologies remain ripe for discovery.

Developmental toxicity is a potent issue. The embryo is incredibly susceptible to the maternal environment and environmental toxins. The first major indication of developmental toxicity was in the 1950s and 1960s when thalidomide was given to pregnant women in over 40 countries to treat nausea and vomiting. Soon later, the developmentally toxic effects of this drug were clearly apparent, as babies were being born with anatomical malformations, such as limb, urinary tract, brain, retinal, facial, and cardiac defects. It is estimated that over 10,000 children were born with deformities due to the utility of this drug, and even more were miscarried due to thalidomide.[95]

The thalidomide crisis is regarded as the biggest man-made medical disaster in history. The toxicity of thalidomide was clear due to the external and anatomical defects it caused. However, the globe is currently experiencing a suite of other medical disasters, such as rising climate change, toxic pesticides used on global food supplies, and microplastic

pollution. While the cumulative and long-term effects of these phenomena are difficult to robustly analyze, recent research has revealed the developmentally toxic effects of many phenomena, such as the role of perfluoroalkyl acids, a material with anti-adhesive properties, inducing hepatotoxicity, neurotoxicity, and developmental toxicity[96], metals such as iron, copper, mercury, and nickel resulting in DNA damage and lipid peroxidation,[97] and pesticides affecting male fertility via damage to spermatozoa and Leydig cell functionality.[98]

Cardiac developmental toxicity is an additional area of pressing concern. The heart is the first organ to form and function in human embryonic development[99] and is responsible for the distribution of essential nutrients to the fetus, thus making the proper formation of the heart a paramount step in human development. In fact, the heart is highly susceptible to maternal and environmental factors *in utero*. Lehtoranta et al.[100] showed that maternal hyperglycemia caused fetal cardiac hyperplasia, arrythmia, and atrioventricular valve regurgitation in rats. Zhang et al.[101] show how the most environmentally abundant polycyclic aromatic hydrocarbon, phenanthrene, influences zebrafish cardiotoxicity through producing pericardial edema, abnormal heart looping, and a hypertrophic ventricle. Blanchette et al.[102] characterized the effects of over 100 pharmaceuticals and environmental chemicals on iPSC-derived cardiomyocytes and found significant influences on cytotoxicity and QT prolongation, an extension of repolarization that is associated with arrhythmia. While these studies are invaluable to understanding and ensuring the safety of newborns and mothers alike, the models utilized are either too simplistic or not relevant to fully understand the full picture surrounding human heart development and may be missing critical elements involved in toxicity. In this way, our

developmentally mature heart organoids represent an artery to discovering and investigating novel developmental toxicities, mechanisms, and therapies.

1.8. SIGNIFICANCE

1.8.1. Novelty of the patterned heart organoid model

Here, we report an advanced set of developmentally inspired conditions to induce further developmentally relevant cellular, biochemical, and structural changes in human heart organoids in a high throughput setting by complete self-assembly, bringing heart organoids one step closer to 6-10-week-old gestational hearts. The methods introduced here take inspiration from developmental and maturation timeline paradigms which elicit distinct intra-organoid chamber morphologies, cellular compositions, transcriptomes, functionalities, and metabolic profiles generated in part through a retinoic acid morphogen gradient present only in our most advanced developmental maturation strategy. We show that this protocol is reproducible across multiple human pluripotent stem cell lines, including embryonic and induced pluripotent stem cells.

1.8.2. Novelty of the ondansetron and congenital heart disease model

We also provide proof-of-concept of the model's utility for disease modeling and pharmacological studies by investigating the transcriptional, cellular and electrophysiological effects of ondansetron on embryonic heart development. This study represents the first developmental investigation into the human-relevant cardiac safety of ondansetron use during pregnancy. Altogether, our methodology is highly automatable, scalable, and overall amenable to high-throughput screening approaches for the investigation of human heart development, cardiac diseases, toxicity testing and pharmacological discovery.

1.9. AIMS

Aim 1: Generation of developmental maturation strategies for heart organoid development

Aim 2: Molecular and structural characterization of developmentally maturated human heart organoids

Aim 3: Utilizing human heart organoids to investigate ondansetron-induced congenital heart defects

CHAPTER 2: METHODS

2.1. CELL AND ORGANOID CULTURE

2.1.1. Stem cell culture

PSC methodologies represent profound opportunities for novel scientific discoveries. However, proper care and culture of PSCs is a delicate process requiring meticulous handling and documentation to ensure reliable and reproducible results. The following human induced pluripotent stem cell (iPSC) and human embryonic stem cell (ESC) lines were used for this study: iPSC-L1 (iPSC, male), ATCC-BYS0111 (iPSC, male), H9 (ESC, female, WiCell, WA09). iPSC-L1 was developed in house by Sendai reprogramming and quality controlled for pluripotency and normal karyotype following standard approaches[103], and has been described before by us an others[78,104]. Pluripotency, genomic stability, and *Mycoplasma* contamination were routinely tested for all hPSC lines used. hPSCs were cultured in Essential 8 Flex Medium with 1% penicillin streptomycin (Thermo) in 6-well plates on growth factor reduced Matrigel (Corning) inside an incubator at 37 ^{o}C and 5% CO_2. hPSCs were passaged using ReLeSR passaging reagent (STEMCELL Technologies) upon reaching 60-80% confluency.

2.1.2. Self-assembling human heart organoid differentiation.

Like PSC handling, the generation of human heart organoids is even more of a delicate process. Growing the organoids seen in this dissertation can be thought of as a two-part process, involving firstly the differentiation of PSCs to early embryonic heart-like structures, then secondly, their maturation into patterned heart tube-like constructs. This section explains the differentiation of PSCs to early embryonic heart-like structures. hPSCs were grown to 60% confluency on 6-well plates and dissociated using Accutase

(Innovative Cell Technologies) to obtain a single-cell solution. hPSCs were collected and centrifuged at 300 x *g* for 5 minutes and resuspended in Essential 8 Flex medium containing 2μM ROCK inhibitor (Thiazovivin) (Millipore Sigma). hPSCs were counted using a Moxi cell counter (Orflo Technologies) and were seeded at a concentration of 10,000 cells per well in round bottom 96 well ultra-low attachment plates (Costar) on day -2 in a volume of 100 μL. The plate was then centrifuged at 100 *g* for 3 minutes (**Figure 7**) and subsequently placed inside a 37 ^{o}C and 5% CO_2 incubator.

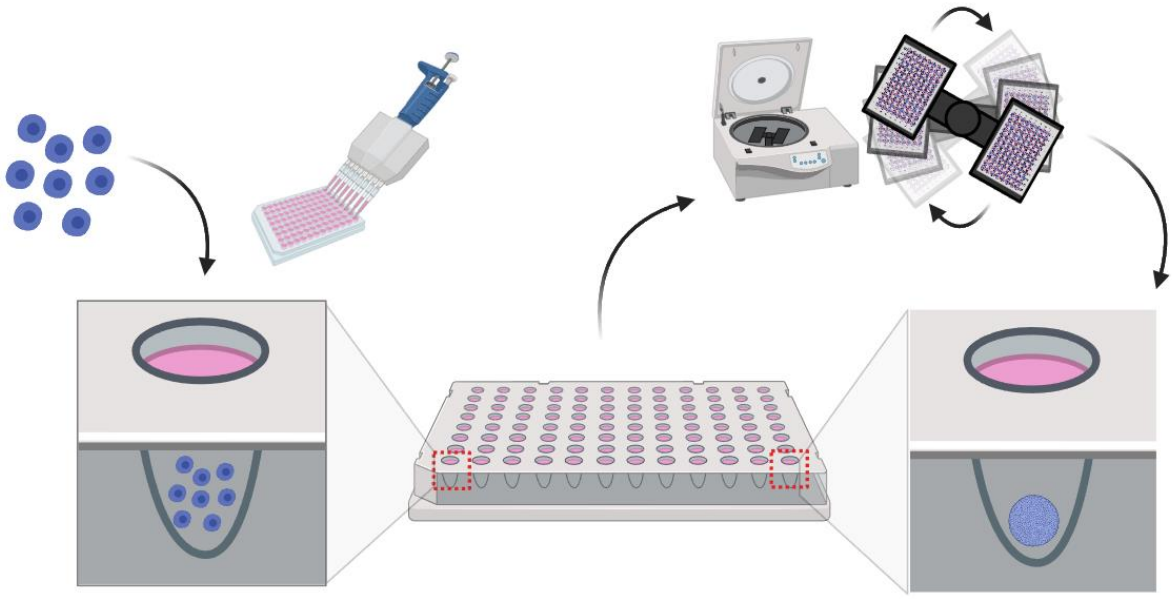

Figure 7. Initial formation of heart organoids from hPSCs. Created with Biorender.com.

After 24 hours (day -1), 50 μL was removed from each well and 200 μL of fresh Essential 8 Flex Medium was added to each well to obtain a final volume of 250 μL per well. The plate was then placed inside a 37 ^{o}C and 5% CO_2 incubator. After 24 hours (day 0), 166 μL of medium was removed from each well. Then, 166 μL of RPMI with B27 supplement without insulin (Gibco) supplemented with 1% penicillin streptomycin (Gibco) (hereafter termed “RPMI/B27 minus insulin”) containing CHIR99021, BMP4, and Activin A was

added to each well to obtain final concentrations of 4 μM CHIR99021, 36 pM (1.25 ng/mL) BMP4, and 8 pM (1.00 ng/mL) Activin A. The plate was subsequently placed inside a 37 ^{o}C and 5% CO_2 incubator. After exactly 24 hours (day 1), 166 μL of medium was removed from each well and replaced with 166 μL of fresh RPMI/B27 minus insulin. On day 2, 166 μL of medium was removed from each well and 166 μL of RPMI/B27 minus insulin with Wnt-C59 (Selleck) was added to obtain a final concentration of 2 μM Wnt-C59 inside each well. The plate was then incubated for 48 hours. On day 4, 166 μL was removed and replaced with fresh RPMI/B27 minus insulin and incubated for 48 hours. On day 6, 166 μL was removed and replaced with 166 μL RPMI with B27 supplement (with insulin) and 1% penicillin streptomycin (hereafter termed RPMI/B27). The plate was incubated for 24 hours. On day 7, 166 μL of media was removed from each well and 166 μL of RPMI/B27 containing CHIR99021 was added to obtain a final concentration of 2 μM CHIR99021 per well. The plate was incubated for 1 hour. After 1 hour, 166 μL of medium was removed from each well and 166 μL of fresh RPMI/B27 was added to each well. The plate was incubated for 48 hours. From days 9 to 19, every 48 hours, media changes were performed by removing 166 μL of media from each well and adding 166 μL of fresh RPMI/B27. This protocol is illustrated in **Figure 8**.

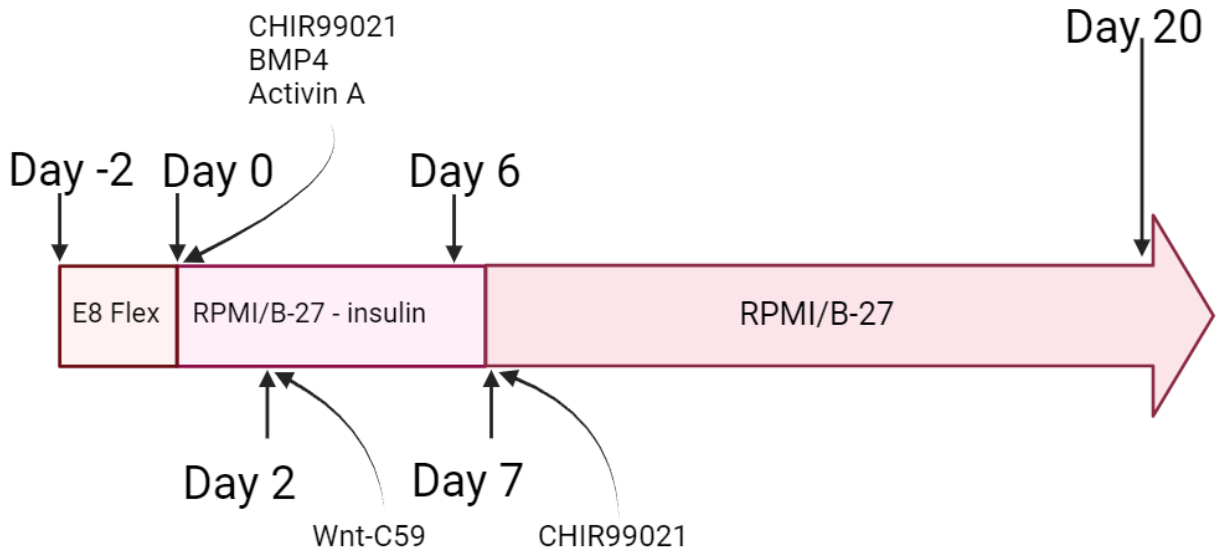

Figure 8. Heart organoid differentiation protocol. Created with Biorender.com.

2.1.3. Developmental induction conditions

Organoids were initially generated and differentiated according to the protocol outlined above, then were maturated according to the following developmental induction conditions, constituting an important sequential step in mimicking human embryonic cardiac development. Beginning on day 20, organoids were subjected to developmental induction conditions (**Figure 9**): 1) control strategy is a continuation of culture within RPMI/B27 from day 20 to day 30, performing standard media changes every 48 hours; 2) maturation medium (MM) strategy is employed from day 20 to day 30, performing media changes every 48 hours using MM media, consisting of stock RPMI/B27 with 52.5 μM palmitate-BSA, 40.5 μM oleate-BSA (Sigma), 22.5 μM lineolate-BSA (Sigma), 120 μM L-carnitine (Sigma) and 30 nM T3 hormone (Sigma); 3) enhanced maturation medium 1 (EMM1) strategy is employed from day 20 to day 30, performing media changes every 48 hours using EMM1 media, consisting of stock RPMI 1640 Medium, no glucose (Gibco)

supplemented with B27 (with insulin), 1% penicillin streptomycin (Gibco), 52.5 µM palmitate-BSA, 40.5 µM oleate-BSA (Sigma), 22.5 µM lineolate-BSA (Sigma), 120 µM L-carnitine (Sigma), 30 nM T3 hormone (Sigma), 0.4 mM ascorbic acid (Thermo Fisher Scientific) and 4 mM glucose (Gibco); 4) enhanced maturation medium 2/1 (EMM2/1) strategy is employed from day 20 to day 30, performing media changes every 48 hours, utilizing a combination of two media. From day 20 to day 26, EMM2 media is utilized which consists of stock RPMI 1640 Medium, no glucose (Gibco) supplemented with B27 (with insulin), 1% penicillin streptomycin (Gibco), 52.5 µM palmitate-BSA, 40.5 µM oleate-BSA (Sigma), 22.5 µM lineolate-BSA (Sigma), 120 µM L-carnitine (Sigma), 30 nM T3 hormone (Sigma), 0.4mM ascorbic acid (Thermo Fisher Scientific), 4 mM Glucose (Gibco) and 50 ng/mL LONG R^3 IGF-1 (*Repligen*). Continuing the EMM2/1 strategy, from day 26 to day 30, EMM1 media is utilized. Organoids are collected on day 30 for analysis.

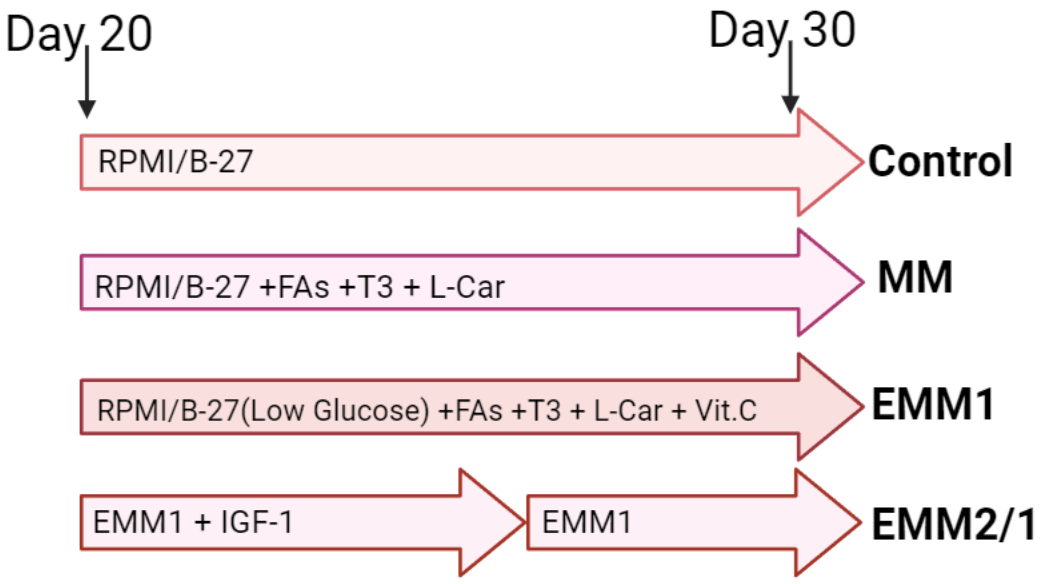

Figure 9. Developmental induction strategies and application. Created with Biorender.com.

2.1.4. Heart organoid dissociation

To perform certain end-point assays, such as single-cell RNA sequencing (upcoming section), the organoids, which are large, bulky structures consisting of hundreds of thousands of cells, must be dissociated into single cells for proper handling and measurement. Organoids were collected on day 30 from each maturation strategy (control, MM, EMM1, EMM2/1). Organoids were individually placed into separate 1.5mL microcentrifuge tubes (Eppendorf), dissociated and pooled. Organoids were dissociated into a single-celled suspension using a modified protocol of the STEMdiff Cardiomyocyte Dissociation Kit (STEMCELL Technologies). Upon being transferred to a microcentrifuge tube, organoids were washed with PBS, submerged in 200 µL of warm dissociation media (37 °C), and placed on a thermal mixer at 37 °C and 300 RPM for 5 minutes. Then, the supernatant was collected and transferred to a 15 mL centrifuge tube (Corning) containing 5mL of respective media (control, MM, EMM1, etc.) containing 2% BSA (Thermo Fisher Scientific). An additional 200 µL of warm dissociation media (37 °C) was then added back to the organoid on a thermal mixer (37 °C). The organoid dissociation media solution was then pipetted up and down gently 3-5 times. The organoid was allowed to sit on the thermal mixer for an additional 5 minutes. If the organoid remained visible, the process was repeated. Once the organoid was no longer visible, the microcentrifuge tube solution was pipetted up and down gently 3-5 times and its entire contents were transferred to the 15 mL centrifuge tube containing the respective media + 2% BSA and cells. These tubes were then centrifuged at 300 x *g* for 5 minutes. The supernatant was aspirated, and the cell pellets were resuspended in respective media + 2% BSA. Using a hemocytometer, viability, cell counts, and aggregate percentage were acquired. Four organoids were

pooled per condition for single cell RNA sequencing (scRNA-seq). Cell viability was then assessed using trypan blue (Gibco) mixed with the cell solution at a 1:1 volume ratio and was incubated for 5 minutes at room temperature. A hemocytometer was then used to count the cells and to assess viability.

2.1.5. Compound treatments

Ondansetron hydrochloride (Sigma) was prepared at 200 μM in DMSO and was further diluted in DMEM/F12 before being sterile-filtered via a 0.22 μm PVDF filter (Sigma). Ondansetron was applied to heart organoids at final concentrations of 1μM, 10μM, and 100μM in EMM2/1 medium, and was applied from Day 9 to Day 20 of culture. Organoids were collected on Day 30 for analysis. Doxorubicin Hydrochloride (Sigma) was diluted to 1mM in DMEM/F12 and was applied to heart organoids at a final concentration of 10μM for 48 hours from either Day 13 to Day 15 or from Day 28 to Day 30 of culture. 4-Diethylaminobenzaldehyde (DEAB) (Sigma) was prepared at 1M in DMSO, diluted further to 10mM using DMSO, then finally diluted to 1mM in DMEM/F12. Retinoic Acid (RA) (Sigma) was prepared at 1M in DMSO and diluted to 100μM in DMEM/F12. Diluted solutions of DEAB and RA were sterile filtered via 0.22 μm PVDF filters (Sigma). DEAB was applied to heart organoids at a final concentration of 10μM. RA was applied to heart organoids at a final concentration of 1μM. DEAB, RA, and DEAB+RA were applied to heart organoids from Day 20 to Day 30 of culture using the EMM2/1 strategy. Organoids were collected on Day 30 for analysis.

2.1.6. Lentiviral Transduction

Lentiviral transduction is a critical technique used to introduce specific, custom genetic elements into cells of interest and represents many important applications in medicine, molecular biology, and biotechnology. This process is multifaceted and comprises multiple sequential steps. The first step is bacterial transformation, in which plasmids containing genetic sequences of interest are introduced to bacteria for their production or amplification of the plasmids. Then, more specifically, lentiviral transfection is performed with HEK293T (Horizon Inspired Cell Solutions) cells with the Flip-GFP plasmid (VectorBuilder) and the packaging plasmids pMD2 and psPAX2 using lipofectamine with Plus reagent (Thermo) to create a lentivirus. Flip-GFP is a modified form of GFP that yields fluorescence only upon a conformational change induced by the cleavage of its backbone by caspase-3, a critical regulator of cellular apoptosis. The lentivirus was then added to iPSC-L1 cells with 8 µg/ml polybrene (Fisher Scientific) and incubated overnight. Puromycin selection was carried out for 3–5 days until all cells lacking lentivirus were absent from the well. Surviving clones were selected, collected, replated, and further expanded to give rise to the FlipGFP line. **Figure 10** provides an illustration of this process.

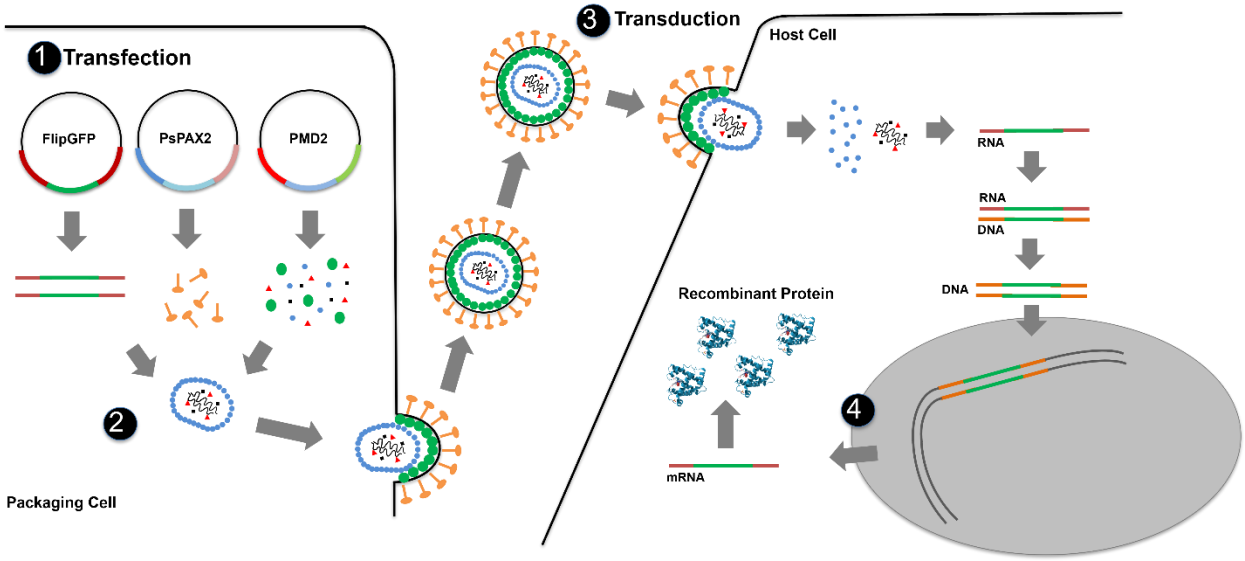

Figure 10. Depiction of lentiviral transfection and transduction.

2.2. IMAGING

2.2.1. Immunofluorescence

Visualizing the presence and location of proteins in cells and tissues represents a paramount element of quantification and hypothesis testing in science. A common method to achieve this is immunofluorescence, in which proteins or antigens are targeted via antibodies for specific visualization of their distribution and localization. These antibodies are fluorescently labeled with different fluorophores that are excited by varying wavelengths of light and emit in varying, longer wavelengths of light to allow for specific identification of proteins of interest. Human heart organoids were transferred from the round bottom ultra-low attachment 96 well plate to 1.5 mL microcentrifuge tubes (Eppendorf) using a cut 200 µL pipette tip (to increase tip bore diameter as to not disturb the organoid). Organoids were fixed in 4% paraformaldehyde (VWR) in PBS for 30 minutes. Following this, organoids were washed using PBS-Glycine (1.5 g/L) three times for 5 minutes each. Organoids were then blocked and permeabilized using a solution

containing 10% Donkey Normal Serum (Sigma), 0.5% Triton X-100 (Sigma), and 0.5% BSA (Thermo Fisher Scientific) in PBS on a thermal mixer at 300 RPM at 4 °C overnight. Organoids were then washed 3 times using PBS and incubated with primary antibodies (**Table A.1** and **Table A.2** in Appendix) within a solution containing 1% Donkey Normal Serum, 0.5% Triton X-100, and 0.5% BSA in PBS (hereafter termed “Antibody Solution”) on a thermal mixer at 300rpm at 4 °C for 24 hours. Following, organoids were washed 3 times for 5 minutes each using PBS. Organoids were then incubated with secondary antibodies (**Table 1** in Appendix) in Antibody Solution on a thermal mixer at 300rpm at 4 °C for 24 hours in the dark. Subsequently, organoids were washed 3 times for 5 minutes each using PBS and mounted on glass microscope slides (Fisher Scientific). 90-µm polybead microspheres (Polyscience, Inc.) were placed between the slide and a No. 1.5 coverslip (VWR) to provide support pillars such that the organoids could retain three dimensionality. Organoids were covered with VECTASHIELD (Fisher Scientific) to segregate beads from organoids. Organoids were transferred to the glass microscope slides using a cut 200 µL pipette tip and mounted using a clearing solution described previously[105]. T-tubule staining was performed using FITC-conjugated Wheat Germ Agglutinin (WGA) lectins (Sigma) (**Table 2** in Appendix). **Figure 11** provides an illustration of this procedure.

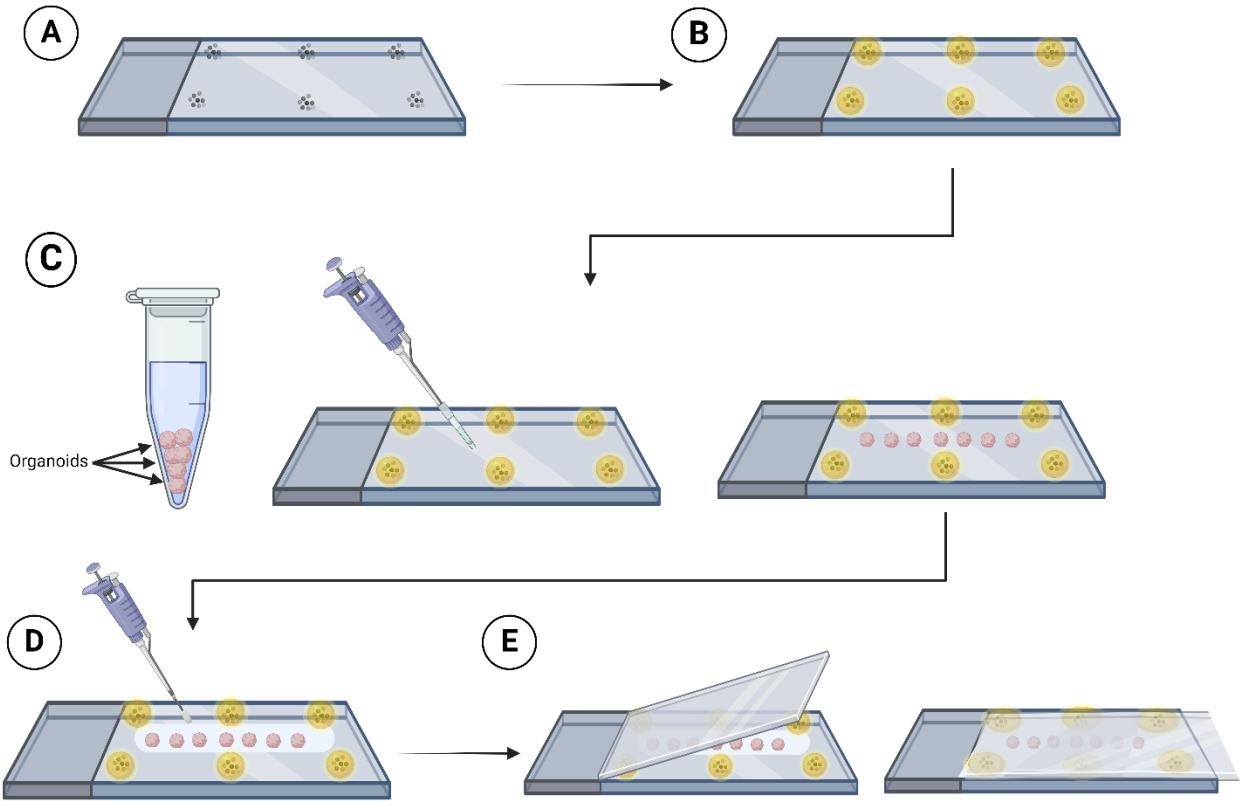

Figure 11. Mounting organoids following immunofluorescence preparation. a, Polybeads are placed on the slide. b, Beads are covered with VECTASHIELD. c, Organoids are transferred to the slide. d, Clearing solution is delivered to the slide atop the organoids. e, A coverslip is placed atop the organoids. Schematic was created using Biorender.com.

2.2.2. Confocal Microscopy and Image Analysis

The acquisition of images following immunofluorescence can be achieved by a variety of methods such as two photon microscopy, light sheet microscopy, and confocal microscopy. Confocal microscopy is a technique that allows for precise optical sectioning of specimens and rejects out-of-focus light through employing a laser scanning system. Immunofluorescence images were acquired using a confocal laser scanning microscope (Nikon Instruments A1 Confocal Laser Microscope). Images were analyzed using ImageJ. When comparing images across or between conditions, for each channel of an image

being measured, pixel intensity values of images were equalized to that of the control or EMM2/1 condition, where appropriate. To measure organoid diameter and area, the straight line and freehand tools were used, respectively. To measure mitochondrial (MitoTracker) area, Cav-3+ area, KCNJ2+ puncta, MYL2+ area, MYL7+ area, and PECAM1+ area, the auto threshold function was utilized, and the area was measured. To measure ALDH1A2+ TBX18+ area, the auto threshold function was utilized to for ALDH1A2+ expression, and the freehand selection tool was used to select TBX18+ organoid area; the ALDH1A2+ thresholded area was calculated within this TBX18+ space. To measure TNNT2+ and WT1+ chamber size, punta, and positive signal area the organoid was imaged at the middle plane (50% of thickness as measured by confocal microscopy; see end of section for more detail and rationale). Then, the oval selection tool was utilized, and the wall of the organoid was used as the boundary region of the respective area (TNNT2 or WT1) to be drawn. For area measurements that utilized the whole organoid (low magnification images), datapoints were normalized to organoid area. To measure FlipGFP fluorescence intensity, the mean gray value was calculated. To measure Pearson's coefficient, the JaCOP colocalization plugin was used[106]. Thresholds were generated for the equalized image intensity values. A spatial resolution of 1.243 micrometers per pixel was utilized. The percentage of chambered organoids were quantified by visual screening for the distinct separation of MYL3 and NR2F2 staining.

2.2.3. Transmission Electron Microscopy

Another imaging modality utilized to acquire sub-cellular, extremely high-resolution images of biological specimens is electron microscopy. Transmission electron microscopy enables the visualization of nanometer scale features like organelles and

macromolecules. Human heart organoids were fixed on Day 15 and Day 30 for each condition in 2.5% glutaraldehyde (Electron Microscopy Solutions) in PBS for 45 minutes, washed three times in PBS for 5 minutes each, then stored at 4 ^{o}C. Samples were then washed with 100mM phosphate buffer and postfixed with 1% osmium tetroxide in 100mM phosphate buffer, dehydrated in a gradient series of acetone and infiltrated and embedded in Spurr (Electron Microscopy Sciences). 70 nm thin sections were obtained with a Power Tome Ultramicrotome (RMC, Boeckeler Instruments. Tucson, AZ) and post stained with uranyl acetate and lead citrate. A JEOL 1400Flash Transmission Electron Microscope (Japan Electron Optics Laboratory, Japan) was used to acquire images at an accelerating voltage of 100k. Data was processed using Fiji. 16 total slices from 4 organoids per condition were used in the assessment and quantification of sarcomere length and mitochondrial size. Sarcomere length was measured using the straight-line tool between Z disks. Mitochondrial area was measured using the freehand selection tool.

2.2.4. Mitochondrial Imaging

Mitochondria are paramount organelles involved in energy production and are essential for cellular function, metabolism, and cell survival. Intracellular mitochondrial presence within human heart organoids was visualized using Mitotracker Deep Red FM (Thermo Fisher Scientific) (**Table 2** in Appendix). Mitotracker was prepared according to the manufacturer's instructions. A 150 nM solution of Mitotracker was prepared in respective medium (control, MM, EMM1, etc.). Additionally, NucBlue (Thermo Fisher Scientific) was used to visualize cell nuclei (**Table 2** in Appendix). NucBlue was prepared by adding 2 drops per milliliter of 150 nM Mitotracker solution (described above). Organoids were washed twice using 166 µL of RPMI 1640 basal medium, then 166 µL of the

Mitotracker/NucBlue solution was added to achieve a final concentration of 100 nM. Organoids were incubated for 30 minutes at 37 ^{o}C and 5% CO_2. Organoids were then washed twice using their respective medium (control, MM, EMM1, etc.) and transferred to a chambered coverglass slide (Cellvis) using a cut 200 µL pipette tip. Images were acquired using a Cellvivo microscope (Olympus). Samples were excited at 465 nm excitation and 630 nm emission was collected (for Mitotracker). Concurrently, samples were excited at 360 nm and emission was collected at 460 nm (for NucBlue). Data was processed using Fiji. An auto threshold was generated to measure mitochondrial area surrounding each nucleus.

2.2.5. Raman Microscopy

Analyzing the chemical composition and molecular structure of materials at a microscopic scale is possible through employing Raman microscopy. Raman microscopy allows the measurement of a Raman spectrum, representing molecular vibrational energy levels and providing a unique molecular fingerprint of the sample at specific locations. The Raman spectra of the organoids were acquired by using a Renishaw inVia Confocal Raman spectrometer connected to a Leica microscope (Leica DMLM, Leica Microsystems, Buffalo Grove, IL, USA). A 785 nm near-IR laser, Nikon Flour 60x NA= 1.00 water immersion objective lens, and 1,000 milli-second exposure time with the average number of 100 accumulations were used for the data acquisition of each scanning position of the organoids. To circumvent a strong background signal, a quartz slide (Chemglass Life Sciences, NJ, USA) was used as a substrate for the Raman spectra acquisition. Organoids were collected on Day 30 for analysis. A schematic of this setup is provided in **Figure 12**.

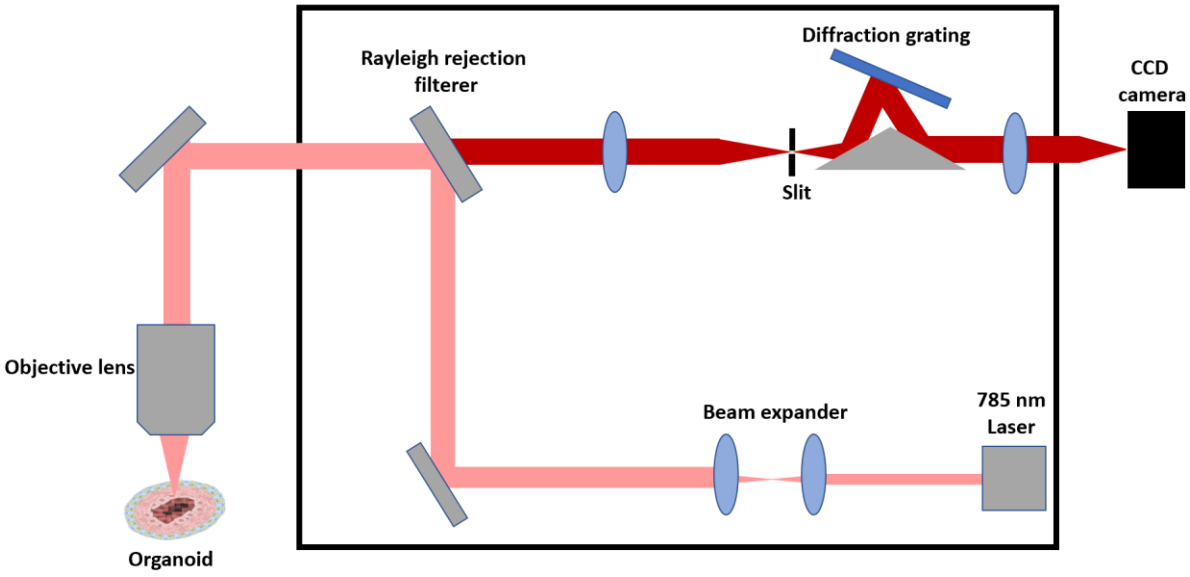

Figure 12. Schematic diagram for the Renishaw confocal Raman spectrometer for use with human heart organoids. Created with BioRender.com.

2.2.6. Optical Coherence Tomography

Non-invasive imaging techniques have enabled a new era of medical diagnostics and serve as a new pillar of clinical decision making. Additionally, these techniques can be employed in basic scientific research settings. One modality called Optical Coherence Tomography (OCT) allows for the obtainment of high-resolution cross-sectional images of biological tissues in a label-free, non-invasive manner. A Spectral-Domain Optical Coherence Tomography system similar to our previous work[104,107] was used for label-free longitudinal imaging of the heart organoids. A superluminescent diode (EXALOS, EXC250023-00) was used as the light source with a center wavelength of ~1300 nm and a 3 dB spectrum range of ~180 nm. A spectrometer (Wasatch Photonics, Cobra 1300) based on a 2048-pixel InGaAs line-scan camera (Sensors Unlimited, GL2048) was used to provide a maximum A-scan rate of 147 kHz. A 5X objective lens was used and the transverse and axial resolutions were measured to be ~2.8 μm and ~3.0 μm in tissue,

respectively. Longitudinal 3D OCT imaging was performed every other day from Day 20 to Day 30 on iPSC-L1 organoids. Each 3D OCT scan comprised 600 A-scans per B scan and 600 B-scans. Each organoid required ~22 seconds for image acquisition using an exposure time of ~40 μs for each A-scan. Eight organoids from each group were imaged and used for analysis. The media level in each well was adjusted during imaging to reduce image artifacts and minimize light absorption. Re-scaling of acquired OCT images was performed using ImageJ (NIH) to obtain isotropic pixel size in all three dimensions. Registration of the same organoids on different days, cavity segmentation, and 3D rendering were performed using Amira software (Thermo Fisher Scientific). The total volume and cavities inside the organoids were quantified from the segmentation data. A schematic of the OCT system is provided in **Figure 13**.

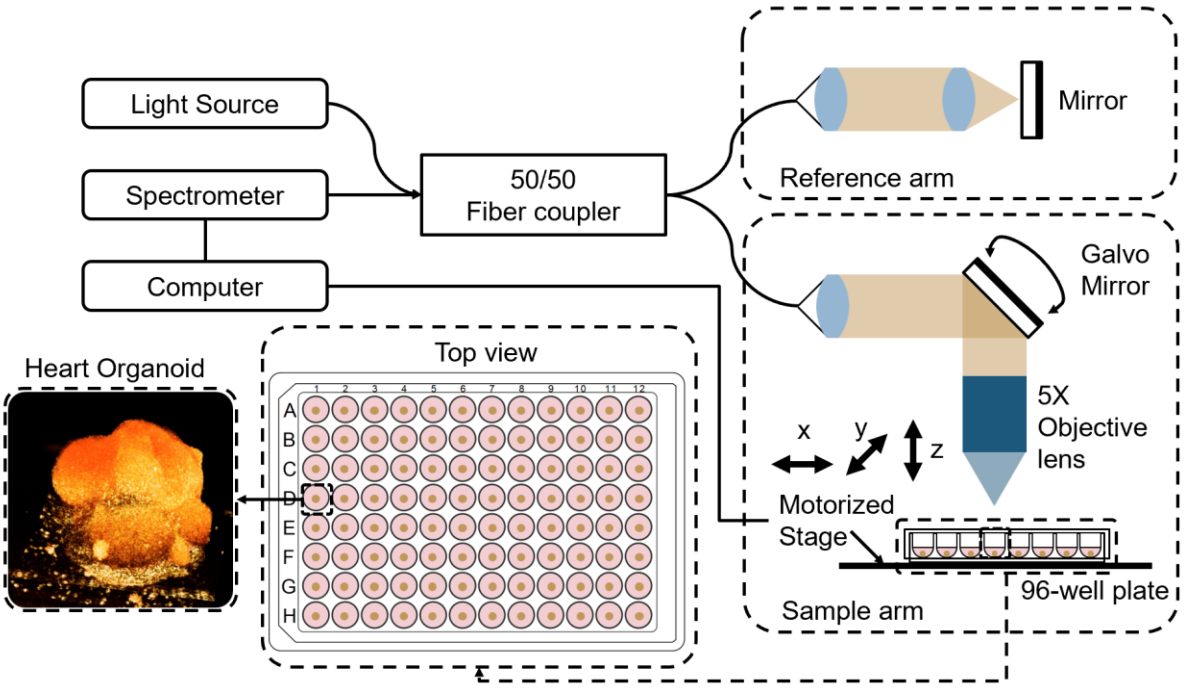

Figure 13. Schematic of custom-built optical coherence tomography (OCT) system for heart organoid imaging. Created with BioRender.com.

2.3. TRANSCRIPTOMICS

2.3.1. Single-cell RNA sequencing

The identification of unique molecular and genetic features from individual cell types within a tissue of interest represents a very powerful technique to precisely dissect and investigate mechanisms of physiological disease and development. This technique is known as single-cell RNA sequencing (scRNA-seq), a distinct and much more robust method compared to bulk RNA sequencing, in which an entire tissue or cellular specimen is analyzed as a singular unit, yielding a dataset containing pooled information on RNA expression from the entire specimen analyzed. The intrinsic disadvantage to this method is the fact that, not only will RNA expression be different simply between cells of the same type, but even more, between differing types of cells. These expression differences are averaged in the final dataset in bulk RNA sequencing. This disadvantage is addressed in scRNA-seq. The preparation of samples with cellular barcodes, formation of droplets, and microfluidics are critical steps in scRNA-seq. Commonly, scRNAseq is performed by encapsulating individual cells into small oil droplets along with cellular barcodes which facilitates the identification of RNA on a cell-to-cell basis, resulting in the high-throughput analysis of gene expression of individual cells in heterogeneous cellular populations. **Figure 14** describes the single cell RNA sequencing process.

Libraries were prepared using the 10x Chromium Next GEM Single Cell 3' Kit, v3.1 and associated components. Completed libraries were QC'd and quantified using a combination of Qubit dsDNA HS, Agilent 4200 TapeStation HS DNA1000 and Invitrogen Collibri Library Quantification qPCR assays. The libraries were pooled in equimolar proportions and the pool quantified again using the Invitrogen Collibri qPCR assay. The

pool was loaded onto two lanes of an Illumina NovaSeq 6000 SP flow cell (v1.5) and sequencing was performed in a custom paired end format, 28 cycles for read 1, 2 10 cycle index reads and 90 cycles for read 2. A v1.5, 100 cycle NovaSeq reagent cartridge was used for sequencing. The 28bp read 1 includes the 10x cell barcodes and UMIs, read 2 is the cDNA read. Output of Real Time Analysis (RTA) was demultiplexed and converted to FastQ format with Illumina Bcl2fastq v2.20.0. After demultiplexing, reads from each of the sample libraries were further processed using 10x Genomics cellranger count (v6.1.2). Counted data were processed using Seurat[108] and integrated using Harmony[109]. UMAP dimensional reduction plots were generated using the standard Seurat default Louvain algorithm. Cell-cell communication analysis and visualization was performed using Liana[110], SCpubr[111] and CellTalker based on Ramilowski et al. 2015 ligand-receptors database[112]. For stage determination, 10x and Visium single-cell sequencing data of embryonic human hearts were obtained from Asp et al. 2019[113] and Cui et al. 2019[114] (GSE106118) and integrated as described above. Visium data was also processed without regard to spatial data. The UMAP datasets presented in grey are due to a lack of succinctly presented annotations from the publicly available datasets. For the stage determination analysis, we used the 4 most well integrated clusters among all datasets (organoid and embryological) (ACM, VCM, PEDC and EPC). At the next stage, single-cell data was converted to pseudobulk data using Seurat2Phantasus tool (https://github.com/ParkLaboratory/Seurat2Phantasus), batch effect was removed using Combat-seq[115]. Pseudobulk data analysis and PCA generation were performed using Phantasus[116]. After that, the top 1000 most highly expressed mRNAs were determined and mRNAs associated with ribosomes were removed, after which PCA was generated.

Enrichr[117–119] was used to assess gene ontologies. Pathview Web was used to generate biological pathway graphs[120,121].

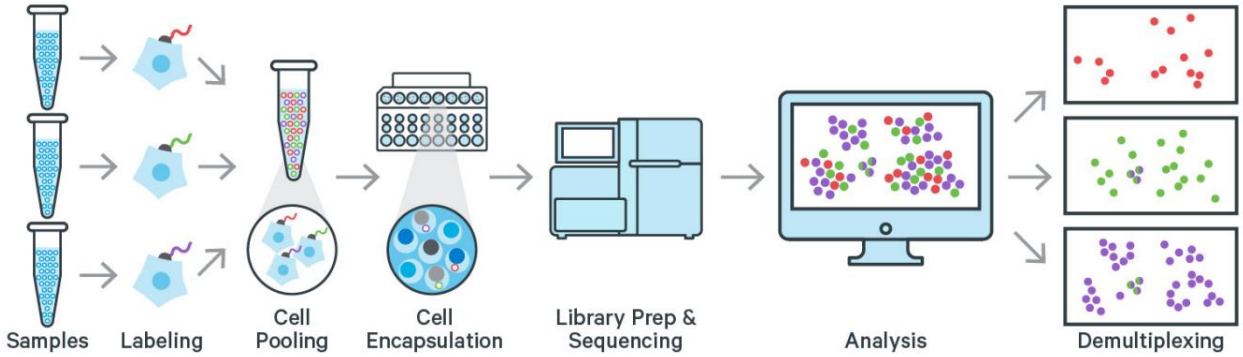

Figure 14. Overview of 10X Chromium single cell RNA sequencing workflow.

2.3.2. Real time quantitative polymerase chain reaction

Another widely popular transcriptomic method is quantitative polymerase chain reaction (RT-qPCR). RT-qPCR is a versatile technique used for amplifying specific DNA sequences to quantify gene expression in real-time using fluorescent dyes or probes. Using specific primers and a DNA polymerase along with a series of heating and cooling cycles, target DNA is amplified and fluorescence (levels of DNA) is quantified. Organoids were collected on day 20, 21, 23, 25, and 30 and stored in RNAprotect (Qiagen) at -20 ^{o}C. RNA was extracted using the Qiagen RNEasy Mini Kit according largely to the manufacturer's instructions. Organoids were lysed using the Bead Mill 4 Homogenizer (Fisher Scientific) at speed 2 for 30 seconds. RNA concentration was measured using a NanoDrop One (Thermo Fisher Scientific). A minimum threshold of 10 ng/µL was required to proceed with reverse transcription. cDNA was generated using the Quantitect Reverse Transcription Kit (Qiagen) and stored at -20 ^{o}C. Primers for real time qPCR were designed using the Primer Quest tool (Integrated DNA Technologies). SYBR Green (Thermo Fisher

Scientific) was used as the DNA intercalating dye and the amplifier for the reaction vessel. Real time qPCR was performed using the QuantStudio 5 Real-Time PCR system (Applied Biosystems) using a total reaction volume of 20 µL. Gene expression levels were normalized to *HPRT1* expression in each independent sample. Log2 fold change values were obtained using the double delta cycle threshold method. At least 4 independent samples were run for each gene expression assay at each timepoint per condition. mRNA expression figures are displayed as log2-fold change relative to control.

2.4. FUNCTIONAL ANALYSES

2.4.1. Beating measurements

The contractile activity of the heart is what drives blood flow throughout the body, delivering oxygen and nutrients to cells and tissues for proper functionality. To obtain a basic metric of the contractile activity of our organoids, the organoids were removed from a 37 ^{o}C, 5% CO_2 incubator. Within 10 minutes of removal, organoids were assessed for beating metrics. Beat frequency was measured by counting the number of beats occurring in 30 seconds. This number was multiplied by 2 to obtain a “beats per minute” metric.

2.4.2. Calcium Imaging

The contraction of the heart is controlled by highly coordinated balances and traversal of ionic densities inside and outside the cell. One of the most critical ions involved in this process is calcium. Cardiomyocyte calcium uptake ultimately regulates the interaction of myosin and actin filaments to facilitate the contraction of the cell. Calcium transient activity within the human heart organoids was assessed using Fluo-4 AM (Thermo Fisher Scientific) (**Table 2** in Appendix). Fluo-4 AM was solubilized in DMSO per the manufacturer’s instructions. A 1.5 µM solution of Fluo-4 was prepared in the

corresponding medium (control, MM, EMM1, EMM2/1). Organoids were washed twice using RPMI 1640 basal medium, then Fluo-4 AM was added at a final concentration of 1 μM and incubated for 30 minutes at 37 ^{o}C and 5% CO_2. Organoids were then washed twice using their respective medium (control, MM, EMM1, etc.) and transferred to a chambered coverglass slide (Cellvis) using a cut 200 μL pipette tip. Videos were acquired using a Cellvivo microscope (Olympus) at 100X magnification at 100 frames per second over 10 total seconds as an image stack. Samples were excited at 494 nm excitation and 506 nm emission was collected. Data was processed using Fiji and Microsoft Excel. Individual cardiomyocytes from the acquired images were randomly selected using the freehand selection tool, and the mean gray value over time was quantified. Baseline F_0 of fluorescence intensity F was calculated using the average of the lowest 50 intensity values in the acquired dataset. Fluorescence change $\Delta F/F_0$ was calculated using the equation:

$$\frac{\Delta F}{F_0} = \frac{(F - F_0)}{F_0}$$

2.4.3. Voltage Imaging

While calcium activity is a paramount element to cardiac contractility, other ions such as sodium and potassium play critical roles at regulating the proper functionality of cardiomyocytes. Voltage activity within human heart organoids was assessed using di-8-ANEPPS (Thermo Fisher Scientific) (**Table 2** in Appendix). Di-8-ANEPPS was solubilized in DMSO per the manufacturer's instructions. A 15 μM solution of di-8-ANEPPS was prepared in respective medium (control, MM, EMM1, etc.). Organoids were washed twice using RPMI 1640 basal medium, then di-8-ANEPPS was added at a final concentration

of 10 μM and incubated for 30 minutes at 37 °C and 5% CO_2. Organoids were then washed twice using their respective medium (control, MM, EMM1, etc.) and transferred to a chambered coverglass slide (Cellvis) using a cut 200 μL pipette tip. Videos were acquired using a Cellvivo microscope (Olympus) at 100 frames per second over 10 total seconds as an image stack at either 20X magnification (ondansetron) or 100X magnification (maturation electrophysiology). Samples were excited at 465 nm excitation and 630 nm emission was collected. Data was processed using Fiji and Microsoft Excel. At 20X, the whole organoid was captured, and at 100X, areas with dozens of cardiomyocytes were captured, which were then randomly selected and quantified in the analysis pipeline. Baseline F_0 of fluorescence intensity F was calculated using the average of the lowest 50 intensity values in the acquired dataset. Fluorescence change $\Delta F/F_0$ was calculated using the same method as with calcium imaging presented above. The area of interest was selected using the freehand selection tool, then the mean gray value over time was quantified. APD30 and APD90 were measured from the midpoint of the upstroke until 30% or 90% repolarization, respectively[122].

2.4.4. Seahorse metabolic analysis

The heart is an incredibly energy-demanding organ and relies on various metabolic pathways for the efficient production of ATP. Under normal physiological conditions, the largest contributor to ATP generation is mitochondrial oxidative phosphorylation, occurring via the electron transport chain. Less of a contributor in adults, yet still critically important in both normal physiological conditions and early embryonic heart development, is glycolysis. The metabolic state and utilization of energy sources (glucose, fatty acids) are informative indicators of cardiac functionality, disease states, and maturity.

An Agilent Seahorse XFe96 (Agilent) was used to perform real-time extracellular flux assays. The day before the assay, 200µL of XF Calibrant was loaded into each well of the 96-well utility plate included with the sensor cartridge and the sensors were submerged in a 37 ºC non-CO_2 incubator overnight. The day before the assay, poly-lysine (Sigma) was used to coat XFe96 spheroid microplates. Poly-lysine was prepared at 100 µg/mL in water and 30 µL of this solution was added to each well of the microplate. After sitting for 20 minutes, the poly-lysine solution was aspirated from the wells and washed two times with sterile water. Then, the plate was allowed to air dry for a minimum of 30 minutes. Then, the plate was warmed for 30 minutes in a 37 ºC non-CO_2 incubator for 30 minutes. Finally, 100 µL of 37 ºC DMEM/F12 was added to each well of the microplate and the microplate was returned to a 37 ºC non-CO_2 incubator overnight. The following steps describe actions performed on the day of the assay, in order. XF RPMI was prepared (phenol red-free) (Agilent) was used as the base medium of the assay which was supplemented with 1mM pyruvate (Agilent), 2mM glutamine (Agilent), 11.1 mM glucose (Gibco), and 12.2µM L-carnitine (Sigma). Using this prepared XF RPMI, drug solutions from the Cell Mito Stress Test kit (Agilent) were resuspended, vortexed for 1 minute, and let rest at room temperature for 1 hour. In this time, the poly-lysine-coated XFe96 spheroid microplates were removed from the incubator and the DMEM/F12 was removed from the plate, washed 1x with 166 µL of prepared XF RPMI, and finally, 175 µL of prepared XF RPMI was added to each well. Then, day 30 organoids in each condition were washed with 166 µL of prepared XF RPMI two times and were transferred to the XFe96 spheroid microplate coated with poly-lysine. Organoids were transferred to the wells using a cut p200 pipette tip. It was ensured that organoids were centered in the well. Following this,

the plate was placed in a 37 ºC non-CO_2 incubator for 1 hour. Drug solutions (oligomycin, FCCP, and Rot/AA) were loaded into ports A, B, and C, respectively. Port concentrations of oligomycin, FCCP, and Rot/AA were 25μM, 20μM, and 20μM, respectively, such that their final concentrations in solution were 2.5μM, 2μM, and 2μM, respectively. The assay was configured such that the baseline phase ran for 6 cycles, and the oligomycin, FCCP, and Rot/AA stages ran for 10 cycles each. Each cycle constituted a 3-minute mixing, a 0-minute waiting, and a 3-minute measuring phase. Data was normalized to organoid area.

2.5. STATISTICS AND DATA AVAILABILITY

2.5.1. Statistics and reproducibility

GraphPad Prism 9 and Excel were used for all analyses. All data presented were normally distributed. Statistical significance was evaluated using one-way ANOVA with Tukey, Dunnett, and Brown-Forsyth and Welch post-test corrections, or using unpaired t-tests, when appropriate ($p < 0.05$). All data presented as mean ± s.e.m. Specific number of independent organoids used and number of independent experiments (batches) for every experiment is indicated in figure legends. If not explicitly stated, images and data presented should be assumed to be from the iPSC L1 cell line.

2.5.2. Data availability

scRNA-Sequencing data sets have been deposited in the National Center for Biotechnology Information Gene Expression Omnibus repository under accession code GSE218582.

CHAPTER 3: AIM 1: GENERATION OF DEVELOPMENTAL MATURATION STRATEGIES FOR HEART ORGANOID DEVELOPMENT

3.1. BACKGROUND AND RATIONALE

3.1.1. Model systems of the human heart

Laboratory models of the heart are used to better understand the etiology and mechanisms of CVDs in high detail. Several model systems to research CVDs are extensively used, including monolayer *in vitro* systems such as primary, embryonic stem cell (ESC)-derived and induced pluripotent stem cell (iPSC)-derived cardiomyocyte cultures, to genetically engineered non-myocyte cell lines possessing cardiac ion channels. ESC[123] and iPSC[8] technologies have enabled rapid advancements in disease modeling and drug discovery in recent years[26,84,88,124,125] and represent novel and ripe avenues for pursuit. Other *in vitro* 3D-culture systems such as cardiac spheroids and engineered heart tissues[12,30,34,126–128] are used to increase physiological mimicry, such as multiple cardiac cell types or mechanical forces. Additionally, non-human animal models possess distinct, non-human physiology, metabolism, electrophysiology and pharmacokinetic profiles which often do not align with humans, nor do they predict human-relevant responses accurately[129,130]. For example, the resting heart rate in mice is 10-fold higher than a human's resting heart rate, and the mouse QT interval is 13% that of the average human.[44,45]

Nevertheless, many of these systems fail to fully recapitulate the complex nature of the human heart due to a variety of reasons, including the absence of endogenous extracellular matrix (ECM) and non-cardiomyocyte cardiac cell types, as well as the lack

of physiological morphology and cellular organization[8,9], limiting their basic and translational ceilings.

3.1.2. Innovations and pitfalls in pluripotent stem cell and organoid technologies

The introduction of human-relevant models is paramount to the discovery of effective, clinically translatable solutions to CVDs and CHDs. Over the last ten years, innovations in human induced pluripotent stem cell (hiPSC)[124,131,132] and organoid[125,133] technologies have advanced techniques and provided platforms to better model and study human systems with increasing precision. For example, protocols for the generation of iPSC- or organoid-based systems of the brain (cortical neurons[88], cerebral organoids[84]), kidney (nephron progenitors[134], renal organoids[86]), lung (alveolar epithelial cells[135], pulmonary organoids[85]), and retina (retinal pigment epithelial cells[136], retinal organoids[137]) are recent, novel expeditions into this uncharted realm of human-relevant systems. These systems have resulted in the identification of novel mechanisms for neurodevelopmental disorders[88–90], chronic kidney disease[91], and even COVID-19[92]. However, while cardiac-based iPSC derivation protocols are potent[11,19,53,138], until recently, protocols for the creation of heart organoids have remained elusive.

Recently, we and others have described methodologies to create early embryonic human heart organoids from pluripotent stem cells (PSCs). These methods enable the study of human heart development and disease[78–81,139] in a dish to a degree unseen before due to their cardiac-specific cellular complexity and high physiological relevance. Yet, these systems still fall short of recapitulating important aspects of human heart development and the late embryonic human heart, such as anterior-posterior patterning and coronary

vascularization, and lack important cell populations contributing to heart structure, such as neural crest cells. Thus, there is a pressing need to develop more sophisticated *in vitro* heart organoid model systems to better understand and properly investigate human heart development and disease pathology.

3.1.3. A patterned human primitive heart organoid model with atrial and ventricular chambers driven by an endogenous retinoic acid gradient

This chapter reports a methodology to generate sophisticated 3D heart systems in high-throughput, possessing multiple relevant cardiac cell types such as atrial and ventricular cardiomyocytes, endothelial cells, epicardial cells, proepicardial-derived cells, conductance cells, stromal cells, and valvular cells. In the most advanced developmental induction condition, atrial and ventricular cardiomyocytes are organized into distinct atrial and ventricular chambers, metabolic rates and metabolic gene expression are elevated and maturated, and functionality is increased with higher levels of t-tubules and ion channels, all driven by an endogenous retinoic acid gradient. This chapter discusses the initial characterization of heart organoids having undergone various developmental induction strategies.

3.2. RESULTS

3.2.1. Developmental induction methods for improving human heart organoid developmental modeling

We recently detailed a protocol for the generation of self-organizing early embryonic human heart organoids which constitutes the starting step for the methodology described below. Heart organoids were differentiated from hiPSC embryoid bodies to the cardiac lineage between days 0 and 7 through a timewise 3-step Wnt pathway modulation strategy, and then cultured until day 20 in RPMI/B27[78]. To examine the effect of more advanced organoid culture strategies mimicking *in utero* conditions on heart organoid development, we took day 20 early embryonic-like heart organoids and employed four different developmental induction strategies from day 20 to day 30 **(Figure 15)**.

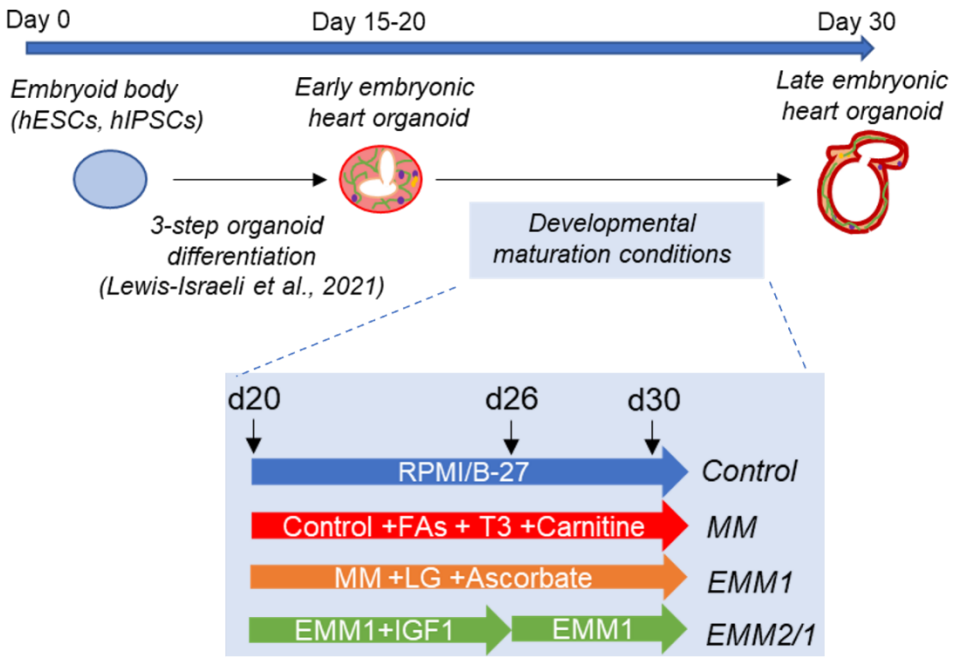

Figure 15. A schematic diagram depicting the differentiation protocol for creating human heart organoids and the media conditions for the four maturation strategies (control, MM, EMM1, and EMM2/1).

These strategies are partly based on previous human and animal developmental studies[46–48,140,141] and represent gradual increasing steps in complexity relevant to *in utero* conditions (in order of less complex to more complex: control, maturation medium, enhanced maturation medium 1, enhanced maturation medium 2/1). Our control strategy represents a continuation of organoid culture in the base medium used for organoid formation, RPMI/B27. The maturation medium (MM) strategy uses RPMI/B27 with added fatty acids (an embryonic relevant concentration of oleic acid, linoleic acid, and palmitic acid)[48,141] and L-carnitine[142] to facilitate a developmentally relevant transition from glucose utilization to fatty acid metabolism characteristic of the fetal human heart[143–147]. The MM strategy also uses T3 hormone, a potent activator of organ growth during embryonic development and metabolic maturation that has been shown to stimulate cardiovascular growth[148,149]. The enhanced maturation medium 1 (EMM1) strategy uses the same basal composition as MM but decreases the concentration of glucose to cardiac physiological levels[150–152] (from 11.1 mM to 4 mM to further encourage the transition to fatty acid oxidation) and adds ascorbic acid as a reactive oxygen species scavenger to counteract the increased oxidative stress[153,154]. Enhanced maturation medium 2/1 (EMM2/1) strategy utilizes a combination of two different media formulations. During days 20-26, EMM2 media is utilized which uses the same basal composition as EMM1 and contains IGF-1. IGF-1 plays important roles during embryonic and fetal development in tissue growth and maturation, especially in the heart, as proven in murine and human studies[75,155,156]. From day 26 onwards, EMM1 media is utilized in the EMM2/1 strategy. EMM2/1 constituted our most advanced condition and mimicked *in utero* heart development to the greatest extent. More detailed descriptions of all developmental

induction strategies along with concentrations of respective media formulations can be found in the Methods section.

3.2.2. Primary characterization of developmentally maturated organoids

Following our original protocol[78], organoids experienced a period of rapid growth from day 0 to day 10, increasing in diameter while retaining their spherical structure **(Figure 16)**, and then began to condense and become more defined up to day 30 in all maturation conditions.

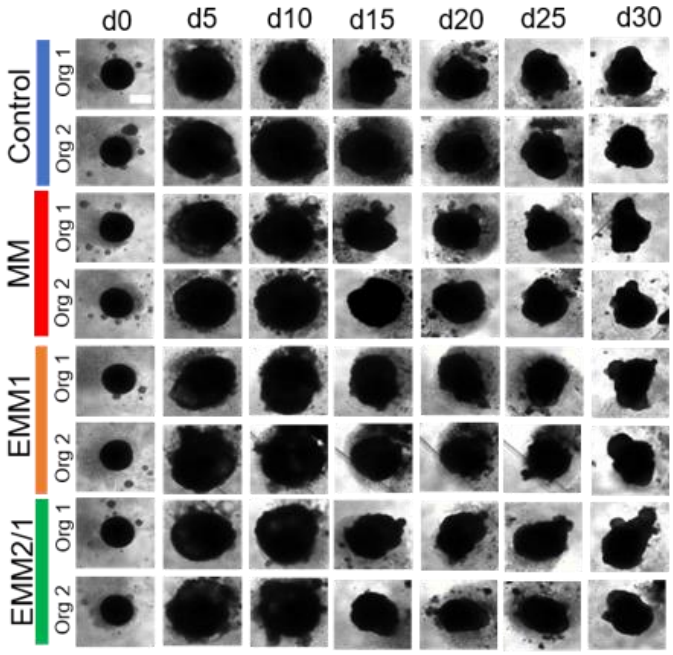

Figure 16. Brightfield images of organoids throughout the 30-day culture period. Two representative organoids are shown for each condition (data representative of 23-24 independent organoids per condition across five independent experiments). Scale bar = 400 µm.

Organoids developed distinct elliptical morphologies after day 20, elongating as observed by brightfield microscopy and growing to long diameters between 1000 and 1600 µm, with short diameters ranging from 600 to ~1000 µm on day 30 **(Figure 16, Figure 17a)**.

Organoid area revealed similar trends for each condition, between 0.6 mm^2 to ~0.9 mm^2 **(Figure 17b)**. By day 30 of culture, nearly 100% of organoids in every condition were beating across five independent experiments **(Figure 17c)**. Transmission electron microscopy (TEM) images indicated the presence of well-developed myofibrils and the formation of sarcomeres **(Figure 18a)** in all conditions, with sarcomeres in the EMM1 and EMM2/1 conditions displaying significantly increased lengths of 1.58 ± 0.323 µm and 1.41 ± 0.187 µm, respectively, compared to Day 15 organoids **(Figure 18b)**. qRT-PCR revealed the expression of hallmark cardiomyocyte marker genes from day 20 to day 30 as expected (*MYL2*, *MYL7*, *MYH7*, and *MYH6)* at various timepoints of differentiation **(Figure 19)**.

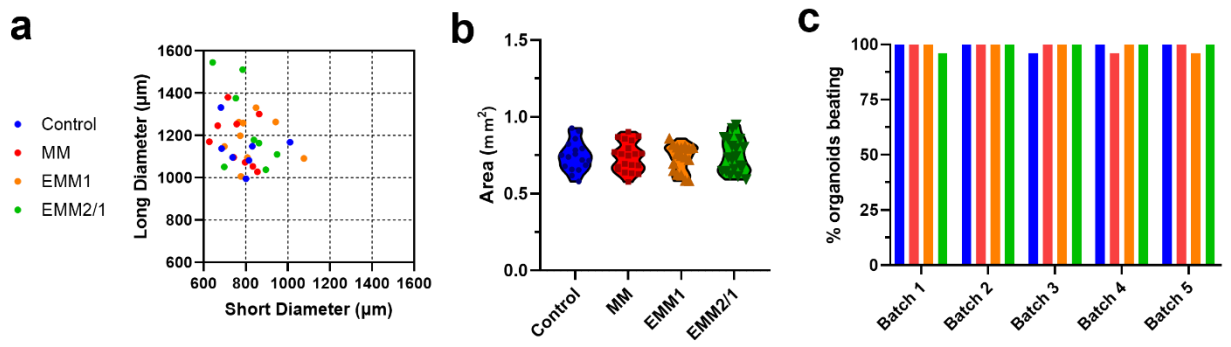

Figure 17. Quantification of organoid metrics. a, Quantification of long diameter and short diameter at day 30 of culture for each maturation strategy (n=7-8 independent organoids per condition). b, Quantification of organoid area at day 30 of organoid culture for each maturation strategy (n=7-8 independent organoids per condition across two independent experiments). Data presented as a violin plot with all points. c, Quantification of percentage of organoids visibly beating under brightfield microscopy in each condition from 5 different organoid batches (n=22-24 independent organoids in each condition across five independent experiments).

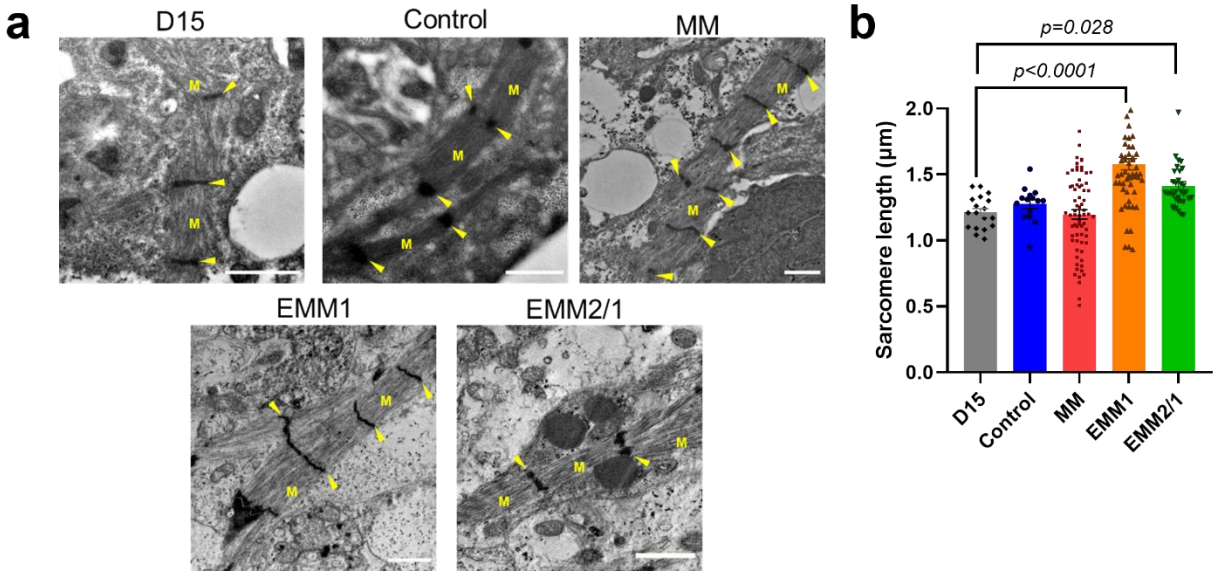

Figure 18. a, TEM images displaying sarcomeres, myofibrils (M) and I-bands (arrows) in day 15 organoids and in organoids from each maturation condition at day 30 (n=4 independent organoids per condition). Scale bars = 1 µm. b, Quantification of sarcomere length within TEM images. Data presented as mean ± s.e.m (n=4 independent organoids per condition). One-way ANOVA with Brown-Forsythe and Welch multiple comparisons tests.

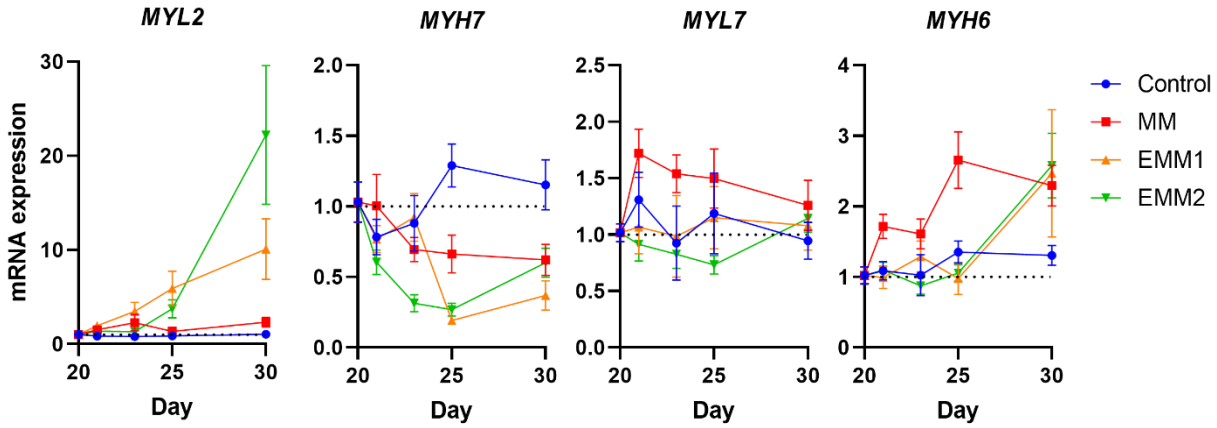

Figure 19. mRNA expression of key sarcomeric genes involved in cardiomyocyte maturation between days 20 and 30 of culture for each condition (n=7-14 independent organoids per day per condition per gene across three independent experiments). Data presented as log2 fold change normalized to Day 20. Values = mean ± s.e.m.

Additionally, using a transgenic Flip-GFP human pluripotent stem cell line (Flip-GFP fluoresces only upon apoptotic cascade activation)[157], we found no significant levels of apoptosis in heart organoids from day 20 to day 30 **(Figure 20a)** and found no differences

in apoptosis between any of the tested conditions **(Figure 20b),** in agreement with previous observations[78]. A 48-hour doxorubicin treatment was used as a positive control and displayed high levels of fluorescence **(Figure 20c)**.

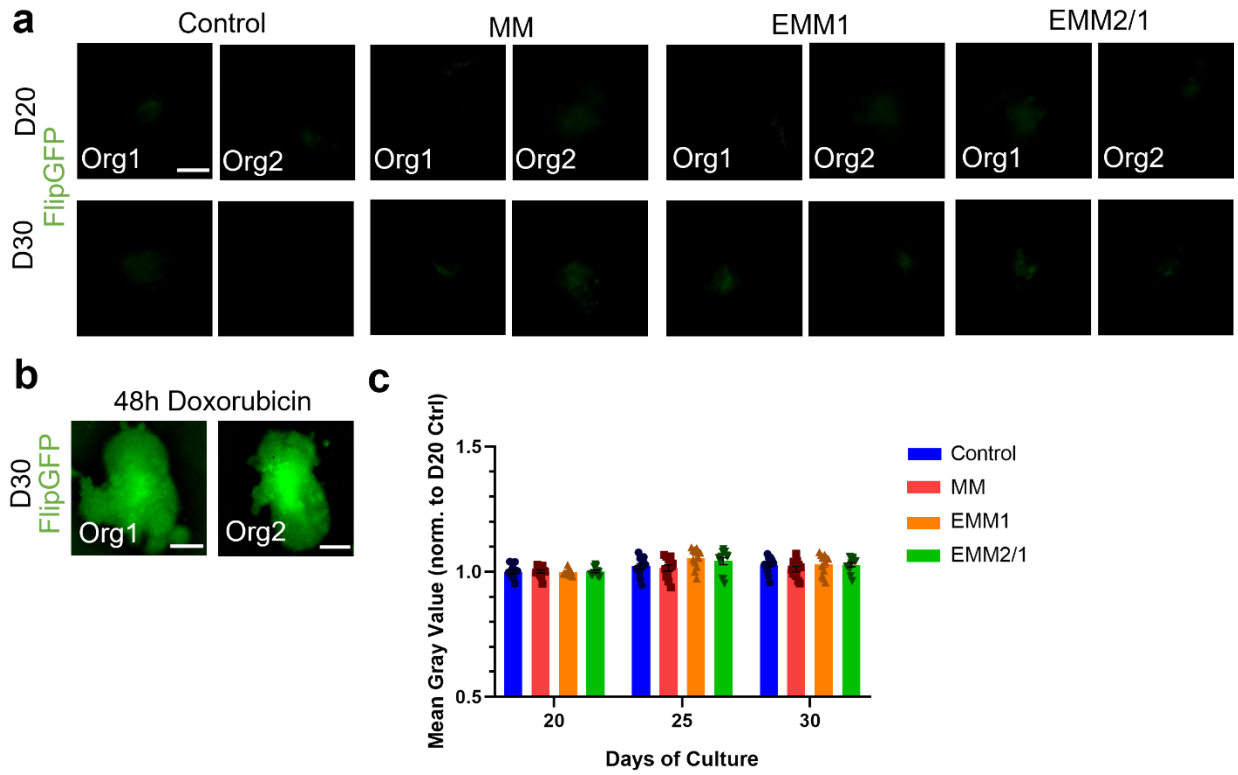

Figure 20. Longitudinal assessment of apoptosis across all maturation conditions. a, Representative fluorescence images of day 20 and day 30 organoids from each condition displaying FlipGFP fluorescence signal (n=12 independent organoids per condition per day across two independent experiments). b, Representative fluorescence images of day 30 EMM2/1 organoids following a 48-hour exposure to doxorubicin displaying FlipGFP fluorescence signal (n=6 independent organoids per condition across two independent experiments). c, Quantification of fluorescence intensity from images presented in (a) (n=12 independent organoids per condition per day across two independent experiments). Data presented as fold change normalized to day 20. Values = mean ± s.e.m., matched two-way ANOVA with Tukey's multiple comparisons test.

3.3. DISCUSSION

For decades, animal models and simplistic *in vitro* monolayer or 3D culture strategies have been employed to research cardiovascular diseases. However, these systems are

unsuitable to properly and fully investigate cardiac disease states in humans. Advancing *in vitro* cardiac model systems to incorporate and possess more elements of *in vivo* cardiac physiology and development is a paramount and essential step towards capturing the full portrait of human cardiac development and disease. While cardiac maturation protocols for other 2D and 3D systems have yielded promising results, the development of holistic cardiac maturation strategies for heart organoids remains completely unexplored.

In this way, we designed and applied four different strategies for heart organoid maturation inspired on facets of human cardiac development and on previous reports of metabolic and hormonal maturation strategies performed on monoculture cardiomyocytes *in vitro*.[46–48]. These strategies incorporate the fatty acids palmitic acid, oleic acid, and linoleic acid to stimulate mitochondrial growth and supply substrates for fatty acid oxidation, the principal energy source for cardiac energetics. In a similar vein, we decreased the concentration of glucose in the maturation medium to yield similar concentrations as that observed *in vivo*, and to increase the reliance of cells on the fatty acids to further drive the organoids towards physiologically relevant metabolic profiles. Moreover, we introduced L-carnitine to facilitate efficient transfer of fatty acids to the mitochondria. To counteract increases in reactive oxygen species generation due to suspected large increases in fatty acid oxidation, we added ascorbic acid to serve as a reactive oxygen species scavenger. We also added triiodothyronine (T3), a main thyroid hormone involved in fetal development and the growth and maturation of the heart. T3 has been shown to facilitate critical increases in gene expression relating to proliferation, differentiation, and contraction essential to proper maturation of the heart. Lastly, we

added IGF-1 to our most advanced maturation strategy, EMM2/1. IGF-1 plays important roles during embryogenesis and cardiac development, driving cardiomyocyte differentiation and proliferation, as proven in murine and human studies[75,155,156].

After a 10-day application of these different strategies, the gross morphological features between organoids in all conditions, as observed by brightfield microscopy, did not show significant differences. However, significant differences at the cellular level (aligned and lengthened sarcomeres) and transcriptional level (enhanced cardiomyocyte gene expression) were present in the MM, EMM1, and EMM2/1 conditions, suggesting an intricate influence on heart organoid development through the use of developmental induction conditions. Additionally, apoptosis was not detected in any of the developmental induction conditions throughout their entire 10-day duration of application. This paper, and the experiments detailed in this section, explore the effects of a novel maturation method applied to self-assembling heart organoids to enhance its physiological mimicry surrounding cardiac development at early stages.

CHAPTER 4: AIM 2: MOLECULAR AND STRUCTURAL CHARACTERIZATION OF DEVELOPMENTALLY MATURATED HUMAN HEART ORGANOIDS

4.1. BACKGROUND AND RATIONALE

4.1.1. Elucidation of complex cardiac phenotypes in vitro

Cardiac maturation studies for *in vitro* human heart systems have been explored extensively in the last decade. However, few have attempted or succeeded to elucidate a combination of complex structural features, cellular organization, morphogen gradients, and maturation profiles reminiscent to that of the developing or adult human heart.

The human heart possesses layers of stratified, anisotropic muscle fibers that control the mechanics of force production, pumping efficacy, and resistance to mechanical tear, shear and stress.[158] Additionally, the four-chambered structure of the human heart possesses dedicated inflow and outflow tracts to ultimately create an efficient biological machine. MacQueen et al.[34] highlighted an electrospinning modality to create nanofibrous, anisotropic left ventricle-like structures with key anisotropic fiber orientation and cardiomyocyte organization. However, this method fails to incorporate other essential elements of the heart, such as epicardial cells, other myocyte cells of the heart, and other necessary structures such as the atria. Kupfer et al.[159] showcase the development of a 3D printed chambered heart construct using hiPSCs and an ECM scaffold composed of gelatin, collagen, laminin, and fibronectin. They differentiate hiPSCs within this chambered scaffold and observe robust cardiomyocyte development possessing t-tubules, cell-cell junctions, and functional electrical activity responsive to pharmacological agents like verapamil and isoproterenol. Interestingly, they control the functionality with electrical pacing and measure the interior pressure dynamics of these constructs.

Unfortunately, the authors do not observe a distinction between atrial or ventricular cardiomyocytes, there is no spatial organization present within the constructs, and there exist no other non-myocytes aside from their base cardiomyocyte population. Additionally, the utility of gelatin and lack of other cardiac ECM proteins such as aggrecan and perlecan constitute a non-physiological microenvironment that may inhibit cell growth and differentiation. These efforts show promise in the development of an *in vitro* cardiac system possessing complex, chambered features, yet fall short in their true, translational and physiological relevance due to a lack of relevant cardiac cell types.

The physiological and developmental process of heart development depends on myriad factors such as timely migration, proliferation, specification, and mechanical cues. Moreover, morphogen gradients represent powerful signaling systems involved in both heart development and disease. Morphogens like retinoic acid (RA), sonic hedgehog (Shh), fibroblast growth factor (FGF) and Wnts are essential and instrumental molecules that temporally and spatially orchestrate and inform the proper development of the heart.[160] In fact, the mechanisms of these morphogens and their downstream effects on transcriptional regulation are leveraged in many cardiac differentiation protocols to generate populations of cardiac-specific cell types for *in vitro* research. However, here, proteins and synthetic small molecule inhibitors are added to the cells exogenously. While in many cases this is a necessary step to initiate lineage commitment in PSCs *in vitro*, the developmental mimicry is flawed and is limited. For example, in the developing heart *in utero*, retinoic acid is synthesized from retinol by the enzyme ALDH1A2 in epicardial cells and atrial progenitor cells in the posterior end of the heart tube.[77,161–163] This localized production of retinoic acid establishes an anterior-posterior axis, providing

signaling cues for the formation of the ventricles, atria, and inflow and outflow tract, while also contributing to the specification of cardiogenic progenitors and other structures, such as heart valves.[164,165] In fact, Niederreither et al. showed that the absence of retinoic acid leads to severe cardiac malformations and results in embryonic lethality[166]. Moreover, retinoic acid guides the migration and maturation of cardiac neural crest cells, cells that instruct formation of the outflow tract. A retinoic acid knockout study caused impairments in these processes and subsequent malformations in the outflow tract.[166] The endogenous recapitulation of these morphogens in a spatially-restricted manner may play a key role in unlocking complex cardiac phenotypes *in vitro*, and there is a need to establish more unified and human-relevant systems to properly investigate human heart development and disease.

Towards this end, Meier et al.[94] reported the generation of epicardial organoids named “epicardioids”. Through using exogenous retinoic acid, their organoids obtain enhanced epicardial and myocardial transcriptomic and organizational phenotypes, with multiple epicardial and ventricular subtypes. They also show the relevance of epicardioids to model stress-induced myocardial hypertrophy through using endothelin-1, a vasoconstrictor known to induce hypertrophy *in vivo* and *in vitro*. However, their model fails to develop atrial cardiomyocytes or provide functional evidence for nodal cardiomyocytes. Moreover, a very limited endothelial population exists in their epicardioids with little transcriptomic evidence to support confocal imaging experiments. Overall, this model provides a unique perspective on the dynamics of epicardial cells in human heart development.

Additionally, Schmidt et al.[167] recently published a report on the generation of multi-chambered heart organoids. First, they separately differentiate PSCs towards varying cardiac lineages in 3D, such as right and left ventricles, atria, outflow tract, and atrioventricular canal, using RNAseq, scRNAseq, electrical functional assays, and low magnification staining of cryosections to confirm the unique, separate organoid identities. Then, they combined the atrium, left ventricle, and right ventricle organoid and allowed them to combine into one functional unit, showing their ability to form a single functional unit that facilitates electrical progression. They also show how their separate organoids can serve as models to investigate genetic defects in *ISL1*, *TBX5*, and *FOXF1*, and to investigate the influence of teratogens and other drugs, such as thalidomide. While this study provides a novel platform for dissecting the developmental biology in normal and pathological instances for individual cardiac regions, it lacks physiological relevance due to the absence of critical cardiac cell types such as epicardial and endothelial cells, and does not recapitulate self-assembly in the formation of the individual cardiac regions. Importantly, too, this method is very difficult and complicated compared to other streamlined methods and will fail to reach broader audiences. In total, while recent advances have been made to create more representative cardiac models *in vitro*, a model that achieves high physiological and developmental complexity with relevant transcriptomic and morphological maturation, patterning, and relevant cell types remains to be created.

4.2. RESULTS

4.2.1. Transcriptomic characterization of developmentally maturated heart organoids by single-cell RNA sequencing reveals cell type complexity and differences in cellular composition

To characterize the cellular and transcriptomic composition of heart organoids in each of our developmental induction conditions, we performed scRNA-seq on day 34 of organoid culture and plotted the integrated UMAP clustering for each condition **(Figure 21)**.

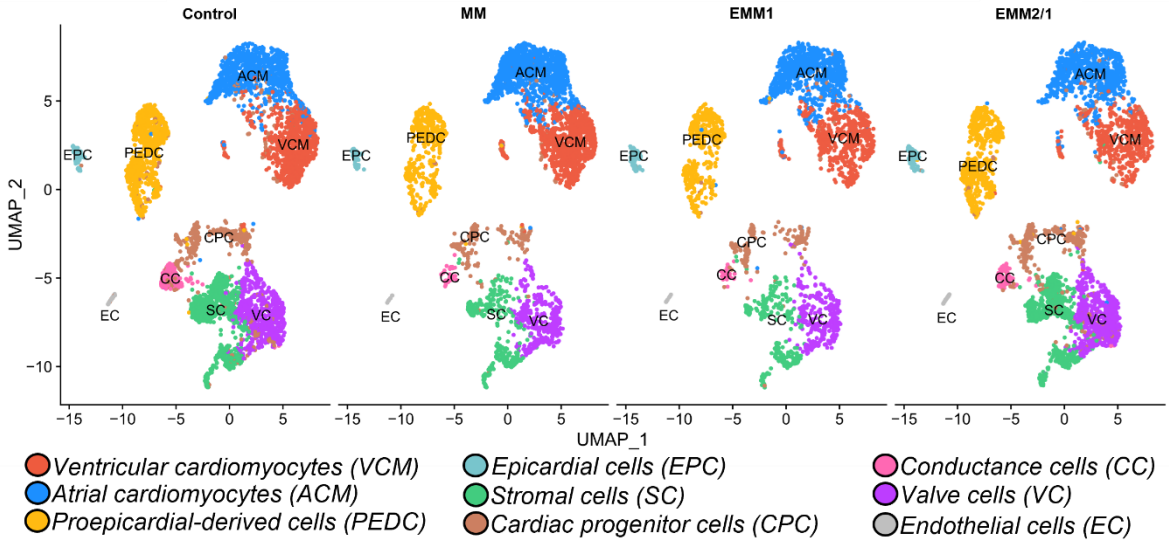

Figure 21. UMAP dimensional reduction plots of integrated single-cell RNA sequencing data for each condition in day 34 organoids. Cluster identities are in the legend below.

Ventricular and atrial cardiomyocytes (VCMs and ACMs, respectively), valve cells (VCs), proepicardial derived cells (PEDCs), epicardial cells (ECs), stromal cells (SCs), cardiac progenitor cells (CPCs), conductance cells (CCs), and endothelial cells (ECs) were revealed in all conditions of heart organoids. The abundance of several significant cell groups varied according to the developmental medium conditions. Control organoids

were composed of 17% VCMs, 17% ACMs, 3% VCs, 17% PEDCs, 1% EPCs, 18% SCs, 10% CPCs, 5% CCs, and 1% ECs **(Figure 22)**.

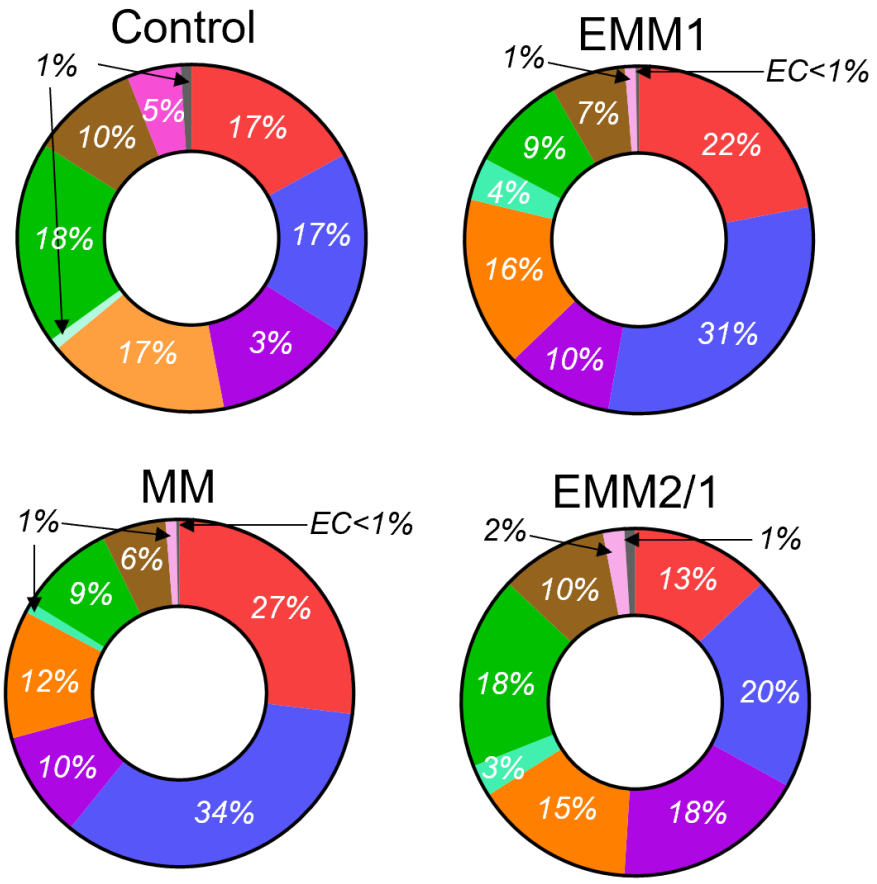

Figure 22. Quantification of total cell count percentages per cluster. Colors of regions correspond to those found in the legend in **Figure 21**.

Relative to control, MM organoids displayed an increased percentage of both VCMs and ACMs (27% and 34%, respectively), increased VCs (10%), decreased PEDCs (12%), 1% EPCs, decreased SCs (9%), decreased CPCs (6%), and decreased CCs (1%). Relative to control, EMM1 organoids contained an increased percentage of VCMs (22%), increased ACMs (31%), increased VCs (10%), decreased PEDCs (16%), increased EPCs (4%), decreased SCs (9%), decreased CPCs (7%), and decreased CCs (1%). Relative to control, EMM2/1 organoids exhibited a decreased VCM percentage (13%),

increased ACMs (20%), increased VCs (18%), decreased PEDCs (15%), increased EPCs (3%), 18% SCs, 10% CPCs, and decreased CCs (2%). Differential gene expression analyses determined signature genes which were used to identify clusters **(Figure 23).** ACMs possessed high expression of *MYH6* , *MYL7, NPPA, and GJA5*[12,113,114,168]*.* VCMs displayed high expression of *MYL3, MYH7, TNNC1, and HSPB7*[113,114,169–172]. PEDCs showed high expression of *PDGFRB, SEMA3D*, *POSTN*, and *TCF21*[173–177]. EPCs shared slight similarity with PEDCs, yet also presented higher differentially expressed genes including *WT1*, *TBX18*, *ITLN1*, and *TNNT1*[94,113,178–180]. CCs displayed high expression of *STMN2*, *CHGA*, *SCG2*, and *INSM1*; genes that are involved in neuron growth, development and neuroendocrine signaling[181–186] and shared similarity with neural crest and Schwann cells identified in human embryonic heart datasets[113]. ECs possessed high expression of *PECAM1*, *ESAM*, *SOX18*, and *FLT*[113,187–190]*.* SCs were identified by expression of *SOX2*, *ANXA4*, *SOX9*, *CD24*[113,191–195]. VCs were identified via the expression of *DLK1*, *ID2*, *DKK2*, and *WNT7B*[114,196–200]. Taken together, these results showed that heart organoids possessed similar cell types as those that are found in the 1st trimester developing human heart, and suggested, in agreement with previous studies on cardiac development[113,114], that developmental induction conditions can exert dramatic effects on the expansion and maturation of cardiac cell types to better reflect *in vivo* heart development.

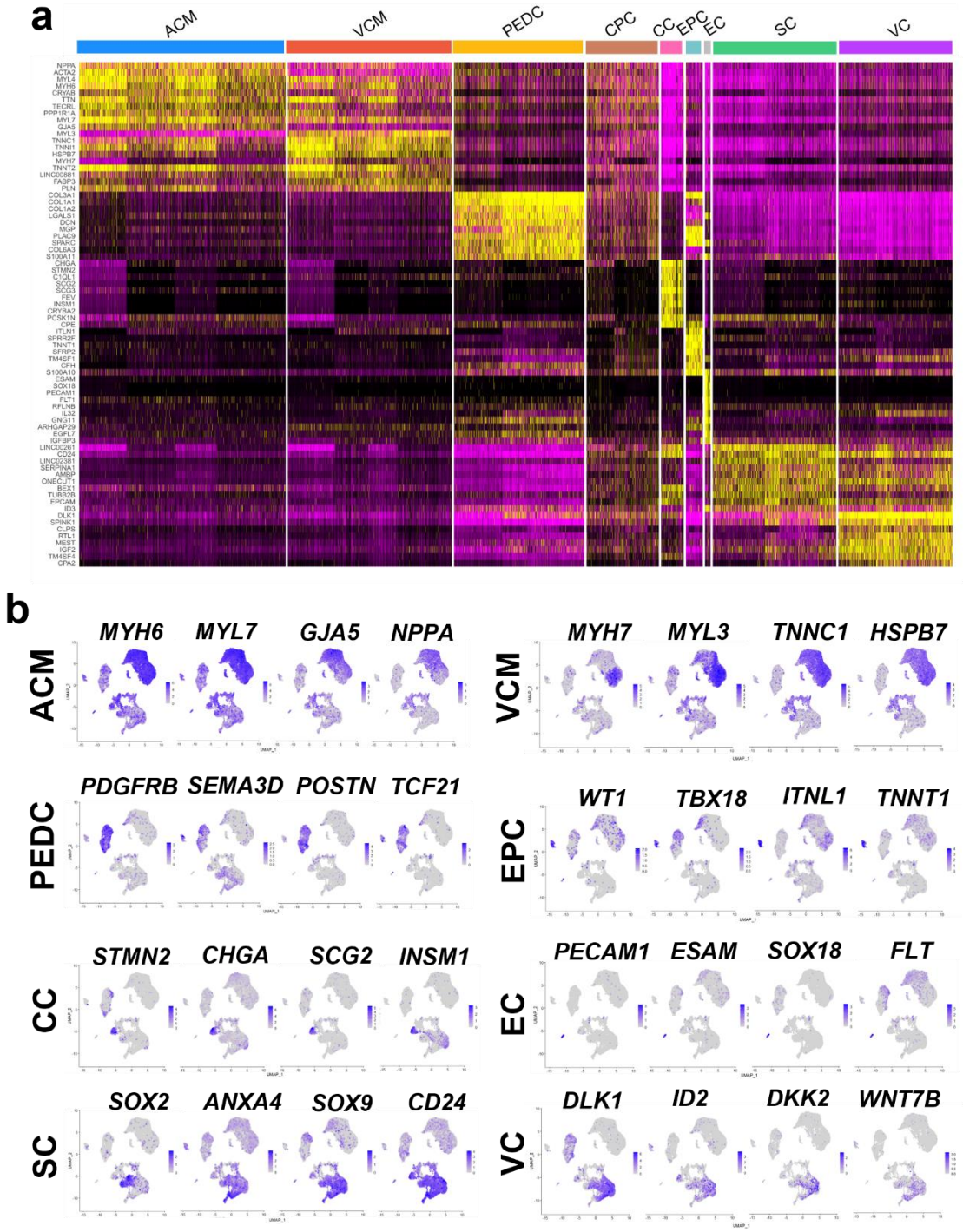

Figure 23. a, Differential expression heatmap displaying the top 10 differentially expressed genes for all clusters. b, Feature plots displaying key marker genes for each cluster. Color intensity represents the relative value of gene expression per gene.

Marker genes corresponding to various other cardiac cell types and processes were identified in all conditions, such as cardiac fibroblasts, left-right asymmetry, proliferation, first heart field (FHF) and second heart field (SHF). Genes specific for cardiac fibroblasts were identified within the PEDC cluster, showing expression of *DCN*, *LUM*, *OGN*, and *POSTN, and COL1A1*[113,201,202] **(Figure 24)**. Organoids also recapitulated key genes involved in left-right asymmetry in all conditions such as *PITX2*, *PRRX2*, *LEFTY1 and PRRX1*[203–206] **(Figure 25)**. Additionally, organoids displayed high upregulation of proliferation markers such as *MKI67*, *PCNA*, *AURKB*, and *CDK1* in all conditions, indicating that important growth and remodeling are still undergoing at day 34 of differentiation[207–209] **(Figure 26)**. Cells of the first heart field (FHF) and second heart field (SHF) contribute to linear heart tube expansion and subsequent chamber formation and are important for proper cardiac morphogenesis[210]. Various FHF and SHF markers were observed in organoids in all conditions **(Figure 27, Figure 28)**. FHF markers *HAND1*, *TBX5*, and *HCN4*[66,211–215] were all upregulated in the VCM and ACM clusters for all conditions, while *HAND1* appeared to be more highly expressed by VCMs, *TBX5* more highly expressed by ACMs, and *HCN4* more restricted to ACMs in the EMM2/1 condition.

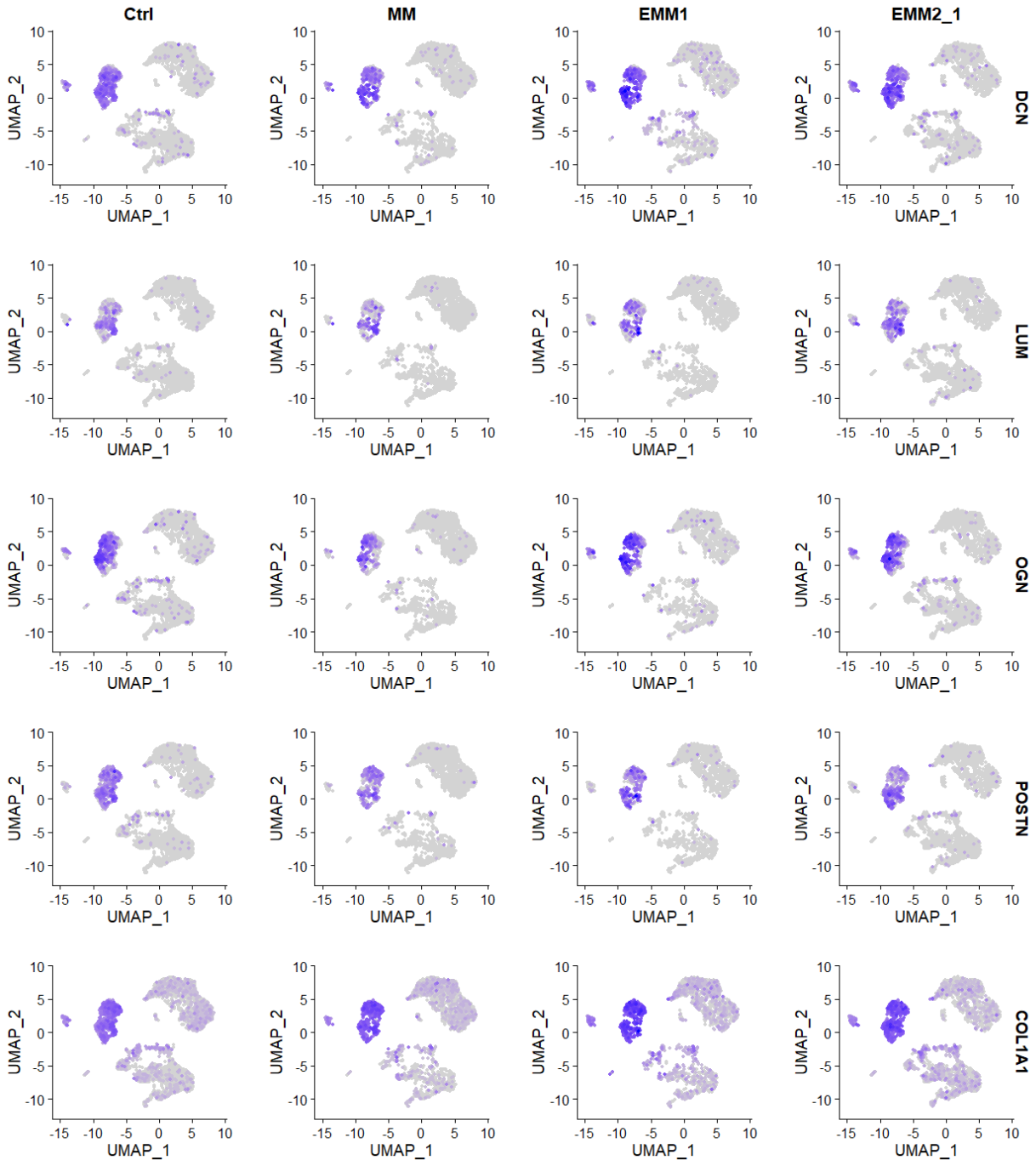

Figure 24. Feature plots of cardiac fibroblast-related genes within single cell RNA sequencing datasets in each condition.

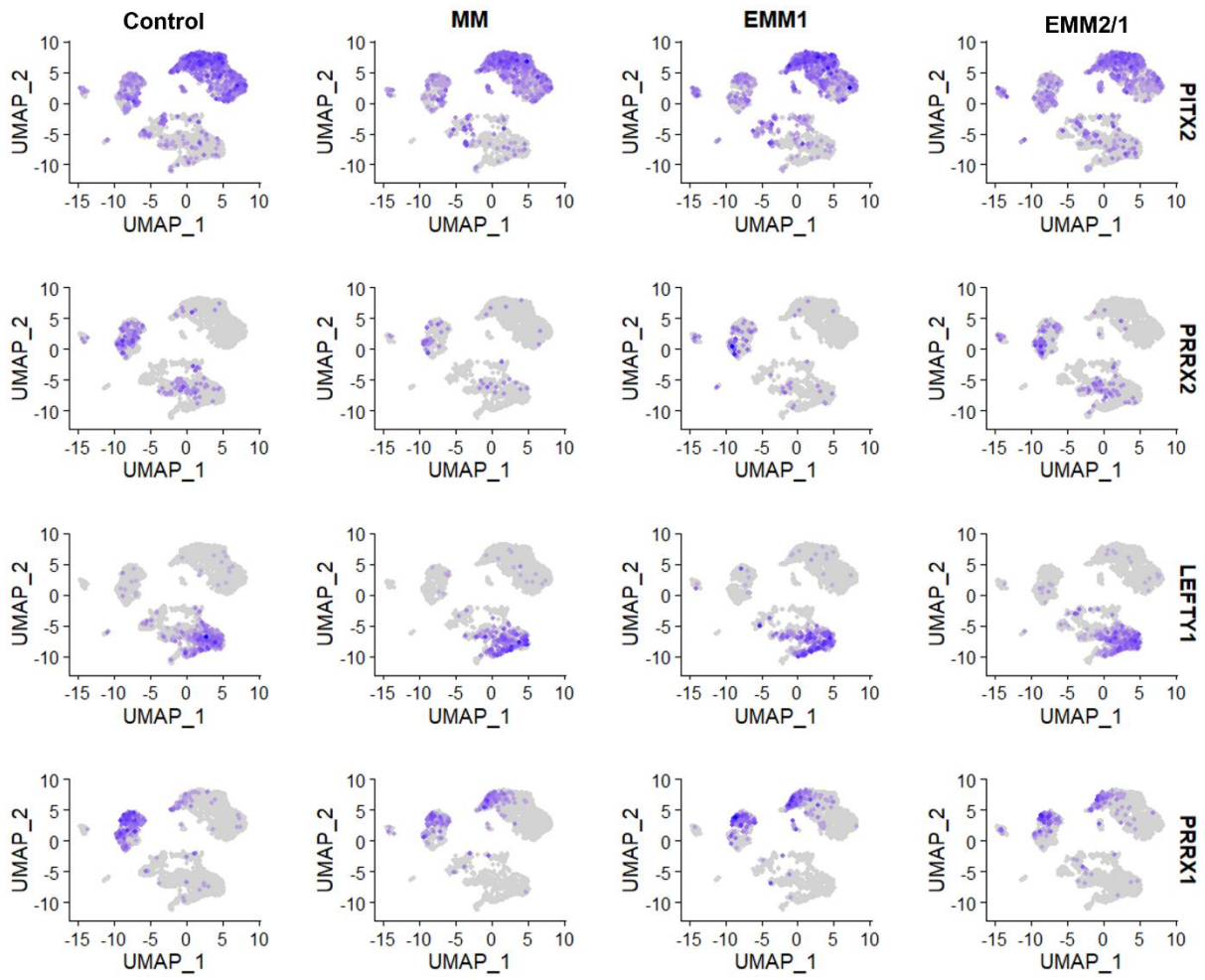

Figure 25. Feature plots of left-right asymmetry-related genes within single cell RNA sequencing datasets in each condition.

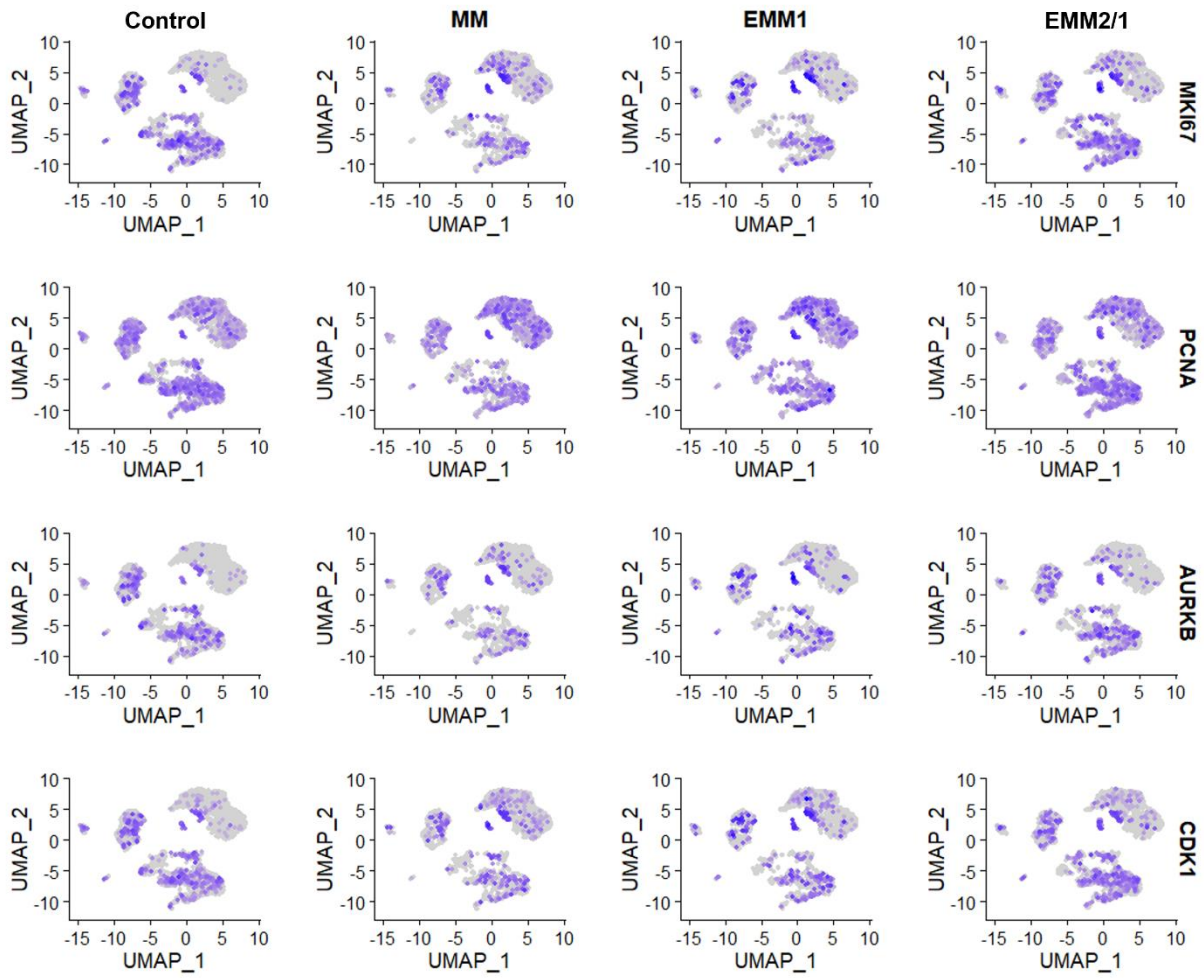

Figure 26. Feature plots of proliferation-related genes within single cell RNA sequencing datasets in each condition.

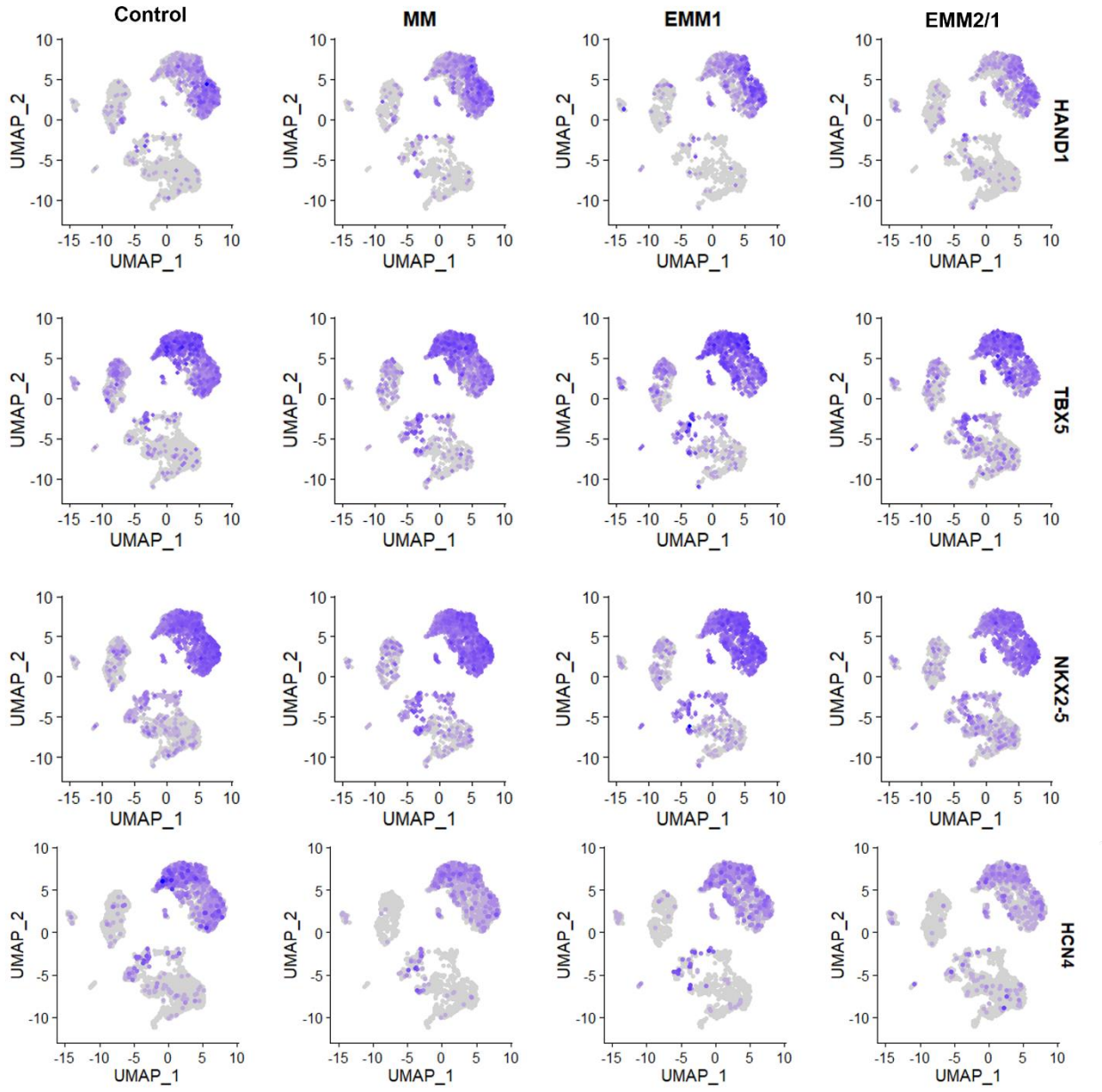

Figure 27. Feature plots of first heart field-related genes within single cell RNA sequencing datasets in each condition.

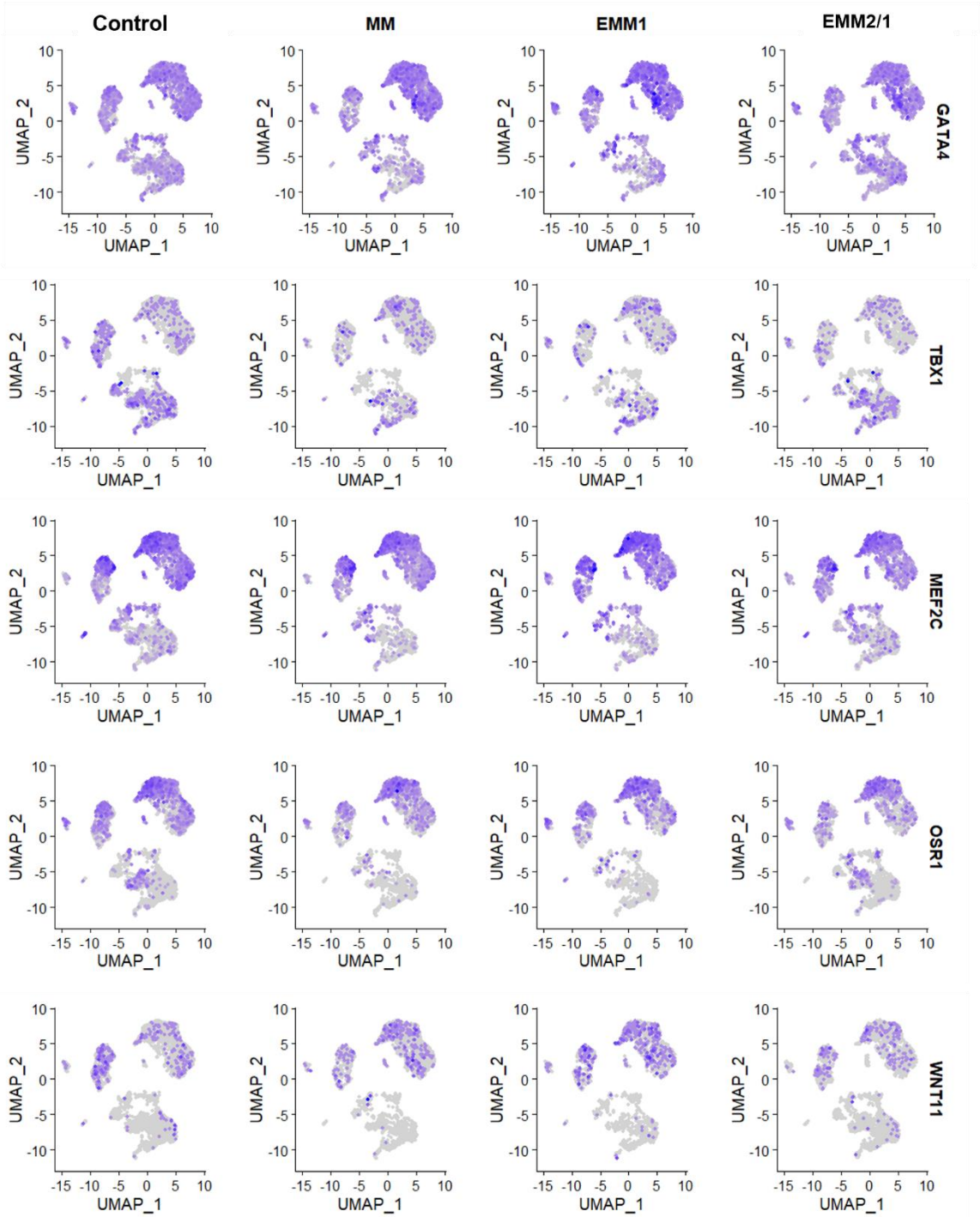

Figure 28. Feature plots of second heart field-related genes within single cell RNA sequencing datasets in each condition.

Interestingly, these patterns of gene expression appear to mimic cardiac developmental principles, with *HAND1* playing a large role in overall cardiac morphogenesis, particularly

with ventricular development[66,214], with *TBX5* being expressed in the left ventricle and atria throughout embryonic development[212], and with *HCN4* acting as a marker of the first heart field and as a transient marker of conduction precursors[215]. Additionally, genes relating to the SHF such as *GATA4*, *TBX1*, *MEF2C*, *OSR1*, and *WNT11*[216–220] were widely expressed in heart organoids. *GATA4* was expressed by ACMs, VCMs, PEDCs and EPCs, *TBX1* was expressed in all clusters, *MEF2C* was upregulated in the ACM, VCM, and PEDC clusters, and *OSR1* and *WNT11* were expressed in the ACM, VCM, EPC, and PEDC clusters for all conditions. These gene networks in our heart organoids appear to closely mimic those observed in human heart development, as *GATA4* has been shown to be expressed in cardiac lineage cells and to be essential in the formation of the proepicardium and epicardium[221], and with MEF2C being required for proper cardiac morphogenesis[222], and with *OSR1* being implicated in atrial septation[223]. In addition, genes related to outflow tract development such as *RSPO3*[224] and *WNT5A*[225,226], *TBX2*[227]*, and TBX3*[228] were shown to be upregulated in various clusters for all conditions **(Figure 29)**. Further, additional markers for valve development, such as *FN1*, *THBS1*, *CXCL12*, and *CCND1*[197,200,229] are shown (**Figure 30**). Additional quantification of *WT1*, *TNNT2*, *PECAM1*, *ALDH1A2*, and *TBX18* shows the individual distribution of gene expression across major clusters (**Figure 31)**.

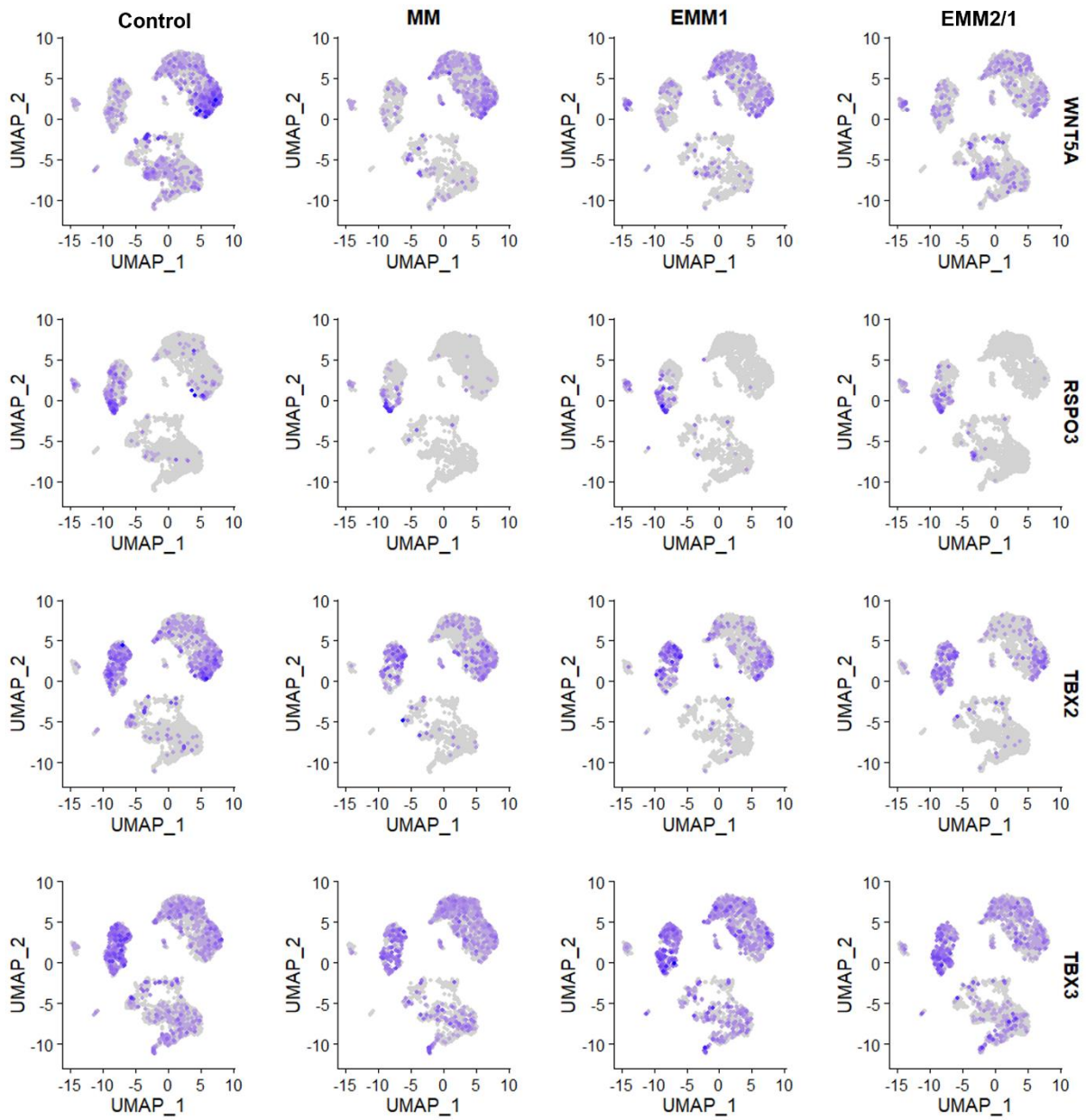

Figure 29. Feature plots of outflow tract-related genes within single cell RNA sequencing datasets in each condition.

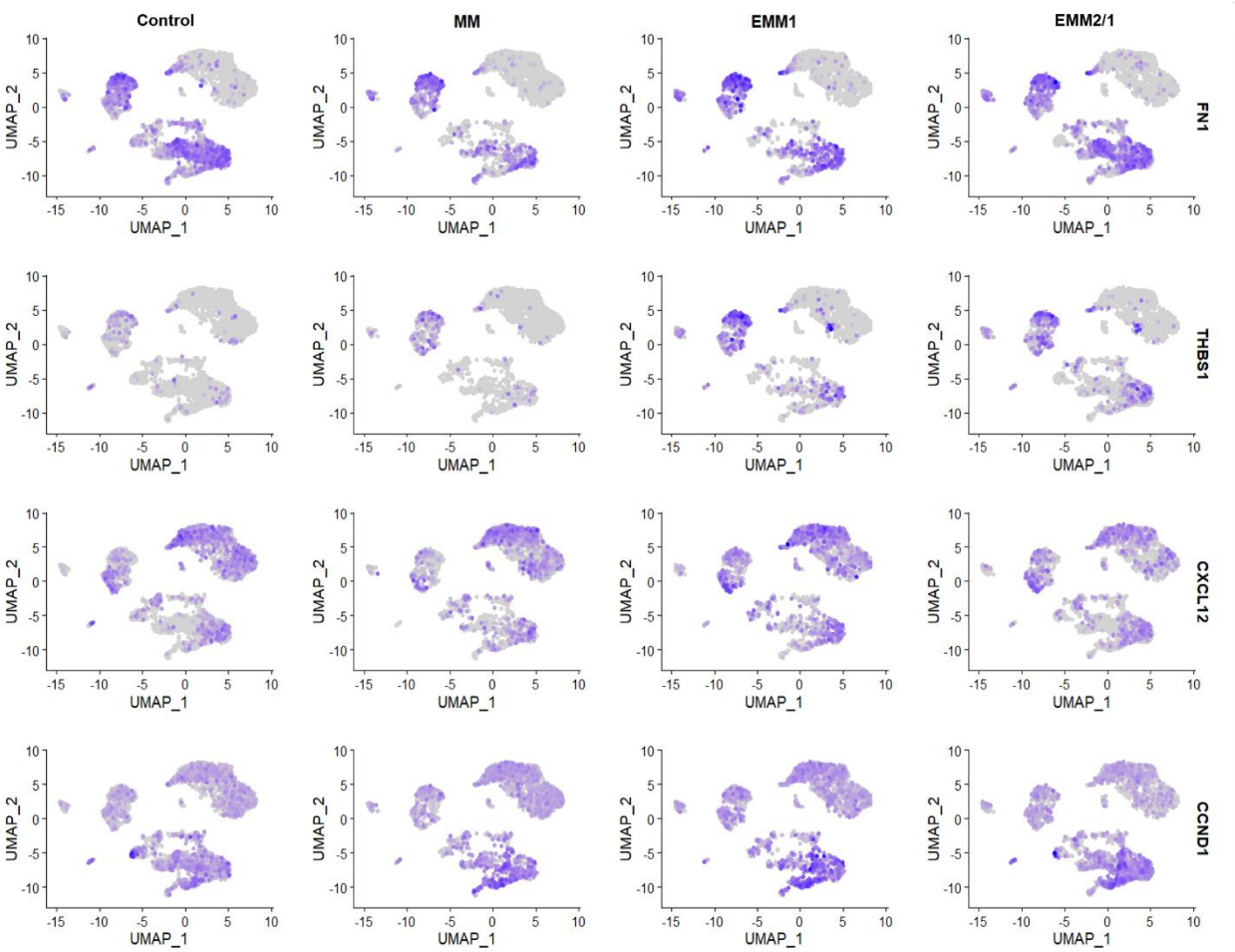

Figure 30. Feature plots of valve development-related genes within single cell RNA sequencing datasets in each condition.

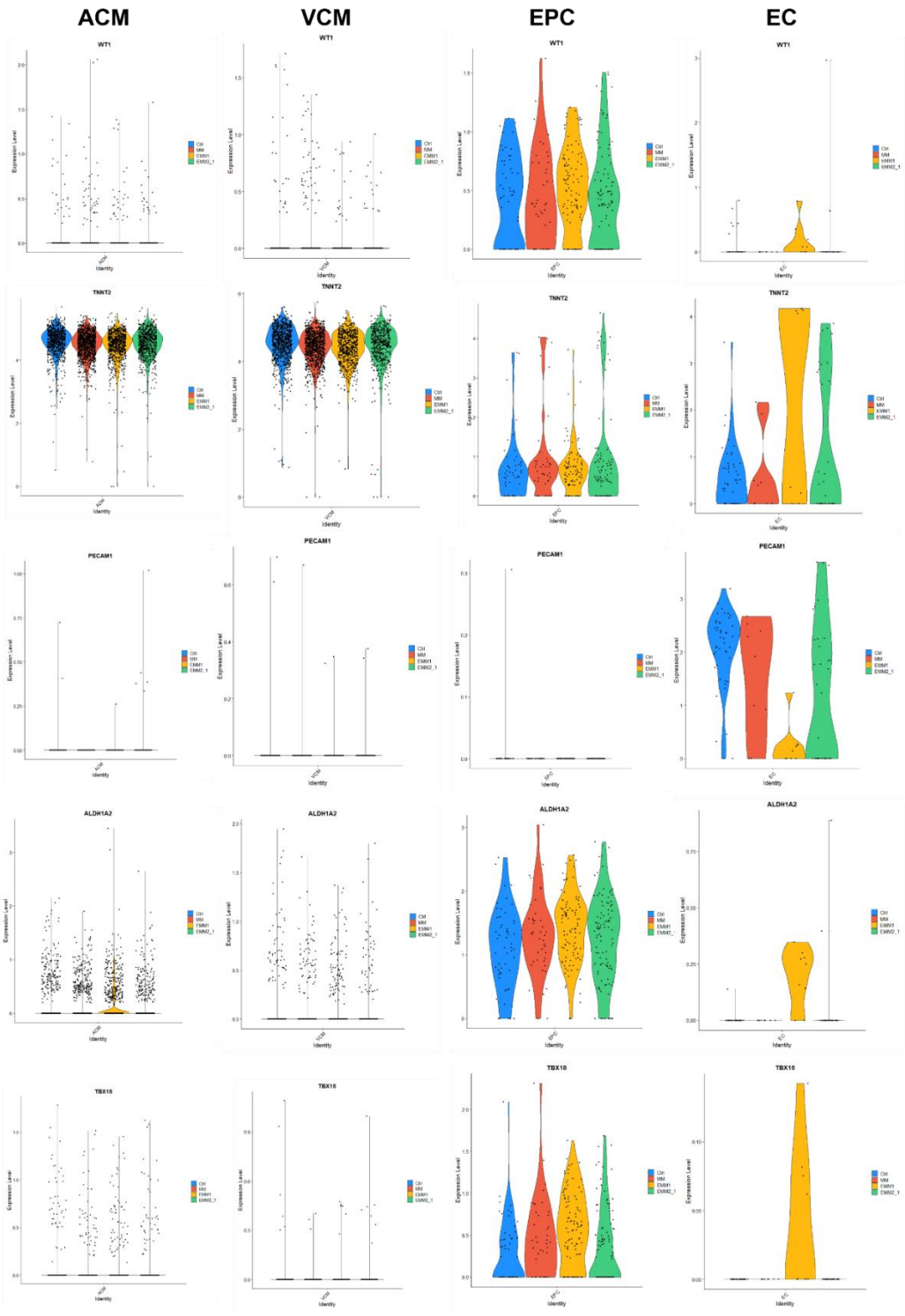

Figure 31. Violin plots for genes in the ACM, VCM, EPC, and EC clusters for all four conditions (control = blue, MM = red, EMM1 = orange, EMM2/1 = green.

Extending these analyses, we utilized publicly available data from the Human Cell Atlas Project[113], using data from gestational day 45 (GD45) hearts and from 5 weeks to 13 weeks of gestation[114] to compare our human heart organoids to that of developing human hearts. Based on their time in culture, our human heart organoids should be closest to GD45 or 6-7 gestational week human fetal hearts **(Figure 32)**.

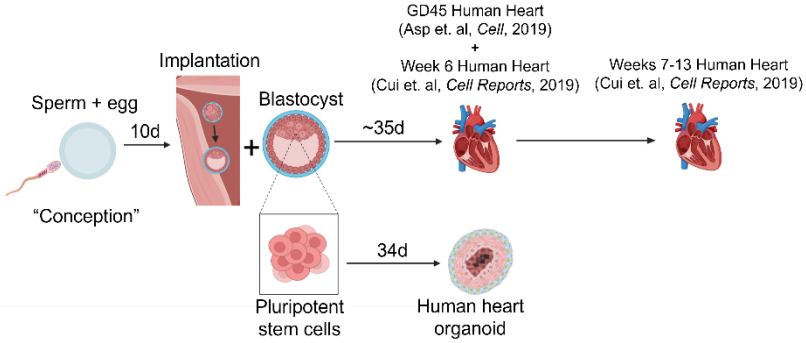

Figure 32 Schematic of timeline comparing human embryonic heart development and human heart organoid development. Created using BioRender.com.

We integrated these scRNA-seq datasets and discovered high overlap between our cell type annotations and that presented from the Human Cell Atlas Project **(Figure 33)**, with atrial and ventricular cardiomyocytes, proepicardial-derived cells (named fibroblast-like, smooth muscle cells, and epicardium-derived cells in the Human Cell Atlas Project dataset), endothelial cells, and epicardial cells displaying a high degree of clustering between datasets. ACMs, VCMs, and EPCs in the organoids showed similar percentages of total cellular makeup (13-32%, 15-26%, and 1-4%, respectively, per condition) compared to gestational human hearts[113], with ACMs, VCMs, and EPCs in GD45 gestational human hearts showing 32%, 14%, and 3.8% of total makeup, respectively. Interestingly, our valve cells mapped closely to capillary endothelial cells and our stromal cells mapped closely to immune cells, which may be due to shared gene programs

surrounding endothelial-to-mesenchymal transition processes[230] (valve cells and capillary endothelial cells) or transcriptional pathways implicated in the interplay between stromal cells and immune cells during cardiac repair and regeneration[231]. Our conductance cell cluster was mapped to an unannotated cluster of cells from the embryological datasets, even though our conductance cell cluster displays similar gene expression profiles to the cardiac neural crest and Schwann progenitor cell cluster in the Human Cell Atlas Project dataset[113], which may be due to a lack of extra-cardiac signaling pathways in the organoids, or may be due to unaccounted noise between the datasets.

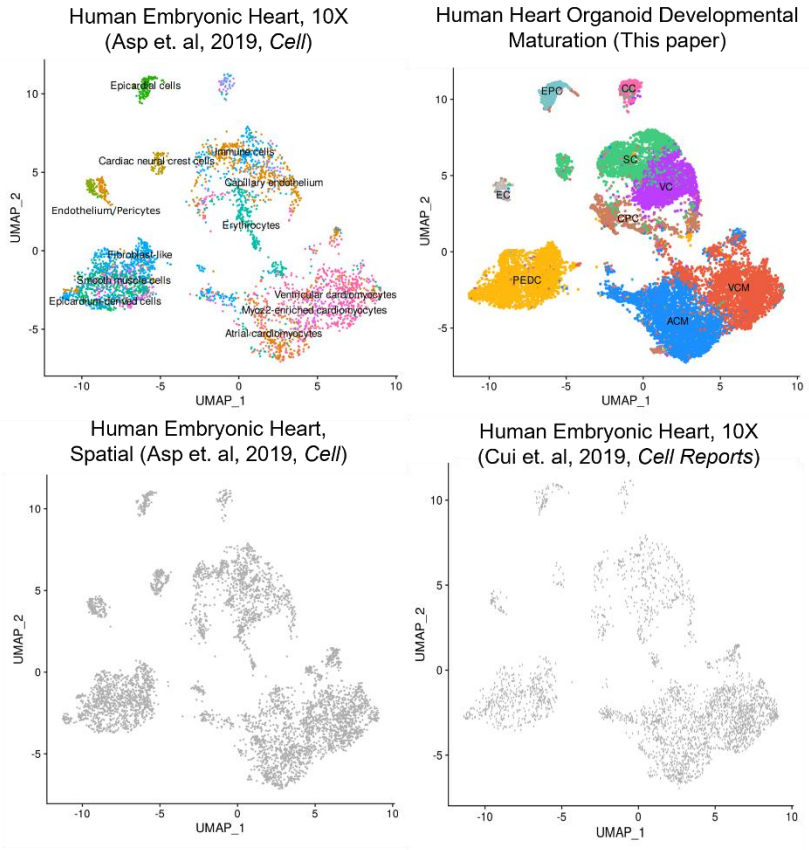

Figure 33. UMAP projections displaying human embryonic heart and human heart organoid scRNAseq datasets. Cluster naming for (Asp et al, Cell, 2019) is preserved from original text. Cluster identity and color for the human heart organoid dataset is preserved from that shown in **Figure 21**.

We then used these datasets to compare gene expression profiles at the single-cell level **(Figure 34, Figure 35)**. Using the top 1000 differentially expressed genes in each dataset from the VCM, ACM, PEDC, and EPC-mapped clusters, we showed a high degree of similarity between organoids from each condition and that from embryonic hearts **(Figure 34)**, with control organoids and EMM2/1 organoids clustering closely to week 6 embryonic hearts, whereas MM and EMM1 organoids clustered closer to weeks 7-13 embryonic hearts, which may indicate that the MM and EMM1 strategies accelerate *in vitro* development at a rate higher than biological development. We also assessed individual gene expression levels and show a high degree of similarity between embryonic hearts and human heart organoids across all major clusters (**Figure 35)**, including hallmark genes for atrial cardiomyocytes (*MYL7*, *NPPA*, and *GJA5*), ventricular cardiomyocytes (*MYH7*, *MYL3*, and *IRX4*), proepicardial-derived cells (*PDGFRB*, *POSTN*, and *TCF21*), epicardial cells (*WT1*, *TBX18*, and *TNNT1*), endothelial cells (*PECAM1*, *ESAM*, and *SOX18*), and valve cells (*SOX9*, *UGDH*, and *FLRT2*). Organoids were shown to be committed to the mesodermal fate with null commitment toward ectodermal or endodermal fates (**Figure 36**)[78] (GSE153185).

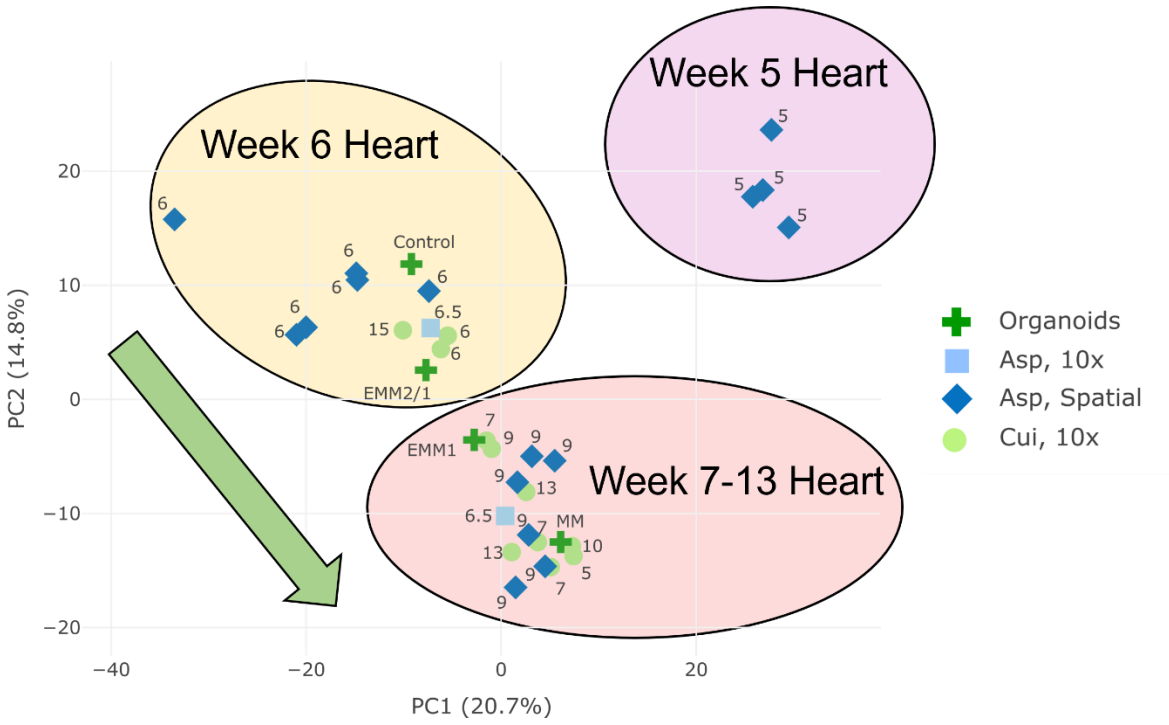

Figure 34. PCA plot for scRNA-seq datasets presented in **Figure 33**.

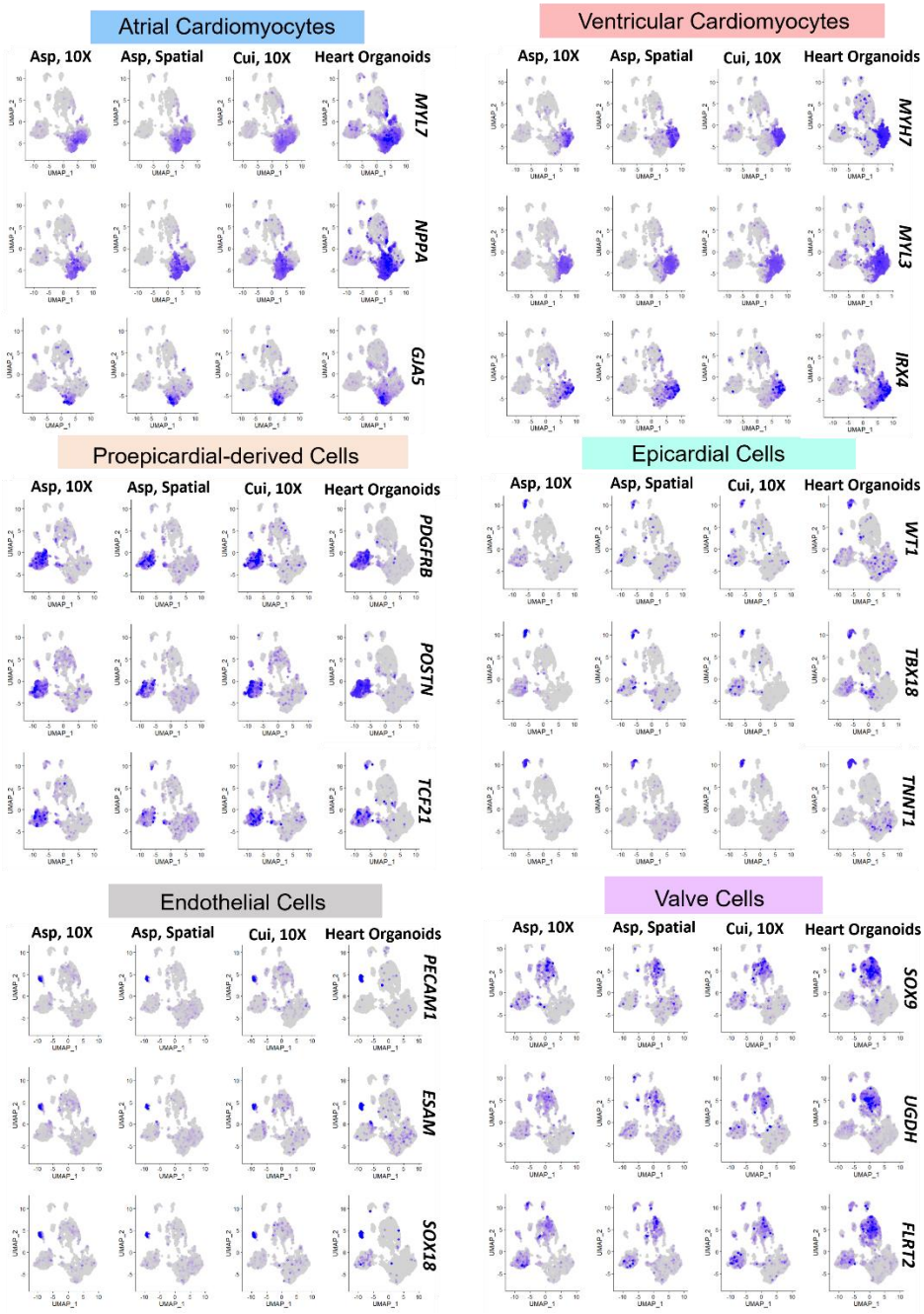

Figure 35. Feature plots displaying key marker genes for each cluster in the Asp 2019, Cui 2019, and human heart organoid datasets. Clusters of interest include: Atrial Cardiomyocytes, Ventricular Cardiomyocytes, Proepicardial-derived Cells, Epicardial Cells, Endothelial Cells, and Valve Cells. Color intensity represents the relative value of gene expression per gene.

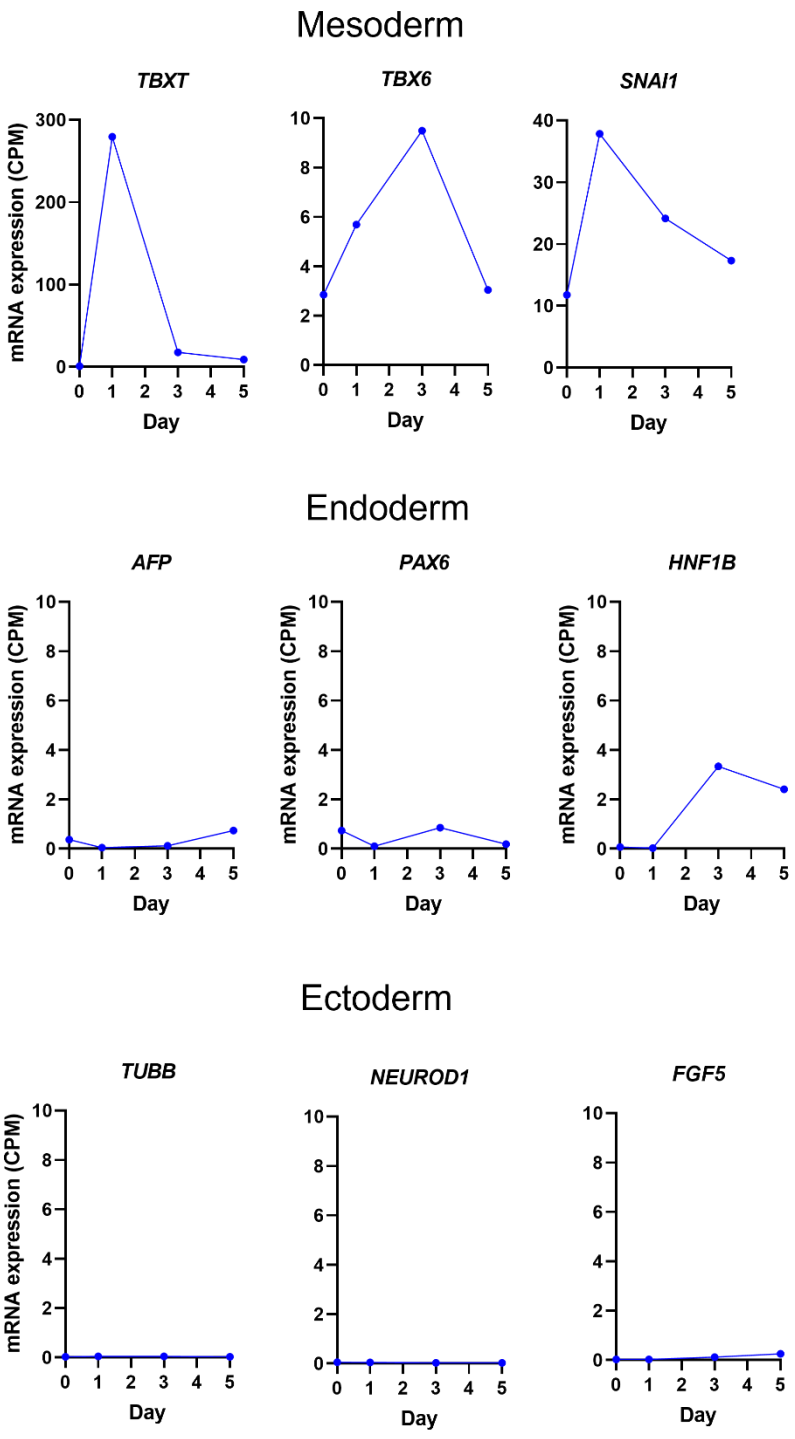

Figure 36. RNA sequencing data from days 0-5 organoid differentiation showing expression values for key mesodermal, endodermal, and ectodermal markers (n=8 organoids per time point). CPM = counts per million.

Additionally, we show that genes in the conductance cell cluster and stromal cell cluster show resemblance to embryological datasets and show that metabolic genes across organoid and embryological datasets share similar expression profiles across cell types and clusters **(Figure 37)**.

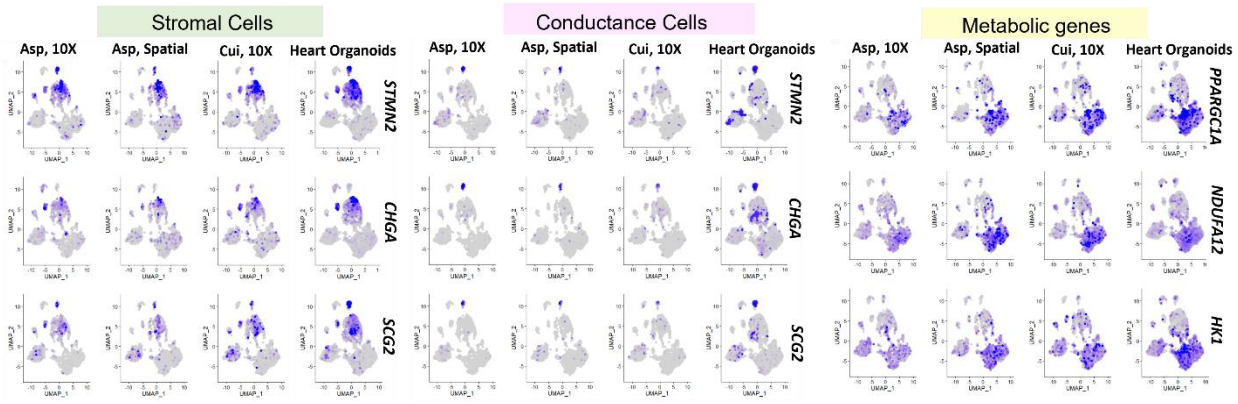

Figure 37. Feature plots of stromal cell (a) conductance cell (b) and metabolic markers (c) across embryonic heart datasets and heart organoid datasets.

To complement the above scRNA-seq analyses, dot plots describing the average and percent expression of key lineage-defining differentially expressed genes for individual clusters are depicted for each developmental induction condition illustrating the cellular complexity of our heart organoids at day 34 **(Figure 38)**. As we and others have shown before[78,80,125,133,232], the high cellular complexity of the organoids drives self-organization and cell-cell communication.

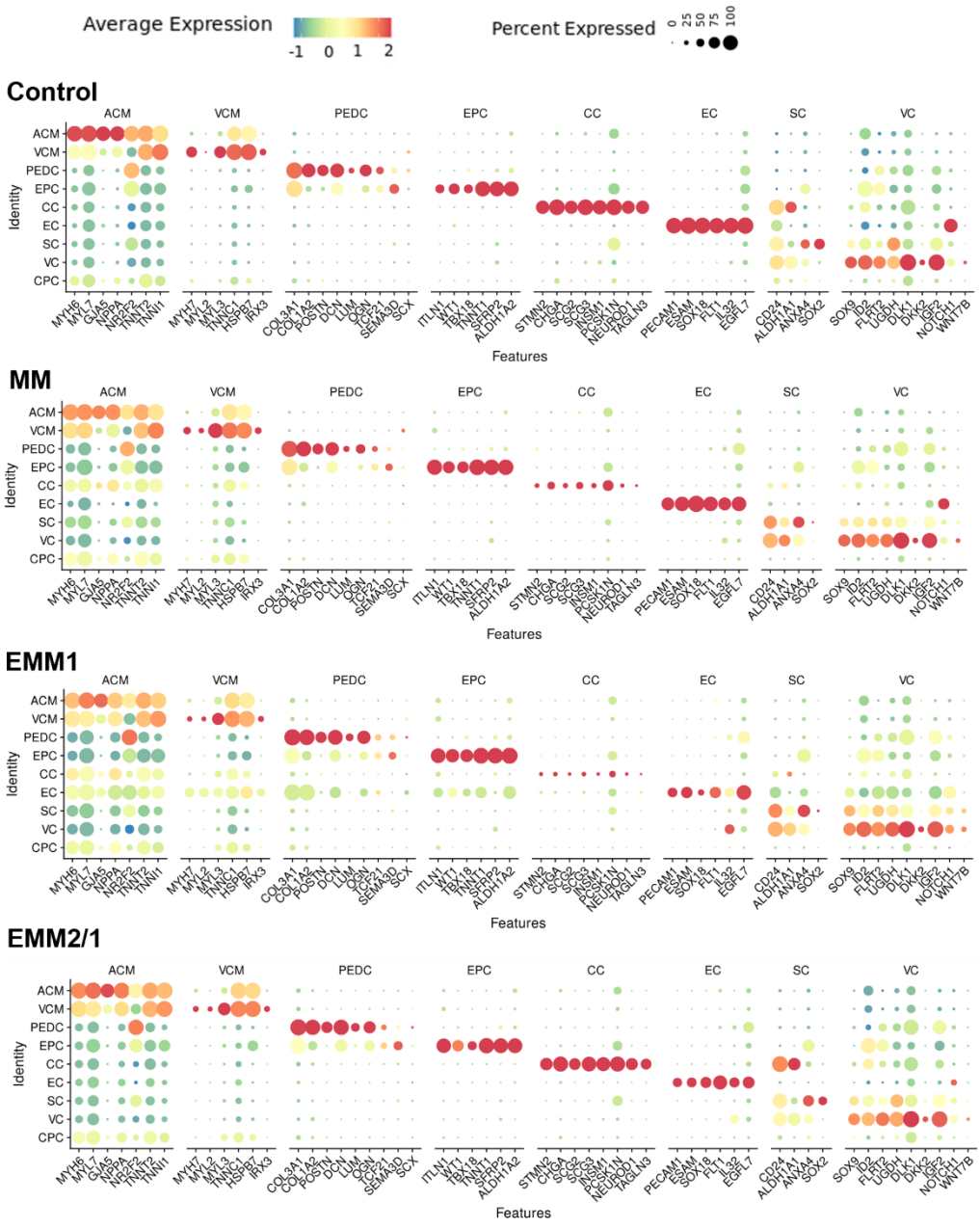

Figure 38. Dot plots of differentially expressed marker genes in each cluster for each condition. Color is indicative of the average expression level across all cells, and the size of the circle is indicative of the percentage of cells within a particular cluster that express the respective gene.

We performed computational analysis of cell-cell communication networks for key genes found in the organoids. We identified various complex receptor-ligand communication pathways within our human heart organoids in each condition **(Figure 39)**. Receptor-

ligand networks include JAG1-NOTCH1, PDGFRs, IGF2-IGF2R, INSR, and VEGF, among others.

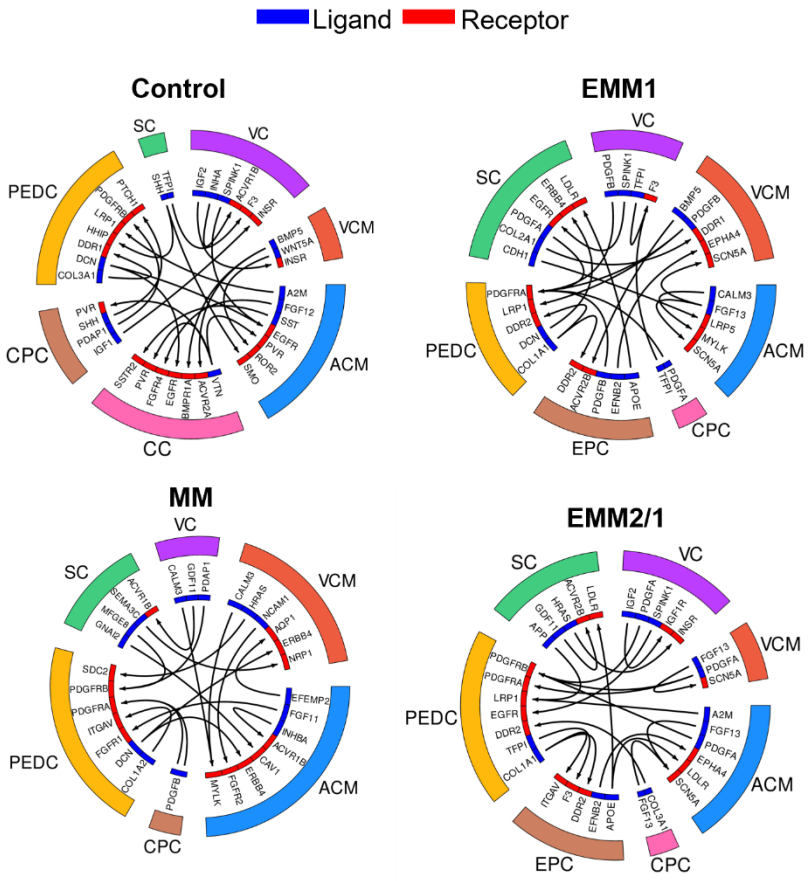

Figure 39. Visualization of cell-cell ligand-receptor communication networks for each condition. The colors of clusters (exterior) match that of UMAP projections. Ligands are indicated as blue bands and receptors are indicated by red bands. Arrows within depict pairing from ligands to receptors.

4.2.2. Quantification of metabolic maturation states in human heart organoids under developmental induction conditions

The early developing human heart relies heavily on glycolysis for energy expenditure. As it continues to grow, it decreases its reliance on glycolysis and switches to fatty acid oxidation for the bulk of energy consumption[145,147,233–235]. Therefore, we sought to

determine the effect that our developmental induction conditions exerted on mitochondrial growth and metabolic transcriptional activity within heart organoids. Through the addition of MitoTracker, a mitochondrial-permeable fluorescent dye, we visualized live mitochondrial content within heart organoids at day 30 of culture **(Figure 40)**. Control organoids displayed few and diffuse mitochondria, while EMM2/1 organoids possessed the most developed mitochondrial content of all conditions (abundance, morphology) (**Figure 40a**). An increasing trend of mitochondrial content in MM, EMM1, and EMM2/1 organoids (fold change of 1.73 ± 0.10, 2.60 ± 0.11, and 3.10 ± 0.18, respectively) was quantified relative to control, suggesting that developmentally maturated organoids had an increasingly higher capacity for aerobic respiration and responded positively to maturation stimuli **(Figure 40b)**.

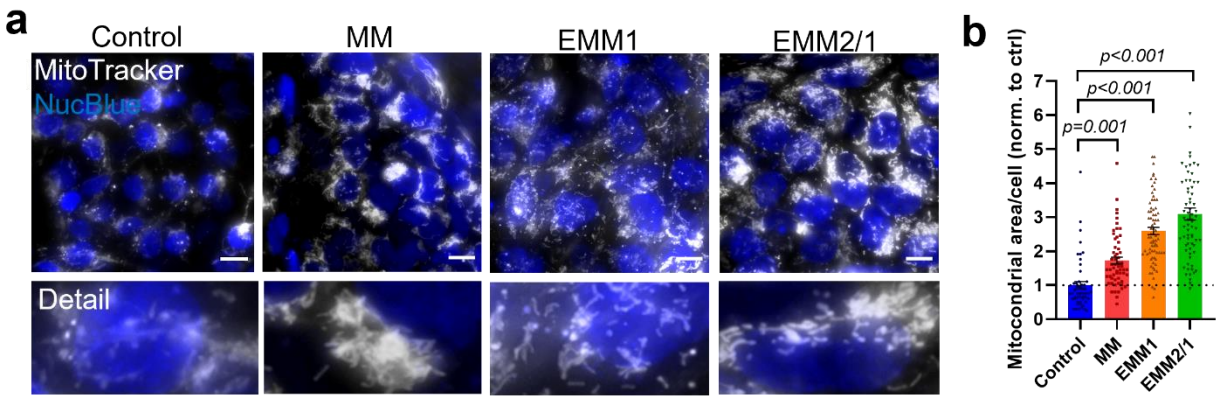

Figure 40. a, Mitochondrial labeling within day 30 human heart organoids in each condition (n=6 independent organoids per condition). White = Mitotracker, blue = NucBlue. Scale bars = 10 µm. Detailed images of mitochondria are shown below each main image. b, Quantification of mitochondrial area surrounding each individual nucleus (n=6 independent organoids per condition, n=50-70 measurements per condition). Values = mean ± s.e.m., one-way ANOVA with Brown-Forsythe and Welch multiple comparisons tests.

TEM revealed high-magnification detail on mitochondrial presence within organoids at day 30 of culture **(Figure 41a)**. Compared to day 15 mitochondrial size, control organoid mitochondrial size was similar **(Figure 41b)**. However, mitochondrial size within MM, EMM1 and EMM2/1 organoids dramatically increased relative to that of control organoids. We employed qRT-PCR at different timepoints from day 20 to day 30 of organoid culture to explore the differential gene expression of two key OXPHOS genes in cardiac metabolic maturation: *PPARGC1A*, a master regulator of mitochondrial biogenesis[236], and *CPT1B*, a critical rate-limiting fatty acid transporter element[237,238] **(Figure 42)**. *PPARGC1A* expression was up to 2.5-fold higher in EMM2/1 organoids from days 21 to 25 relative to control and ended at a fold change of 1.5-fold higher by day 30. Expression for MM and EMM1 organoids also exhibited an increase from days 21 to 25 relative to control, albeit not as high as EMM2/1. By day 30, expression in EMM1 organoids remained similar to control while MM and EMM2/1 organoids displayed 1.2-fold and 1.7-fold higher levels, respectively. *CPT1B* expression increased 1.5-fold at day 30 in the EMM2/1 condition relative to control, yet expression in MM remained similar or decreased for EMM1 organoids.

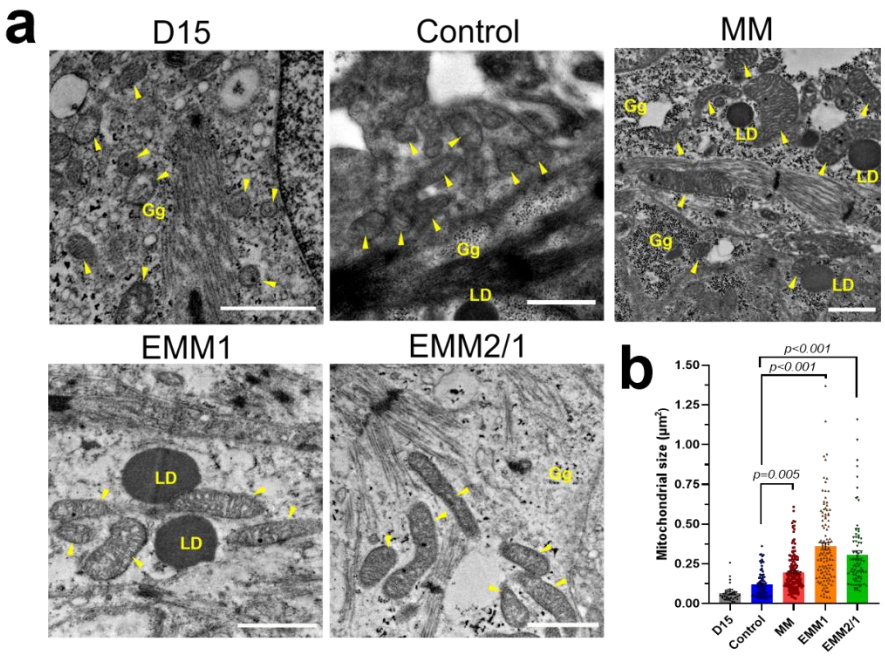

Figure 41. a, TEM images display mitochondria in day 15 organoids and in organoids from each maturation condition at day 30 (n=4 independent organoids per condition). Yellow arrows indicate mitochondria, LD = lipid droplets, Gg = glycogen granules. Scale bars = 1 µm. b, Quantification of mitochondrial area from TEM images. Values = mean ± s.e.m., one-way ANOVA with Brown-Forsythe and Welch multiple comparisons tests (n=4 independent organoids per condition, n=40-144 mitochondria measured per condition).

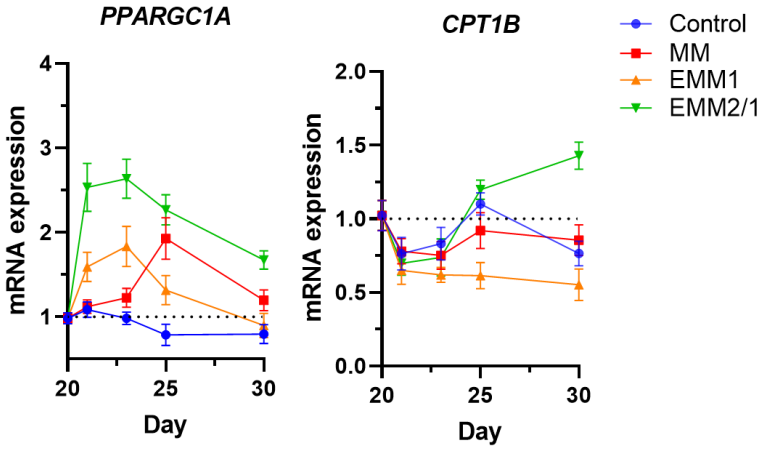

Figure 42. mRNA expression of metabolic genes PPARGC1A and CPT1B between days 20 and 30 of culture for each condition (n=8 independent organoids per condition across three independent experiments). Data presented as log2 fold change normalized to Day 20. Values = mean ± s.e.m.

To investigate real-time metabolic parameters, we performed Seahorse Mito Stress Test assays with organoids in each condition at day 30 **(Figure 43a)**. Organoids in the EMM2/1 condition displayed marked increases in basal respiration **(Figure 43b)**, maximal respiration **(Figure 43c)**, and percent spare respiratory capacity **(Figure 43d)** compared to control; aligning closely with the metabolic enhancement present in EMM2/1 organoids displayed in previously shown mitochondrial and metabolic data.

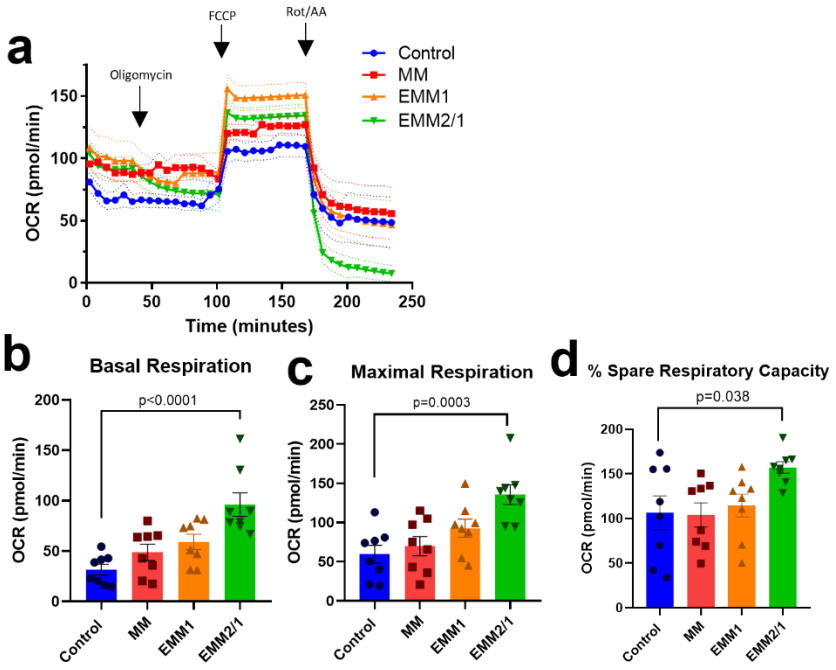

Figure 43. a, Oxygen consumption rate measurements from Agilent Seahorse XFe96 metabolic stress test assay in all conditions (n=8 independent organoids per condition across two independent experiments). Values = mean ± s.e.m.. (b-d,) Quantifications from oxygen consumption rate assay (n=8 independent organoids per condition) including b, Basal respiration, c, Maximal respiration, and d, Spare respiratory capacity.

Supporting these findings using scRNA-seq data, key genes involved in cardiac metabolism were found to be upregulated in organoids from the MM, EMM1, and EMM2/1 conditions in the ACM and VCM clusters **(Figure 44)**, including: *CKMT2*, a gene that encodes a mitochondrial creatine kinase and is important for metabolic efficiency and

implicated in cardiac maturation[15,239–241]; *NMRK2*, a gene active in high energy states and involved in both cardiac maturation and lipid metabolism[15,242]; and *KLF9*, a gene related to adipogenesis and cardiac metabolic maturation[15,243,244].

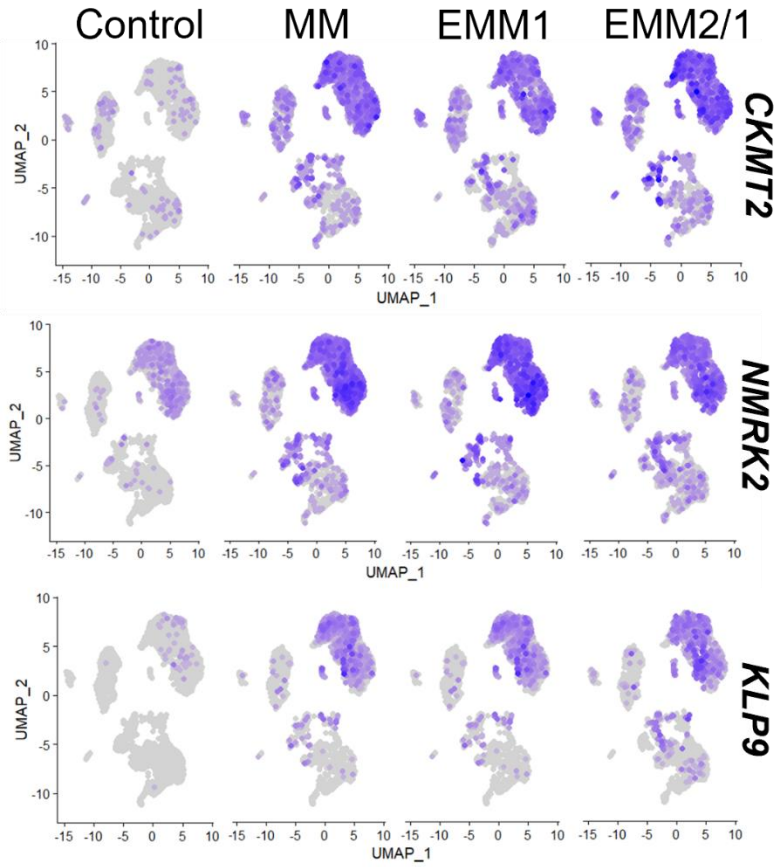

Figure 44. Feature plots displaying key metabolic genes upregulated in the VCM and ACM clusters. Color intensity represents the relative value of gene expression per gene.

We then used gene expression data from the ACM and VCM clusters in each condition to look for a wider set of metabolic markers as the organoids developed in the different conditions. We found that organoids in the EMM2/1 condition expressed much higher levels of key metabolic genes compared to control, including those involved in fatty acid metabolism, amino acid metabolism, TCA cycle, and mitochondrial dynamics **(Figure 45)**. Overall, these results suggested that developmental induction strategies can elicit distinct

metabolic growth patterns and that EMM2/1 organoids exhibit the most marked recapitulation of significant aspects of cardiac metabolic growth *in vitro*.

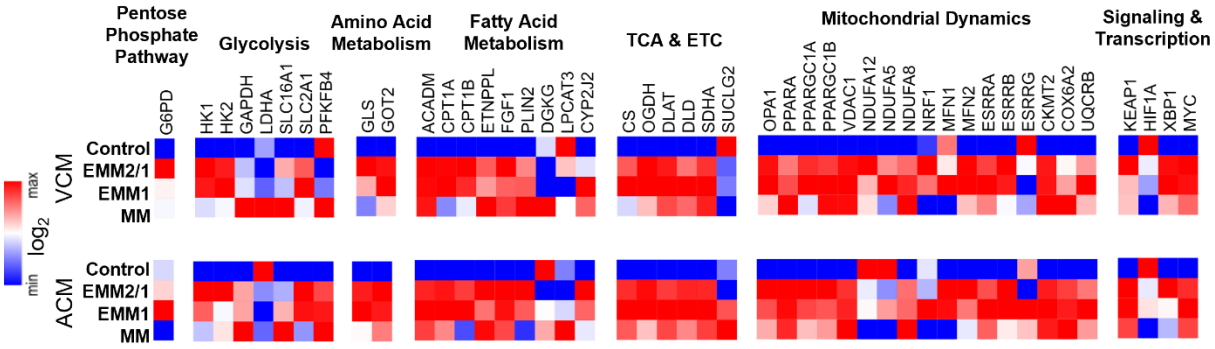

Figure 45. Expression heatmaps of key metabolic genes in the VCM and ACM clusters in each condition. Data displayed as log2 fold change and normalized to each column (for each gene).

4.2.3. Developmental induction conditions promote progressive electrophysiological maturation in human heart organoids

The emergence and presence of the cardiac conduction system, including specific ion channels and membrane receptors, such as those surrounding calcium, potassium, and sodium currents, represent critical elements of the cardiomyocyte action potential[245–247] and fetal heart development[248,249]. We sought to characterize the functionality of heart organoids under developmental induction conditions through electrophysiology and immunofluorescence for key markers. We assessed calcium transient activity of individual cardiomyocytes within human heart organoids at day 30 using the membrane-permeable dye Fluo-4. Organoids in all conditions exhibited distinct and regular calcium transient activities with varying peak amplitude and action potential frequencies **(Figure 46a)**. Control and MM organoids presented smaller peak amplitudes when compared to EMM1

and EMM2/1 organoids, indicating less robust contractions **(Figure 46b)**, and presented similar beat frequencies ~1.5 Hz. EMM1 organoids displayed abnormally high beating rates (~2.5 Hz) for the heart at this stage, while EMM2/1 organoids showed beat frequencies at ~1-1.5 Hz **(Figure 46c)**.

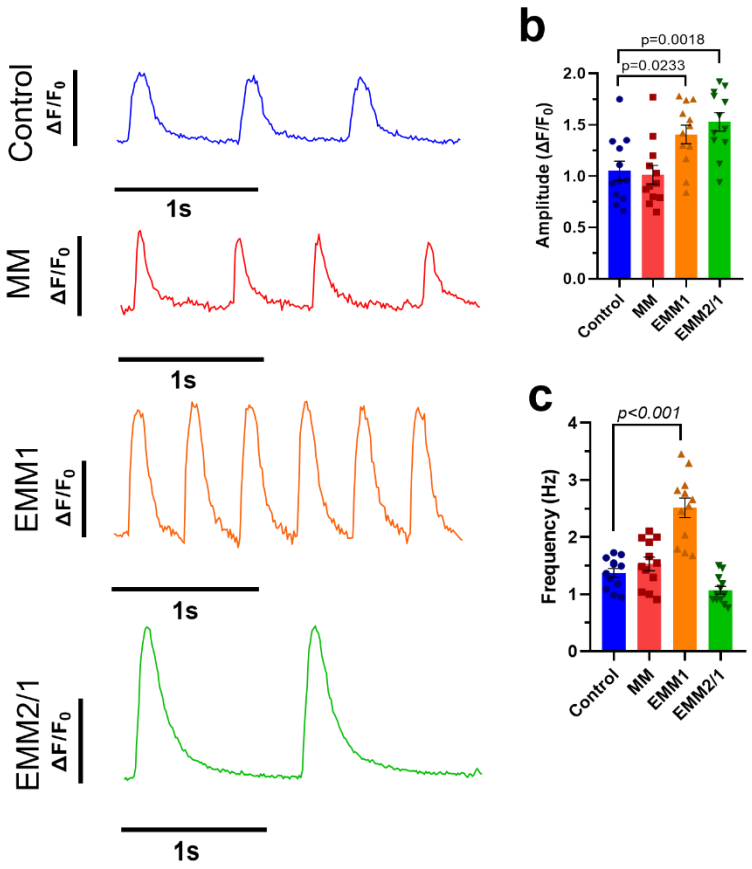

Figure 46. Representative calcium transient traces within day 30 human heart organoids from each condition (n=12 independent organoids per condition across three independent experiments). Traces represent data from an individual cardiomyocyte within human heart organoids. b, Quantification of peak amplitude of calcium transient traces from each condition (n=12 independent organoids per condition across three independent experiments). A minimum of 2 regions and 16 peaks were quantified and averaged for each organoid. Values = mean ± s.e.m. c, Quantification of calcium transient peak frequency for each condition (n=12 independent organoids per condition across three independent experiments). A minimum of 2 regions and 16 peaks were quantified and averaged for each organoid. Values = mean ± s.e.m.

In general, and except for EMM1 organoids, developmentally induced organoids presented beating rates compatible with what has been described for early human embryos at GD45[250,251] (60-80 beats per minute). Calcium traces from organoids in all conditions were shown to be reproducible **(Figure 47)**.

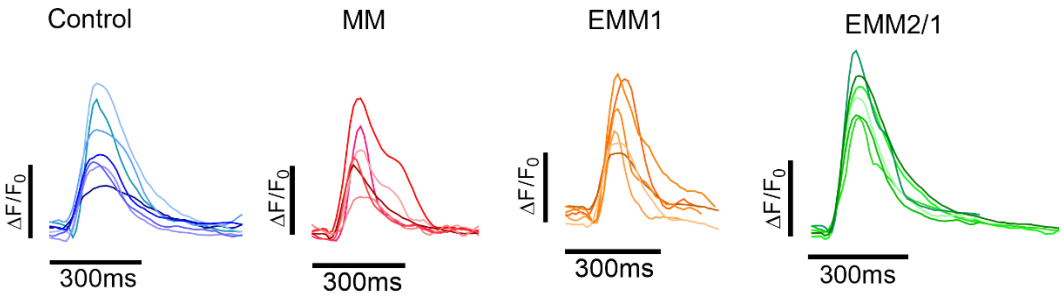

Figure 47. Representative calcium transient traces within day 30 human heart organoids from each condition (n=7, 6, 6, and 6 independent organoids for control, MM, EMM1, and EMM2/1, respectively). Traces represent data from an individual cardiomyocyte within human heart organoids.

Cardiomyocyte action potential activity encompasses the complex orchestration of various ion currents, such as calcium, potassium, and sodium, and supporting channels such as ryanodine receptors[252]. We investigated the expression levels of various electrophysiologically-relevant genes in heart organoids and discovered a robust expression pattern in ACM and VCM clusters across all conditions **(Figure 48)**, including *RYR*, *ATP2A2*, *SCN5A*, *KCNJ2*, and *KCNH2*. Expression levels for all genes appeared to increase slightly to moderately for the EMM2/1 condition relative to control. Notably, *KCNJ2* expression increased dramatically for all maturation conditions relative to control,

particularly in the EMM2/1 condition. An additional ion channel of critical importance is the hERG channel[253–255] encoded by the gene *KCNH2*. Mutations and perturbations in this channel can lead to shortening or prolongation of the QT interval[254,256–258], and drug interactions with this channel can lead to cardiac arrythmia which represents a critical bottleneck surrounding drug discovery and development[259,260]. Interestingly, *KCNH2* displayed high expression levels within the ACM and VCM clusters in all conditions of our organoids.

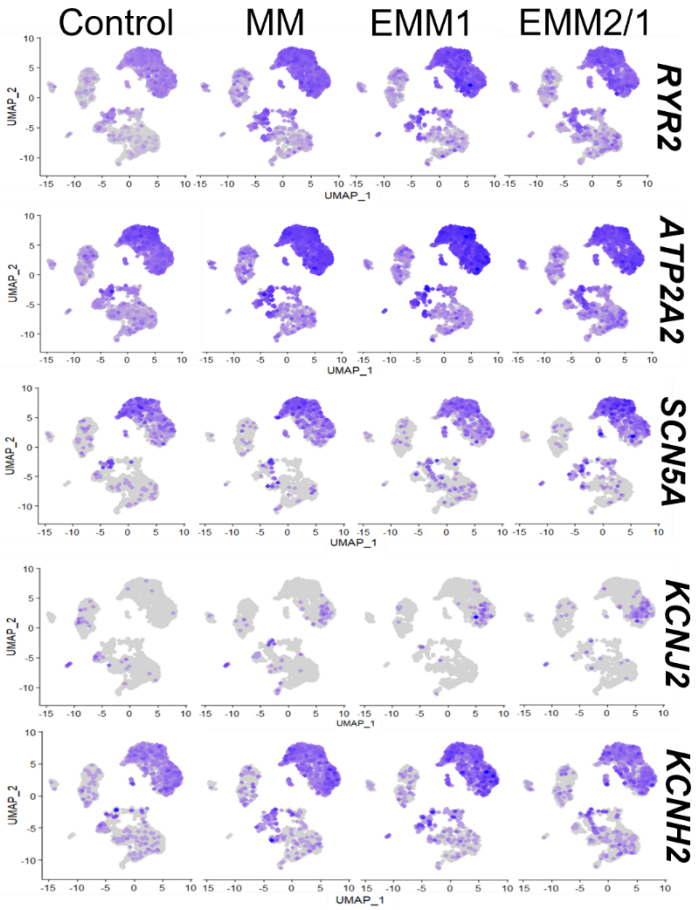

Figure 48. Feature plots displaying key electrophysiological genes differentially expressed in the VCM and ACM clusters in each condition. Color intensity represents the relative value of gene expression per gene.

Further, autonomic control of the cardiac conduction system through adrenergic signaling plays a significant role in heart physiology[261–263], and underlies a range of CVDs from heart failure and hypertension to arrythmia[264,265]. We identified the presence of critical beta-adrenergic receptor genes, *ADRB1* and *ADRB2*, encoding beta-adrenergic receptors 1 and 2 within our organoids in each condition **(Figure 49)**. While *ADRB2* was expressed in both the ACM and VCM clusters in each condition, *ADRB1* showed expression within the ACM and VCM clusters in MM, EMM1 and EMM2/1 conditions, but was only expressed in the ACM cluster in the control condition. *ADRB3* was sparsely expressed relative to *ADRB1* and *ADRB2*, which stays true to cardiac physiology[113,266–268].To investigate the temporal dynamics of key ion channels through the application of our developmental maturation strategies, we utilized qRT-PCR from day 20 to day 30 of organoid culture to assess levels of calcium (*ATP2A2*), sodium (*SCN5A*), and potassium (*KCNJ2*) transporters **(Figure 50)**. *ATP2A2* expression increased in all conditions relative to control, with EMM2/1 exhibiting the most marked upregulation of 4-fold (relative to control) at day 25 and day 30. *SCN5A* expression was upregulated for all conditions from day 21 to day 30 relative to day 20. Notably, MM and EMM2/1 organoids displayed a 3-fold increase at day 30 relative to day 20, while control organoids only displayed a 2-fold increase. *KCNJ2* expression steadily decreased in the EMM1 condition relative to control, with MM organoids exhibiting upregulation at day 30. Meanwhile, EMM2/1 displayed upregulation compared to control throughout the culture period up until day 30. We investigated the voltage activity within control and EMM2/1 heart organoids via the potentiometric dye di-8-ANEPPS and identified unique actional potentials within individual cardiomyocytes indicative of the presence of specialized atrial- and nodal-like cells but,

interestingly, ventricular-like action potentials were only observed in EMM2/1 organoids **(Figure 51)**.

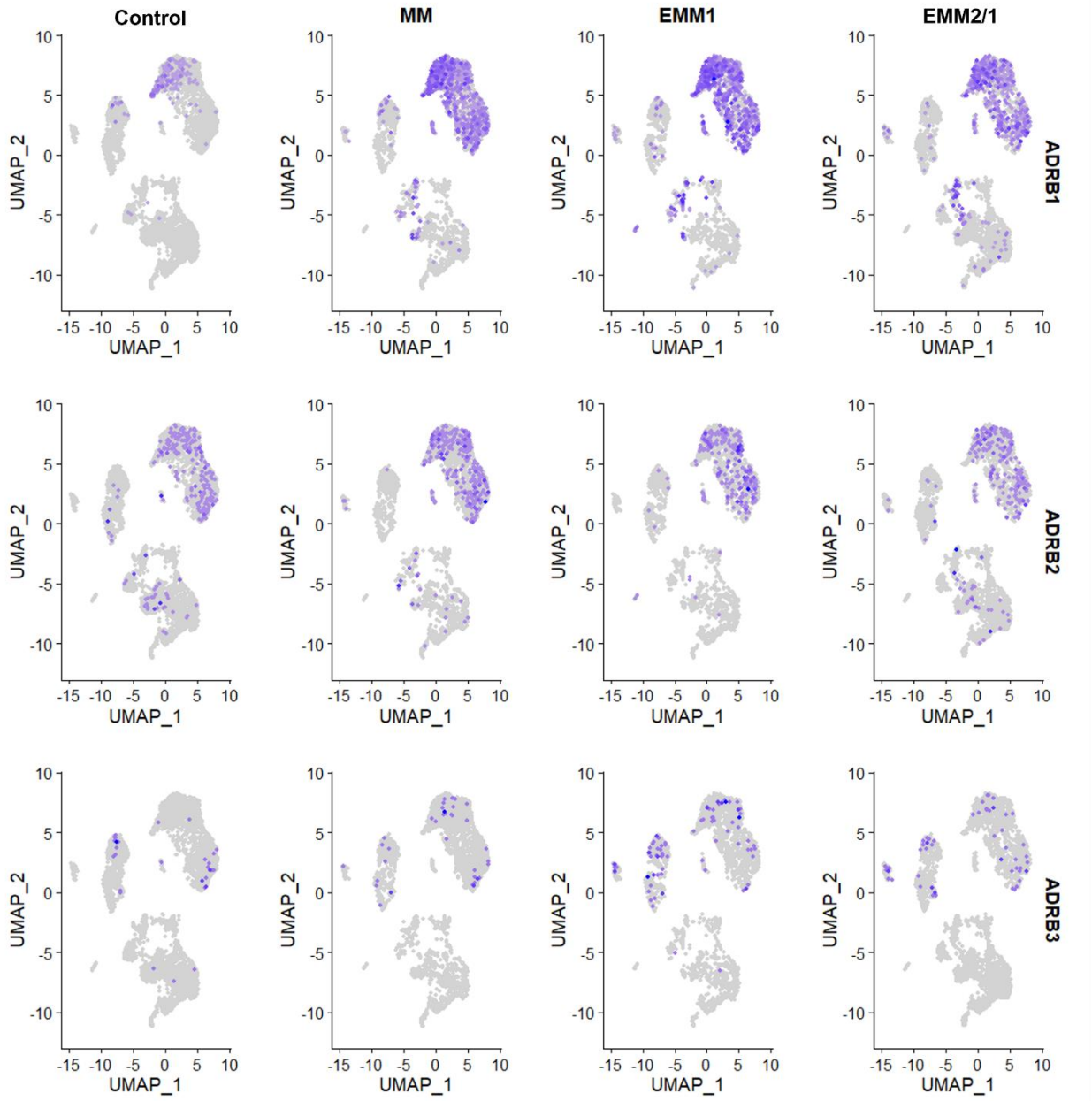

Figure 49. Feature plots of β-adrenoreceptor genes within single cell RNA sequencing datasets in each condition.

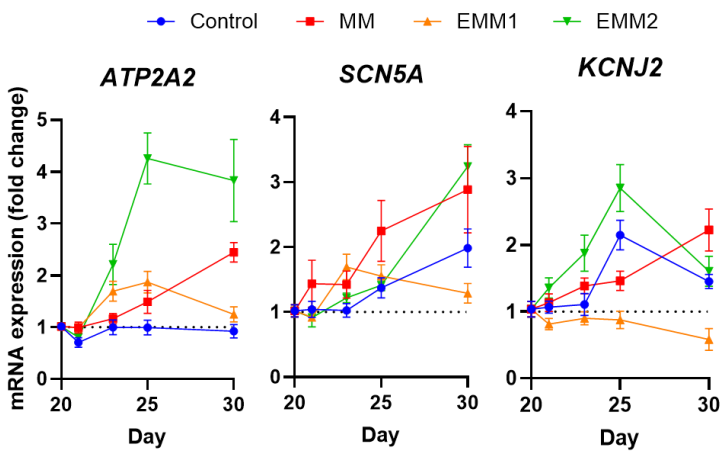

Figure 50. mRNA expression of key electrophysiological genes between days 20 and 30 of culture for each condition (n=8 independent organoids per day per condition per gene across three independent experiments). Data presented as log2 fold change normalized to Day 20. Values = mean ± s.e.m.

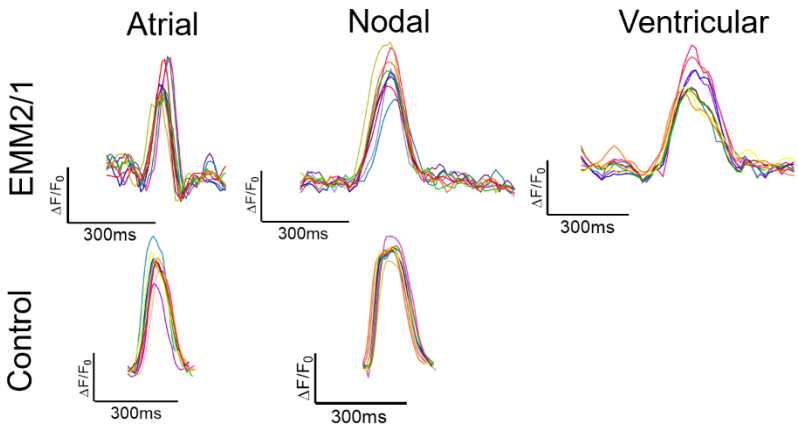

Figure 51. Representative voltage tracings of organoids in the EMM2/1 and control conditions depicting atrial-, nodal-, and ventricular-like action potentials (n=9 individual cells from 3 independent organoids per action potential subtype per condition across three independent experiments).

Proper excitation-contraction coupling, depolarization, and repolarization of cardiomyocytes depends on specialized invaginations of the sarcolemma (t-tubules), which are indicative of cardiomyocyte maturation[269,270]. We assessed t-tubule presence

in human heart organoids at day 30 via caveolin-3 immunofluorescence imaging (**Figure 52a)** and discovered t-tubules among and surrounding sarcomeres ($TNNT2^+$) within organoids in each condition, with increasing t-tubule density quantified in the EMM2/1 condition **(Figure 52b)**. We also utilized fluorescently labeled wheat germ agglutinin (WGA) to assess t-tubules in human heart organoids at day 30 **(Figure 53a, Figure 54b)** and discovered similar results indicating EMM2/1 organoids possessed marked increases in t-tubule density. We assessed the presence of KCNJ2 via confocal microscopy **(Figure 54a)**. $KCNJ2^+$ puncta were observed in each condition, with a 2-fold increased presence in the EMM2/1 condition relative to control **(Figure 54b)**, supporting previous data displaying increased amounts of KCNJ2 transcripts in EMM2/1 organoids. Together, this data shows that our developmentally maturated organoid platform, specifically the EMM2/1 strategy, produces organoids that recapitulate significant electrophysiological aspects of cardiac development, physiology, and disease.

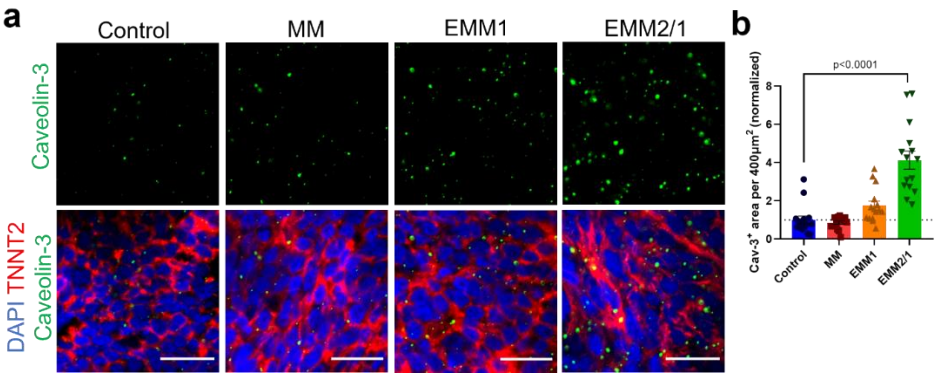

Figure 52. a, Representative immunofluorescence images of caveolin-3 puncta within TNNT2+ regions in organoids for each condition (n=15 independent organoids per condition across three independent experiments). Green = caveolin-3, red = TNNT2, blue = DAPI. Scale bar = 20 μm. b, Quantification of the caveolin-3 positive area per 400 square μm for each condition from images presented in (a) (n=15 independent organoids per condition across three independent experiments). Data presented as fold change normalized to control. Values = mean ± s.e.m., one-way ANOVA with Brown-Forsythe and Welch multiple comparisons tests.

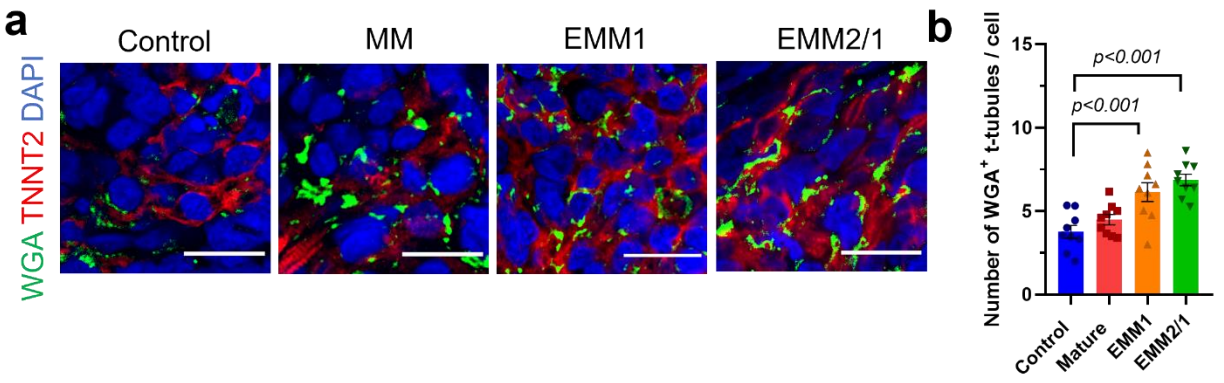

Figure 53. a, Representative immunofluorescence images of KCNJ2+ puncta within TNNT2+ regions in organoids for each condition (n=14 independent organoids per condition across three independent experiments). KCNJ2 = green, TNNT2 = red, DAPI = blue. Scale bar = 20 μm. b, Quantification of the total number of KCNJ2+ puncta for each condition from images presented in (a) (n=14 independent organoids per condition across three independent experiments). Data presented as fold change normalized to control. Values = mean ± s.e.m., one-way ANOVA with Dunnett's multiple comparisons tests.

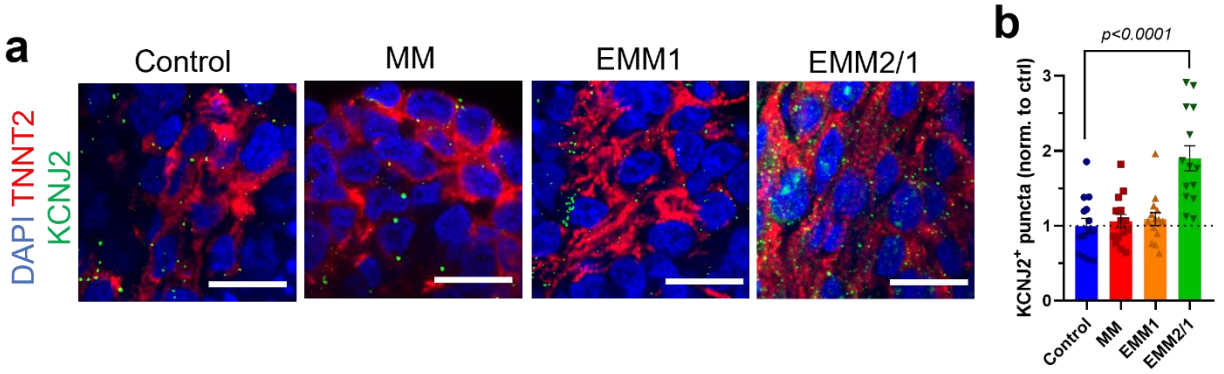

Figure 54. a, Immunofluorescence images of WGA staining (t-tubules) within TNNT2+ regions in day 30 organoids for each condition (n=8 organoids per condition). Green = WGA, TNNT2 = red, DAPI = blue). Scale bar = 20 μm. b, Quantification of t-tubules surrounding individual nuclei for each condition (n=8 organoids per condition). Values = mean ± s.e.m., one-way ANOVA with Dunnett's multiple comparisons tests.

4.2.4. Developmental induction promotes the emergence of a proepicardial organ and formation of atrial and ventricular chambers by self-organization

We have shown that developmentally induced heart organoids present improved cellular, biochemical, and functional properties when compared to their control counterparts and exhibited multiple features reminiscent of GD45 human fetal hearts. However, previous heart organoid attempts have lacked anatomically relevant cardiac structure and morphology to a great extent, including our previous work[78–80]. Given the significant changes observed through applying the EMM2/1 strategy, we decided to characterize morphological changes that took place under this improved condition. Organoids were harvested on day 30 of culture and stained for WT1 (proepicardium and epicardial cells) and TNNT2 (cardiomyocytes) **(Figure 55a)**. Organoids in each developmental induction condition displayed $TNNT2^+$ and $WT1^+$ cells, consistent with our previous observations[78], indicating the presence of epicardial and cardiomyocyte populations distributed throughout the organoids. Assessing both surface and interior planes of the organoids, organoids in all conditions possessed two distinct “chambers” marked via $WT1^+$ and $TNNT2^+$ cells. $TNNT2^+$ cells were densely packed and formed a thick myocardial wall in the lower chamber, while also present in the upper region in a less dense arrangement directly underneath $WT1^+$ cells **(Figure 56)**. In EMM2/1, $WT1^+$ cells were found densely covering the outer surface of the upper region. This clear organization pattern was not observed in the control, MM or EMM1 culture conditions. We quantified the area of $WT1^+$ and $TNNT2^+$ chambers across all maturation conditions **(Figure 55b, Figure 55c).** We found no difference in $TNNT2^+$ chamber area in MM and EMM1 organoids relative to

control but found that EMM2/1 organoids display a 1.54-fold increased area relative to control. Additionally, we found no difference in $WT1^+$ chamber area in MM organoids relative to control, whereas EMM1 and EMM2/1 organoids displayed increased areas (fold change) of 1.77 and 1.98, respectively. This data shows that organoids in all undergo significant morphological changes that lead to morphological organization, especially in the EMM2/1 condition, which included the emergence of an organoid with advanced myocardial dual-chamber morphology as well as a proepicardial pole.

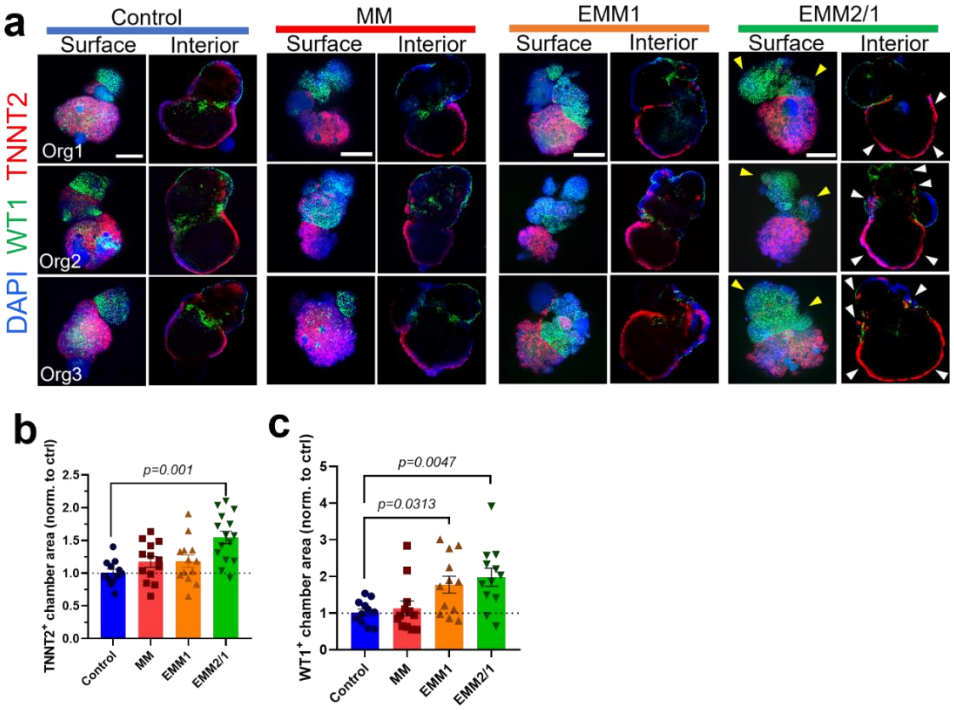

Figure 55. a, Representative surface and interior immunofluorescence images of individual day 30 organoids in all conditions displaying WT1 (green), TNNT2 (red), and DAPI (blue). Three organoids are displayed for each condition (n=12-15 independent organoids per condition across two independent experiments). Yellow arrows represent WT1+ cells on outer surface. White arrows represent TNNT2+ cells on lower chamber wall. Scale bars = 200 μm. b, Quantification of TNNT2+ chamber area and c, and WT1+ chamber area in each condition from images presented in (a) (n=12-15 independent organoids per condition across two independent experiments). Values are presented as fold change normalized to control. Values = mean ± s.e.m., one-way ANOVA with Dunnett's multiple comparisons test.

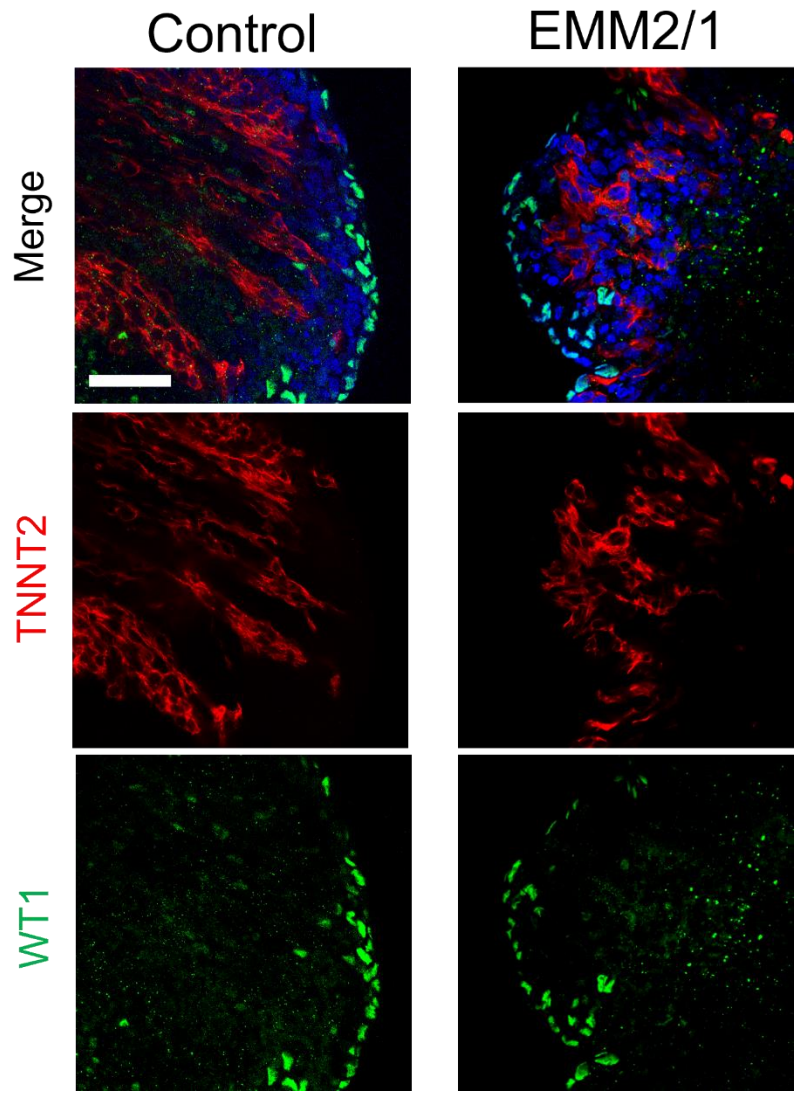

Figure 56. Representative immunofluorescence images of WT1+ and TNNT2+ cells at interior planes of organoids for the control and EMM2/1 conditions at Day 30 (n=12-15 independent organoids per condition across two independent experiments). WT1 = green, TNNT2 = red, DAPI = blue. Scale bar = 50 μm.

We could determine that ventricular (MYL2) and atrial (MYL7) myosins were spatially restricted, particularly in EMM2/1 organoids **(Figure 57a)**. All organoids expressed MYL7 throughout the bulk of the organoid, but expression was strongly localized to the upper chamber in EMM2/1, suggestive of an atrial-like chamber. In the control and MM conditions, organoids possessed MYL2 in a high variety of locations that were not

restricted to a polar end of the organoid or to either chamber, suggesting disorganization. On the other hand, organoids in the EMM1 and EMM2/1 conditions displayed an increased presence of MYL2⁺ staining and degree of organization, showcasing MYL2 restricted to one polar end of the organoids and with EMM2/1 organoids displaying a 5.5-fold increase in MYL2⁺ area **(Figure 57b)**; suggesting the formation of a ventricular-like chamber. However, as these proteins are known to be inconsistently expressed at all stages of heart development, further investigation utilizing more specific proteins and genes for ventricular and atrial chamber identity are necessary to truly define these two cellular populations and their localization within the organoid. Overall, this organization is reminiscent of heart tube anterior-posterior patterning present *in utero* during development (see **Figure 65** for a schematic).

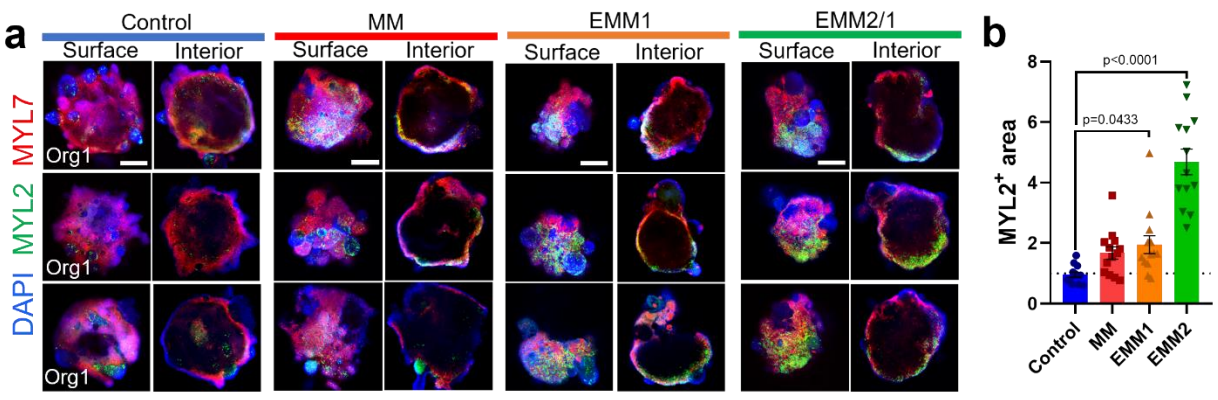

Figure 57. a, Representative surface and interior immunofluorescence images of individual day 30 organoids in all conditions displaying MYL2 (green), MYL7 (red), and DAPI (blue). Three organoids are displayed for each condition (n=13 independent organoids per condition across three independent experiments). Scale bars = 200 μm. b, Quantification of MYL2+ area in each organoid in each condition from images presented in (a) (n=9-13 independent organoids per condition across three independent experiments). Values are presented as fold change normalized to control. Values = mean ± s.e.m., one-way ANOVA with Dunnett's multiple comparisons test.

To further investigate the identity of ventricular- and atrial-like chambers in the human heart organoids, we performed staining for additional atrial and ventricular chamber markers NR2F2 (atrial) and MYL3 (ventricular) **(Figure 58a)**. EMM2/1 organoids displayed a distinct, increased degree of separation between the two chambers, while control organoids showed a larger overlap of these two proteins **(Figure 58b)**; indicating that EMM2/1 organoids possess a greater degree of specification and maturity of chamber development **(Figure 59)**.

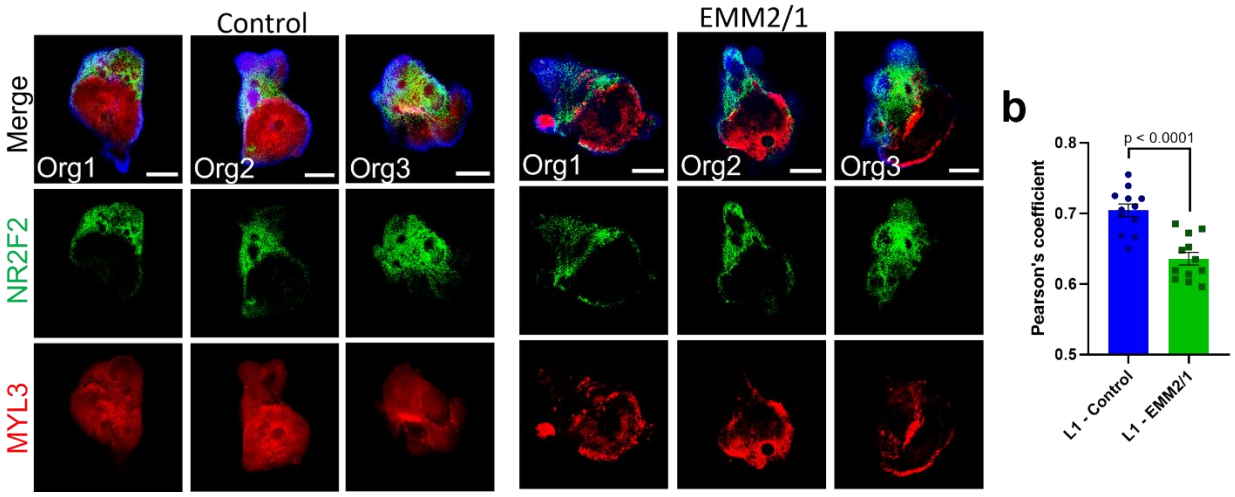

Figure 58. a, Representative immunofluorescence images of individual day 30 organoids in all conditions displaying atrial marker NR2F2 (green), ventricular marker MYL3 (red), and DAPI (blue). Three organoids are displayed for each condition (n=12 organoids per condition across two independent experiments). Scale bars = 200 μm. b, Quantification of colocalization (Pearson's coefficient) between NR2F2 (green) and MYL3 (red) from images presented in (a). Values = mean ± s.e.m., unpaired t-test.

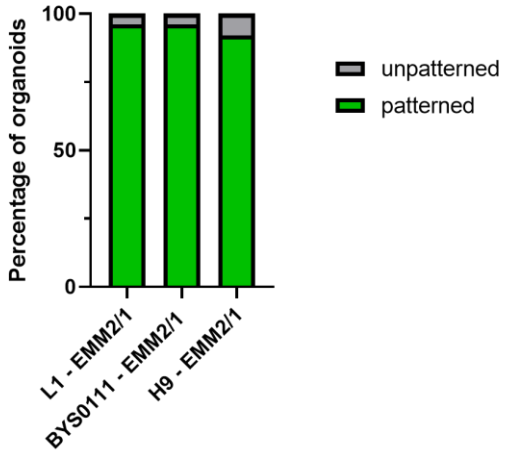

Figure 59. Percentage of chambered organoids at day 30 in the EMM2/1 condition across multiple cell lines (n=12 organoids for L1 organoids; n=11 organoids per condition for BYS0111 organoids; n=12 organoids per condition for H9 organoids; all across two independent experiments).

Remarkably, these results were highly reproducible in other PSC lines, including BYS0111 (iPSC) and H9 (ESC) **(Figure 60)**. While L1 control and EMM2/1 organoids were shown again for reproducibility and comparative purposes **(Figure 60a, Figure 60b)**, control BYS0111 organoids displayed similar overlap of NR2F2 and MYL3, while EMM2/1 BYS0111 organoids showed distinct separation of NR2F2 and MYL3 **(Figure 60a, Figure 60c)**, with $MYL3^{+}$ cells highlighting thick myocardial walls in the EMM2/1 condition. Control H9 organoids displayed decreased expression of both NR2F2 and MYL3 compared to EMM2/1 H9 organoids, with EMM2/1 H9 organoids exhibiting distinct separation of $NR2F2^{+}$ and $MYL3^{+}$ chambers **(Figure 60a, Figure 60d)**.

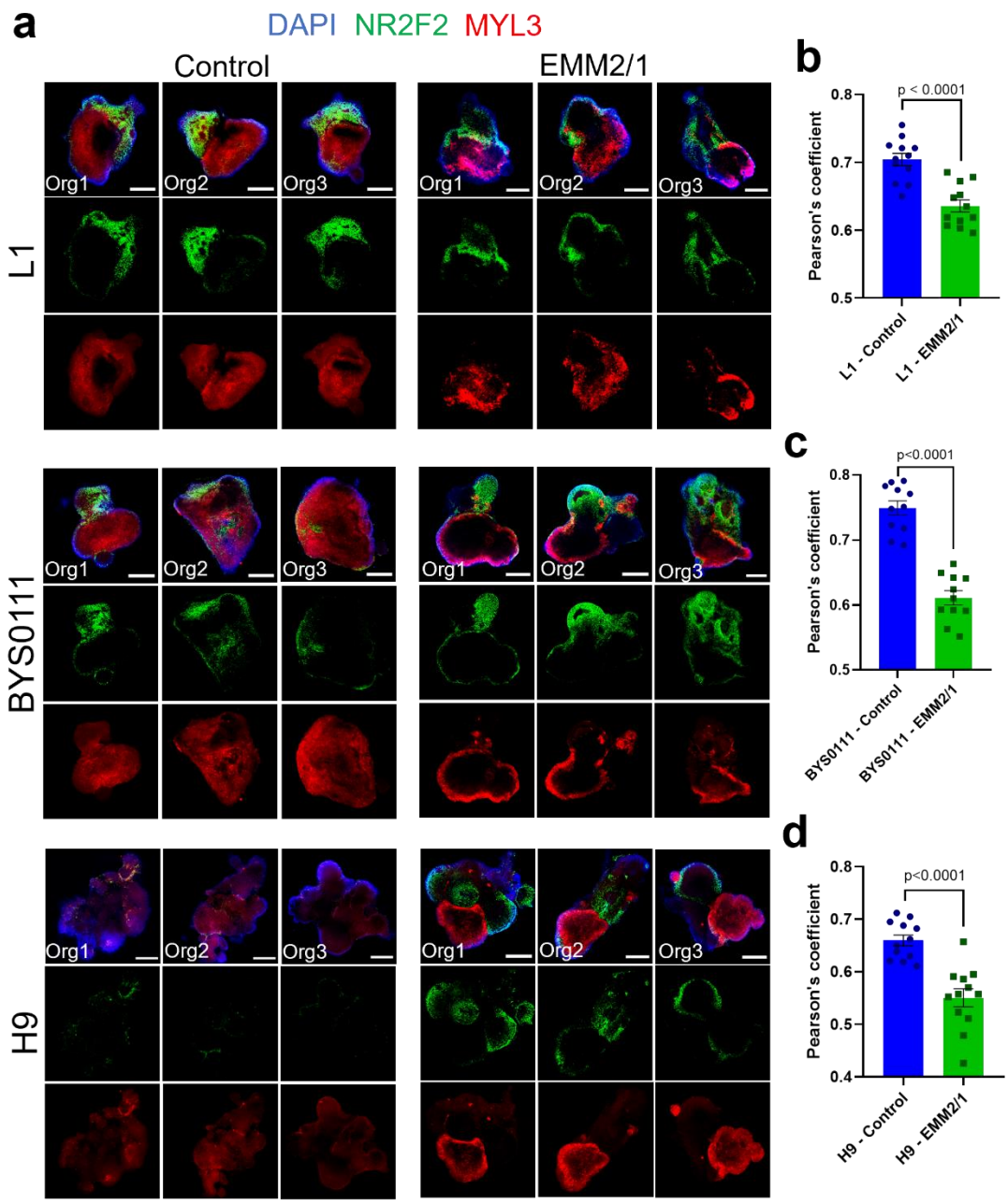

Figure 60. a, Representative immunofluorescence images of individual day 30 organoids in both Control and EMM2/1 conditions from the cell lines L1, BYS0111, and H9 displaying NR2F2 (green), MYL3 (red), and DAPI (blue). Three organoids are displayed per condition per cell line (n=12 independent organoids per condition for L1 organoids; n=11 organoids per condition for BYS0111 organoids; n=12 organoids per condition for H9 organoids; all across two independent experiments). Scale bars = 200 μm. b-d, Quantification of colocalization (Pearson's coefficient) between NR2F2 (green) and MYL3 (red) from images presented in (a) for L1 (b), BYS0111 (c), and H9 (d) organoids. Values = mean ± s.e.m., unpaired t-test.

To support these immunofluorescence results describing the potential identity of atrial and ventricular chambers in our heart organoids, we investigated gene expression patterns using scRNA-seq data in the ACM and VCM clusters **(Figure 61a)**. ACMs displayed increased gene expression for hallmark atrial chamber identity markers such as *NR2F2*, *TBX5*, *NPPA*, and *NR2F1*[58–65] compared to VCMs **(Figure 61b)**. Meanwhile, VCMs showcased increased gene expression for hallmark ventricular chamber identity markers such as *MYL3*, *HEY2*, *IRX4*, and *HAND1*[66–71] compared to ACMs **(Figure 61c)**. These results highlight not only the recapitulation of post-heart tube and primitive heart morphology in our heart organoid platform, but also the reproducibility of our findings.

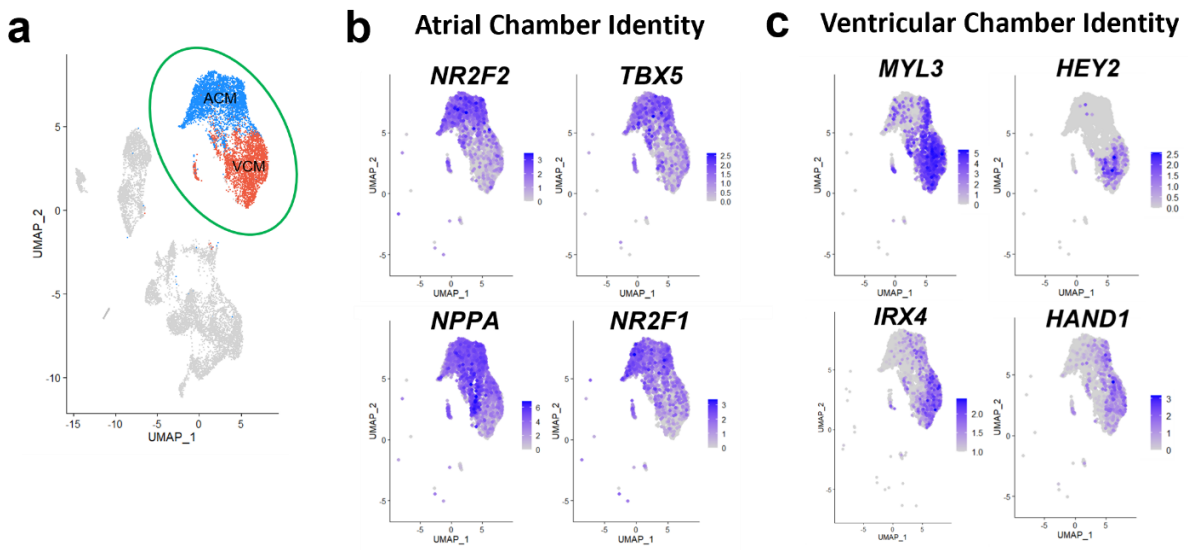

Figure 61. a, Feature plot highlighting scRNA-seq VCM and ACM clusters. b, Feature plot displaying hallmark atrial chamber identity genes that are differentially expressed in the ACM cluster and c, ventricular chamber identity genes that are differentially expressed in the VCM cluster. Color intensity represents the relative value of gene expression per gene.

Optical coherence tomography (OCT) was used to provide detailed characterization of the chambers in live organoids over time, and to measure the growth and monitor dynamics of chamber development under developmental induction conditions via a

custom-made OCT microscopy system amenable to high-content screening[104,107] **(Figure 62)**. We found that chambers exhibited dynamic behavior initially and coalesced into larger structures over time. EMM2/1 conditions led to the largest internal chambers within our human heart organoids between day 20 and day 30 of culture, with typically two large internal chambers as previously observed by confocal microscopy **(Figure 62a, Figure 62b)**. While MM organoids displayed a single internal chamber, organoids grown in the control, EMM1 and EMM2/1 conditions possessed multiple, smaller, interconnected chambers. Control and EMM2/1 organoids possessed chambers throughout the bulk of the organoids while EMM1 organoids showed chambers predominantly towards one side of the organoid. These data confirmed the formation of well-established cardiac chambers and further supported our observations on the effects of developmental induction conditions. The process by which chambers seem to form might be a limitation of our model, as it does not follow the biological paradigm, but this is also to be expected as there is no vasculature or external circulation to support chamber development in a more physiological manner.

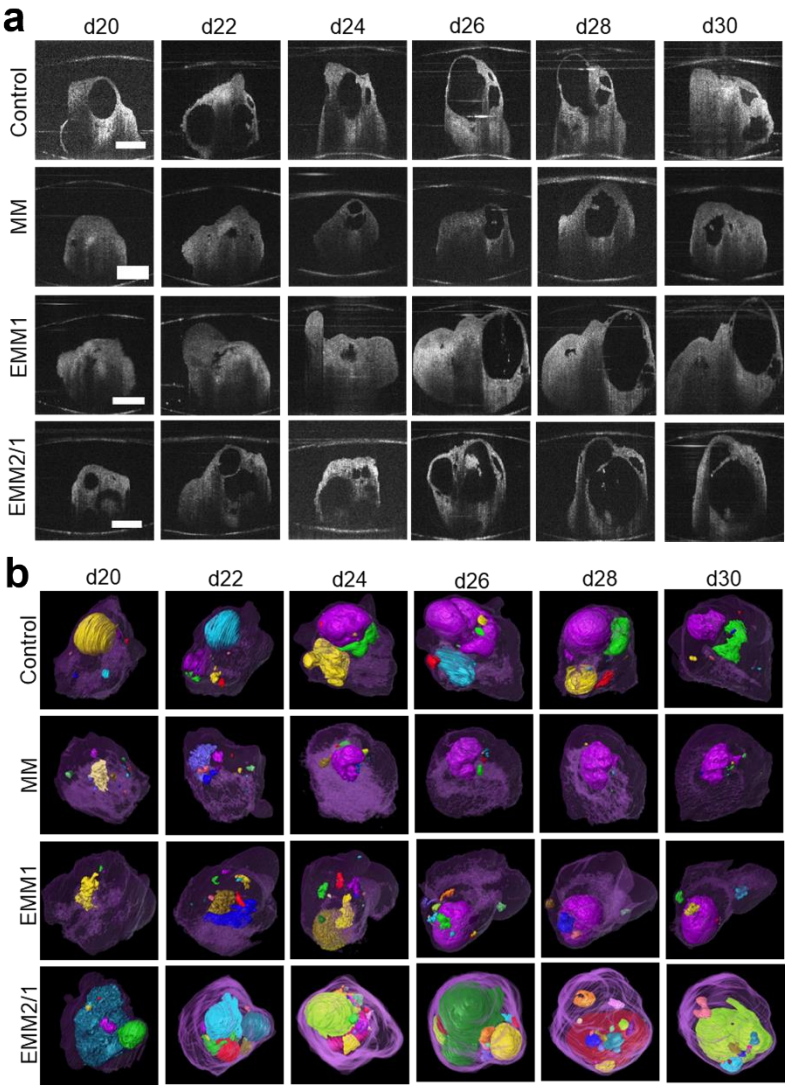

Figure 62. a, Longitudinal OCT cross-sectional scans of heart organoids from day 20 to day 30 in each condition. Scale bars = 500 μm. Images shown represent 6 organoids per condition across two independent experiments. b, 3D segmentation of OCT scans from images presented in (a) reveal the temporally dynamic volumetric visualization of chamber identity in each condition.

We also assessed vasculature formation in developmental induction conditions. Endothelial cell (PECAM1^{+}) vasculature formation was examined at day 30 of culture via immunofluorescence and confocal microscopy **(Figure 63, Figure 64)**. Assessment of organoids on surface and interior planes revealed the presence of endothelial cells amongst the myocardial regions of all organoids **(Figure 63).** Organoids in the EMM1 and

EMM2/1 conditions presented less PECAM1^{+} cells than control and MM organoids. Control and MM organoids displayed robust, interconnected endothelial cell networks and throughout myocardial (TNNT2^{+}) tissue **(Figure 64a)**. We quantified total PECAM1^{+} area, and MM organoids showed no significant difference compared to control organoids, while EMM1 and EMM2/1 organoids possessed only 52% and 61% of PECAM1^{+} area compared to control, respectively **(Figure 64b)**, consistent with scRNA-seq data that shows a decrease in endothelial gene expression in EMM1, and EMM2/1 organoids compared to control **(Figure 38)**. High magnification images of organoids further show the morphological transitory state of the endothelial cells within cardiomyocyte-rich regions **(Figure 64c).** Overall, this data suggests that vascularization of the organoids might be partially eclipsed by factors in EMM1 and EMM2/1 conditions, possibly due to timing or concentration of growth factors, and will require further investigation to fine tune medium conditions.

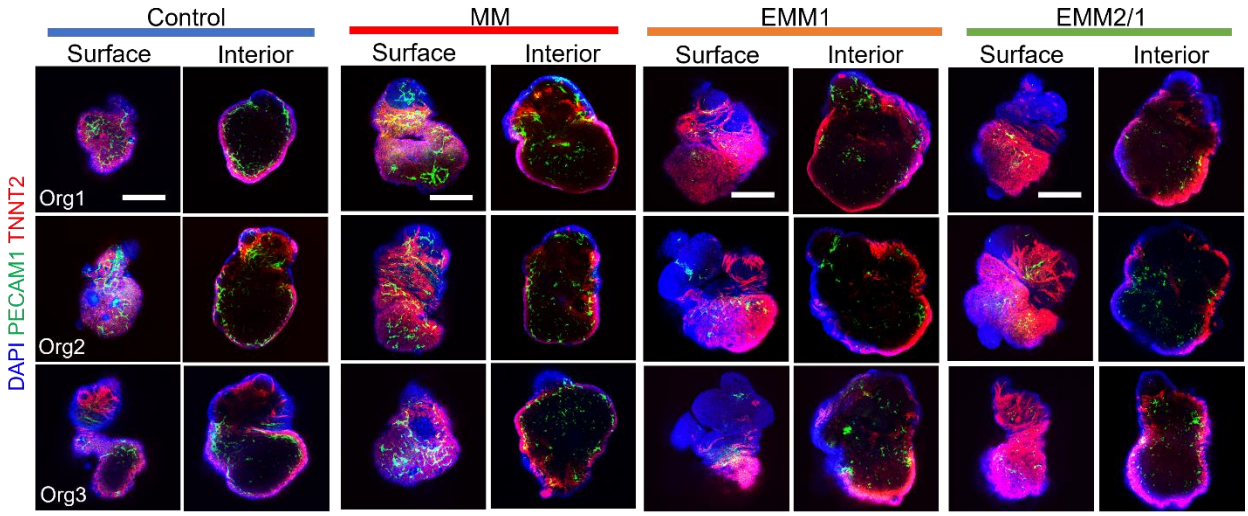

Figure 63. Representative immunofluorescence images from the surface and interior of day 30 organoids with DAPI (blue), TNNT2 (red), and PECAM1 (green) in each condition (n=7-8 independent organoids per condition across two independent experiments).Scale bars = 200 μm.

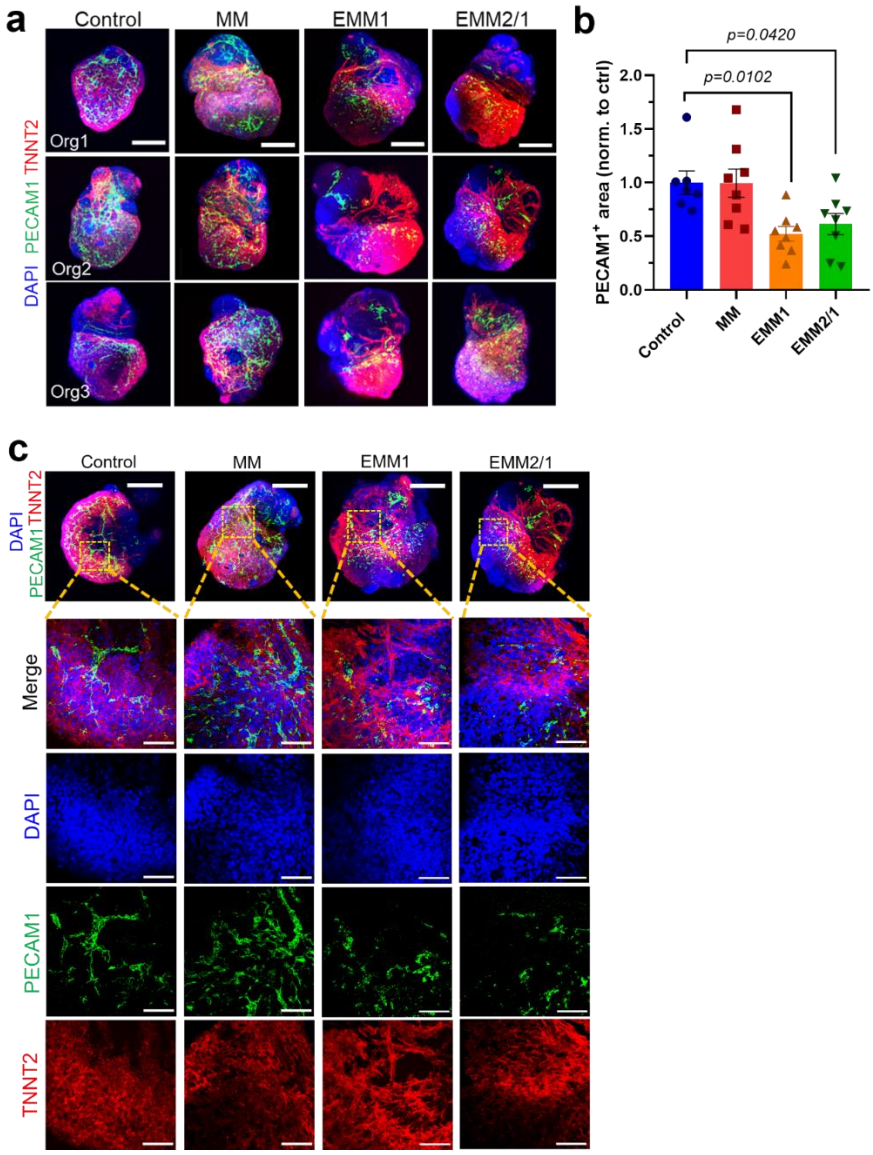

Figure 64. a, Representative day 30 organoid immunofluorescence images with DAPI (blue), TNNT2 (red), and PECAM1 (green) (n=7, 8, 8, and 8 independent organoids for control, MM, EMM1, and EMM2/1, respectively). Images presented as maximum intensity projections. Scale bars = 200 μm. b, Quantification of PECAM1+ area presented in (b) (n=7, 8, 8, and 8 independent organoids for control, MM, EMM1, and EMM2/1, respectively). Data presented as log fold change normalized to control. Values = mean ± s.e.m., one-way ANOVA with Dunnett's multiple comparisons test. c, Representative high magnification immunofluorescence images of organoids in each condition with DAPI (blue), TNNT2 (red), and PECAM1 (green(n=7, 8, 8, and 8 independent organoids for control, MM, EMM1, and EMM2/1, respectively). Scale bars = 50 μm. The images on top are representative low magnification organoids (Scale bar = 200 μm) for each condition with the yellow square representing area of high magnification. Images presented as maximum intensity projections.

4.2.5. An endogenous retinoic acid gradient is responsible for the spontaneous anterior-posterior heart tube patterning in EMM2/1 organoids

The emergence of a retinoic acid gradient originating at the posterior pole of the heart tube (produced by the epicardium and primitive atrium) is a critical developmental step in mammalian cardiogenesis[77,161–163]. This gradient establishes the anterior-posterior axis that provides cues for the formation of the ventricles, atria and inflow and outflow tract, while also contributing to the specification of cardiogenic progenitors and other structures[164,165] **(Figure 65)**. To determine whether the post heart tube stage structure observed in EMM2/1 organoids (**Figure 55, Figure 56, Figure 57, Figure 58, Figure 59, Figure 60, Figure 61**) was induced by endogenous retinoic acid signaling, we performed Raman microscopy to detect its molecular signature using a microscope designed for this purpose (**Figure 12)**. We identified the presence of myosin, troponin T, tropomyosin, collagen I and other related molecular signatures in organoids in all conditions as expected, but the presence of retinoic acid was specifically identified only in EMM2/1 organoids **(Figure 66a)**. Retinoic acid synthesis is carried out largely by retinaldehyde dehydrogenase 2 (ALDH1A2) during embryogenesis[165,271,272]. We utilized qRT-PCR at day 30 of organoid culture to assess levels of *ALDH1A2* in all conditions **(Figure 66b)**. *ALDH1A2* expression was shown to increase by ~2.2-fold in the EMM2/1 condition relative to control, with no significant changes in expression displayed in the MM or EMM1 conditions.

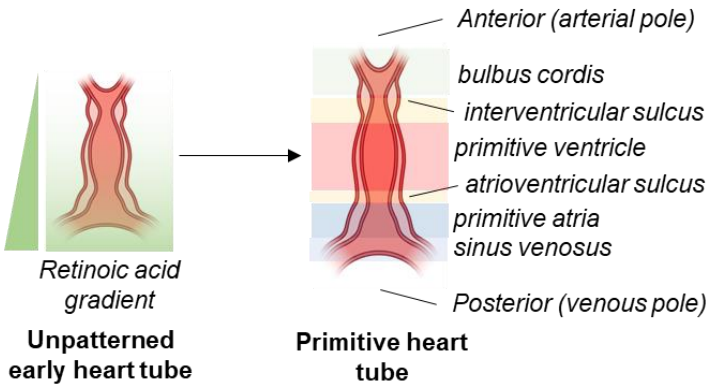

Figure 65. Schematic representation of in vivo cardiac heart tube formation, highlighting the localization and intensity of the retinoic acid gradient from the anterior (arterial pole) to the posterior (venous pole) of the primitive heart tube.

To assess the cell-specific dynamics of retinoic acid production in our organoids, we used scRNA-seq data to show that *ALDH1A2* is expressed in EPCs, PEDCs, and ACMs in our organoids **(Figure 66c)**; consistent with expression patterns reported *in vivo*[77,161–163].

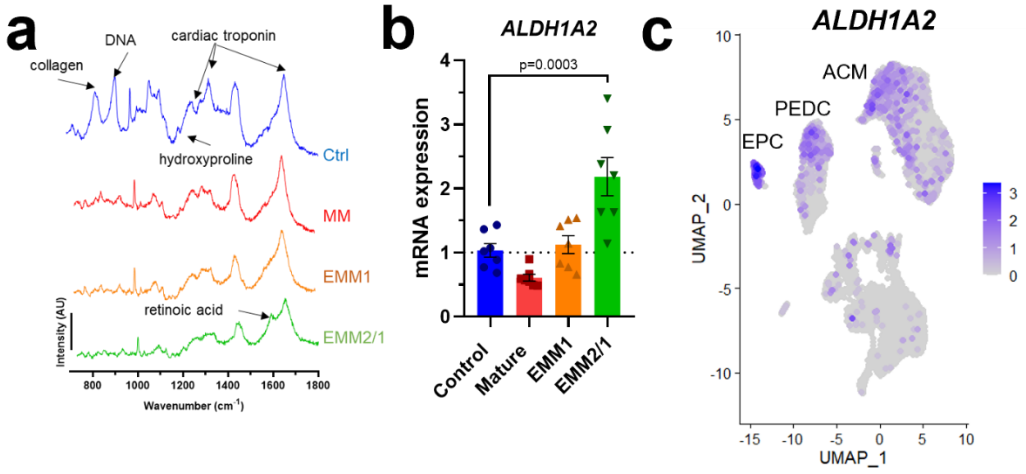

Figure 66. a, Raman spectroscopy intensity plots for organoids from all four developmental maturation conditions at day 30 of culture. Peaks of interest are marked. Data presented is representative of n=3 independent organoids per condition. b, mRNA expression of ALDH1A2 in all conditions at day 30 (n=7 independent organoids per condition across two independent experiments). Data presented as log2 fold change normalized to control. Values = mean ± s.e.m., one-way ANOVA with Dunnett's multiple comparisons test. c, Feature plot displaying expression of ALDH1A2. Color intensity represents the relative value of gene expression.

To complement this analysis and to further investigate the localization of retinoic acid production in our organoids, we performed immunostaining with antibodies for ALDH1A2 and TBX18 (an epicardial transcription factor, to label the proepicardial/atrial pole)[180,273,274] for organoids in all conditions at day 30 (**Figure 67, Figure 68a**). We found that only EMM2/1 organoids possess a localized, polarized expression of ALDH1A2 which colocalized with proepicardial organ TBX18^{+} cells, confirming that the retinoic acid gradient patterning the organoids was coming from the proepicardial/atrial pole (posterior pole of the heart tube *in utero*) **(Figure 65, Figure 67, Figure 68a)**.

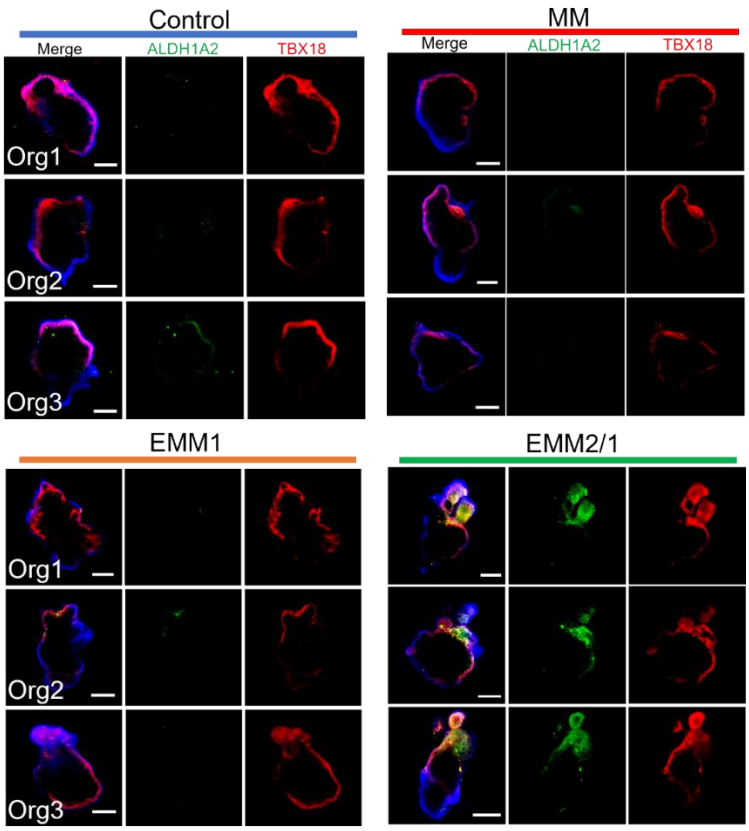

Figure 67. Representative immunofluorescence images of individual day 30 organoids in all conditions displaying ALDH1A2 (green), epicardial marker TBX18 (red), and DAPI (blue). Three organoids are displayed for each condition (representative of n=22-24 independent organoids per condition across three independent experiments). Scale bar = 200 μm.

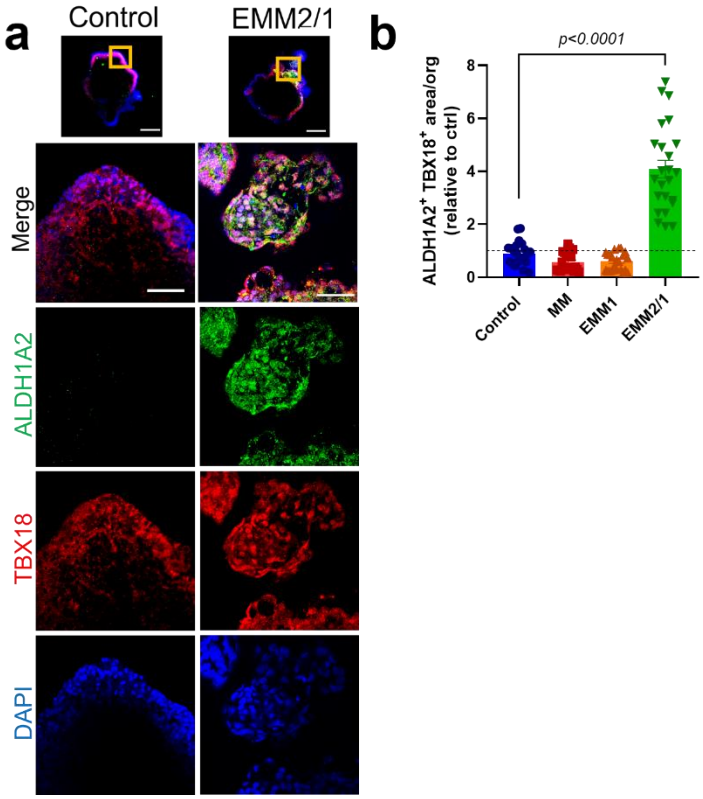

Figure 68. a, High magnification images of EMM2/1 and control organoids shown in (c), displaying ALDH1A2 (green), TBX18 (red), and DAPI (blue). Yellow square in image at top (Scale bar = 200 μm) represents area of high magnification. Scale bar = 50 μm. b, Quantification of ALDH1A2+ TBX18+ area within organoids in each condition from images presented in (Figure 75) (n=22-24 independent organoids per condition across three independent experiments). Data presented as fold change normalized to control. Values = mean ± s.e.m., one-way ANOVA with Dunnett's multiple comparisons test.

Control, MM and EMM1 organoids did not display ALDH1A2 expression. We quantified the area of colocalization between ALDH1A2 and TBX18 and show that EMM2/1 organoids were significantly more responsive to the induction of retinoic acid synthesis **(Figure 68b)**. Furthermore, these results were reproduced in the two additional PSC lines BYS0111 and H9 **(Figure 69)**. While L1 control and EMM2/1 organoids were displayed once again for reproducibility and comparative purposes **(Figure 69a, Figure 69b)**,

control and EMM2/1 BYS0111 organoids displayed similar patterns of ALDH1A2 and TBX18 expression as was shown for L1 organoids. EMM2/1 BYS0111 organoids also displayed markedly increased amounts of polarized ALDH1A2^{+}TBX18^{+} cells compared to control BYS0111 organoids **(Figure 69a, Figure 69c)**. H9 organoids displayed a similar degree of recapitulation, with EMM2/1 H9 organoids showcasing marked increases in ALDH1A2^{+}TBX18^{+} cells compared to control H9 organoids **(Figure 69a, Figure 69d)**.

Control and EMM2/1 organoids from all three cell lines also displayed similarly robust and reproducible transcriptomic signatures **(Figure 70)** for *ALDH1A2* and other important genes such as *MYL2*, *MYL7*, *WT1*, and *PPARGC1A*, as determined by qRT-PCR. We confirmed that the proepicardial pole is also the atrial pole by performing immunostaining for WT1 and MYL3 and show that the proepicardial pole is opposite to that of the ventricular pole (**Figure 71**).

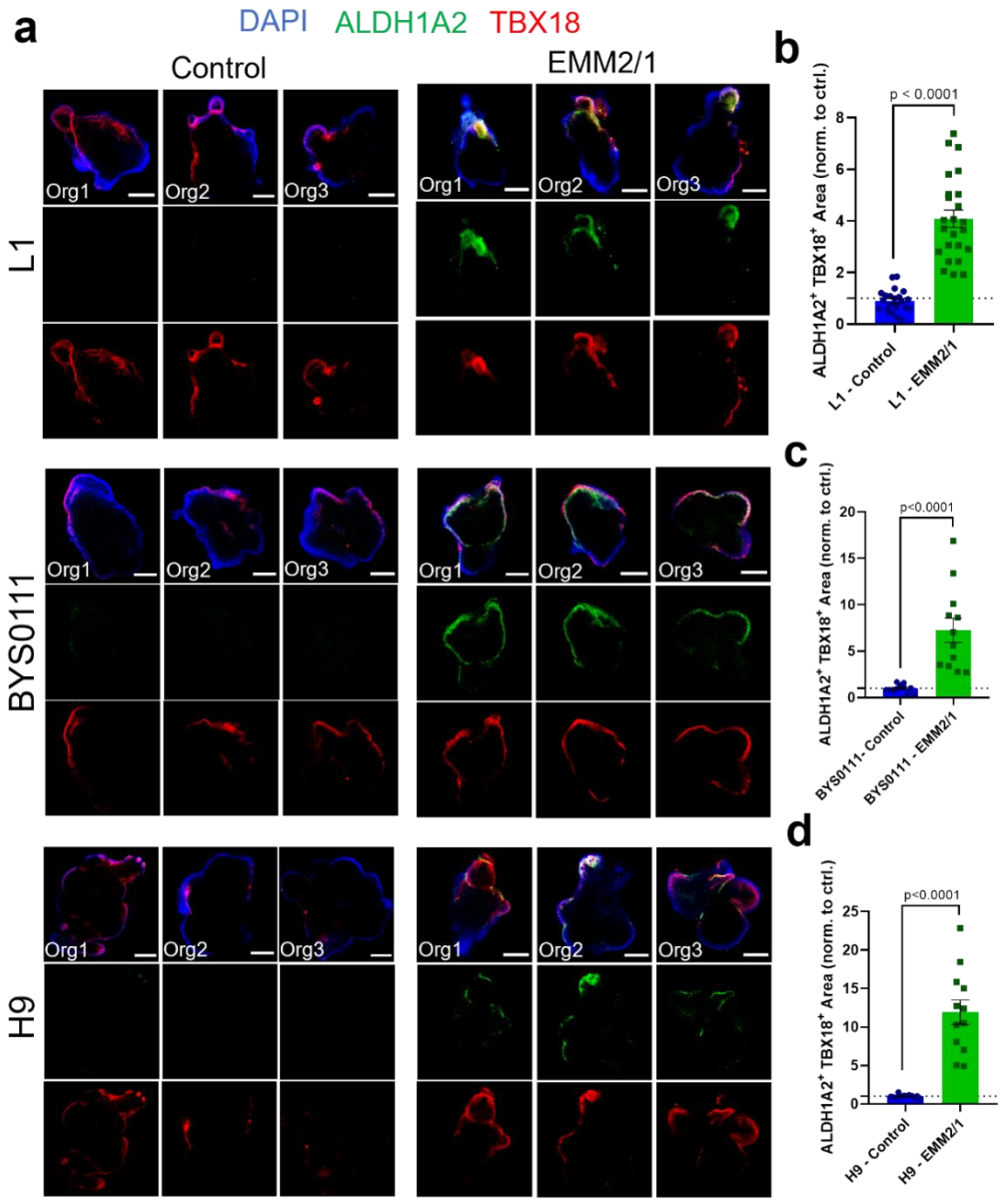

Figure 69. a, Representative immunofluorescence images of individual day 30 organoids in both Control and EMM2/1 conditions from the cell lines L1, BYS0111, and H9 displaying ALDH1A2 (green), TBX18 (red), and DAPI (blue). Three organoids are displayed per condition per cell line (n=22 or 24 independent organoids for control or EMM2/1, respectively, for L1 organoids across three independent experiments; n=12 organoids per condition for BYS0111 organoids across two independent experiments; n=12 organoids per condition for H9 organoids across two independent experiments). Scale bars = 200 µm. b-d, Quantification of ALDH1A2+ TBX18+ area within organoids in each condition from images presented in (a) for L1 (b), BYS0111 (c), and H9 (d) organoids. Data presented as fold change normalized to Control. Values = mean ± s.e.m., unpaired t-test.

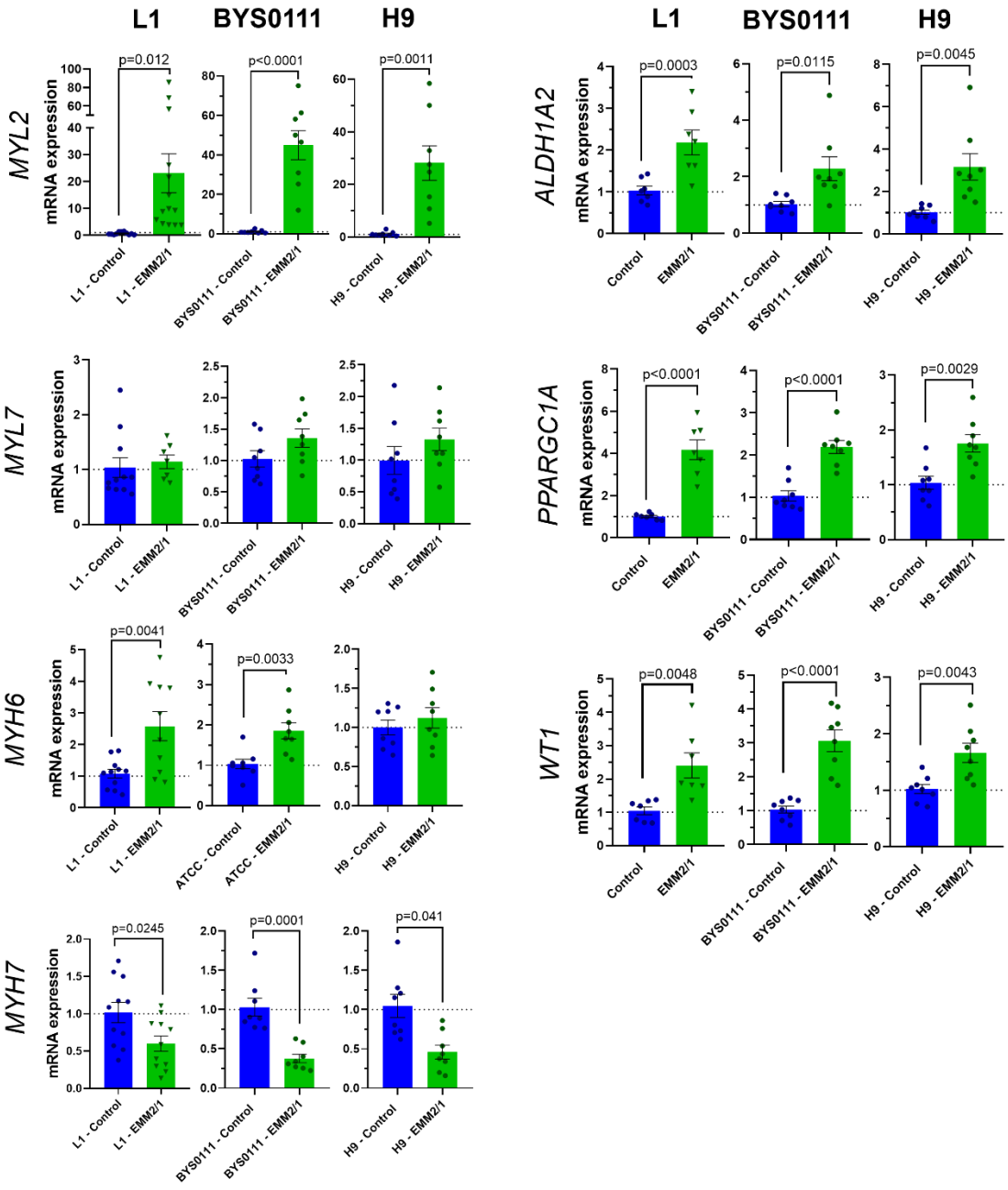

Figure 70. mRNA expression of select genes in the Control and EMM2/1 conditions from L1, BYS0111 and H9 organoids at day 30 (n=7-14 independent organoids per condition for L1 organoids across three independent experiments; n=8 organoids per condition for BYS0111 organoids across two independent experiments; n=8 organoids per condition for H9 organoids across two independent experiments). Genes presented are MYL2, MYL, MYH6, MYH7, ALDH1A2, PPARGC1A, and WT1. Data presented as log2 fold change normalized to Control for each cell line. Values = mean ± s.e.m., unpaired t-test.

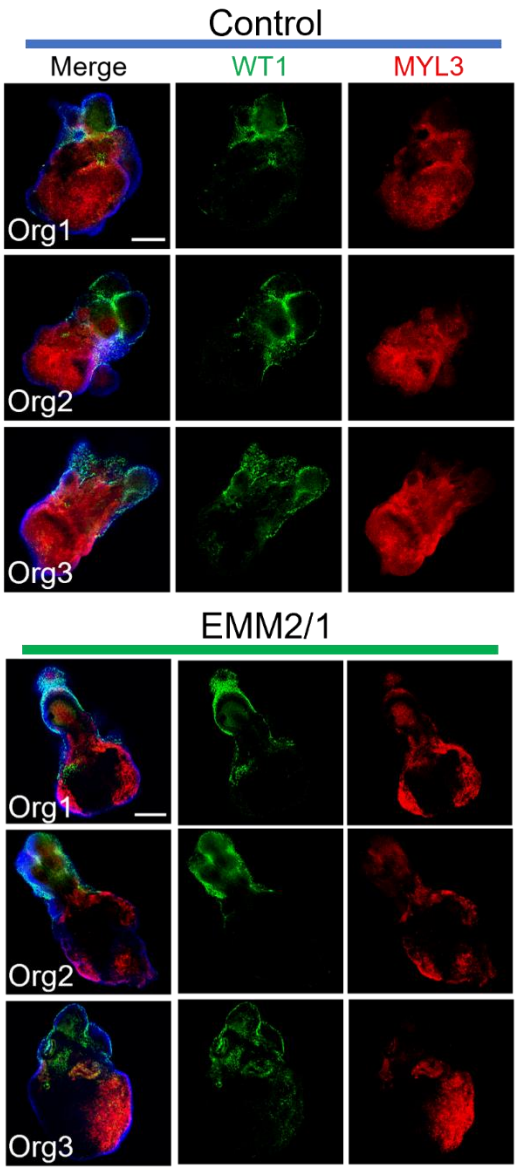

Figure 71. Representative immunofluorescence images of individual day 30 organoids in both Control and EMM2/1 conditions displaying WT1 (green), MYL3 (red), and DAPI (blue). Three organoids are displayed per condition (n=12 organoids per condition across two independent experiments). Scale bars = 200 μm.

To further demonstrate the functional importance of the endogenous retinoic acid signaling observed in EMM2/1 organoids, we inhibited ALDH1A2 and retinoic acid production using the highly specific inhibitor DEAB, and through immunostaining for NR2F2 and MYL3, we showed that ALDH1A2 inhibition led to significantly impaired heart

organoid patterning in EMM2/1 conditions **(Figure 72a, Figure 72b, Figure 72c)**. Organoids with inhibited ALDH1A2 displayed 0.35-fold and 0.42-fold reductions in MYL3^{+} and NR2F2^{+} areas relative to untreated organoids, respectively **(Figure 72b, Figure 72c)**. Furthermore, we also showed that addition of exogenous retinoic acid to EMM2/1 conditions did not lead to further differences in patterning, suggesting that EMM2/1 organoids produce sufficient retinoic acid for normal patterning on their own (**Figure 72**). Together, these data show the ability of EMM2/1 organoids to endogenously synthesize retinoic acid in a spatially restricted manner colocalized with the epicardium (TBX18), a phenomenon that closely mimics the processes observed in *in utero* heart development and heart tube patterning.

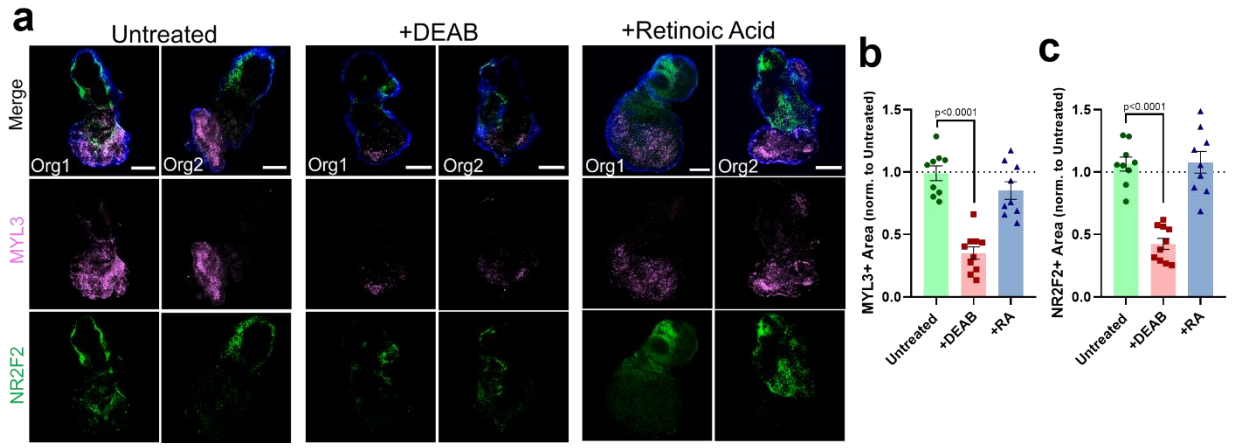

Figure 72. a, Representative immunofluorescence images of individual day 30 EMM2/1 organoids following exposure to either deoxyaminobenzaldehyde (DEAB), retinoic acid (RA), or no treatment (untreated). Staining was performed for ventricular marker MYL3 (pink), atrial marker NR2F2 (green), and DAPI (blue). Two organoids are displayed for each condition (n=9 independent organoids per condition across two independent experiments). Scale bar = 200 μm. b, Quantification of NR2F2+ area and c, MYL3+ area of organoids presented in (a) (n=9 independent organoids per condition across two independent experiments). Values = mean ± s.e.m., one-way ANOVA with Dunnett's multiple comparisons test.

4.3. DISCUSSION

Laboratory models of the human heart have made considerable progress over the last several decades, beginning with animal models and primary cardiomyocyte culture and moving onwards to induced pluripotent stem cell-derived cardiac tissues (e.g., cardiomyocytes) and tissue engineering approaches (3D printing, biomaterials). The latest advances in human heart models are heart organoids generated from pluripotent stem cells[36,78–80]. While these model systems have certainly yielded transformative research findings in the fields of cardiac disease, heart development, and cardiac toxicity testing[25,26,30,78,275], these systems do not possess the true complexity of the *in utero* human heart, owing to a lack of maturity and faithfulness to human physiology, morphology, cellular organization, and functionality. These shortcomings severely limit the scope of relevance of traditional model systems. To circumvent these limitations, we designed and implemented simple and highly reproducible methods for developmental induction strategies inspired by *in utero* biological steps, producing human heart organoids with higher anatomical complexity and physiological relevance along first trimester fetal development.

This chapter presents our findings that the EMM2/1 strategy most closely recapitulated heart development *in vitro*, and enabled organoids to acquire high levels of complexity and anatomical relevance by inducing progressive transcriptional maturation, mitochondrial and metabolic maturation, electrophysiological maturation, increased morphological and cellular complexity, and most importantly, by recapitulating anterior-posterior heart tube patterning by endogenous retinoic acid signaling and self-

organization. Importantly, results from using the EMM2/1 strategy over control were found to be reproducible across organoids derived from three pluripotent stem cell lines.

Single-cell gene expression across multiple cardiac cell clusters revealed that EMM2/1 organoids yielded high similarity to *in vivo* 6.5 post-conception week (GD45) developing human hearts[113]. Implementation of developmental induction strategies did not lead to the emergence of new cardiac lineages as the same cardiac cell types were observed in all conditions but did lead to expansion and reduction of certain populations, such as atrial and ventricular cardiomyocytes, and mesenchymal cell types (stromal cells) in what seems to be a process of fine tuning and remodeling. Interestingly, we could also observe the appearance of valvular and conductance cell types throughout all developmental induction conditions, a phenomenon not described before in heart organoids. Remarkably, nonetheless, organoids displayed a high degree of similarity to two independent embryonic human heart datasets across all major cardiac cell clusters.

The metabolic transition from glycolysis to fatty acid oxidation is a paramount step in the late stages of cardiac development, preparing the heart for increased energy expenditure as well as inducing transcriptional regulation and stimulating physiological maturation[145,147,233–235,276]. Efforts have been pursued to simulate these phenomena in vitro with cardiomyocytes and engineered heart tissues and have found beneficial effects from modified glucose concentrations and the addition of fatty acids[32,46,48,128,140]. However, these systems are simplistic models and do not possess the high physiological complexity as observed in human heart organoids. We showed that human heart organoids respond dramatically to developmental maturation stimuli and metabolically maturate and possess increased mitochondrial growth, density, gene expression profiles,

and oxygen consumption rates, particularly through the EMM2/1 strategy. These dramatic responses compared to traditional methods may be the result of synergy between multiple cardiac cell subtypes, such as epicardial cells and cardiac fibroblasts, which have been shown to stimulate cardiomyocyte growth and function[277,278].

Proper and gradual electrophysiological maturation throughout the cardiac syncytium, including the complex interplay between various ion channels and their subtypes as well as depolarization through t-tubules, comprises critical aspects of cardiac development and functionality[245–248,269,270,279]. Here, we show that organoids from the EMM2/1 strategy develop distinct calcium transients with increasing physiological mimicry due to their increased amplitude and decreased frequency. Additionally, organoids in the EMM2/1 strategy develop higher levels of t-tubules, inward-rectifying potassium ion channels, and hERG channels compared to other maturation strategies. In fact, many efforts towards in vitro cardiomyocyte maturation have struggled or failed to elicit the presence of t-tubules[280,281] and inward-rectifying potassium ion channels remain critical to establishing low resting membrane potential[282,283]. Moreover, cardiac hERG channels represent a paramount channel of importance for pharmacological screening due to its high arrhythmogenic potential if interfered with[259,260]. Nonetheless, the summation of multiple ion transients results in the cardiac action potential which is the ultimate driving force for human heart contraction and functionality. We show that cardiomyocytes within our EMM2/1 organoids possess ventricular-, atrial-, and nodal-like action potentials, opening the door for electrophysiological applications in drug screening.

The embryonic heart begins as an unpatterned contracting tube and undergoes cellular and structural changes through morphogenetic signaling events to pattern along the

anterior-posterior axis, loop, and eventually form the 4-chambered primitive heart[284,285]. We investigated the morphological landscape of our organoids following the application of our maturation strategies and found that EMM2/1 organoids formed a two-chambered structure with cardiomyocytes forming one chamber with atrial identity and another with ventricular fate. Dense epicardial layering at the atrial chamber identified the proepicardial organ as the posterior pole of the heart tube[286] and revealed that EMM2/1 organoids were spontaneously patterning along the aforementioned anterior-posterior axis, a phenomenon that was exclusively observed in EMM2/1 organoids. Further investigations found that self-organization and patterning in EMM2/1 was driven by an endogenous retinoic acid signaling gradient, identified by using a combination of Raman and confocal microscopy. ALDH1A2, an enzyme required for retinoic acid synthesis, was observed to be spatially restricted to the posterior end of EMM2/1 organoids, and co-localized with TBX18, an epicardial transcription factor confirming that the proepicardial organ was functional. Further, the patterning role that retinoic acid plays in EMM2/1 organoids was confirmed through inhibiting ALDH1A2, with inhibited organoids showcasing diminished patterning and expression of hallmark chamber identity proteins. Moreover, organoid patterning and gene expression profiles in EMM2/1 organoids were shown to be reproducible across three independent cell lines and across multiple independent experiments (L1 (iPSC), BYS0111 (iPSC), H9 (ESC)). Taken together, these data support the hypothesis that our organoids recapitulate events that take place during *in utero* gestation where the proepicardial organ surrounds the posterior pole of the patterned heart tube where posterior atrial cardiomyocytes and proepicardial cells produce retinoic

acid to form a signaling gradient that further instructs the remainder of the heart tube with patterning and specification information[113,165,180,273,286].

CHAPTER 5: AIM 3: UTILIZING HUMAN HEART ORGANOIDS TO INVESTIGATE ONDANSETRON-INDUCED CONGENITAL HEART DEFECTS

5.1. BACKGROUND AND RATIONALE

5.1.1. Ondansetron and congenital heart defects

CHDs are a major cause of morbidity and mortality at both global and national levels.[287] The developing embryo and fetus are incredibly susceptible to genetic, maternal, and environmental factors.[288] The heart is the first organ to fully form and function during human embryonic development[99] and is responsible for the delivery of nutrients and oxygen to the fetus through the circulatory system, thus making the proper formation of the heart a paramount step in embryogenesis. In fact, the heart is highly susceptible to genetic and environmental factors *in utero*.[289,290] Developmental toxicity is even possible with well-known pharmaceuticals, such as caffeine, ibuprofen, and ACE inhibitors.

An additional pharmaceutical of interest is ondansetron, a 5-HT_3 receptor antagonist and antiemetic used for treating nausea and vomiting during pregnancy[291]. Despite the lack of studies proving its safety for use during pregnancy, ondansetron is the most commonly prescribed drug for preventing morning sickness during pregnancy. In fact, up to 25% of pregnant women take ondansetron off-label during this period[292]. Ondansetron use during pregnancy has been linked to congenital heart defects and orofacial defects[293–296] in epidemiological studies. Lemon et al.[293] describe an increased risk for the development of ventricular septal defects while taking ondansetron, and Danielsson et al.[295] found no statistically significant risk for a major malformation with the use of ondansetron during pregnancy, but did conclude that the risks for a cardiovascular defect and a cardiac septum defect were increased and statistically significant with the use of ondansetron.

Nonetheless, consensus in the field is divided[297–299], with Parker et al.[299] arguing that epidemiological data from two independent studies shows that ondansetron use during the first trimester was not associated with an increased risk for developing a congenital heart defect, but did yield modest increases in risk for the development of cleft palate and renal agenesis-dysgenesis. Additionally, the electrophysiological effects of ondansetron have been studied *in vivo* using animal models[294,300,301] and on cardiomyocytes *in vitro*[302–305]. Danielsson et al.[294] investigated the effects of ondansetron on embryonic rat heart rhythm and found concentration dependent bradycardia, arrhythmia, and cardiac anatomical malformations. Additionally, Blinova et al.[302] describe the proarrhythmic potential of ondansetron in an hiPSC-derived cardiomyocyte platform, showcasing elevated repolarization rates and being classified as an intermediate risk for developing arrythmia in two different computational models.

However, epidemiological studies, *in vivo* animal studies, and current *in vitro* models are unable to capture the human-relevant risks pertaining to intricate embryonic and fetal developmental mechanisms and ignore miscarriage statistics altogether – a significant metric, as improper heart development often results in an early miscarriage. Altogether, the thorough and direct investigation of the safety of ondansetron use during pregnancy pertaining to human heart development is lacking and requires deeper attention.

5.2. RESULTS

5.2.1. Ondansetron treatment during heart organoid development captures congenital heart disease phenotypes associated with its use in the clinic

We sought to investigate the effects of ondansetron during human heart organoid development. We used clinical data on ondansetron dosing strategies to determine relevant concentrations for heart organoid studies[293]. We applied ondansetron at three different concentrations to heart organoids from day 9 until day 30 in the EMM2/1 strategy and noticed stark differences in beating behavior and gross morphology at day 30, with organoids in the 10 µM and 100 µM conditions exhibiting a marked decrease in beating frequency. Due to ondansetron's chemistry as a 5-HT_3 receptor antagonist, the electrophysiological effects in this respect were expected. We then assessed organoid morphology for atrial and ventricular cells, using MYL7 and MYL2 markers respectively **(Figure 73a)**[306,307], at day 30. A clear dose-dependent reduction in $MYL2^+$ ventricular cells was found when ondansetron was applied **(Figure 73a)**. We quantified these results and showed that $MYL2^+$ area decreased to 0.55-fold and 0.18-fold in organoids in the 10 µM and 100 µM conditions, respectively, relative to untreated organoids **(Figure 73b)**, while $MYL7^+$ area remained unchanged across all conditions **(Figure 73c)**. Furthermore, organoids in the 100 µM condition also appeared to be structurally less organized with less defined chamber walls and loose chamber separation compared to untreated.

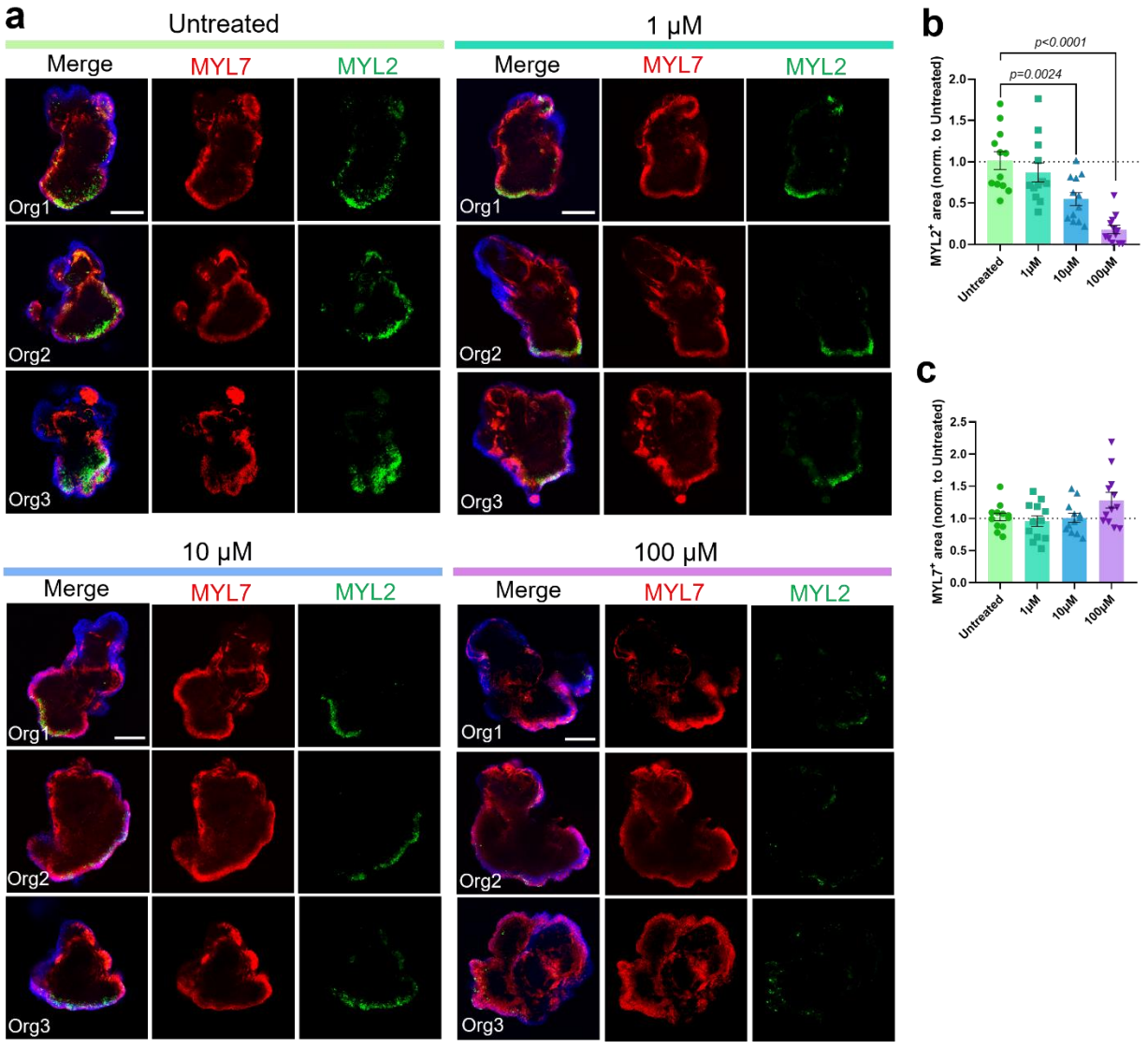

Figure 73. a, Representative immunofluorescence images of individual day 30 EMM2/1 organoids following exposure to varying concentrations of ondansetron (1 µM, 10 µM, or 100 µM) or no treatment (untreated) from day 9 to day 30 of culture. Staining was performed for ventricular marker MYL2 (green), atrial marker MYL7 (red), and DAPI (blue). Three organoids are displayed for each condition (n=12 independent organoids per condition across two independent experiments). Scale bar = 200 µm. b, Quantification of MYL2+ area and c, MYL7+ area for each condition (n=12 independent organoids per condition across two independent experiments). Data presented as fold change normalized to untreated. Values = mean ± s.e.m., one-way ANOVA with Dunnett's multiple comparisons test.

To support these results, we performed qRT-PCR on organoids in all conditions and show that *MYL2* expression decreased to 0.58-fold and 0.40-fold in the 10 and 100 µM

conditions, respectively, relative to untreated **(Figure 74)**. Together, this data suggests that ondansetron perturbs critical steps of ventricular heart development in heart organoids reminiscent of most clinical phenotypes associated with its use, namely, ventricular septal defects.

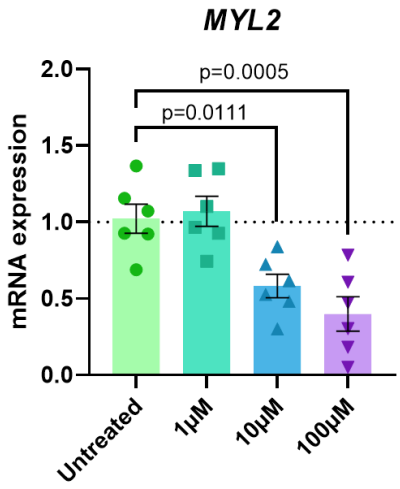

Figure 74. mRNA expression of ventricular marker MYL2 in all conditions at day 30 (n=6 independent organoids per condition across two independent experiments). Data presented as log2 fold change normalized to control. Values = mean ± s.e.m., one-way ANOVA with Dunnett's multiple comparisons test.

Ondansetron has also been implicated in inducing arrythmias and in prolonging the QT interval[294,300,302,308,309]. Thus, we investigated the electrophysiological effects of ondansetron on heart organoid development **(Figure 75)** via the potentiometric dye di-8-ANEPPS. Action potentials for organoids in the 10 and 100 μM conditions were markedly different compared to untreated **(Figure 75a, Figure 75b)**, displaying decreased frequencies **(Figure 75c)**, amplitudes **(Figure 75d)**, and increased APD30/90 **(Figure 75e, Figure 75f)**, which is consistent with the known effects of ondansetron on hERG potassium channel blockade[309].

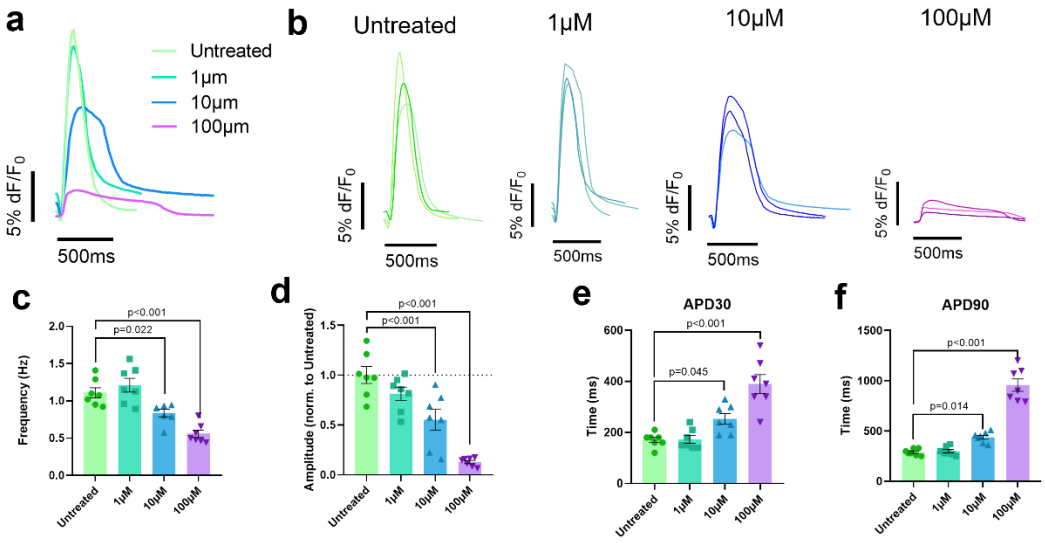

Figure 75. a,b, Representative voltage tracings of organoids showing three voltage traces from independent organoids in each condition (n=6 independent organoids per condition across two independent experiments). c,d,e,f, Quantification of voltage tracings from individual organoids in each condition from traces presented in a and b (n=6 independent organoids per condition across two independent experiments), displaying frequency (c), amplitude (d), APD30 (e), and APD90 (f). Values = mean ± s.e.m., one-way ANOVA with Dunnett's multiple comparisons test.

We also found that ondansetron did not contribute to apoptosis in human heart organoids **(Figure 76a, Figure 76b)**, but over time it did induce progressive loss of beating **(Figure 76c)**, suggesting that prolonged ondansetron use might have deleterious effects for electrophysiological maturation of the embryonic/fetal heart. Collectively, these data provide insight into the morphological and electrophysiological safety of ondansetron during human heart development and provide proof-of-concept for future investigations towards improving both the safety and efficacy of gestational medications and the pathology of congenital heart diseases.

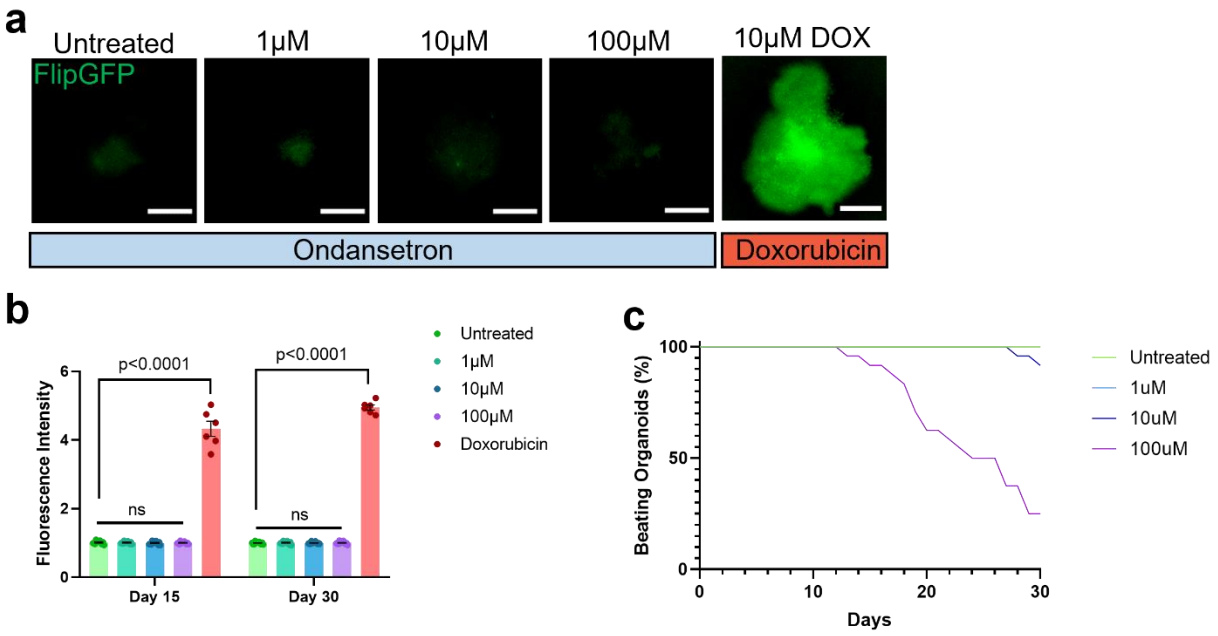

Figure 76. a, Representative fluorescence images of day 30 EMM2/1 organoids from each condition displaying FlipGFP fluorescence signal following Ondansetron treatment from day 9 to day 30 and Doxorubicin treatment from day 28 to day 30 (across two independent experiments each: n=12 independent organoids per condition; n=6 independent organoids for doxorubicin group). Scale bars = 200 µm. b, Quantification of fluorescence intensity from images presented in (a) and from organoids at day 15 (across two independent experiments each: n=12 independent organoids per condition; n=6 independent organoids for doxorubicin group). Data presented as fold change normalized to Untreated (Day 30). Values = mean ± s.e.m., matched two-way ANOVA with multiple comparisons. c, Quantification of percentage of beating organoids throughout treatment period for each Ondansetron condition from day 0 to day 30 (n=24 independent organoids per condition across two independent experiments).

5.3. DISCUSSION

Cardiac organogenesis is a highly organized and carefully orchestrated process involving the interplay of millions of cells, and perturbations to this process can lead to congenital heart defects. Heart organoids represent a new avenue to explore heart development and congenital heart defects directly in humans and could be instrumental for disease modeling and pharmacological studies. For these reasons, we decided to investigate the effects of ondansetron (Zofran), a 5-HT_3 receptor antagonist and antiemetic used for

treating nausea and vomiting[291] and the most common prescription medication for preventing nausea and vomiting during pregnancy, with up to 25% of pregnant women taking it off-label during this period[292]. Ondansetron has been epidemiologically linked to congenital heart defects (particularly ventricular septal defects) and orofacial defects[293–296], although consensus in the field is divided[297–299] and well-designed studies to thoroughly and directly investigate its safety are lacking. Moreover, ondansetron is not FDA approved for use during pregnancy and is prescribed off label for this use. The initial approval of ondansetron was for the indication of preventing nausea and vomiting during chemotherapy. Due to its widespread efficacy and general safety, it gained popularity and eventually made its way to aid expectant mothers.

We investigated the effects of ondansetron treatment during heart organoid development and found that ondansetron exposure causes electrophysiological alterations as expected due to its chemistry as a serotonin inhibitor. More interestingly, however, ondansetron also directly and strongly inhibited ventricular cardiomyocyte differentiation or maturation, even at low doses, by an unknown mechanism. We visualized the quantity and localization of MYL2, a principle ventricular muscle protein, showing a dose-dependent decrease in MYL2 expression with clinically relevant ondansetron treatments. This phenotype corresponds with epidemiological clinical findings which associate ondansetron use during pregnancy with ventricular septal defects[293,295,296]. This finding is important as it has significant implications in the clinic and suggests ondansetron should be administered with caution during pregnancy. Moreover, this study serves as validation that the patterned human heart organoid model can function as a relevant and sensitive model for investigating human heart disease and toxicological safety. Ultimately, here we

show that EMM2/1 organoids can be used as a model platform for investigating the role of ondansetron in congenital heart defects.

CHAPTER 6: CONCLUSION AND FUTURE DIRECTIONS

6.1. CONCLUSION

In summary, we describe here a developmental induction strategy inspired by hallmarks of *in utero* development for producing patterned human heart tube organoids that highly recapitulate human first trimester heart development. Our EMM2/1 developmental induction strategy yields several unique and crucial characteristics representative of an early fetal human heart, including the presence of anterior-posterior patterning with an endogenous retinoic acid gradient originating at the posterior end, polar separation of atrioventricular chambers, and a posterior, proepicardial pole; all shown in heart organoids from three independent cell lines. The EMM2/1 strategy also results in atrial and ventricular cardiomyocytes, valvular cells, conductance cells, epicardial cells, proepicardial cells and more, as well as large hollow chambers, functional electrophysiology, and increased mitochondrial density and metabolic transcriptional profiles. Moreover, EMM2/1 organoids display a high degree of similarity compared to embryonic human hearts at similar stages of development. To highlight the relevance and applicability of our model for disease modeling, we show that EMM2/1 organoids recapitulate and reveal potential mechanisms of ondansetron toxicity in the developing heart. To the extent of our knowledge, this is the first time the human heart tube has been reconstructed to this level of detail *in vitro*. Overall, our findings represent a significant advancement in human synthetic development and offer a valuable platform for cardiac disease modeling and pharmacological research.

6.2. LIMITATIONS

While our maturated human heart organoid technology opens exciting avenues for modeling the human heart *in vitro*, important limitations remain. First, further investigation is necessary to clarify the role of other important cellular populations, such as conductance cells and endothelial/coronary vasculature. EMM2/1 conditions had seemingly negative effects on organoid vascularization, a topic that deserves more attention as conditions can be further refined. Second, the lack of circulation constitutes a significant drawback that needs to be addressed, possibly through using microfluidic devices. Third, further developmental steps need to be introduced to continue increasing the physiological relevance of the organoids. This includes correcting the lack of embryonic tissue-resident macrophage populations or the contributions of the neural crest. Finally, more anatomical events need to be modeled, such as outflow tract and atrioventricular canal formation, heart looping and chamber septation.

6.3. FUTURE DIRECTIONS

All these developmental features highlight the technological leap taken to model the developing human heart *in vitro* and prove the potential of our methodology for establishing heart models for the study of normal heart development, congenital heart defects, cardiac pharmacology, regeneration, and other cardiovascular disorders in the future. Through mimicking early stages of heart development, these organoids can be used to investigate teratogens and environmental factors, such as pollutants and the influence of diet. Additionally, the role of myriad genetic mutations can be probed and characterized with higher fidelity than ever before. Similarly, investigating the efficacy and safety of pharmaceutical drugs, a continually increasing approach to treat and manage

diseases and pain, with this platform is highly advantageous. Heart organoids represent an untapped platform for increased precision in pharmaceutical discovery, development, and safety testing. To this end, the utility of chemotherapeutics is a field that is directly related to heart health. Chemotherapeutics can be highly toxic to the heart[310], and the mechanisms and solutions surrounding this cardiotoxicity remain elusive. Cardiac development is a highly intricate process and the perturbations of many factors influencing cardiac development described above remain incompletely explored in humans.

Additionally, the utility of heart organoids to aid in the regenerative capacity of the human heart may prove a fruitful vein of research. The human heart possesses an extremely limited capacity to regenerate and repair itself following damage and is a principal contributor to the morbidity and mortality surrounding heart disease. While attempts have been made to utilize cell-based regenerative approaches[311–313], a solution has yet to prove successful in clinical trials and human hearts remain non-regenerative. The increased cellular and structural maturity and physiological relevance of human heart organoids paired with their complex endogenous communication networks may prove efficacious in regeneration and repair.

The ability to create heart organoids from patient-specific iPSCs represents an unprecedented opportunity to transform the landscape of clinical trials. With this technology, scientists can perform “clinical trials in a dish” by using patient-derived iPSCs to not only guide clinical decision making, but also to perform clinical trials spanning more robust and diverse racial backgrounds, gender, age, and other complicating factors. At the same time, this technology mitigates the risks involved during current clinical trials

and can safeguard the patient from added, unnecessary, and unexpected risks, like cardiac arrythmia. The outdated trial and error process of determining the right drug or formulation for patient use can be streamlined with iPSC-derived organoid technology, and more importantly, can save patient lives at the same time.

Attempts at creating or fabricating ventricles and hearts *in vitro* via 3D printing and related strategies have captured headlines for decades.[34,314] Nonetheless, these strategies suffer from a lack of cellular complexity and physiological and anatomical relevance and functionality. The cellular complexity of our heart organoids paired with their spatial organization of cardiac cell types through endogenous recapitulation of anterior posterior patterning, atrial and ventricular chamber formation, and retinoic acid signaling highlights the ability to holistically recreate cardiogenesis and represents a crucial step forward towards the generation of synthetic human hearts in a dish.

BIBLIOGRAPHY

1. Feigin VL, Stark BA, Johnson CO, et al. Global, regional, and national burden of stroke and its risk factors, 1990–2019: a systematic analysis for the Global Burden of Disease Study 2019. *The Lancet Neurology*. 2021;20(10):795-820. doi:10.1016/S1474-4422(21)00252-0

2. Saloni Dattani, Fiona Spooner, Hannah Ritchie and Max Roser (2023) - “Causes of Death” Published online at OurWorldInData.org. Retrieved from: “https://ourworldindata.org/causes-of-death” [Online Resource].

3. Mensah GA, Roth GA, Fuster V. The Global Burden of Cardiovascular Diseases and Risk Factors. *Journal of the American College of Cardiology*. 2019;74(20):2529-2532. doi:10.1016/j.jacc.2019.10.009

4. Projections of Cardiovascular Disease Prevalence and Costs: 2015-2035. Accessed January 31, 2024. https://www.heart.org/-/media/Files/Get-Involved/Advocacy/Burden-Report-Technical-Report.pdf

5. Racial Differences by Gestational Age in Neonatal Deaths Attributable to Congenital Heart Defects --- United States, 2003--2006. Accessed February 2, 2024. https://www.cdc.gov/mmwr/preview/mmwrhtml/mm5937a3.htm

6. Bredenoord AL, Clevers H, Knoblich JA. Human tissues in a dish: The research and ethical implications of organoid technology. *Science*. 2017;355(6322):eaaf9414. doi:10.1126/science.aaf9414

7. Ordovás JM, Smith CE. Epigenetics and cardiovascular disease. *Nat Rev Cardiol*. 2010;7(9):510-519. doi:10.1038/nrcardio.2010.104

8. Takahashi K, Yamanaka S. Induction of Pluripotent Stem Cells from Mouse Embryonic and Adult Fibroblast Cultures by Defined Factors. *Cell*. 2006;126(4):663-676. doi:10.1016/j.cell.2006.07.024

9. Lian X, Hsiao C, Wilson G, et al. Robust cardiomyocyte differentiation from human pluripotent stem cells via temporal modulation of canonical Wnt signaling. *Proceedings of the National Academy of Sciences*. 2012;109(27):E1848-E1857. doi:10.1073/pnas.1200250109

10. Kattman SJ, Witty AD, Gagliardi M, et al. Stage-Specific Optimization of Activin/Nodal and BMP Signaling Promotes Cardiac Differentiation of Mouse and Human Pluripotent Stem Cell Lines. *Cell Stem Cell*. 2011;8(2):228-240. doi:10.1016/j.stem.2010.12.008

11. Devalla HD, Schwach V, Ford JW, et al. Atrial-like cardiomyocytes from human pluripotent stem cells are a robust preclinical model for assessing atrial-selective pharmacology. *EMBO Molecular Medicine*. 2015;7(4):394-410. doi:10.15252/emmm.201404757

12. Lee JH, Protze SI, Laksman Z, Backx PH, Keller GM. Human Pluripotent Stem Cell-Derived Atrial and Ventricular Cardiomyocytes Develop from Distinct Mesoderm Populations. *Cell Stem Cell*. 2017;21(2):179-194.e4. doi:10.1016/j.stem.2017.07.003

13. Zhang Q, Jiang J, Han P, et al. Direct differentiation of atrial and ventricular myocytes from human embryonic stem cells by alternating retinoid signals. *Cell Res*. 2011;21(4):579-587. doi:10.1038/cr.2010.163

14. Yechikov S, Kao HKJ, Chang CW, et al. NODAL inhibition promotes differentiation of pacemaker-like cardiomyocytes from human induced pluripotent stem cells. *Stem Cell Research*. 2020;49:102043. doi:10.1016/j.scr.2020.102043

15. Funakoshi S, Fernandes I, Mastikhina O, et al. Generation of mature compact ventricular cardiomyocytes from human pluripotent stem cells. *Nat Commun*. 2021;12(1):3155. doi:10.1038/s41467-021-23329-z

16. Iyer D, Gambardella L, Bernard WG, et al. Robust derivation of epicardium and its differentiated smooth muscle cell progeny from human pluripotent stem cells. *Development*. 2015;142(8):1528-1541. doi:10.1242/dev.119271

17. Bao X, Lian X, Hacker TA, et al. Long-term self-renewing human epicardial cells generated from pluripotent stem cells under defined xeno-free conditions. *Nat Biomed Eng*. 2016;1(1):1-12. doi:10.1038/s41551-016-0003

18. Zhang H, Tian L, Shen M, et al. Generation of Quiescent Cardiac Fibroblasts From Human Induced Pluripotent Stem Cells for In Vitro Modeling of Cardiac Fibrosis. *Circ Res*. 2019;125(5):552-566. doi:10.1161/CIRCRESAHA.119.315491

19. Giacomelli E, Meraviglia V, Campostrini G, et al. Human-iPSC-Derived Cardiac Stromal Cells Enhance Maturation in 3D Cardiac Microtissues and Reveal Non-cardiomyocyte Contributions to Heart Disease. *Cell Stem Cell*. 2020;26(6):862-879.e11. doi:10.1016/j.stem.2020.05.004

20. Paik DT, Tian L, Lee J, et al. Large-Scale Single-Cell RNA-Seq Reveals Molecular Signatures of Heterogeneous Populations of Human Induced Pluripotent Stem Cell-Derived Endothelial Cells. *Circulation Research*. 2018;123(4):443-450. doi:10.1161/CIRCRESAHA.118.312913

21. Moretti A, Bellin M, Welling A, et al. Patient-Specific Induced Pluripotent Stem-Cell Models for Long-QT Syndrome. *New England Journal of Medicine*. 2010;363(15):1397-1409. doi:10.1056/NEJMoa0908679

22. Ma D, Wei H, Lu J, et al. Generation of patient-specific induced pluripotent stem cell-derived cardiomyocytes as a cellular model of arrhythmogenic right ventricular cardiomyopathy. *European Heart Journal*. 2013;34(15):1122-1133. doi:10.1093/eurheartj/ehs226

23. Siu CW, Lee YK, Ho JCY, et al. Modeling of lamin A/C mutation premature cardiac aging using patient-specific induced pluripotent stem cells. *Aging (Albany NY)*. 2012;4(11):803-822.

24. Karakikes I, Stillitano F, Nonnenmacher M, et al. Correction of human phospholamban R14del mutation associated with cardiomyopathy using targeted nucleases and combination therapy. *Nat Commun*. 2015;6(1):6955. doi:10.1038/ncomms7955

25. Liang P, Lan F, Lee AS, et al. Drug Screening Using a Library of Human Induced Pluripotent Stem Cell–Derived Cardiomyocytes Reveals Disease-Specific Patterns of Cardiotoxicity. *Circulation*. 2013;127(16):1677-1691. doi:10.1161/CIRCULATIONAHA.113.001883

26. Kodo K, Ong SG, Jahanbani F, et al. iPSC-derived cardiomyocytes reveal abnormal TGF-β signalling in left ventricular non-compaction cardiomyopathy. *Nat Cell Biol*. 2016;18(10):1031-1042. doi:10.1038/ncb3411

27. Yang C, Xu Y, Yu M, et al. Induced pluripotent stem cell modelling of HLHS underlines the contribution of dysfunctional NOTCH signalling to impaired cardiogenesis. *Human Molecular Genetics*. 2017;26(16):3031-3045. doi:10.1093/hmg/ddx140

28. Dick E, Kalra S, Anderson D, et al. Exon Skipping and Gene Transfer Restore Dystrophin Expression in Human Induced Pluripotent Stem Cells-Cardiomyocytes Harboring DMD Mutations. *Stem Cells and Development*. 2013;22(20):2714-2724. doi:10.1089/scd.2013.0135

29. Beauchamp P, Moritz W, Kelm JM, et al. Development and Characterization of a Scaffold-Free 3D Spheroid Model of Induced Pluripotent Stem Cell-Derived Human Cardiomyocytes. *Tissue Engineering Part C: Methods*. 2015;21(8):852-861. doi:10.1089/ten.tec.2014.0376

30. Richards DJ, Li Y, Kerr CM, et al. Human cardiac organoids for the modelling of myocardial infarction and drug cardiotoxicity. *Nat Biomed Eng*. 2020;4(4):446-462. doi:10.1038/s41551-020-0539-4

31. Polonchuk L, Chabria M, Badi L, et al. Cardiac spheroids as promising in vitro models to study the human heart microenvironment. *Sci Rep*. 2017;7(1):7005. doi:10.1038/s41598-017-06385-8

32. Mills RJ, Titmarsh DM, Koenig X, et al. Functional screening in human cardiac organoids reveals a metabolic mechanism for cardiomyocyte cell cycle arrest. *PNAS*. 2017;114(40):E8372-E8381. doi:10.1073/pnas.1707316114

33. Nunes SS, Miklas JW, Liu J, et al. Biowire: a platform for maturation of human pluripotent stem cell–derived cardiomyocytes. *Nat Methods*. 2013;10(8):781-787. doi:10.1038/nmeth.2524

34. MacQueen LA, Sheehy SP, Chantre CO, et al. A tissue-engineered scale model of the heart ventricle. *Nat Biomed Eng*. 2018;2(12):930-941. doi:10.1038/s41551-018-0271-5

35. Annabi N, Tsang K, Mithieux SM, et al. Highly Elastic Micropatterned Hydrogel for Engineering Functional Cardiac Tissue. *Advanced Functional Materials*. 2013;23(39):4950-4959. doi:10.1002/adfm.201300570

36. Lee J, Sutani A, Kaneko R, et al. In vitro generation of functional murine heart organoids via FGF4 and extracellular matrix. *Nat Commun*. 2020;11(1):4283. doi:10.1038/s41467-020-18031-5

37. Rossi G, Broguiere N, Miyamoto M, et al. Capturing Cardiogenesis in Gastruloids. *Cell Stem Cell*. 2021;28(2):230-240.e6. doi:10.1016/j.stem.2020.10.013

38. Gao E, Lei YH, Shang X, et al. A Novel and Efficient Model of Coronary Artery Ligation and Myocardial Infarction in the Mouse. *Circulation Research*. 2010;107(12):1445-1453. doi:10.1161/CIRCRESAHA.110.223925

39. Patten RD, Aronovitz MJ, Deras-Mejia L, et al. Ventricular remodeling in a mouse model of myocardial infarction. *American Journal of Physiology-Heart and Circulatory Physiology*. 1998;274(5):H1812-H1820. doi:10.1152/ajpheart.1998.274.5.H1812

40. Kubota T, McTiernan CF, Frye CS, et al. Dilated Cardiomyopathy in Transgenic Mice With Cardiac-Specific Overexpression of Tumor Necrosis Factor-α. *Circulation Research*. 1997;81(4):627-635. doi:10.1161/01.RES.81.4.627

41. Li J, Thorne LN, Punjabi NM, et al. Intermittent Hypoxia Induces Hyperlipidemia in Lean Mice. *Circulation Research*. 2005;97(7):698-706. doi:10.1161/01.RES.0000183879.60089.a9

42. Ghnenis A, Padmanabhan V, Vyas A. Sexual dimorphism in testosterone programming of cardiomyocyte development in sheep. *American Journal of Physiology-Heart and Circulatory Physiology*. 2022;322(4):H607-H621. doi:10.1152/ajpheart.00691.2021

43. Wasserman AH, Huang AR, Lewis-Israeli YR, et al. Oxytocin promotes epicardial cell activation and heart regeneration after cardiac injury. *Frontiers in Cell and Developmental Biology*. 2022;10. Accessed February 5, 2024. https://www.frontiersin.org/articles/10.3389/fcell.2022.985298

44. Passier R, van Laake LW, Mummery CL. Stem-cell-based therapy and lessons from the heart. *Nature*. 2008;453(7193):322-329. doi:10.1038/nature07040

45. Roussel J, Champeroux P, Roy J, et al. The Complex QT/RR Relationship in Mice. *Sci Rep*. 2016;6(1):25388. doi:10.1038/srep25388

46. Feyen DAM, Mercola M, McKeithan WL, et al. Metabolic Maturation Media Improve Physiological Function of Human iPSC-Derived Cardiomyocytes. *Cell Reports*. 2020;32(3):107925. doi:10.1016/j.celrep.2020.107925

47. Yang X, Rodriguez M, Pabon L, et al. Tri-iodo-l-thyronine promotes the maturation of human cardiomyocytes-derived from induced pluripotent stem cells. *Journal of Molecular and Cellular Cardiology*. 2014;72:296-304. doi:10.1016/j.yjmcc.2014.04.005

48. Yang X, Rodriguez ML, Leonard A, et al. Fatty Acids Enhance the Maturation of Cardiomyocytes Derived from Human Pluripotent Stem Cells. *Stem Cell Reports*. 2019;13(4):657-668. doi:10.1016/j.stemcr.2019.08.013

49. Mihic A, Li J, Miyagi Y, et al. The effect of cyclic stretch on maturation and 3D tissue formation of human embryonic stem cell-derived cardiomyocytes. *Biomaterials*. 2014;35(9):2798-2808. doi:10.1016/j.biomaterials.2013.12.052

50. Chan YC, Ting S, Lee YK, et al. Electrical Stimulation Promotes Maturation of Cardiomyocytes Derived from Human Embryonic Stem Cells. *J of Cardiovasc Trans Res*. 2013;6(6):989-999. doi:10.1007/s12265-013-9510-z

51. Young JL, Engler AJ. Hydrogels with time-dependent material properties enhance cardiomyocyte differentiation in vitro. *Biomaterials*. 2011;32(4):1002-1009. doi:10.1016/j.biomaterials.2010.10.020

52. Ronaldson-Bouchard K, Ma SP, Yeager K, et al. Advanced maturation of human cardiac tissue grown from pluripotent stem cells. *Nature*. 2018;556(7700):239-243. doi:10.1038/s41586-018-0016-3

53. Burridge PW, Thompson S, Millrod MA, et al. A Universal System for Highly Efficient Cardiac Differentiation of Human Induced Pluripotent Stem Cells That Eliminates Interline Variability. *PLOS ONE*. 2011;6(4):e18293. doi:10.1371/journal.pone.0018293

54. Christoffels VM, Habets PEMH, Franco D, et al. Chamber Formation and Morphogenesis in the Developing Mammalian Heart. *Developmental Biology*. 2000;223(2):266-278. doi:10.1006/dbio.2000.9753

55. Sylva M, Van Den Hoff MJB, Moorman AFM. Development of the human heart. *American J of Med Genetics Pt A*. 2014;164(6):1347-1371. doi:10.1002/ajmg.a.35896

56. Van Vliet P, Wu SM, Zaffran S, Pucéat M. Early cardiac development: a view from stem cells to embryos. *Cardiovascular Research*. 2012;96(3):352-362. doi:10.1093/cvr/cvs270

57. von Gise A, Pu WT. Endocardial and Epicardial Epithelial to Mesenchymal Transitions in Heart Development and Disease. *Circulation Research*. 2012;110(12):1628-1645. doi:10.1161/CIRCRESAHA.111.259960

58. Wu S pin, Cheng CM, Lanz RB, et al. Atrial Identity Is Determined by a COUP-TFII Regulatory Network. *Developmental Cell*. 2013;25(4):417-426. doi:10.1016/j.devcel.2013.04.017

59. Schwach V, Verkerk AO, Mol M, et al. A COUP-TFII Human Embryonic Stem Cell Reporter Line to Identify and Select Atrial Cardiomyocytes. *Stem Cell Reports*. 2017;9(6):1765-1779. doi:10.1016/j.stemcr.2017.10.024

60. Li G, Xu A, Sim S, et al. Transcriptomic Profiling Maps Anatomically Patterned Subpopulations among Single Embryonic Cardiac Cells. *Developmental Cell*. 2016;39(4):491-507. doi:10.1016/j.devcel.2016.10.014

61. Bruneau BG, Logan M, Davis N, et al. Chamber-Specific Cardiac Expression of Tbx5 and Heart Defects in Holt–Oram Syndrome. *Developmental Biology*. 1999;211(1):100-108. doi:10.1006/dbio.1999.9298

62. Plageman Jr TF, Yutzey KE. Microarray analysis of Tbx5-induced genes expressed in the developing heart. *Developmental Dynamics*. 2006;235(10):2868-2880. doi:10.1002/dvdy.20923

63. de Lange FJ, Moorman AFM, Christoffels VM. Atrial cardiomyocyte-specific expression of Cre recombinase driven by an Nppa gene fragment. *genesis*. 2003;37(1):1-4. doi:10.1002/gene.10220

64. Christoffels VM, Hoogaars WMH, Tessari A, Clout DEW, Moorman AFM, Campione M. T-box transcription factor Tbx2 represses differentiation and formation of the cardiac chambers. *Developmental Dynamics*. 2004;229(4):763-770. doi:10.1002/dvdy.10487

65. Duong TB, Ravisankar P, Song YC, et al. Nr2f1a balances atrial chamber and atrioventricular canal size via BMP signaling-independent and -dependent mechanisms. *Developmental Biology*. 2018;434(1):7-14. doi:10.1016/j.ydbio.2017.11.010

66. McFadden DG, Barbosa AC, Richardson JA, Schneider MD, Srivastava D, Olson EN. The Hand1 and Hand2 transcription factors regulate expansion of the embryonic cardiac ventricles in a gene dosage-dependent manner. *Development*. 2005;132(1):189-201. doi:10.1242/dev.01562

67. Fodor WL, Darras B, Seharaseyon J, Falkenthal S, Francke U, Vanin EF. Human Ventricular/Slow Twitch Myosin Alkali Light Chain Gene Characterization, Sequence, and Chromosomal Location. *Journal of Biological Chemistry*. 1989;264(4):2143-2149. doi:10.1016/S0021-9258(18)94153-0

68. Barton PJ, Cohen A, Robert B, et al. The myosin alkali light chains of mouse ventricular and slow skeletal muscle are indistinguishable and are encoded by the same gene. *Journal of Biological Chemistry*. 1985;260(14):8578-8584. doi:10.1016/S0021-9258(17)39512-1

69. Nakagawa O, Nakagawa M, Richardson JA, Olson EN, Srivastava D. HRT1, HRT2, and HRT3: a new subclass of bHLH transcription factors marking specific cardiac, somitic, and pharyngeal arch segments. *Dev Biol*. 1999;216(1):72-84. doi:10.1006/dbio.1999.9454

70. Bao ZZ, Bruneau BG, Seidman JG, Seidman CE, Cepko CL. Regulation of Chamber-Specific Gene Expression in the Developing Heart by Irx4. *Science*. 1999;283(5405):1161-1164. doi:10.1126/science.283.5405.1161

71. Bruneau BG, Bao ZZ, Tanaka M, et al. Cardiac Expression of the Ventricle-Specific Homeobox Gene Irx4 Is Modulated by Nkx2-5 and dHand. *Developmental Biology*. 2000;217(2):266-277. doi:10.1006/dbio.1999.9548

72. Pérez-Pomares JM, Phelps A, Sedmerova M, Wessels A. Epicardial-like cells on the distal arterial end of the cardiac outflow tract do not derive from the proepicardium but are derivatives of the cephalic pericardium. *Developmental Dynamics*. 2003;227(1):56-68. doi:10.1002/dvdy.10284

73. Virágh S, Gittenberger-de Groot AC, Poelmann RE, Káimán F. Early development of quail heart epicardium and associated vascular and glandular structures. *Anat Embryol*. 1993;188(4):381-393. doi:10.1007/BF00185947

74. Viragh S, Challice CE. The origin of the epicardium and the embryonic myocardial circulation in the mouse. *The Anatomical Record*. 1981;201(1):157-168. doi:10.1002/ar.1092010117

75. Li P, Cavallero S, Gu Y, et al. IGF signaling directs ventricular cardiomyocyte proliferation during embryonic heart development. *Development*. 2011;138(9):1795-1805. doi:10.1242/dev.054338

76. von Gise A, Zhou B, Honor LB, Ma Q, Petryk A, Pu WT. WT1 regulates epicardial epithelial to mesenchymal transition through β-catenin and retinoic acid signaling pathways. *Developmental Biology*. 2011;356(2):421-431. doi:10.1016/j.ydbio.2011.05.668

77. Stuckmann I, Evans S, Lassar AB. Erythropoietin and retinoic acid, secreted from the epicardium, are required for cardiac myocyte proliferation. *Developmental Biology*. 2003;255(2):334-349. doi:10.1016/S0012-1606(02)00078-7

78. Lewis-Israeli YR, Wasserman AH, Gabalski MA, et al. Self-assembling human heart organoids for the modeling of cardiac development and congenital heart disease. *Nat Commun*. 2021;12(1):5142. doi:10.1038/s41467-021-25329-5

79. Hofbauer P, Jahnel SM, Papai N, et al. Cardioids reveal self-organizing principles of human cardiogenesis. *Cell*. 2021;184(12):3299-3317.e22. doi:10.1016/j.cell.2021.04.034

80. Drakhlis L, Biswanath S, Farr CM, et al. Human heart-forming organoids recapitulate early heart and foregut development. *Nat Biotechnol*. 2021;39(6):737-746. doi:10.1038/s41587-021-00815-9

81. Andersen P, Tampakakis E, Jimenez DV, et al. Precardiac organoids form two heart fields via Bmp/Wnt signaling. *Nat Commun*. 2018;9(1):3140. doi:10.1038/s41467-018-05604-8

82. George RM, Maldonado-Velez G, Firulli AB. The heart of the neural crest: cardiac neural crest cells in development and regeneration. *Development*. 2020;147(20):dev188706. doi:10.1242/dev.188706

83. Cahill TJ, Sun X, Ravaud C, et al. Tissue-resident macrophages regulate lymphatic vessel growth and patterning in the developing heart. *Development*. 2021;148(3):dev194563. doi:10.1242/dev.194563

84. Lancaster MA, Renner M, Martin CA, et al. Cerebral organoids model human brain development and microcephaly. *Nature*. 2013;501(7467):373-379. doi:10.1038/nature12517

85. Miller AJ, Dye BR, Ferrer-Torres D, et al. Generation of lung organoids from human pluripotent stem cells in vitro. *Nat Protoc*. 2019;14(2):518-540. doi:10.1038/s41596-018-0104-8

86. Takasato M, Er PX, Chiu HS, et al. Kidney organoids from human iPS cells contain multiple lineages and model human nephrogenesis. *Nature*. 2015;526(7574):564-568. doi:10.1038/nature15695

87. Vlachogiannis G, Hedayat S, Vatsiou A, et al. Patient-derived organoids model treatment response of metastatic gastrointestinal cancers. *Science*. 2018;359(6378):920-926. doi:10.1126/science.aao2774

88. Paşca SP, Portmann T, Voineagu I, et al. Using iPSC-derived neurons to uncover cellular phenotypes associated with Timothy syndrome. *Nat Med*. 2011;17(12):1657-1662. doi:10.1038/nm.2576

89. Sun G, Chiuppesi F, Chen X, et al. Modeling Human Cytomegalovirus-Induced Microcephaly in Human iPSC-Derived Brain Organoids. *Cell Reports Medicine*. 2020;1(1):100002. doi:10.1016/j.xcrm.2020.100002

90. Bershteyn M, Nowakowski TJ, Pollen AA, et al. Human iPSC-Derived Cerebral Organoids Model Cellular Features of Lissencephaly and Reveal Prolonged Mitosis of Outer Radial Glia. *Cell Stem Cell*. 2017;20(4):435-449.e4. doi:10.1016/j.stem.2016.12.007

91. Forbes TA, Howden SE, Lawlor K, et al. Patient-iPSC-Derived Kidney Organoids Show Functional Validation of a Ciliopathic Renal Phenotype and Reveal Underlying Pathogenetic Mechanisms. *The American Journal of Human Genetics*. 2018;102(5):816-831. doi:10.1016/j.ajhg.2018.03.014

92. Jacob F, Pather SR, Huang WK, et al. Human Pluripotent Stem Cell-Derived Neural Cells and Brain Organoids Reveal SARS-CoV-2 Neurotropism Predominates in Choroid Plexus Epithelium. *Cell Stem Cell*. 2020;27(6):937-950.e9. doi:10.1016/j.stem.2020.09.016

93. Benson DW, Silberbach GM, Kavanaugh-McHugh A, et al. Mutations in the cardiac transcription factor NKX2.5 affect diverse cardiac developmental pathways. *J Clin Invest*. 1999;104(11):1567-1573.

94. Meier AB, Zawada D, De Angelis MT, et al. Epicardioid single-cell genomics uncovers principles of human epicardium biology in heart development and disease. *Nat Biotechnol*. Published online April 3, 2023:1-14. doi:10.1038/s41587-023-01718-7

95. Vargesson N. Thalidomide-induced teratogenesis: History and mechanisms. *Birth Defects Research Part C: Embryo Today: Reviews*. 2015;105(2):140-156. doi:10.1002/bdrc.21096

96. Das KP, Grey BE, Rosen MB, et al. Developmental toxicity of perfluorononanoic acid in mice. *Reproductive Toxicology*. 2015;51:133-144. doi:10.1016/j.reprotox.2014.12.012

97. Clarkson TW, Nordberg GF, Sager PR. Reproductive and developmental toxicity of metals. *Scand J Work Environ Health*. 1985;11(3):145-154. doi:10.5271/sjweh.2239

98. Sengupta P, Banerjee R. Environmental toxins: Alarming impacts of pesticides on male fertility. *Hum Exp Toxicol*. 2014;33(10):1017-1039. doi:10.1177/0960327113515504

99. Olson EN. Gene Regulatory Networks in the Evolution and Development of the Heart. *Science*. 2006;313(5795):1922-1927. doi:10.1126/science.1132292

100. Lehtoranta L, Vuolteenaho O, Laine VJ, et al. Maternal hyperglycemia leads to fetal cardiac hyperplasia and dysfunction in a rat model. *American Journal of Physiology-Endocrinology and Metabolism*. 2013;305(5):E611-E619. doi:10.1152/ajpendo.00043.2013

101. Zhang Y, Huang L, Wang C, Gao D, Zuo Z. Phenanthrene exposure produces cardiac defects during embryo development of zebrafish (Danio rerio) through activation of MMP-9. *Chemosphere*. 2013;93(6):1168-1175. doi:10.1016/j.chemosphere.2013.06.056

102. Blanchette AD, Burnett SD, Grimm FA, Rusyn I, Chiu WA. A Bayesian Method for Population-wide Cardiotoxicity Hazard and Risk Characterization Using an In Vitro Human Model. *Toxicological Sciences*. 2020;178(2):391-403. doi:10.1093/toxsci/kfaa151

103. Panopoulos AD, D'Antonio M, Benaglio P, et al. iPSCORE: A Resource of 222 iPSC Lines Enabling Functional Characterization of Genetic Variation across a Variety of Cell Types. *Stem Cell Reports*. 2017;8(4):1086-1100. doi:10.1016/j.stemcr.2017.03.012

104. Ming Y, Hao S, Wang F, et al. Longitudinal morphological and functional characterization of human heart organoids using optical coherence tomography. *Biosens Bioelectron*. 2022;207:114136. doi:10.1016/j.bios.2022.114136

105. Dekkers JF, Alieva M, Wellens LM, et al. High-resolution 3D imaging of fixed and cleared organoids. *Nature Protocols*. 2019;14(6):1756-1771. doi:10.1038/s41596-019-0160-8

106. Bolte S, Cordelières FP. A guided tour into subcellular colocalization analysis in light microscopy. *Journal of Microscopy*. 2006;224(3):213-232. doi:10.1111/j.1365-2818.2006.01706.x

107. Huang Y, Wang S, Guo Q, et al. Optical Coherence Tomography Detects Necrotic Regions and Volumetrically Quantifies Multicellular Tumor Spheroids. *Cancer Res*. 2017;77(21):6011-6020. doi:10.1158/0008-5472.CAN-17-0821

108. Butler A, Hoffman P, Smibert P, Papalexi E, Satija R. Integrating single-cell transcriptomic data across different conditions, technologies, and species. *Nat Biotechnol*. 2018;36(5):411-420. doi:10.1038/nbt.4096

109. Korsunsky I, Millard N, Fan J, et al. Fast, sensitive and accurate integration of single-cell data with Harmony. *Nat Methods*. 2019;16(12):1289-1296. doi:10.1038/s41592-019-0619-0

110. Dimitrov D, Türei D, Garrido-Rodriguez M, et al. Comparison of methods and resources for cell-cell communication inference from single-cell RNA-Seq data. *Nat Commun*. 2022;13(1):3224. doi:10.1038/s41467-022-30755-0

111. Blanco-Carmona E. Generating publication ready visualizations for Single Cell transcriptomics using SCpubr. Published online March 1, 2022:2022.02.28.482303. doi:10.1101/2022.02.28.482303

112. Ramilowski JA, Goldberg T, Harshbarger J, et al. A draft network of ligand-receptor-mediated multicellular signalling in human. *Nat Commun*. 2015;6:7866. doi:10.1038/ncomms8866

113. Asp M, Giacomello S, Larsson L, et al. A Spatiotemporal Organ-Wide Gene Expression and Cell Atlas of the Developing Human Heart. *Cell*. 2019;179(7):1647-1660.e19. doi:10.1016/j.cell.2019.11.025

114. Cui Y, Zheng Y, Liu X, et al. Single-Cell Transcriptome Analysis Maps the Developmental Track of the Human Heart. *Cell Reports*. 2019;26(7):1934-1950.e5. doi:10.1016/j.celrep.2019.01.079

115. Zhang Y, Parmigiani G, Johnson WE. ComBat-seq: batch effect adjustment for RNA-seq count data. *NAR Genom Bioinform*. 2020;2(3):lqaa078. doi:10.1093/nargab/lqaa078

116. Kleverov M, Zenkova D, Kamenev V, Sablina M, Artyomov MN, Sergushichev AA. Phantasus: web-application for visual and interactive gene expression analysis. Published online December 12, 2022:2022.12.10.519861. doi:10.1101/2022.12.10.519861

117. Chen EY, Tan CM, Kou Y, et al. Enrichr: interactive and collaborative HTML5 gene list enrichment analysis tool. *BMC Bioinformatics*. 2013;14(1):128. doi:10.1186/1471-2105-14-128

118. Kuleshov MV, Jones MR, Rouillard AD, et al. Enrichr: a comprehensive gene set enrichment analysis web server 2016 update. *Nucleic Acids Res*. 2016;44(W1):W90-97. doi:10.1093/nar/gkw377

119. Xie Z, Bailey A, Kuleshov MV, et al. Gene Set Knowledge Discovery with Enrichr. *Curr Protoc*. 2021;1(3):e90. doi:10.1002/cpz1.90

120. Luo W, Pant G, Bhavnasi YK, Blanchard SG Jr, Brouwer C. Pathview Web: user friendly pathway visualization and data integration. *Nucleic Acids Research*. 2017;45(W1):W501-W508. doi:10.1093/nar/gkx372

121. Luo W, Brouwer C. Pathview: an R/Bioconductor package for pathway-based data integration and visualization. *Bioinformatics*. 2013;29(14):1830-1831. doi:10.1093/bioinformatics/btt285

122. Hondeghem LM, Carlsson L, Duker G. Instability and Triangulation of the Action Potential Predict Serious Proarrhythmia, but Action Potential Duration Prolongation Is Antiarrhythmic. *Circulation*. 2001;103(15):2004-2013. doi:10.1161/01.CIR.103.15.2004

123. Evans MJ, Kaufman MH. Establishment in culture of pluripotential cells from mouse embryos. *Nature*. 1981;292(5819):154-156. doi:10.1038/292154a0

124. Theodoris CV, Zhou P, Liu L, et al. Network-based screen in iPSC-derived cells reveals therapeutic candidate for heart valve disease. *Science*. 2021;371(6530):eabd0724. doi:10.1126/science.abd0724

125. Lancaster MA, Knoblich JA. Organogenesis in a dish: Modeling development and disease using organoid technologies. *Science*. 2014;345(6194). doi:10.1126/science.1247125

126. Moreira LM, Takawale A, Hulsurkar M, et al. Paracrine signalling by cardiac calcitonin controls atrial fibrogenesis and arrhythmia. *Nature*. 2020;587(7834):460-465. doi:10.1038/s41586-020-2890-8

127. Lee J, Termglinchan V, Diecke S, et al. Activation of PDGF pathway links LMNA mutation to dilated cardiomyopathy. *Nature*. 2019;572(7769):335-340. doi:10.1038/s41586-019-1406-x

128. Tiburcy M, Hudson JE, Balfanz P, et al. Defined Engineered Human Myocardium With Advanced Maturation for Applications in Heart Failure Modeling and Repair. *Circulation*. 2017;135(19):1832-1847. doi:10.1161/CIRCULATIONAHA.116.024145

129. Ingber DE. Human organs-on-chips for disease modelling, drug development and personalized medicine. *Nat Rev Genet*. 2022;23(8):467-491. doi:10.1038/s41576-022-00466-9

130. Gintant G, Burridge P, Gepstein L, et al. Use of Human Induced Pluripotent Stem Cell–Derived Cardiomyocytes in Preclinical Cancer Drug Cardiotoxicity Testing: A Scientific Statement From the American Heart Association. *Circ Res*. 2019;125(10). doi:10.1161/RES.0000000000000291

131. Chen G, Gulbranson DR, Hou Z, et al. Chemically defined conditions for human iPSC derivation and culture. *Nat Methods*. 2011;8(5):424-429. doi:10.1038/nmeth.1593

132. Xu X, Jin K, Bais AS, et al. Uncompensated mitochondrial oxidative stress underlies heart failure in an iPSC-derived model of congenital heart disease. *Cell Stem Cell*. 2022;29(5):840-855.e7. doi:10.1016/j.stem.2022.03.003

133. Clevers H. Modeling Development and Disease with Organoids. *Cell*. 2016;165(7):1586-1597. doi:10.1016/j.cell.2016.05.082

134. Nishinakamura R, Sharmin S, Taguchi A. Induction of nephron progenitors and glomeruli from human pluripotent stem cells. *Pediatr Nephrol*. 2017;32(2):195-200. doi:10.1007/s00467-016-3339-z

135. Jacob A, Morley M, Hawkins F, et al. Differentiation of Human Pluripotent Stem Cells into Functional Lung Alveolar Epithelial Cells. *Cell Stem Cell*. 2017;21(4):472-488.e10. doi:10.1016/j.stem.2017.08.014

136. Buchholz DE, Hikita ST, Rowland TJ, et al. Derivation of Functional Retinal Pigmented Epithelium from Induced Pluripotent Stem Cells. *Stem Cells*. 2009;27(10):2427-2434. doi:10.1002/stem.189

137. Deng WL, Gao ML, Lei XL, et al. Gene Correction Reverses Ciliopathy and Photoreceptor Loss in iPSC-Derived Retinal Organoids from Retinitis Pigmentosa Patients. *Stem Cell Reports*. 2018;10(4):1267-1281. doi:10.1016/j.stemcr.2018.02.003

138. Bizy A, Guerrero-Serna G, Hu B, et al. Myosin light chain 2-based selection of human iPSC-derived early ventricular cardiac myocytes. *Stem Cell Research*. 2013;11(3):1335-1347. doi:10.1016/j.scr.2013.09.003

139. Richards DJ, Coyle RC, Tan Y, et al. Inspiration from heart development: Biomimetic development of functional human cardiac organoids. *Biomaterials*. 2017;142:112-123. doi:10.1016/j.biomaterials.2017.07.021

140. Correia C, Koshkin A, Duarte P, et al. Distinct carbon sources affect structural and functional maturation of cardiomyocytes derived from human pluripotent stem cells. *Scientific Reports*. 2017;7(1):8590. doi:10.1038/s41598-017-08713-4

141. Alvino G, Cozzi V, Radaelli T, Ortega H, Herrera E, Cetin I. Maternal and Fetal Fatty Acid Profile in Normal and Intrauterine Growth Restriction Pregnancies With and Without Preeclampsia. *Pediatr Res*. 2008;64(6):615-620. doi:10.1203/PDR.0b013e31818702a2

142. Longo N, Frigeni M, Pasquali M. Carnitine transport and fatty acid oxidation. *Biochimica et Biophysica Acta (BBA) - Molecular Cell Research*. 2016;1863(10):2422-2435. doi:10.1016/j.bbamcr.2016.01.023

143. Oey NA, Den Boer MEJ, Wijburg FA, et al. Long-Chain Fatty Acid Oxidation during Early Human Development. *Pediatr Res*. 2005;57(6):755-759. doi:10.1203/01.PDR.0000161413.42874.74

144. Iruretagoyena JI, Davis W, Bird C, et al. Metabolic gene profile in early human fetal heart development. *Molecular Human Reproduction*. 2014;20(7):690-700. doi:10.1093/molehr/gau026

145. Chung S, Dzeja PP, Faustino RS, Perez-Terzic C, Behfar A, Terzic A. Mitochondrial oxidative metabolism is required for the cardiac differentiation of stem cells. *Nat Clin Pract Cardiovasc Med*. 2007;4(Suppl 1):S60-S67. doi:10.1038/ncpcardio0766

146. Gaspar JA, Doss MX, Hengstler JG, Cadenas C, Hescheler J, Sachinidis A. Unique Metabolic Features of Stem Cells, Cardiomyocytes, and Their Progenitors. *Circulation Research*. 2014;114(8):1346-1360. doi:10.1161/CIRCRESAHA.113.302021

147. Chung S, Arrell DK, Faustino RS, Terzic A, Dzeja PP. Glycolytic network restructuring integral to the energetics of embryonic stem cell cardiac differentiation. *Journal of Molecular and Cellular Cardiology*. 2010;48(4):725-734. doi:10.1016/j.yjmcc.2009.12.014

148. Klein I, Ojamaa K. Thyroid Hormone and the Cardiovascular System. *N Engl J Med*. 2001;344(7):501-509. doi:10.1056/NEJM200102153440707

149. Chattergoon NN. Thyroid hormone signaling and consequences for cardiac development. *Journal of Endocrinology*. 2019;242(1):T145-T160. doi:10.1530/JOE-18-0704

150. Marconi AM, Paolini C, Buscaglia M, Zerbe G, Battaglia FC, Pardi G. The impact of gestational age and fetal growth on the maternal-fetal glucose concentration difference. *Obstetrics & Gynecology*. 1996;87(6):937-942. doi:10.1016/0029-7844(96)00048-8

151. Bozzetti P, Ferrari MM, Marconi AM, et al. The relationship of maternal and fetal glucose concentrations in the human from midgestation until term. *Metabolism - Clinical and Experimental*. 1988;37(4):358-363. doi:10.1016/0026-0495(88)90136-9

152. Kilby MD, Neary RH, Mackness MI, Durrington PN. Fetal and Maternal Lipoprotein Metabolism in Human Pregnancy Complicated by Type I Diabetes Mellitus1. *The Journal of Clinical Endocrinology & Metabolism*. 1998;83(5):1736-1741. doi:10.1210/jcem.83.5.4783

153. Sugamura K, Keaney John F. Reactive oxygen species in cardiovascular disease. *Free Radical Biology and Medicine*. 2011;51(5):978-992. doi:10.1016/j.freeradbiomed.2011.05.004

154. He F, Zuo L. Redox Roles of Reactive Oxygen Species in Cardiovascular Diseases. *International Journal of Molecular Sciences*. 2015;16(11):27770-27780. doi:10.3390/ijms161126059

155. Liu JP, Baker J, Perkins AS, Robertson EJ, Efstratiadis A. Mice carrying null mutations of the genes encoding insulin-like growth factor I (Igf-1) and type 1 IGF receptor (Igf1r). *Cell*. 1993;75(1):59-72. doi:10.1016/S0092-8674(05)80084-4

156. Ren J, Samson WK, Sowers JR. Insulin-like growth factor I as a cardiac hormone: physiological and pathophysiological implications in heart disease. *J Mol Cell Cardiol*. 1999;31(11):2049-2061. doi:10.1006/jmcc.1999.1036

157. Zhang Q, Schepis A, Huang H, et al. Designing a Green Fluorogenic Protease Reporter by Flipping a Beta Strand of GFP for Imaging Apoptosis in Animals. *J Am Chem Soc*. 2019;141(11):4526-4530. doi:10.1021/jacs.8b13042

158. Sommer G, Schriefl AJ, Andrä M, et al. Biomechanical properties and microstructure of human ventricular myocardium. *Acta Biomaterialia*. 2015;24:172-192. doi:10.1016/j.actbio.2015.06.031

159. Kupfer ME, Lin WH, Ravikumar V, et al. In Situ Expansion, Differentiation, and Electromechanical Coupling of Human Cardiac Muscle in a 3D Bioprinted,

Chambered Organoid. *Circulation Research*. 2020;127(2):207-224. doi:10.1161/CIRCRESAHA.119.316155

160. Reijntjes S, Blentic A, Gale E, Maden M. The control of morphogen signalling: Regulation of the synthesis and catabolism of retinoic acid in the developing embryo. *Developmental Biology*. 2005;285(1):224-237. doi:10.1016/j.ydbio.2005.06.019

161. Guadix JA, Ruiz-Villalba A, Lettice L, et al. Wt1 controls retinoic acid signalling in embryonic epicardium through transcriptional activation of Raldh2. *Development*. 2011;138(6):1093-1097. doi:10.1242/dev.044594

162. Moss JB, Xavier-Neto J, Shapiro MD, et al. Dynamic Patterns of Retinoic Acid Synthesis and Response in the Developing Mammalian Heart. *Developmental Biology*. 1998;199(1):55-71. doi:10.1006/dbio.1998.8911

163. Hochgreb T, Linhares VL, Menezes DC, et al. A caudorostral wave of RALDH2 conveys anteroposterior information to the cardiac field. *Development*. 2003;130(22):5363-5374. doi:10.1242/dev.00750

164. Rhinn M, Dollé P. Retinoic acid signalling during development. *Development*. 2012;139(5):843-858. doi:10.1242/dev.065938

165. Wiesinger A, Boink GJJ, Christoffels VM, Devalla HD. Retinoic acid signaling in heart development: Application in the differentiation of cardiovascular lineages from human pluripotent stem cells. *Stem Cell Reports*. 2021;16(11):2589-2606. doi:10.1016/j.stemcr.2021.09.010

166. Niederreither K, Vermot J, Messaddeq N, Schuhbaur B, Chambon P, Dollé P. Embryonic retinoic acid synthesis is essential for heart morphogenesis in the mouse. *Development*. 2001;128(7):1019-1031. doi:10.1242/dev.128.7.1019

167. Schmidt C, Deyett A, Ilmer T, et al. Multi-chamber cardioids unravel human heart development and cardiac defects. *Cell*. 2023;186(25):5587-5605.e27. doi:10.1016/j.cell.2023.10.030

168. Gollob MH, Jones DL, Krahn AD, et al. Somatic Mutations in the Connexin 40 Gene (*GJA5*) in Atrial Fibrillation. *N Engl J Med*. 2006;354(25):2677-2688. doi:10.1056/NEJMoa052800

169. Takasaki A, Hirono K, Hata Y, et al. Sarcomere gene variants act as a genetic trigger underlying the development of left ventricular noncompaction. *Pediatr Res*. 2018;84(5):733-742. doi:10.1038/s41390-018-0162-1

170. Martins AS, Parvatiyar MS, Feng HZ, et al. In Vivo Analysis of Troponin C Knock-In (A8V) Mice. *Circulation: Cardiovascular Genetics*. 2015;8(5):653-664. doi:10.1161/CIRCGENETICS.114.000957

171. Rosenfeld GE, Mercer EJ, Mason CE, Evans T. Small heat shock proteins Hspb7 and Hspb12 regulate early steps of cardiac morphogenesis. *Developmental Biology*. 2013;381(2):389-400. doi:10.1016/j.ydbio.2013.06.025

172. Wu T, Mu Y, Bogomolovas J, et al. HSPB7 is indispensable for heart development by modulating actin filament assembly. *Proceedings of the National Academy of Sciences*. 2017;114(45):11956-11961. doi:10.1073/pnas.1713763114

173. Smith CL, Baek ST, Sung CY, Tallquist MD. Epicardial-Derived Cell Epithelial-to-Mesenchymal Transition and Fate Specification Require PDGF Receptor Signaling. *Circulation Research*. 2011;108(12):e15-e26. doi:10.1161/CIRCRESAHA.110.235531

174. Mellgren AM, Smith CL, Olsen GS, et al. Platelet-Derived Growth Factor Receptor β Signaling Is Required for Efficient Epicardial Cell Migration and Development of Two Distinct Coronary Vascular Smooth Muscle Cell Populations. *Circulation Research*. 2008;103(12):1393-1401. doi:10.1161/CIRCRESAHA.108.176768

175. Katz TC, Singh MK, Degenhardt K, et al. Distinct Compartments of the Proepicardial Organ Give Rise to Coronary Vascular Endothelial Cells. *Developmental Cell*. 2012;22(3):639-650. doi:10.1016/j.devcel.2012.01.012

176. Kanisicak O, Khalil H, Ivey MJ, et al. Genetic lineage tracing defines myofibroblast origin and function in the injured heart. *Nat Commun*. 2016;7(1):12260. doi:10.1038/ncomms12260

177. Tandon P, Miteva YV, Kuchenbrod LM, Cristea IM, Conlon FL. Tcf21 regulates the specification and maturation of proepicardial cells. *Development*. 2013;140(11):2409-2421. doi:10.1242/dev.093385

178. Knight-Schrijver VR, Davaapil H, Bayraktar S, et al. A single-cell comparison of adult and fetal human epicardium defines the age-associated changes in epicardial activity. *Nat Cardiovasc Res*. 2022;1(12):1215-1229. doi:10.1038/s44161-022-00183-w

179. Moore AW, McInnes L, Kreidberg J, Hastie ND, Schedl A. YAC complementation shows a requirement for Wt1 in the development of epicardium, adrenal gland and throughout nephrogenesis. *Development*. 1999;126(9):1845-1857. doi:10.1242/dev.126.9.1845

180. Greulich F, Farin HF, Schuster-Gossler K, Kispert A. Tbx18 function in epicardial development. *Cardiovascular Research*. 2012;96(3):476-483. doi:10.1093/cvr/cvs277

181. Di Paolo G, Pellier V, Catsicas M, Antonsson B, Catsicas S, Grenningloh G. The phosphoprotein stathmin is essential for nerve growth factor-stimulated differentiation. *Journal of Cell Biology*. 1996;133(6):1383-1390. doi:10.1083/jcb.133.6.1383

182. Mori N, Morii H. SCG10-related neuronal growth-associated proteins in neural development, plasticity, degeneration, and aging. *Journal of Neuroscience Research*. 2002;70(3):264-273. doi:10.1002/jnr.10353

183. Guerra San Juan I, Nash LA, Smith KS, et al. Loss of mouse Stmn2 function causes motor neuropathy. *Neuron*. 2022;110(10):1671-1688.e6. doi:10.1016/j.neuron.2022.02.011

184. Taupenot L, Harper KL, O'Connor DT. The Chromogranin–Secretogranin Family. *New England Journal of Medicine*. 2003;348(12):1134-1149. doi:10.1056/NEJMra021405

185. Kim HJ, Denli AM, Wright R, et al. REST Regulates Non–Cell-Autonomous Neuronal Differentiation and Maturation of Neural Progenitor Cells via Secretogranin II. *J Neurosci*. 2015;35(44):14872-14884. doi:10.1523/JNEUROSCI.4286-14.2015

186. Lan MS, Breslin MB. Structure, expression, and biological function of INSM1 transcription factor in neuroendocrine differentiation. *FASEB J*. 2009;23(7):2024-2033. doi:10.1096/fj.08-125971

187. Privratsky JR, Newman PJ. PECAM-1: regulator of endothelial junctional integrity. *Cell Tissue Res*. 2014;355(3):607-619. doi:10.1007/s00441-013-1779-3

188. Hirata K ichi, Ishida T, Penta K, et al. Cloning of an Immunoglobulin Family Adhesion Molecule Selectively Expressed by Endothelial Cells*. *Journal of Biological Chemistry*. 2001;276(19):16223-16231. doi:10.1074/jbc.M100630200

189. Downes M, Koopman P. SOX18 and the Transcriptional Regulation of Blood Vessel Development. *Trends in Cardiovascular Medicine*. 2001;11(8):318-324. doi:10.1016/S1050-1738(01)00131-1

190. Fong GH, Rossant J, Gertsenstein M, Breitman ML. Role of the Flt-1 receptor tyrosine kinase in regulating the assembly of vascular endothelium. *Nature*. 1995;376(6535):66-70. doi:10.1038/376066a0

191. Kang IS, Suh J, Lee MN, et al. Characterization of human cardiac mesenchymal stromal cells and their extracellular vesicles comparing with human bone marrow derived mesenchymal stem cells. *BMB Rep*. 2020;53(2):118-123. doi:10.5483/BMBRep.2020.53.2.235

192. Eirin A, Zhu XY, Puranik AS, et al. Comparative proteomic analysis of extracellular vesicles isolated from porcine adipose tissue-derived mesenchymal stem/stromal cells. *Sci Rep*. 2016;6(1):36120. doi:10.1038/srep36120

193. Lincoln J, Kist R, Scherer G, Yutzey KE. Sox9 is required for precursor cell expansion and extracellular matrix organization during mouse heart valve

development. *Developmental Biology*. 2007;305(1):120-132. doi:10.1016/j.ydbio.2007.02.002

194. Li Y, Lui KO, Zhou B. Reassessing endothelial-to-mesenchymal transition in cardiovascular diseases. *Nat Rev Cardiol*. 2018;15(8):445-456. doi:10.1038/s41569-018-0023-y

195. Schäck LM, Buettner M, Wirth A, et al. Expression of CD24 in Human Bone Marrow-Derived Mesenchymal Stromal Cells Is Regulated by TGF*β*3 and Induces a Myofibroblast-Like Genotype. *Stem Cells International*. 2015;2016:e1319578. doi:10.1155/2016/1319578

196. Alfieri CM, Cheek J, Chakraborty S, Yutzey KE. Wnt signaling in heart valve development and osteogenic gene induction. *Developmental Biology*. 2010;338(2):127-135. doi:10.1016/j.ydbio.2009.11.030

197. Cheng L, Xie M, Qiao W, et al. Generation and characterization of cardiac valve endothelial-like cells from human pluripotent stem cells. *Commun Biol*. 2021;4(1):1-15. doi:10.1038/s42003-021-02571-7

198. Dill TL, Naya FJ. A Hearty Dose of Noncoding RNAs: The Imprinted DLK1-DIO3 Locus in Cardiac Development and Disease. *Journal of Cardiovascular Development and Disease*. 2018;5(3):37. doi:10.3390/jcdd5030037

199. Tkatchenko TV, Moreno-Rodriguez RA, Conway SJ, Molkentin JD, Markwald RR, Tkatchenko AV. Lack of periostin leads to suppression of Notch1 signaling and calcific aortic valve disease. *Physiol Genomics*. 2009;39(3):160-168. doi:10.1152/physiolgenomics.00078.2009

200. Neri T, Hiriart E, van Vliet PP, et al. Human pre-valvular endocardial cells derived from pluripotent stem cells recapitulate cardiac pathophysiological valvulogenesis. *Nat Commun*. 2019;10(1):1929. doi:10.1038/s41467-019-09459-5

201. Hortells L, Valiente-Alandi I, Thomas ZM, et al. A specialized population of Periostin-expressing cardiac fibroblasts contributes to postnatal cardiomyocyte maturation and innervation. *Proceedings of the National Academy of Sciences*. 2020;117(35):21469-21479. doi:10.1073/pnas.2009119117

202. Quijada P, Trembley MA, Small EM. The Role of the Epicardium During Heart Development and Repair. *Circ Res*. 2020;126(3):377-394. doi:10.1161/CIRCRESAHA.119.315857

203. Ryan AK, Blumberg B, Rodriguez-Esteban C, et al. Pitx2 determines left–right asymmetry of internal organs in vertebrates. *Nature*. 1998;394(6693):545-551. doi:10.1038/29004

204. Ai D, Liu W, Ma L, et al. Pitx2 regulates cardiac left-right asymmetry by patterning second cardiac lineage-derived myocardium. *Dev Biol*. 2006;296(2):437-449. doi:10.1016/j.ydbio.2006.06.009

205. Ocaña OH, Coskun H, Minguillón C, et al. A right-handed signalling pathway drives heart looping in vertebrates. *Nature*. 2017;549(7670):86-90. doi:10.1038/nature23454

206. Meno C, Shimono A, Saijoh Y, et al. lefty-1 Is Required for Left-Right Determination as a Regulator of lefty-2 and nodal. *Cell*. 1998;94(3):287-297. doi:10.1016/S0092-8674(00)81472-5

207. Uxa S, Castillo-Binder P, Kohler R, Stangner K, Müller GA, Engeland K. Ki-67 gene expression. *Cell Death Differ*. 2021;28(12):3357-3370. doi:10.1038/s41418-021-00823-x

208. Whitfield ML, George LK, Grant GD, Perou CM. Common markers of proliferation. *Nat Rev Cancer*. 2006;6(2):99-106. doi:10.1038/nrc1802

209. Nigg EA. Mitotic kinases as regulators of cell division and its checkpoints. *Nat Rev Mol Cell Biol*. 2001;2(1):21-32. doi:10.1038/35048096

210. Kelly RG, Buckingham ME, Moorman AF. Heart fields and cardiac morphogenesis. *Cold Spring Harb Perspect Med*. 2014;4(10):a015750. doi:10.1101/cshperspect.a015750

211. Devine WP, Wythe JD, George M, Koshiba-Takeuchi K, Bruneau BG. Early patterning and specification of cardiac progenitors in gastrulating mesoderm. Bronner ME, ed. *eLife*. 2014;3:e03848. doi:10.7554/eLife.03848

212. Chapman DL, Garvey N, Hancock S, et al. Expression of the T-box family genes, Tbx1–Tbx5, during early mouse development. *Developmental Dynamics*. 1996;206(4):379-390. doi:10.1002/(SICI)1097-0177(199608)206:4<379::AID-AJA4>3.0.CO;2-F

213. Herrmann F, Bundschu K, Kühl SJ, Kühl M. Tbx5 overexpression favors a first heart field lineage in murine embryonic stem cells and in Xenopus laevis embryos. *Developmental Dynamics*. 2011;240(12):2634-2645. doi:10.1002/dvdy.22776

214. Barnes RM, Firulli BA, Conway SJ, Vincentz JW, Firulli AB. Analysis of the Hand1 Cell Lineage Reveals Novel Contributions to Cardiovascular, Neural Crest, Extra-Embryonic, and Lateral Mesoderm Derivatives. *Dev Dyn*. 2010;239(11):3086-3097. doi:10.1002/dvdy.22428

215. Liang X, Wang G, Lin L, et al. HCN4 Dynamically Marks the First Heart Field and Conduction System Precursors. *Circulation Research*. 2013;113(4):399-407. doi:10.1161/CIRCRESAHA.113.301588

216. Rojas A, Kong SW, Agarwal P, Gilliss B, Pu WT, Black BL. GATA4 Is a Direct Transcriptional Activator of Cyclin D2 and Cdk4 and Is Required for Cardiomyocyte Proliferation in Anterior Heart Field-Derived Myocardium. *Molecular and Cellular Biology*. 2008;28(17):5420-5431. doi:10.1128/MCB.00717-08

217. Rana MS, Théveniau-Ruissy M, De Bono C, et al. Tbx1 Coordinates Addition of Posterior Second Heart Field Progenitor Cells to the Arterial and Venous Poles of the Heart. *Circulation Research*. 2014;115(9):790-799. doi:10.1161/CIRCRESAHA.115.305020

218. Barnes RM, Harris IS, Jaehnig EJ, et al. MEF2C regulates outflow tract alignment and transcriptional control of Tdgf1. *Development*. 2016;143(5):774-779. doi:10.1242/dev.126383

219. Zhou L, Liu J, Olson P, Zhang K, Wynne J, Xie L. Tbx5 and Osr1 interact to regulate posterior second heart field cell cycle progression for cardiac septation. *J Mol Cell Cardiol*. 2015;85:1-12. doi:10.1016/j.yjmcc.2015.05.005

220. Cohen ED, Miller MF, Wang Z, Moon RT, Morrisey EE. Wnt5a and Wnt11 are essential for second heart field progenitor development. *Development*. 2012;139(11):1931-1940. doi:10.1242/dev.069377

221. Watt AJ, Battle MA, Li J, Duncan SA. GATA4 is essential for formation of the proepicardium and regulates cardiogenesis. *Proc Natl Acad Sci U S A*. 2004;101(34):12573-12578. doi:10.1073/pnas.0400752101

222. Lin Q, Schwarz J, Bucana C, N. Olson E. Control of Mouse Cardiac Morphogenesis and Myogenesis by Transcription Factor MEF2C. *Science*. 1997;276(5317):1404-1407. doi:10.1126/science.276.5317.1404

223. Zhang KK, Xiang M, Zhou L, et al. Gene network and familial analyses uncover a gene network involving Tbx5/Osr1/Pcsk6 interaction in the second heart field for atrial septation. *Hum Mol Genet*. 2016;25(6):1140-1151. doi:10.1093/hmg/ddv636

224. Vrljicak P, Cullum R, Xu E, et al. Twist1 Transcriptional Targets in the Developing Atrio-Ventricular Canal of the Mouse. *PLOS ONE*. 2012;7(7):e40815. doi:10.1371/journal.pone.0040815

225. Schleiffarth JR, Person AD, Martinsen BJ, et al. Wnt5a Is Required for Cardiac Outflow Tract Septation in Mice. *Pediatr Res*. 2007;61(4):386-391. doi:10.1203/pdr.0b013e3180323810

226. Gessert S, Kühl M. The Multiple Phases and Faces of Wnt Signaling During Cardiac Differentiation and Development. *Circulation Research*. 2010;107(2):186-199. doi:10.1161/CIRCRESAHA.110.221531

227. Harrelson Z, Kelly RG, Goldin SN, et al. Tbx2 is essential for patterning the atrioventricular canal and for morphogenesis of the outflow tract during heart development. *Development*. 2004;131(20):5041-5052. doi:10.1242/dev.01378

228. Mesbah K, Harrelson Z, Théveniau-Ruissy M, Papaioannou VE, Kelly RG. Tbx3 Is Required for Outflow Tract Development. *Circulation Research*. 2008;103(7):743-750. doi:10.1161/CIRCRESAHA.108.172858

229. Fayet C, Bendeck MP, Gotlieb AI. Cardiac valve interstitial cells secrete fibronectin and form fibrillar adhesions in response to injury. *Cardiovascular Pathology*. 2007;16(4):203-211. doi:10.1016/j.carpath.2007.02.008

230. Zhang H, Lui KO, Zhou B. Endocardial Cell Plasticity in Cardiac Development, Diseases and Regeneration. *Circulation Research*. 2018;122(5):774-789. doi:10.1161/CIRCRESAHA.117.312136

231. Forte E, Furtado MB, Rosenthal N. The interstitium in cardiac repair: role of the immune–stromal cell interplay. *Nat Rev Cardiol*. 2018;15(10):601-616. doi:10.1038/s41569-018-0077-x

232. Hofbauer P, Jahnel S, Papai N, et al. Cardioids reveal self-organizing principles of human cardiogenesis. *bioRxiv*. Published online July 6, 2020:2020.07.06.189431. doi:10.1101/2020.07.06.189431

233. Lopaschuk GD, Jaswal JS. Energy metabolic phenotype of the cardiomyocyte during development, differentiation, and postnatal maturation. *J Cardiovasc Pharmacol*. 2010;56(2):130-140. doi:10.1097/FJC.0b013e3181e74a14

234. Piquereau J, Ventura-Clapier R. Maturation of Cardiac Energy Metabolism During Perinatal Development. *Front Physiol*. 2018;9:959. doi:10.3389/fphys.2018.00959

235. Barger PM, Kelly DP. PPAR signaling in the control of cardiac energy metabolism. *Trends Cardiovasc Med*. 2000;10(6):238-245. doi:10.1016/s1050-1738(00)00077-3

236. LeBleu VS, O'Connell JT, Gonzalez Herrera KN, et al. PGC-1α mediates mitochondrial biogenesis and oxidative phosphorylation in cancer cells to promote metastasis. *Nat Cell Biol*. 2014;16(10):992-1003. doi:10.1038/ncb3039

237. Jogl G, Tong L. Crystal Structure of Carnitine Acetyltransferase and Implications for the Catalytic Mechanism and Fatty Acid Transport. *Cell*. 2003;112(1):113-122. doi:10.1016/S0092-8674(02)01228-X

238. Weis BC, Cowan AT, Brown N, Foster DW, McGarry JD. Use of a selective inhibitor of liver carnitine palmitoyltransferase I (CPT I) allows quantification of its contribution to total CPT I activity in rat heart. Evidence that the dominant cardiac CPT I isoform is identical to the skeletal muscle enzyme. *Journal of Biological Chemistry*. 1994;269(42):26443-26448. doi:10.1016/S0021-9258(18)47214-6

239. Cai W, Zhang J, de Lange WJ, et al. An Unbiased Proteomics Method to Assess the Maturation of Human Pluripotent Stem Cell–Derived Cardiomyocytes. *Circulation Research*. 2019;125(11):936-953. doi:10.1161/CIRCRESAHA.119.315305

240. Shadrin IY, Allen BW, Qian Y, et al. Cardiopatch platform enables maturation and scale-up of human pluripotent stem cell-derived engineered heart tissues. *Nat Commun*. 2017;8(1):1825. doi:10.1038/s41467-017-01946-x

241. Aballo TJ, Roberts DS, Bayne EF, et al. Integrated proteomics reveals alterations in sarcomere composition and developmental processes during postnatal swine heart development. *Journal of Molecular and Cellular Cardiology*. 2023;176:33-40. doi:10.1016/j.yjmcc.2023.01.004

242. Diguet N, Trammell SAJ, Tannous C, et al. Nicotinamide Riboside Preserves Cardiac Function in a Mouse Model of Dilated Cardiomyopathy. *Circulation*. 2018;137(21):2256-2273. doi:10.1161/CIRCULATIONAHA.116.026099

243. Pollak NM, Hoffman M, Goldberg IJ, Drosatos K. Krüppel-Like Factors. *JACC: Basic to Translational Science*. 2018;3(1):132-156. doi:10.1016/j.jacbts.2017.09.001

244. Thakkar C, Alikunju S, Rizvi W, Abbas A, Sayed D. Klf9 plays a critical role in GR – dependent metabolic adaptations in cardiomyocytes. Published online May 9, 2023:2023.05.08.539871. doi:10.1101/2023.05.08.539871

245. Bers DM. Cardiac excitation–contraction coupling. *Nature*. 2002;415(6868):198-205. doi:10.1038/415198a

246. Giudicessi JR, Ackerman MJ. Potassium-channel mutations and cardiac arrhythmias--diagnosis and therapy. *Nat Rev Cardiol*. 2012;9(6):319-332. doi:10.1038/nrcardio.2012.3

247. Leblanc N, Hume JR. Sodium current-induced release of calcium from cardiac sarcoplasmic reticulum. *Science*. 1990;248(4953):372-376. doi:10.1126/science.2158146

248. Pennisi DJ, Rentschler S, Gourdie RG, Fishman GI, Mikawa T. Induction and patterning of the cardiac conduction system. *Int J Dev Biol*. 2004;46(6):765-775. doi:10.1387/ijdb.12382942

249. van Weerd JH, Christoffels VM. The formation and function of the cardiac conduction system. *Development*. 2016;143(2):197-210. doi:10.1242/dev.124883

250. Schats R, Jansen CA, Wladimiroff JW. Embryonic heart activity: appearance and development in early human pregnancy. *Br J Obstet Gynaecol*. 1990;97(11):989-994. doi:10.1111/j.1471-0528.1990.tb02469.x

251. Männer J. When Does the Human Embryonic Heart Start Beating? A Review of Contemporary and Historical Sources of Knowledge about the Onset of Blood Circulation in Man. *J Cardiovasc Dev Dis*. 2022;9(6):187. doi:10.3390/jcdd9060187

252. Fleischer S, Inui M. Biochemistry and Biophysics of Excitation-Contraction Coupling. *Annual Review of Biophysics and Biophysical Chemistry*. 1989;18(1):333-364. doi:10.1146/annurev.bb.18.060189.002001

253. Warmke JW, Ganetzky B. A family of potassium channel genes related to eag in Drosophila and mammals. *Proc Natl Acad Sci U S A*. 1994;91(8):3438-3442.

254. Sanguinetti MC, Tristani-Firouzi M. hERG potassium channels and cardiac arrhythmia. *Nature*. 2006;440(7083):463-469. doi:10.1038/nature04710

255. Carss KJ, Deaton AM, Del Rio-Espinola A, et al. Using human genetics to improve safety assessment of therapeutics. *Nat Rev Drug Discov*. Published online October 19, 2022:1-18. doi:10.1038/s41573-022-00561-w

256. Holbrook M, Malik M, Shah RR, Valentin JP. Drug induced shortening of the QT/QTc interval: An emerging safety issue warranting further modelling and evaluation in drug research and development? *Journal of Pharmacological and Toxicological Methods*. 2009;59(1):21-28. doi:10.1016/j.vascn.2008.09.001

257. Sanguinetti MC, Jiang C, Curran ME, Keating MT. A mechanistic link between an inherited and an acquired cardiac arrhythmia: HERG encodes the IKr potassium channel. *Cell*. 1995;81(2):299-307. doi:10.1016/0092-8674(95)90340-2

258. Curran ME, Splawski I, Timothy KW, Vincent GM, Green ED, Keating MT. A molecular basis for cardiac arrhythmia: HERG mutations cause long QT syndrome. *Cell*. 1995;80(5):795-803. doi:10.1016/0092-8674(95)90358-5

259. De Bruin ML, Pettersson M, Meyboom RHB, Hoes AW, Leufkens HGM. Anti-HERG activity and the risk of drug-induced arrhythmias and sudden death. *Eur Heart J*. 2005;26(6):590-597. doi:10.1093/eurheartj/ehi092

260. Fenichel RR, Malik M, Antzelevitch C, et al. Drug-induced torsades de pointes and implications for drug development. *J Cardiovasc Electrophysiol*. 2004;15(4):475-495. doi:10.1046/j.1540-8167.2004.03534.x

261. Ahlquist RP. A study of the adrenotropic receptors. *American Journal of Physiology-Legacy Content*. 1948;153(3):586-600. doi:10.1152/ajplegacy.1948.153.3.586

262. Rockman HA, Koch WJ, Lefkowitz RJ. Seven-transmembrane-spanning receptors and heart function. *Nature*. 2002;415(6868):206-212. doi:10.1038/415206a

263. Logothetis DE, Kurachi Y, Galper J, Neer EJ, Clapham DE. The βγ subunits of GTP-binding proteins activate the muscarinic K+ channel in heart. *Nature*. 1987;325(6102):321-326. doi:10.1038/325321a0

264. Florea VG, Cohn JN. The Autonomic Nervous System and Heart Failure. *Circulation Research*. 2014;114(11):1815-1826. doi:10.1161/CIRCRESAHA.114.302589

265. Lymperopoulos A, Rengo G, Koch WJ. Adrenergic Nervous System in Heart Failure. *Circulation Research*. 2013;113(6):739-753. doi:10.1161/CIRCRESAHA.113.300308

266. Uhlén M, Fagerberg L, Hallström BM, et al. Proteomics. Tissue-based map of the human proteome. *Science*. 2015;347(6220):1260419. doi:10.1126/science.1260419

267. Karlsson M, Zhang C, Méar L, et al. A single-cell type transcriptomics map of human tissues. *Sci Adv*. 2021;7(31):eabh2169. doi:10.1126/sciadv.abh2169

268. Lohse MJ, Engelhardt S, Eschenhagen T. What Is the Role of β-Adrenergic Signaling in Heart Failure? *Circulation Research*. 2003;93(10):896-906. doi:10.1161/01.RES.0000102042.83024.CA

269. Brette F, Orchard C. T-tubule function in mammalian cardiac myocytes. *Circ Res*. 2003;92(11):1182-1192. doi:10.1161/01.RES.0000074908.17214.FD

270. Ibrahim M, Gorelik J, Yacoub MH, Terracciano CM. The structure and function of cardiac t-tubules in health and disease. *Proc Biol Sci*. 2011;278(1719):2714-2723. doi:10.1098/rspb.2011.0624

271. Niederreither K, Dollé P. Retinoic acid in development: towards an integrated view. *Nat Rev Genet*. 2008;9(7):541-553. doi:10.1038/nrg2340

272. Duester G. Retinoic Acid Synthesis and Signaling during Early Organogenesis. *Cell*. 2008;134(6):921-931. doi:10.1016/j.cell.2008.09.002

273. Cai CL, Martin JC, Sun Y, et al. A myocardial lineage derives from Tbx18 epicardial cells. *Nature*. 2008;454(7200):104-108. doi:10.1038/nature06969

274. Lupu IE, Redpath AN, Smart N. Spatiotemporal Analysis Reveals Overlap of Key Proepicardial Markers in the Developing Murine Heart. *Stem Cell Reports*. 2020;14(5):770-787. doi:10.1016/j.stemcr.2020.04.002

275. Kopljar I, Lu HR, Van Ammel K, et al. Development of a Human iPSC Cardiomyocyte-Based Scoring System for Cardiac Hazard Identification in Early Drug Safety De-risking. *Stem Cell Reports*. 2018;11(6):1365-1377. doi:10.1016/j.stemcr.2018.11.007

276. Kolwicz SC, Purohit S, Tian R. Cardiac Metabolism and its Interactions With Contraction, Growth, and Survival of Cardiomyocytes. *Circulation Research*. 2013;113(5):603-616. doi:10.1161/CIRCRESAHA.113.302095

277. Dueñas A, Aranega AE, Franco D. More than Just a Simple Cardiac Envelope; Cellular Contributions of the Epicardium. *Frontiers in Cell and Developmental Biology*. 2017;5. Accessed December 3, 2022. https://www.frontiersin.org/articles/10.3389/fcell.2017.00044

278. Furtado MB, Nim HT, Boyd SE, Rosenthal NA. View from the heart: cardiac fibroblasts in development, scarring and regeneration. *Development*. 2016;143(3):387-397. doi:10.1242/dev.120576

279. Christoffels VM, Moorman AFM. Development of the Cardiac Conduction System. *Circulation: Arrhythmia and Electrophysiology*. 2009;2(2):195-207. doi:10.1161/CIRCEP.108.829341

280. Ribeiro AJS, Ang YS, Fu JD, et al. Contractility of single cardiomyocytes differentiated from pluripotent stem cells depends on physiological shape and substrate stiffness. *Proceedings of the National Academy of Sciences*. 2015;112(41):12705-12710. doi:10.1073/pnas.1508073112

281. Pioner JM, Racca AW, Klaiman JM, et al. Isolation and Mechanical Measurements of Myofibrils from Human Induced Pluripotent Stem Cell-Derived Cardiomyocytes. *Stem Cell Reports*. 2016;6(6):885-896. doi:10.1016/j.stemcr.2016.04.006

282. Goversen B, van der Heyden MAG, van Veen TAB, de Boer TP. The immature electrophysiological phenotype of iPSC-CMs still hampers in vitro drug screening: Special focus on IK1. *Pharmacology & Therapeutics*. 2018;183:127-136. doi:10.1016/j.pharmthera.2017.10.001

283. Hibino H, Inanobe A, Furutani K, Murakami S, Findlay I, Kurachi Y. Inwardly Rectifying Potassium Channels: Their Structure, Function, and Physiological Roles. *Physiological Reviews*. 2010;90(1):291-366. doi:10.1152/physrev.00021.2009

284. Gittenberger-de Groot AC, Bartelings MM, Deruiter MC, Poelmann RE. Basics of Cardiac Development for the Understanding of Congenital Heart Malformations. *Pediatr Res*. 2005;57(2):169-176. doi:10.1203/01.PDR.0000148710.69159.61

285. Hikspoors JPJM, Kruepunga N, Mommen GMC, Köhler SE, Anderson RH, Lamers WH. A pictorial account of the human embryonic heart between 3.5 and 8 weeks of development. *Commun Biol*. 2022;5(1):1-22. doi:10.1038/s42003-022-03153-x

286. Meilhac SM, Buckingham ME. The deployment of cell lineages that form the mammalian heart. *Nat Rev Cardiol*. 2018;15(11):705-724. doi:10.1038/s41569-018-0086-9

287. Wu W, He J, Shao X. Incidence and mortality trend of congenital heart disease at the global, regional, and national level, 1990–2017. *Medicine*. 2020;99(23):e20593. doi:10.1097/MD.0000000000020593

288. Perera F, Herbstman J. Prenatal environmental exposures, epigenetics, and disease. *Reproductive Toxicology*. 2011;31(3):363-373. doi:10.1016/j.reprotox.2010.12.055

289. Vinci MC, Polvani G, Pesce M. Epigenetic Programming and Risk: The Birthplace of Cardiovascular Disease? *Stem Cell Rev and Rep*. 2013;9(3):241-253. doi:10.1007/s12015-012-9398-z

290. Gluckman PD, Hanson MA, Buklijas T, Low FM, Beedle AS. Epigenetic mechanisms that underpin metabolic and cardiovascular diseases. *Nat Rev Endocrinol*. 2009;5(7):401-408. doi:10.1038/nrendo.2009.102

291. Einarson TR, Piwko C, Koren G. QUANTIFYING THE GLOBAL RATES OF NAUSEA AND VOMITING OF PREGNANCY: A META-ANALYSIS. *J Popl Ther Clin Pharmacol*. 2013;20(2). Accessed July 13, 2023. https://www.jptcp.com

292. Taylor LG, Bird ST, Sahin L, et al. Antiemetic use among pregnant women in the United States: the escalating use of ondansetron. *Pharmacoepidemiology and Drug Safety*. 2017;26(5):592-596. doi:10.1002/pds.4185

293. Lemon LS, Bodnar LM, Garrard W, et al. Ondansetron use in the first trimester of pregnancy and the risk of neonatal ventricular septal defect. *International Journal of Epidemiology*. 2020;49(2):648-656. doi:10.1093/ije/dyz255

294. Danielsson B, Webster WS, Ritchie HE. Ondansetron and teratogenicity in rats: Evidence for a mechanism mediated via embryonic hERG blockade. *Reproductive Toxicology*. 2018;81:237-245. doi:10.1016/j.reprotox.2018.08.018

295. Danielsson B, Wikner BN, Källén B. Use of ondansetron during pregnancy and congenital malformations in the infant. *Reproductive Toxicology*. 2014;50:134-137. doi:10.1016/j.reprotox.2014.10.017

296. Zambelli-Weiner A, Via C, Yuen M, Weiner DJ, Kirby RS. First trimester ondansetron exposure and risk of structural birth defects. *Reproductive Toxicology*. 2019;83:14-20. doi:10.1016/j.reprotox.2018.10.010

297. Dormuth CR, Winquist B, Fisher A, et al. Comparison of Pregnancy Outcomes of Patients Treated With Ondansetron vs Alternative Antiemetic Medications in a Multinational, Population-Based Cohort. *JAMA Network Open*. 2021;4(4):e215329. doi:10.1001/jamanetworkopen.2021.5329

298. Huybrechts KF, Hernández-Díaz S, Straub L, et al. Association of Maternal First-Trimester Ondansetron Use With Cardiac Malformations and Oral Clefts in Offspring. *JAMA*. 2018;320(23):2429-2437. doi:10.1001/jama.2018.18307

299. Parker SE, Van Bennekom C, Anderka M, Mitchell AA, Study for the NBDP. Ondansetron for Treatment of Nausea and Vomiting of Pregnancy and the Risk of Specific Birth Defects. *Obstetrics & Gynecology*. 2018;132(2):385. doi:10.1097/AOG.0000000000002679

300. Frommeyer G, Fischer C, Ellermann C, et al. Severe Proarrhythmic Potential of the Antiemetic Agents Ondansetron and Domperidone. *Cardiovasc Toxicol*. 2017;17(4):451-457. doi:10.1007/s12012-017-9403-5

301. Williams PD, Cohen ML, Turk JA. Electrocardiographic effects of zatosetron and ondansetron, two 5HT3 receptor antagonists, in anesthetized dogs. *Drug Development Research*. 1991;24(3):277-284. doi:10.1002/ddr.430240309

302. Blinova K, Dang Q, Millard D, et al. International Multisite Study of Human-Induced Pluripotent Stem Cell-Derived Cardiomyocytes for Drug Proarrhythmic Potential Assessment. *Cell Reports*. 2018;24(13):3582-3592. doi:10.1016/j.celrep.2018.08.079

303. Lu HR, Zeng H, Kettenhofen R, et al. Assessing Drug-Induced Long QT and Proarrhythmic Risk Using Human Stem-Cell-Derived Cardiomyocytes in a Ca2+ Imaging Assay: Evaluation of 28 CiPA Compounds at Three Test Sites. *Toxicological Sciences*. 2019;170(2):345-356. doi:10.1093/toxsci/kfz102

304. Leow JWH, Gu Y, Chan ECY. Investigating the relevance of CYP2J2 inhibition for drugs known to cause intermediate to high risk torsades de pointes. *European Journal of Pharmaceutical Sciences*. 2023;187:106475. doi:10.1016/j.ejps.2023.106475

305. Patel D, Stohlman J, Dang Q, Strauss DG, Blinova K. Assessment of Proarrhythmic Potential of Drugs in Optogenetically Paced Induced Pluripotent Stem Cell-Derived Cardiomyocytes. *Toxicological Sciences*. 2019;170(1):167-179. doi:10.1093/toxsci/kfz076

306. Huang C, Sheikh F, Hollander M, et al. Embryonic atrial function is essential for mouse embryogenesis, cardiac morphogenesis and angiogenesis. *Development*. 2003;130(24):6111-6119. doi:10.1242/dev.00831

307. Chen J, Kubalak SW, Minamisawa S, et al. Selective Requirement of Myosin Light Chain 2v in Embryonic Heart Function*. *Journal of Biological Chemistry*. 1998;273(2):1252-1256. doi:10.1074/jbc.273.2.1252

308. Hafermann MJ, Namdar R, Seibold GE, Page RL. Effect of intravenous ondansetron on QT interval prolongation in patients with cardiovascular disease and additional risk factors for torsades: a prospective, observational study. *Drug, Healthcare and Patient Safety*. 2011;3:53-58. doi:10.2147/DHPS.S25623

309. Kuryshev YA, Brown AM, Wang L, Benedict CR, Rampe D. Interactions of the 5-Hydroxytryptamine 3 Antagonist Class of Antiemetic Drugs with Human Cardiac Ion Channels. *J Pharmacol Exp Ther*. 2000;295(2):614-620.

310. Cai F, Luis MAF, Lin X, et al. Anthracycline-induced cardiotoxicity in the chemotherapy treatment of breast cancer: Preventive strategies and treatment. *Mol Clin Oncol*. 2019;11(1):15-23. doi:10.3892/mco.2019.1854

311. Bejleri D, Streeter BW, Nachlas ALY, et al. A Bioprinted Cardiac Patch Composed of Cardiac-Specific Extracellular Matrix and Progenitor Cells for Heart Repair. *Advanced Healthcare Materials*. 2018;7(23):1800672. doi:10.1002/adhm.201800672

312. Wei HJ, Chen CH, Lee WY, et al. Bioengineered cardiac patch constructed from multilayered mesenchymal stem cells for myocardial repair. *Biomaterials*. 2008;29(26):3547-3556. doi:10.1016/j.biomaterials.2008.05.009

313. Yeung E, Fukunishi T, Bai Y, et al. Cardiac regeneration using human-induced pluripotent stem cell-derived biomaterial-free 3D-bioprinted cardiac patch in vivo. *Journal of Tissue Engineering and Regenerative Medicine*. 2019;13(11):2031-2039. doi:10.1002/term.2954

314. Cui H, Nowicki M, Fisher JP, Zhang LG. 3D Bioprinting for Organ Regeneration. *Advanced Healthcare Materials*. 2017;6(1):1601118. doi:10.1002/adhm.201601118

APPENDIX

ANTIBODIES AND MOLECULAR PROBES USED THROUGH THE DISSERTATION

Table A.1. Primary and secondary antibodies used for imaging purposes in this dissertation.

	Antibody Name	Host Species	Dilution	Catalogue Number	Vendor
Primary	TNNT2	Mouse	1:200	ab8295	Abcam
	TNNT2	Rabbit	1:200	ab45932	Abcam
	WT1	Rabbit	1:200	ab89901	Abcam
	PECAM1	Mouse	1:50	P2B1	DSHB
	MYL2	Rabbit	1:200	ab79935	Abcam
	MYL7	Mouse	1:200	311-011	Synaptic Systems
	TBX18	Mouse	1:200	ab201587	Abcam
	ALDH1A2	Rabbit	1:200	ABN420	Sigma
	KCNJ2	Rabbit	1:500	HPA029109	Sigma
	NR2F2	Rabbit	1:100	ab211777	Abcam
	MYL3	Mouse	1:50	Sc-47719	Santa Cruz Biotechnology
	Caveolin-3	Mouse	1:50	MAB6706-SP	R&D Systems
Secondary	Alexa Fluor 488	Donkey anti-mouse	1:200	A-21202	Thermo Fisher Scientific
	Alexa Fluor 488	Donkey anti-rabbit	1:200	A-21206	Thermo Fisher Scientific
	Alexa Fluor 594	Donkey anti-mouse	1:200	A-21203	Thermo Fisher Scientific
	Alexa Fluor 594	Donkey anti-rabbit	1:200	A-21207	Thermo Fisher Scientific
	Alexa Fluor 647	Donkey anti-rabbit	1:200	A-31573	Thermo Fisher Scientific

Table A.2. Fluorescent molecules used for imaging purposes in this dissertation.

Dye/Molecule	Target	Dilution	Catalogue Number	Vendor
DAPI	Nucleus (DNA)	1:1000	62248	Thermo Fisher Scientific
Di-8-ANEPPS	Cell Membrane	10 μM	D3167	Thermo Fisher Scientific
Fluo-4, AM	Intracellular calcium ions	1 μM	F14201	Thermo Fisher Scientific
MitoTracker	Mitochondria	100 nM	M22426	Thermo Fisher Scientific
NucBlue	Nucleus (DNA)	2 drops/mL	R37605	Thermo Fisher Scientific
WGA/FITC	T-tubules	1:200	L4895	Sigma

PUBLICATIONS, PATENTS, AND PRESENTATIONS

Publications

1. Kostina A, Lewis-Israeli YR, Abdelhamid M, .., **Volmert B**, et al. ER stress and lipid imbalance drive diabetic embryonic cardiomyopathy in an organoid model of human heart development. *Stem Cell Reports*. Published online February 2024:S2213671124000067. doi:10.1016/j.stemcr.2024.01.003

2. Kostina A, **Volmert B**, Aguirre A. Human heart organoids: current applications and future perspectives. *European Heart Journal*. Published online December 16, 2023:ehad841. doi:10.1093/eurheartj/ehad841

3. **Volmert B**, Kiselev A, Juhong A, et al. A patterned human primitive heart organoid model generated by pluripotent stem cell self-organization. *Nat Commun.* 2023;14(1):8245. doi:10.1038/s41467-023-43999-1

4. Hao S, Ren C, Wang F, .., **Volmert B**, et al. Dual-modality imaging system for monitoring human heart organoids beating in vitro. *Opt Lett*. 2023;48(15):3929-3932. doi:10.1364/OL.493824

5. Lewis-Israeli YR, **Volmert BD**, Gabalski MA, Huang AR, Aguirre A. Generation of Self-Assembling Heart Organoids from Human Pluripotent Stem Cells. *Protocol Exchange*; 2022. doi:10.21203/rs.3.pex-1589/v1

6. Ming Y, Hao S, Wang F, .., **Volmert B**, et al. Longitudinal morphological and functional characterization of human heart organoids using optical coherence tomography. *Biosensors and Bioelectronics*. 2022;207:114136. doi:10.1016/j.bios.2022.114136

7. Lewis-Israeli YR, **Volmert BD**, Gabalski MA, Huang AR, Aguirre A. Generating Self-Assembling Human Heart Organoids Derived from Pluripotent Stem Cells. *JoVE*. 2021;(175):63097. doi:10.3791/63097

8. Lewis-Israeli YR, Wasserman AH, Gabalski MA, **Volmert B**, et al. Self-assembling human heart organoids for the modeling of cardiac development and congenital heart disease. *Nat Commun.* 2021;12(1):5142. doi:10.1038/s41467-021-25329-5

9. Chan C, Foster ST, Chan KG, .., **Volmert B**, et al. Repositioned Drugs for COVID-19—the Impact on Multiple Organs. *SN Compr Clin Med*. 2021;3(7):1484-1501. doi:10.1007/s42399-021-00874-8

Patents

Methods for heart organoid maturation. Aitor Aguirre, **Brett Volmert**. Licensed to Stem Cell Technologies.

Presentations

1. **"A patterned human heart tube organoid model generated by pluripotent stem cell self-assembly"**, Poster Presentation, Institute for Quantitative Health Science and Engineering Poster Session, 2024, East Lansing MI

2. **"Growing Mini Human Hearts From Pluripotent Stem Cells"**, Oral Presentation, Institute for Quantitative Health Science and Engineering Zebra Fish Tank Event, 2024, East Lansing, MI

3. **"Quantitative Analysis of In Vitro Images Using ImageJ"**, Oral Presentation, Image Analysis Symposium, 2024, East Lansing, MI

4. **"A patterned human heart tube organoid model generated by pluripotent stem cell self-assembly"**, Poster Presentation, Precision Medicine Symposium, 2023, East Lansing, MI

5. **"Developmental modeling enhances morphological and physiological complexity in self-assembling human heart organoids"**, Poster Presentation, Institute for Quantitative Health Science and Engineering Poster Presentation, 2023, East Lansing MI

6. **“Growing Mini Human Hearts From Stem Cells”**, Oral Presentation, IGNITE MSU, 2023, East Lansing, MI

7. **“Developmental modeling enhances morphological and physiological complexity in self-assembling human heart organoids”**, Poster Presentation, American Heart Association Annual Conference, 2022, Chicago, IL